Topics in Current Chemistry Collections

Alberto Credi *Editor*

Photoactive Semiconductor Nanocrystal Quantum Dots

Fundamentals and Applications

Springer

Topics in Current Chemistry Collections

Aims and Scope

The series Topics in Current Chemistry Collections presents critical reviews from the journal Topics in Current Chemistry organized in topical volumes. The scope of coverage is all areas of chemical science including the interfaces with related disciplines such as biology, medicine and materials science.

The goal of each thematic volume is to give the non-specialist reader, whether in academia or industry, a comprehensive insight into an area where new research is emerging which is of interest to a larger scientific audience.

Each review within the volume critically surveys one aspect of that topic and places it within the context of the volume as a whole. The most significant developments of the last 5 to 10 years are presented using selected examples to illustrate the principles discussed. The coverage is not intended to be an exhaustive summary of the field or include large quantities of data, but should rather be conceptual, concentrating on the methodological thinking that will allow the non-specialist reader to understand the information presented.

Contributions also offer an outlook on potential future developments in the field.

More information about this series at http://www.springer.com/series/14181

Alberto Credi
Editor

Photoactive Semiconductor Nanocrystal Quantum Dots

Fundamentals and Applications

With contributions from

Jaume Garcia-Amorós • Uri Banin • Massimo Baroncini
Yuval Ben-Shahar • Giacomo Bergamini • Carolina Carrillo-Carrión
Paola Ceroni • Alberto Credi • Celso de Mello Donega
Alberto Escudero • Brian A. Korgel • Marcello La Rosa
Wolfgang J. Parak • Freddy T. Rabouw • Françisco M. Raymo
Andrey L. Rogach • Francesco Romano • Lorenzo Sansalone
Serena Silvi • Liang Su • Sicheng Tang • Ek Raj Thapaliya
Yixuan Yu • Xiaoyu Zhang • Yang Zhang • Yu Zhang
Mikhail V. Zyuzin

Springer

Editor
Alberto Credi
CLAN - Center for Light Activated Nanostructures
Dipartimento di Scienze e Tecnologie Agro-alimentari
Università di Bologna, and Istituto ISOF-CNR
Bologna, Italy

Originally published in Top Curr Chem (Z) Volume 374 (2016),

ISSN 2367-4067 ISSN 2367-4075 (electronic)
Topics in Current Chemistry Collections
ISBN 978-3-319-51191-7 ISBN 978-3-319-51192-4 (eBook)
DOI 10.1007/978-3-319-51192-4

Library of Congress Control Number: 2016963802

Printed on acid-free paper

This Springer imprint is published by Springer Nature
The registered company is Springer International Publishing AG
The registered company address is: Gewerbestrasse 11, 6330 Cham, Switzerland

Contents

Top Curr Chem (Z) (2016) 374 78
DOI 10.1007/s41061-016-0078-3

EDITORIAL

Editorial

Alberto Credi[1]

If you type "quantum dot" in your web search engine, you are overwhelmed by pictures showing series of bright vials of different colors, ranging from blue to red. The captions inform you that all of the multi-colored vials in each photo contain the same chemical compound—typically cadmium selenide (CdSe). Although I have been working in the field for a number of years, I am still captured by the fact that these glowing colors are a direct manifestation of quantum theory and arise from nanometer-sized objects that are manufactured with extreme precision in a chemistry laboratory.

Many characteristics of matter undergo a significant change when transitioning from the macroscopic world of our senses to the world of nanometers. This is why the nanoscale has become a new fascinating playground that scientists, with the help of increasingly more sophisticated experimental and theoretical tools, can explore. The nanoscale has also turned out to provide a unique meeting point for researchers working in disciplines as different as physics and medicine, passing through chemistry, biology, materials science and engineering.

Colloidal nanoparticles are appropriate systems both to investigate the unconventional phenomena that can take place at the nanoscale and to exploit them for innovative applications. Optical and electronic properties, for example, are strongly affected by size effects. Thanks to the progress made in materials synthesis, the making of nanoparticles with a strict control of size and shape has become a routine laboratory practice in many instances, and several kinds of colloidal quantum dots are commercially available nowadays.

As a photochemist, I am deeply intrigued by the possibility of constructing nanoparticle-based, made-to-order chromophores and luminophores just by

This is part of the Topical Collection "Photoactive semiconductor nanocrystal quantum dots"; edited by Alberto Credi.

✉ Alberto Credi
alberto.credi@unibo.it

[1] Dipartimento di Scienze e Tecnologie Agro-Alimentari, Università di Bologna, Bologna, Italy

Published online: 07 November 2016

adjusting their diameter. Quantum dots enable the observation of fascinating and uncommon phenomena that arise from their interaction with light, such as blinking, multi-exciton generation and two-photon processes. These properties are important not only for their technological potential but also for their conceptual implications—as noted above, the effects of quantum mechanics are brought to our sight!

As a supramolecular chemist, I am attracted by the almost unlimited possibilities offered by the interfacing of nanoparticles with molecular units, surfaces or other nanomaterials to yield inorganic–organic hybrids with tailored physical and chemical properties. Indeed, in recent years the set of components that may be employed to assemble new systems and materials from the bottom up has been extended from (supra) molecular species to nano-sized particles of various morphologies and chemical composition.

The collection of articles which appears in this issue of *Topics in Current Chemistry* is aimed at providing an overview of the recent advances in the development of photoactive semiconductor nanocrystals. The area is so vast that it could not be exhaustively covered in this compendium. However, my hope is that the articles will entice the reader by providing a taste of the vivacity of the field, stimulating the interest of researchers and raising the curiosity of students and non-specialists. The active engagement of leading scientists in the field ensures that the topics presented in this compendium are of high current interest and are discussed in a competent and authoritative manner. Indeed, the various contributions provide a view of the field from diverse perspectives—from ultrafast excited-state relaxation to light-emitting diodes—and underline both the exciting fundamental challenges and the appealing prospects for practical applications that this dynamic research field can offer.

I would like to express my gratitude to the colleagues and friends who have shared their knowledge and supported this editorial endeavor by providing clear and engaging texts, high-quality schemes and splendid images. I hope that the reader will enjoy reading these articles as much as I did while collecting and assembling them in the issue. Finally, I thank the editorial staff at Springer for their support throughout the development of this topical collection.

Bologna, October 2016

Alberto Credi

Top Curr Chem (Z) (2016) 374:58
DOI 10.1007/s41061-016-0060-0

REVIEW

Excited-State Dynamics in Colloidal Semiconductor Nanocrystals

Freddy T. Rabouw[1,2,3] · Celso de Mello Donega[4]

Received: 12 May 2016 / Accepted: 23 July 2016 / Published online: 9 August 2016

Abstract Colloidal semiconductor nanocrystals have attracted continuous worldwide interest over the last three decades owing to their remarkable and unique size- and shape-, dependent properties. The colloidal nature of these nanomaterials allows one to take full advantage of nanoscale effects to tailor their optoelectronic and physical–chemical properties, yielding materials that combine size-, shape-, and composition-dependent properties with easy surface manipulation and solution processing. These features have turned the study of colloidal semiconductor nanocrystals into a dynamic and multidisciplinary research field, with fascinating fundamental challenges and dazzling application prospects. This review focuses on the excited-state dynamics in these intriguing nanomaterials, covering a range of different relaxation mechanisms that span over 15 orders of magnitude, from a few femtoseconds to a few seconds after photoexcitation. In addition to reviewing the state of the art and highlighting the essential concepts in the field, we also discuss

This article is part of the Topical Collection "Photoactive Semiconductor Nanocrystal Quantum Dots", edited by Alberto Credi.

✉ Celso de Mello Donega
c.demello-donega@uu.nl

Freddy T. Rabouw
f.t.rabouw@uu.nl

[1] Inorganic Chemistry and Catalysis, Debye Institute for Nanomaterials Science, Utrecht University, PO Box 80000, 3508 TA Utrecht, The Netherlands

[2] Soft Condensed Matter, Debye Institute for Nanomaterials Science, Utrecht University, PO Box 80000, 3508 TA Utrecht, The Netherlands

[3] Present Address: Optical Materials Engineering Laboratory, ETH Zurich, 8092 Zurich, Switzerland

[4] Condensed Matter and Interfaces, Debye Institute for Nanomaterials Science, Utrecht University, PO Box 80000, 3508 TA Utrecht, The Netherlands

the relevance of the different relaxation processes to a number of potential applications, such as photovoltaics and LEDs. The fundamental physical and chemical principles needed to control and understand the properties of colloidal semiconductor nanocrystals are also addressed.

Keywords Semiconductor nanocrystals · Colloids · Exciton dynamics · Nanoscale · Auger relaxation

1 Introduction

Since the pioneering work of Brus, Ekimov, and many others in the early 1980–1990s [1–13], the study of semiconductor nanocrystals (NCs) has developed into a mature, dynamic and multidisciplinary research field, which attracts increasing attention worldwide, both for its fundamental challenges and its potential for a number of technologies (light emitting devices, solar cells, luminescent solar concentrators, optoelectronics, sensing, thermoelectrics, biomedical applications, catalysis) [14–32]. Colloidal semiconductor NCs are particularly attractive, since they consist of an inorganic core that is coated with a stabilizing layer of (usually) organic ligand molecules. This hybrid inorganic–organic nature makes them very versatile nanomaterials that combine size-, shape-, and composition-dependent optoelectronic properties of the core with easy surface manipulation and solution processing [16].

Here, we will address the excited-state dynamics in colloidal semiconductor NCs, covering a time scale that spans over 15 orders of magnitude, from a few femtoseconds to seconds after photoexcitation. We intend to provide a critical overview of the field, in which the recent advances are discussed and the outstanding challenges are identified. The relevance of different excited-state relaxation processes to a number of potential applications will also be highlighted. This review is not meant to be exhaustive, but rather to convey a concise account of the state-of-the-art, in which the essential aspects are outlined and discussed. For further details or an in-depth treatment of topics that are beyond the scope of this work, the reader will be referred to the recent literature. This article is organized as follows. In Sect. 2, we discuss how excitons in semiconductor NCs are affected by nanoscale effects. In Sect. 3, the relaxation dynamics of nanoscale excitons in colloidal semiconductor NCs is addressed, with particular emphasis on the processes that occur at different time scales after photoexcitation. In the last section, we summarize the essential aspects discussed and the outlook for the field.

2 Excitons in Semiconductor Nanocrystals

2.1 Quantum Confinement Effects: Squeezing and Shaping Nanoscale Excitons

Absorption by a semiconductor of a photon with energy equal to or larger than its bandgap (E_g) promotes an electron from the valence band (VB) to the conduction

band (CB), leaving a hole in the VB, and forming an exciton (i.e., an electron–hole pair bound by Coulomb interaction). The impact of spatial confinement to the nanoscale depends on characteristic length scales associated with the physical property under consideration. In the case of the properties of excitons in semiconductors, this characteristic length scale is given by the exciton Bohr radius (a_0), which ranges from $\sim$2 to $\sim$50 nm, depending on the material [33]. For semiconductor NC sizes of approximately a_0 and smaller, the exciton wave function is affected by spatial confinement [33]. This induces size-dependent changes in the density of electronic states and in the energy separation between them, which are manifested in an increase of the bandgap (or HOMO–LUMO energy gap) and the appearance of discrete energy levels near the band edges with decreasing NC dimensions (Fig. 1) [33–35]. This effect is commonly referred to as quantum confinement, and makes it possible to tune the optical spectra (absorption and photoluminescence, PL) of semiconductor NCs through a wide spectral window by simply changing their size, while keeping their composition constant (Fig. 1). Further, the degree of quantum confinement may be different in different directions of the NC, depending on its size and shape (Fig. 2) [33, 35]. If the exciton is

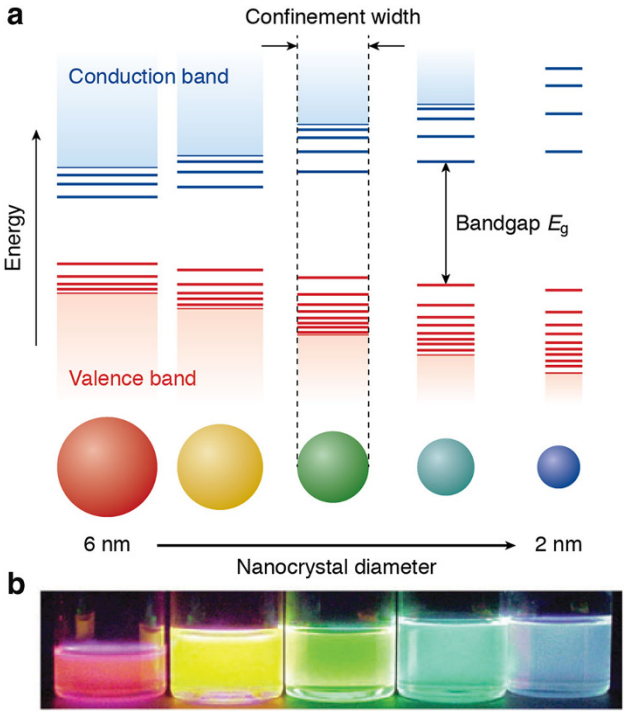

Fig. 1 **a** Schematic representation of the quantum confinement effects: the bandgap (or HOMO–LUMO gap) of the semiconductor nanocrystal increases with decreasing size, while discrete energy levels arise at the band-edges. The energy separation between the band-edge levels also increases with decreasing size. **b** Photograph of five colloidal dispersions of CdSe QDs with different sizes, under excitation with a UV-lamp in the dark. The color of the photoluminescence changes from red to blue as the QD diameter is reduced from 6 to 2 nm. Adapted from Ref. [16] with permission of the Royal Society of Chemistry

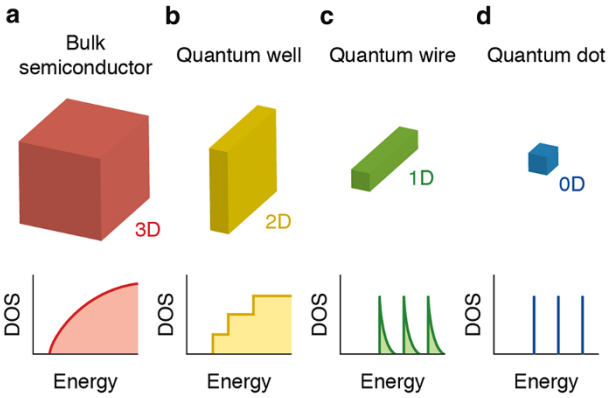

Fig. 2 Schematic illustration of the energy level structure of a bulk semiconductor (**a**), and semiconductor nanostructures (**b**–**d**) with reduced dimensionality. **b** 2D semiconductor nanostructure or quantum well. **c** 1D semiconductor nanostructure or quantum wire. **d** 0D semiconductor nanostructure or quantum dot. *DOS* represents the density of electronic states

spatially confined in all directions, a quantum dot (QD) is obtained, while NCs in which the exciton is confined only in the diameter direction are referred to as quantum wires. Quantum confinement in the thickness direction only (2D confinement) results in a quantum well. Quantum rods are NCs in transition from the zero-dimensional confinement regime of QDs to the 1D confinement regime of quantum wires. This makes the optoelectronic properties of semiconductor NCs also strongly shape-dependent. In the quantum confinement regime, the size and shape of semiconductor NCs also have an impact on the exciton fine-structure. The exciton fine-structure is the way in which the energy states of the exciton are split by effects of the crystal field asymmetry, NC shape anisotropy, and electron–hole exchange interaction [36–38]. Exciton fine-structure splitting is analogous to singlet–triplet splitting in organic molecules, but the energy splittings for an exciton in a NC are typically smaller, namely only a few meV. Effects of the exciton fine-structure are therefore relevant only at low temperatures (below 100 K), where they affect the temperature- and magnetic-field dependences of the exciton lifetimes. These effects are beyond the scope of this review. The interested reader is referred to a number of publications addressing this topic in detail [36–48].

Phonons (i.e., lattice vibrations) have a pervasive role in semiconductors, and therefore coupling of charge carriers and excitons to phonons plays a decisive role in a wide range of properties [49]. The interaction between phonons and excitons in nanoscale semiconductors is expected to differ from that in bulk materials due to both quantum confinement effects on the exciton energy levels and dimensional confinement of phonon modes (i.e., the phonon wavelength cannot be larger than the NC size) [49]. Coupling of photogenerated carriers to phonons provides an important energy relaxation pathway, thus being essential to a number of photophysical processes in semiconductor NCs (e.g., exciton relaxation dynamics, carrier cooling, thermal transport) [42, 50–53]. Moreover, coupling to acoustic phonon modes determines the homogeneous linewidths of optical transitions

[54, 55], while coupling to optical phonon modes has been observed to relax selection rules at low temperatures, yielding distinct phonon-assisted transitions (the so-called phonon replicas) [56, 57].

2.2 Composition Effects: Tailoring the Property Gamut

As mentioned in Sect. 2.1 above, the exciton Bohr radius is a material property. As a result, different semiconductors experience quantum confinement at different NC sizes, depending on their exciton Bohr radius. Moreover, the bulk bandgap of different semiconductor materials covers a range of energies from the infrared to the ultraviolet. As a result, the bandgap of different semiconductor NCs is tunable over different spectral windows [16, 26, 33, 35]. For example, the lowest energy absorption transition of CdSe QDs can be tuned from 1.75 eV (the bulk E_g value) to 2.65 eV for diameters ranging from $\sim$10 nm ($a_0 = 4.9$ nm) to 2 nm [58], while that of PbSe QDs can be tuned from 0.3 eV (the bulk E_g value) to 1.5 eV for diameters ranging from $\sim$100 nm ($a_0 = 46$ nm) to 2 nm [59]. The optoelectronic properties of semiconductor NCs can thus be tailored by choosing their composition and controlling their size and shape.

The control over the properties of colloidal NCs can be extended further by using NCs consisting of two (or more) different semiconductors joined together by heterointerfaces, i.e., hetero-NCs [16]. The spatial localization of the photogenerated charge carriers in hetero-NCs can be manipulated by controlling the band offsets of the materials that are combined at the heterointerface (Fig. 3) [16]. In type-I hetero-NCs both carriers are confined in the same material (e.g., CdSe/ZnS, InP/ZnS). In contrast, in type-II hetero-NCs a spatially indirect exciton is formed, as the electron and hole wave functions are centered in different materials, and thus in different segments of the hetero-NC (e.g., CdSe/ZnTe, CdSe/CdTe). In type-I$^{1/2}$ (or quasi-type-II) hetero-NCs one carrier is delocalized over the whole volume of the hetero-NC, while the other is localized in one of the segments (e.g., CdSe/CdS, ZnSe/CdSe). This allows the electron–hole spatial overlap to be tailored by controlling the size, shape, and composition of each segment of the hetero-NC, which has a dramatic impact on several properties (viz., quantum yields, stability, PL wavelength [15, 16, 21, 60, 61], reabsorption cross section [22, 29, 62–64], radiative lifetimes [60, 64–66], exciton-phonon coupling strength [67–69], Auger recombination [66, 70–72], hot carrier relaxation [51, 73], thermal quenching [74, 75]). The general trend is that the exciton lifetime, exciton-phonon coupling, and PL wavelength increase when going from the type-I to the type-II localization regimes, while Auger recombination rates and hot carrier relaxation rates are reduced. This is beneficial not only for technologies relying on efficient charge separation, such as solar cells, photodetectors, and photocatalysis, but also for applications requiring light emission, such as luminescent solar concentrators (reduced reabsorption losses) [22, 29] and lasers (lower lasing threshold) [14]. However, short lifetimes and narrow bandwidths are preferred for application in LEDs, since this increases the output saturation threshold and the color-rendering index [19]. The electron–hole wave function overlap in hetero-NCs has also been shown to affect the exciton fine-structure [76–79].

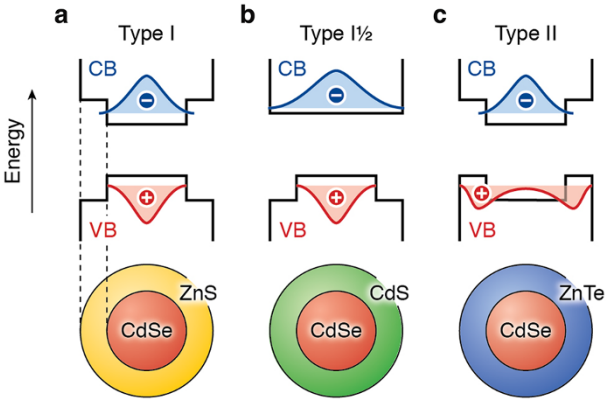

Fig. 3 Schematic representation of the three limiting charge carrier localization regimes in core/shell semiconductor hetero-NCs. The energy of the bulk conduction and valence band edges (CB and VB; *black solid lines*) sets the potential energy of the charge carriers, while the effective mass from the bulk band structure determines the kinetic energy. The wave functions of the lowest-energy electron (*blue*) and hole (*red*) states are schematically depicted. The charge carriers tend to localize in the part of the hetero-NC with the lowest potential energy. **a** In type-I hetero-NCs, such as CdSe/ZnS, both charge carriers co-localize in the same part. **b** In type-I½ hetero-NCs, such as CdSe/CdS, one charge carrier delocalizes over the entire NC while the other one is localized in one part. **c** In type-II hetero-NCs, such as CdSe/ZnTe, the two charge carriers are spatially separated, each in a different part, forming a spatially indirect exciton

The properties of colloidal semiconductor hetero-NCs can also be tuned under constant size, shape, and total composition by making use of controlled interdiffusion. The elemental distribution profile of hetero-NCs can go from a core/shell geometry with a sharp heterointerface to a homogenous alloy QD, via gradient alloy NCs of increasing homogeneity which seamlessly connect these two extremes [80–82]. In this way, the optoelectronic properties can be continuously tuned from those of core/shell hetero-NCs (type-I, type-II or type-$I^{1/2}$) to those of homogeneous alloy NCs, with preservation of the total volume and composition of the NC [80–83]. Moreover, core/shell hetero-NCs with a gradient alloy heterointerface have been shown to possess unique properties, such as reduced Auger recombination rates and lower threshold for amplified spontaneous emission [84]. Alloy QDs and graded interface core/shell hetero-NCs can also be directly synthesized and have attracted increasing interest in the last few years, leading to the investigation of several II-VI and IV-VI compositions [viz., Cd(Te,Se), Cd(S,Se), Pb(S,Se), (Cd,Zn)Se, (Cd,Zn)S, (Cd,Zn)(S,Se)] [80–89].

Another effective strategy to impart novel properties (e.g., optical or magnetic) to semiconductor NCs is the intentional introduction of impurities (doping) [90]. Doping of bulk materials is a very well developed field, which underpins most of our present technologies, since the properties of materials for lighting, electronic and optoelectronic applications are largely controlled by dopants. In contrast, the precise doping of NCs is still an underdeveloped field, which is however booming and has delivered great successes and many novel materials in recent years [28, 91–100].

Over the last few years, potential toxicity and environmental impact have become important driving forces in the quest for novel semiconductor NCs and hetero-NCs [32], since the best-developed systems to date are based on Cd- and Pb-chalcogenides. A remarkable degree of control over size, shape and composition has been achieved for these types of NCs [14–16, 19, 21, 26, 28, 61], but widespread deployment into consumer products is severely limited by toxicity concerns. This has motivated an increasing research effort on alternative compositions that are based on less toxic elements, such as copper chalcogenides (e.g., $CuInS_2$) [24, 26, 32], InP [26, 101], and Si [102].

2.3 Nanoscale Surfaces: far from "Superficial"

The most prevalent nanoscale effect is the increase in the surface-to-volume ratio with decreasing size. Surface atoms comprise only a very small fraction of the constituents of bulk solids, and therefore have a negligible contribution to the material properties. In contrast, the fraction of atoms at surfaces and/or (hetero) interfaces is significant at the nanoscale and becomes increasingly larger as the NC dimensions are further reduced. As a result, the contribution of the surface atoms to the properties of the NC becomes increasingly larger, eventually giving rise to completely novel properties. Surface atoms have fewer neighbors, and therefore possess a higher free energy and unsatisfied chemical bonds (the so-called dangling bonds). The increasingly larger surface/volume ratio of NCs will thus render them more reactive and dynamic than bulk crystals, which impacts a number of properties, such as melting temperatures, solubility, plasticity, catalytic activity, crystal structure, and colloidal dispersibility [16, 103].

The NC surface is a dynamic interface between the inorganic semiconductor core and the ligand shell. The interaction between the semiconductor core and the ligands is crucially relevant during the synthesis of colloidal NCs, since it affects both the thermodynamics and kinetics of their nucleation and growth [16]. It is thus largely responsible for the remarkable degree of control achieved over the size, shape, and composition of semiconductor NCs and hetero-NCs [16]. Another important consequence of the large contribution of surface atoms to the properties of NCs is the enhancement of the solid-state diffusion rates. This has made it possible to use nanoscale cation exchange and/or controlled interdiffusion as post-synthetic strategies to tailor the properties of NCs and hetero-NCs while preserving their size, shape, and heterostructure, by tuning their composition and/or elemental distribution profile [82, 104–122]. These techniques have also been recently used to achieve doping of semiconductor NCs [96, 97, 100].

The larger surface-to-volume ratio of NCs affects the optoelectronic properties. The best-known effect is that unshared atomic orbitals of surface atoms can give rise to localized energy levels within the HOMO–LUMO gap of the NC, which are known as trap states. These states can be detrimental to the PL quantum yield of the NC, if carrier localization into these states is followed by nonradiative exciton relaxation (i.e., energy dissipation as heat by coupling to vibrations) [16]. Radiative recombination between delocalized and trapped carriers may also occur, giving rise to PL that is strongly red-shifted with respect to the band-gap of the NC (the so-

called trap PL). This emission is typically characterized by very broad bandwidths and low quantum efficiencies. It is thus often desirable to eliminate dangling bonds and defects at the surface of semiconductor NCs. This can be achieved by overcoating the NC either with a shell of a different semiconductor (thus forming a hetero-NC, see Sect. 2.2 above) or with suitable ligands that form strong bonds with the surface atoms, thereby shifting the energies of the surface states away from the HOMO–LUMO gap of the NC [16, 123]. Other ligands may in fact generate localized interfacial states or mid-gap states that trap one of the carriers and induce PL quenching (e.g., hole trapping by alkanethiols on CdSe QDs [82, 123, 124]), or directly shift the NC electronic states due to electrostatic or orbital mixing effects [64, 123, 125–127]. The capping ligand shell can be viewed as a self-assembled monolayer (SAM) at the surface of the NC [16, 123]. The internal structure of this SAM can also affect the PL of the NCs, either positively, by fostering surface reconstruction that eliminates trap states [16], or negatively, by imposing disorder to the surface [16, 128].

2.4 Collective Effects in NC Superstructures: When 1 + 1 is Larger Than 2

An attractive feature of colloidal semiconductor NCs and hetero-NCs is that they can be used as solution-processable building blocks for nanostructured thin-films, either by directly depositing the colloidal suspension of NCs or hetero-NCs (the so-called NC inks) onto a substrate and evaporating the solvent [20, 23], or by allowing the NCs or hetero-NCs to self-organize into long-range three- or two-dimensionally ordered superlattices at air–liquid interfaces and subsequently transferring the superstructure to a suitable substrate [129, 130]. Colloidal NCs can also self-assemble into three-dimensionally ordered colloidal superparticles [131]. The geometry and properties of these superstructures can be tailored by the size, shape, composition and surface chemistry of the NC or hetero-NC building blocks [129–138]. In particular, surface ligands have been shown to have a dramatic impact on the directionality of the self-organization process [135, 139–143], leading in some cases to atomically aligned NC superlattices [135, 139, 143]. NC thin-films and superlattices hold promise for a variety of optoelectronic devices, such as light emitting devices, solar cells, photodetectors, and field-effect transistors [129, 130], since they may give rise to a number of novel properties dominated by collective interactions such as energy transfer, charge carrier transfer and migration, and inter-NC electronic coupling.

Another interesting type of superstructure is obtained by attaching colloidal semiconductor NCs (typically CdSe, CdTe, PbSe, or $CuInS_2$) to nanostructured mesoporous films of wide band gap oxide semiconductors, such as TiO_2 or SnO_2. Depending on the band alignments, fast electron injection from the NC into the mesoporous film will occur, making it possible to use such superstructures as QD-sensitized solar cells, akin to the well-known dye-sensitized Grätzel solar cells [144–147].

3 Excited-State Dynamics in Semiconductor Nanocrystals

In this section, we discuss the excited-state dynamics of semiconductor NCs and hetero-NCs, i.e., the processes that occur in a NC after excitation eventually leading to the emission of light. Following excitation, a NC makes the transition from one level to another until eventually relaxing back to the ground state. This sequence of events involves time scales that span over 15 orders of magnitude, from a few femtoseconds to a few seconds after photoexcitation. The possible relaxation pathways and the balance between their rates determine how efficiently light is emitted and at what wavelength. We will limit our discussion to processes occurring at room temperature, since these are more relevant for potential applications, and will thus neglect exciton fine-structure effects (see Sect. 2.1 above). Excited-state dynamics that are dictated by inter-NC interactions, such as energy migration [35, 130, 148–150] and charge carrier transport [130, 151], or energy transfer between NCs and acceptor molecules (usually referred to as Förster resonance energy transfer, FRET) [31, 35, 152] are also beyond the scope of this review, and we refer the interested reader to prior publications that focus on these aspects.

3.1 Relaxation of Hot-Carrier States: fs to ps Timescales

Directly after photoexcitation a NC is in a high-energy state, where usually both electron and hole occupy levels deep in the conduction and valence band. In other words, they have energy in excess of the band edge, and are usually referred to as "hot carriers". Typically the excess carrier energy is rapidly lost as heat on a picosecond timescale or faster [153–161] (Fig. 4a). Studies of this cooling process, and attempts to suppress it, have until now mainly focused on Cd- and Pb-based NCs, using photoluminescence spectroscopy and transient absorption spectroscopy. The mechanism of rapid cooling is not precisely known, but thought to involve coupling to vibrations as well as Auger-coupling between electrons and holes [51, 162–165].

There has been interest in making use of hot-carrier energy in NCs, by reducing the cooling efficiency. The possibility of multi-exciton generation (MEG), also called carrier multiplication (CM), has been investigated for several years, most commonly in Pb-chalcogenide NCs [166–172], but also for other NC materials [173–176]. In the process of multi-exciton generation, a hot carrier with excess energy higher than the bandgap can relax to the ground state while generating an additional electron–hole pair (Fig. 4b). This process has been theoretically predicted to happen on a fs to ns timescale [177]. Multi-exciton generation has the potential to increase the efficiency of QD solar cells to above the Shockley-Queisser limit [178], and is therefore of great interest (see Fig. 5). Many studies have reported the possibility of efficient MEG in NCs, but other studies have challenged too optimistic values for efficiency and energy threshold [169, 175, 176]. As a variation to multi-exciton generation in *individual* QDs, the phenomenon of space-separated quantum cutting has been reported for *ensembles* of QDs of Si. Here, the hot-carrier

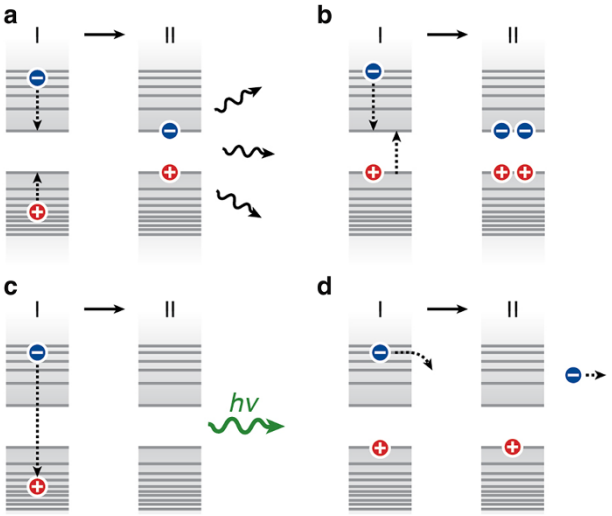

Fig. 4 Schematic representation of possible relaxation pathways for hot-carrier states. **a** Thermalization by means of electron–hole Auger coupling and/or coupling to vibrations. **b** Multi-exciton generation, where the hot-carrier energy is converted into an additional electron–hole pair. **c** Hot-exciton emission. **d** Ejection of a hot charge carrier to the environment of the NC

energy in one QD is transferred to a neighboring QD, after which both can emit [179, 180].

NCs can show direct light emission from hot-exciton states (Fig. 4c). *Interband* hot-carrier emission is due to recombination of a hot carrier in one band (e.g., an electron in the conduction band), with a carrier in the other band. This emission is blue-shifted with respect to that from the ground-state exciton, and decays on a timescale of picoseconds or faster [73, 172, 181]. In addition, the possibility of *intraband* hot-carrier emission has recently been demonstrated in Cd-based and Hg-based NCs [182, 183]. In this process, a hot carrier relaxes to a lower energy level in the same band by the emission of an infrared photon. A particular variation of hot-carrier interband emission occurs in hetero-NCs, if charge carrier localization to the equilibrium situation (as according to the band alignment; see Fig. 3) is inhibited. For example, in CdSe/CdS hetero-NCs hole localization from the high-bandgap material CdS to the CdSe core can be suppressed at high excitation power when multiple mutually repulsive valence band holes simultaneously co-exist in the hetero-NC (Coulomb blockade effect). It has been shown that this leads to significant emission from the CdS arms in CdSe/CdS tetrapods [184–186] or from the CdS shell in CdSe/CdS dot-in-bulk NCs [187].

Another way to reduce the loss of hot-carrier energy is to offer charge transfer pathways that compete with cooling (Fig. 4d). To achieve this, a charge transfer time constant of at most a few picoseconds is necessary. Hot-electron transfer on femtosecond timescales has been demonstrated from PbSe QDs to TiO_2 [188]. Moreover, transfer from hot-carrier states inside the QD to states on the surface or in the environment has been proposed to contribute to photo-ionization and blinking

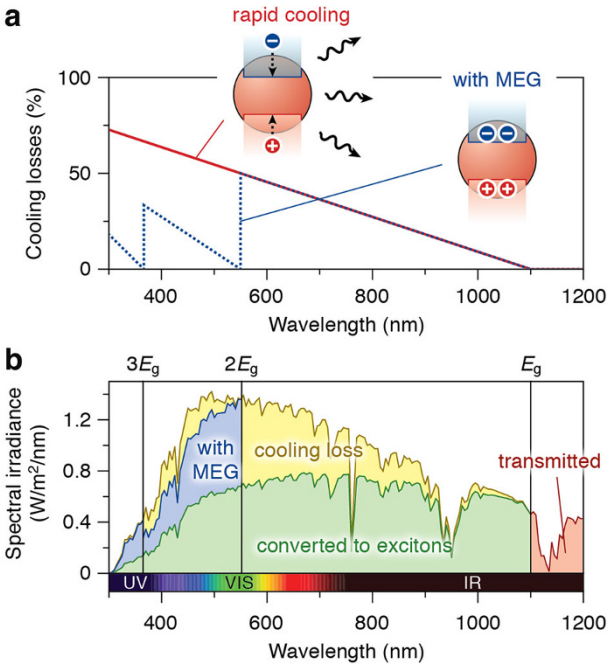

Fig. 5 Multi-exciton generation for solar cell applications. We consider a QD solar cell with a band gap of 1.1 eV (=1100 nm). **a** The fraction of energy lost due to cooling in the transition from light to excitons in a QD. The *red line* denotes the situation where all excess carrier energy is lost by cooling. For example, absorption of a photon with an energy of 2 eV (=620 nm; *red*) results in an electron–hole pair with an energy of 1.1 eV (=the bandgap), while 0.9 eV is lost by cooling. The *blue dashed line* is the optimal situation where all excess carrier energy is used for multi-exciton generation. For example, a photon of 2.2 eV (=565 nm; *yellow/green*) has sufficient energy to create two electron–hole pairs with a combined energy of 2.2 eV, and no cooling losses. **b** The solar spectrum (AM1.5), with the potential benefit of multi-exciton generation indicated. Without multi-exciton generation, only the *green shaded area* is converted to excitons, while the *yellow* and *blue* (30 % of the total solar intensity) are lost to cooling. Optimal multi-exciton generation can prevent cooling losses of the *blue shaded area* (34 % of the total cooling loss). The wavelengths corresponding to once, twice, and three times the QD band gap are indicated, as well as the part of the solar spectrum that does not match the QD absorption (*red shaded area*)

[189, 190]. Charge transfer from hot-electron states is of potential use for solar cell applications, where currently thermalization constitutes a major part of the energy conversion losses [191] (see also Fig. 5b). To enable efficient hot-electron transfer, the competing process of cooling must be suppressed. This could be achieved in designed hetero-NCs to decouple the hot electron from the hole in the valence band as well as from ligand vibrations [51].

3.2 Auger Decay of Multi-Carrier States: ps to ns Time Scales

After the carriers have cooled down to the edges of valence and conduction band via the pathways depicted in Fig. 4, the next important relaxation pathway is Auger decay. An Auger process is the transfer of energy from one charge carrier in the NC

to another. This process plays an important role in semiconductor NCs whenever there are three or more charge carriers present, of which at least one electron and one hole. The most common NC states likely to undergo an Auger process are trion states, i.e., charged states with an electron–hole pair in the NC as well as an additional charge carrier in a quantum confined energy level, and the biexciton state, i.e., the state with two electron–hole pairs in the NC. Figure 6 illustrates the most commonly considered Auger processes. These are Auger processes that involve charge carriers in delocalized levels (i.e., the quantum confined orbitals that extend over the entire NC). The final state of an Auger process always has a charge carrier in a highly excited level (situations II in Fig. 5), which then usually undergoes rapid cooling as in Fig. 4a. The net result of an Auger process is therefore energy loss as heat. Trapped charge carriers can be involved in Auger processes in NCs [192–194]. Auger processes involving trapped charge carriers are poorly understood and not further discussed here, but should be investigated further.

For the use of semiconductor NCs as photoluminescent centers, e.g., in LEDs, laser gain material, or biomedical tracers, it is usually desired that optical cycling is as efficient as possible. This means that every photon absorbed should lead to a photon emitted. Therefore, to minimize Auger losses, the NC must be uncharged (i.e., no trion Auger decay; Fig. 6a, b) and the excitation intensity must be sufficiently low to prevent the generation of biexcitons (Fig. 6c). However, under

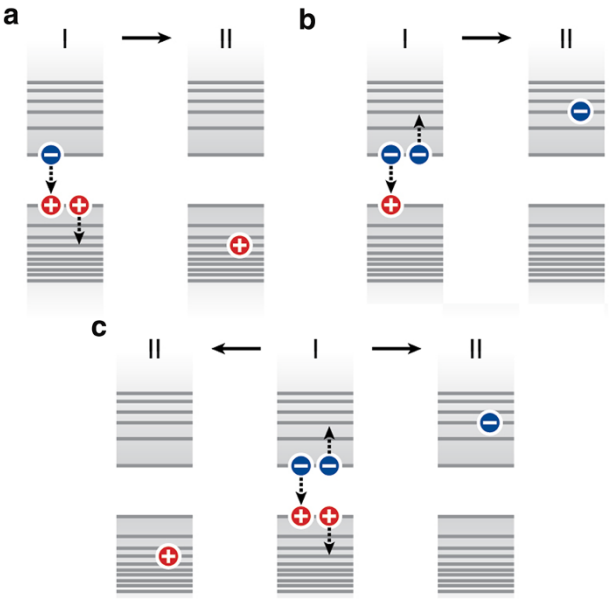

Fig. 6 Examples of Auger processes in semiconductor NCs in the trion (i.e., charged) or biexciton state. **a** In the positive trion state, the recombination energy of an electron–hole pair can be transferred to the additional hole. **b** In the negative trion state, the recombination energy of an electron–hole pair can be transferred to the additional electron. **c** In the biexciton state, the recombination energy of an electron–hole pair can be transferred either to the additional hole (the "positive trion pathway"; to the *left*) or to the additional electron (the "negative trion pathway"; to the *right*) [201]

illumination NCs charge up intermittently and seemingly randomly, leading to a phenomenon known as PL intermittency or "blinking" (see Sect. 3.4 below) [195, 196], while for applications such as lasing high excitation intensities are a necessity [14, 197, 198]. As a result, the possibility of Auger quenching cannot always be avoided. It should be noted that at the highest operating powers in lasers, stimulated emission easily outcompetes Auger recombination, but Auger recombination nevertheless negatively affects the lasing threshold in typical QD lasers.

In recent years, considerable research efforts have been devoted to understanding Auger decay in semiconductor NCs [199–201]. The timescale of Auger processes is typically on the order of 1–100 ps in single component NCs such as PbSe [199], Si [173], PbS [202], CdTe [203], Ge [204], InAs [205], or Pb-perovskites [161]. The Auger timescales in NCs are faster than those in the corresponding bulk material [204]. The difference in Auger rates between bulk (slower) and nanocrystalline (faster) materials, is believed to be due to two reasons. First, all interactions between charge carriers in NCs, including Auger interaction, are enhanced because of their spatial and dielectric confinement (i.e., they are spatially confined in a small volume with high dielectric constant ε_1, which is embedded in a medium with lower dielectric constant ε_2). This increases the Coulomb interaction energy between carriers, which mediates Auger scattering. Second, the conservation rule for translational momentum that suppresses Auger processes in bulk materials is less strict in NCs, because spatial confinement leads to uncertainty in momentum (Heisenberg principle). Figure 7 schematically illustrates the momentum selection rule that governs Auger interaction rates in NCs, using negative trion decay as an example.

The trion Auger dynamics in semiconductor NCs have been investigated under pulsed excitation using photoluminescence measurements. Under strong excitation, NCs charge intermittently (see also Sect. 3.4), which allows one to investigate the

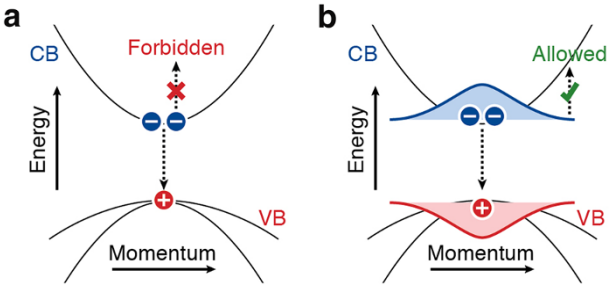

Fig. 7 A simple picture of momentum conservation for Auger processes in NCs. Negative trion Auger recombination is depicted in the electronic dispersion diagram of a typical direct-gap semiconductor. **a** Recombination of an electron–hole pair at the band edge of a bulk semiconductor involves no change in translational momentum (*vertical downward arrows*). The excess electron can therefore not accept the recombination energy to make an energy and momentum conserving transition. **b** In a NC, on the other hand, the quantum confined energy levels have no well-defined translational momentum. In other words, the charge carrier wavefunctions contain many spatial frequency components (*red* and *blue shaded areas*). The momentum selection rule is therefore not so strict in a NC. Consequently, the Auger process can be much faster, depending on the overlap between charge carrier wavefunctions in momentum space [224, 225]

properties of trions on the single-NC level [72, 206–208]. However, this method is only applicable to NCs where the trion state luminescence can be clearly distinguished from the neutral exciton luminescence. For many types of NCs, the blinking behavior is complicated by the involvement of multiple states [209], and one cannot rely on random charging to investigate charged states. Methods of controlled electrochemical or photochemical charging of luminescent NCs have been developed as an alternative for the studies of luminescence from charged NCs [190, 210, 211]. Not only do these methods offer control over the charge state of QDs, they also allow for statistically significant measurements on entire ensembles [211], while single-NC experiments are necessarily limited to a small number of NCs.

Ensemble transient absorption experiments are most commonly used to study multi-exciton dynamics in NCs [161, 173, 199, 203–205]. Analysis of the fast photoluminescence decay components of NCs under strong excitation can also provide information about multi-exciton decay rates [170, 212]. Both methods rely on a significant multi-exciton population in the NCs, and therefore require strong laser excitation. One must be careful that under such conditions, the interpretation of data can become complicated if NCs charge up or defects are generated [157, 161]. Alternatively, information about biexciton dynamics and quantum efficiencies can be obtained from photon correlation analysis on the single-NC level [213, 214] or the ensemble level [215].

Auger recombination negatively affects the performance of NCs for applications such as light emitting diodes [216], lasers [84], or solar cells under concentrated illumination [217]. As discussed above, Auger processes in NCs are rapid and efficient because of spatial confinement of charge carriers. Therefore, the most obvious way to reduce Auger recombination rates is to increase the size of NCs [199, 201, 204, 211, 218]. However, this may not always be a desired strategy if one wants to make use of quantum confinement effects to tune the electronic properties of NCs. For more subtle control over Auger processes, hetero-NCs have been developed with designed charge carrier confinement potentials [219, 220]. The most commonly studied hetero-NC composition for reduced Auger losses is CdSe/CdS in various shapes and sizes [72, 84, 206, 221–223]. It was first predicted theoretically [224, 225] and later confirmed experimentally [84, 221–223] that an alloyed core–shell interface leads to suppressed Auger recombination. An alloyed hetero-interface creates a smooth confinement potential for charge carriers in which high-momentum components in the wavefunctions are reduced in amplitude (see Fig. 7). Indeed, Auger recombination rates in NCs are strongly dependent on the exact size and shape of the NC [201], leading to wide variations in Auger dynamics within a NC ensemble [226, 227]. Hence, it seems that the careful design of uniform ensembles of hetero-NCs with smooth confinement potentials is the pathway to NCs with reduced Auger losses.

3.3 Radiative Decay in Semiconductor Nanocrystals: ns to μs Time Scales

The most studied electron–hole recombination channel in semiconductor NCs is spontaneous radiative decay. Not only do many experimental methods rely on the

detection of photons emitted in a radiative decay pathway, but radiative decay of excited NC states is also often the desired pathway for applications. Several types of spontaneous radiative decay are possible in semiconductor NCs, depending on the composition. For most NC compositions under moderate excitation, radiative decay is predominantly due to recombination of two delocalized charge carriers (electron and hole) in the lowest-energy quantum confined states of the two respective bands. The electron and hole wavefunctions, and hence the characteristics of the emission, are determined by the composition, size and geometry of the NC, as illustrated in Figs. 1, 2 and 3. With the development of NCs and hetero-NCs of a wide variety of sizes, shapes, and compositions, precise control over spontaneous emission from the lowest-energy exciton has been achieved. Radiative recombination of a delocalized carrier with a trapped (i.e., localized) carrier may also occur (trap PL), but is usually characterized by low quantum efficiencies, since carrier trapping favors non-radiative decay pathways by decreasing the electron–hole wave function overlap while increasing the coupling between the localized carrier and its immediate vicinity. In the case of NCs doped with luminescent ions (e.g., ZnSe:Mn^{2+} [228] or $LaPO_4$:Tb^{3+} [229]), radiative recombination occurs primarily at the dopant.

In this section, we discuss what determines the photoluminescence quantum efficiency of NCs and the rate of radiative decay. Auger quenching diminishes the quantum efficiency of the emission when a NC is charged or when multiple electron–hole pairs are present (see Sect. 3.2 above). However, uncharged NCs under weak illumination may find alternative non-radiative decay pathways, which lower the quantum efficiency. Below, spontaneous radiative decay in semiconductor NCs is first discussed, followed by non-radiative decay pathways that can lead to a photoluminescence quantum efficiency below unity.

The rate of radiative decay of a delocalized electron–hole pair in a semiconductor NC can be estimated as [36, 230]

$$\gamma_{\mathrm{rad}} = C\lambda^{-1}\rho K. \tag{1}$$

Here C is a pre-factor that depends on the type of semiconductor, λ is the emission wavelength, and ρ is the density of optical states experienced by the exciton (see below for further explanation). K is the electron–hole overlap integral squared.

Figure 8a shows typical values for the radiative lifetime (the inverse of the radiative decay rate) in common and emerging types of zero-dimensional NCs (i.e., QDs): lead chalcogenides (PbE; E = S, Se) [231, 232], copper indium chalcogenides [233, 234] ($CuInE_2$; E = S, Se), cadmium chalcogenides (CdE, E = Se, Te) [58, 235], indium phosphide (InP) [48], silicon (Si) [236], and cesium lead halides ($CsPbX_3$) [161, 237]. A rough trend is visible that radiative lifetimes are longer for longer emission wavelengths. Indeed, Eq. (1) shows that, for a given QD material, the radiative lifetime (which is the inverse of γ_{rad}) should scale linearly with emission wavelength. Nevertheless, the various QD materials deviate from a general linear dependence between radiative lifetime and emission wavelength (dashed line). These deviations are due to variations in the pre-factor C and the density of optical states ρ.

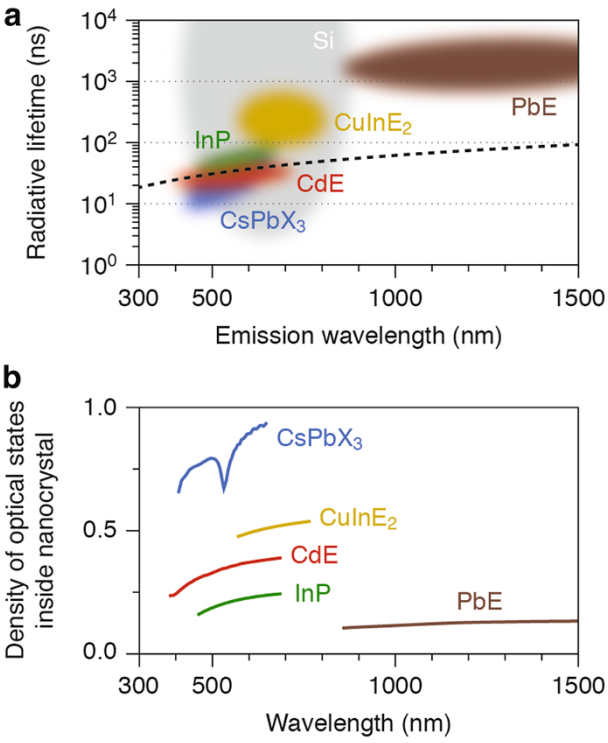

Fig. 8 The rate of radiative decay in colloidal quantum dots. **a** Typical radiative lifetimes and emission wavelengths obtainable for some common and emerging QDs: lead chalcogenides (PbE with E = S, Se; *brown*) [231, 232], copper indium chalcogenides ($CuInE_2$ with E = S, Se; *yellow*) [233, 234], cadmium chalcogenides (CdE with E = Se, Te; *red*) [58, 235], indium phosphide (InP; *green*) [48], silicon (Si; *gray*) [236], and cesium lead halides ($CsPbX_3$ with X = Cl, Br, I; *blue*) [161, 237]. The differently colored clouds indicate the approximate range of combinations for radiative lifetime and emission wavelength that can be found in these materials. The *dashed line* denotes a linear dependence between radiative lifetime and emission wavelength (see text for details). **b** The density of optical states ρ (Eq. 2) for QDs of various semiconductor materials dispersed in a medium with refractive index $n = 1.5$, such as toluene or poly(methyl methacrylate), normalized to the density of optical states in vacuum. The refractive index data were taken from Ref. [306] for $CsPbBr_3$ (*blue line*), from http://www.filmetrics.com for CdTe (*red*), InP (*green*), and PbS (*brown*), and from Ref. [307] for $CuGaS_2$ (*yellow*; as a close analogue of $CuInE_2$ materials)

The pre-factor C is a material-specific constant that accounts for the electronic properties of the QD material. In PbE, CdE, InP, and $CsPbX_3$, where the radiative decay is due to recombination of delocalized electron–hole pair (i.e., the lowest energy exciton), C depends for example on how strongly light couples valence and conduction band states, and also the exciton fine-structure [36].

The density of optical states ρ is a factor of potentially large influence on the radiative decay. It depends on the refractive index of the QD, the shape of the QD, and the polarization of the emission, as well as on the photonic environment of the QD. For example, photonic crystals [238] or plasmonic structures [239] can enhance or suppress radiative decay of QDs. For QDs dispersed in an organic medium, as they are commonly prepared and analyzed, the density of optical states ρ is

determined by the refractive index of the medium n and the refractive index contrast with the QD material itself n_{QD}:

$$\rho = n\left|\frac{3n^2}{2n^2 + n_{QD}^2}\right|^2. \tag{2}$$

Indeed, the radiative decay rate of excitons in core–shell QDs [240] and of luminescent doped ions in NCs [226] depends on the solvent refractive index as described by Eq. (2). The factor $\left|\frac{3n^2}{2n^2+n_{QD}^2}\right|^2$ in Eq. (2) is also known as the local-field factor, and describes the effect of the refractive index contrast between the QD and the surrounding medium. Figure 8b shows that the values of the local-field factor range over one order of magnitude for different QD materials.

The electron–hole overlap integral squared [230] can be expressed as

$$K = \left|\int \psi_e(\mathbf{r})\psi_h(\mathbf{r})d\mathbf{r}\right|^2 \tag{3}$$

where $\psi_e(\mathbf{r})$ and $\psi_h(\mathbf{r})$ are the electron and hole wavefunctions. The factor K is commonly used to reduce the radiative decay rate of excitons in NCs, by making type-I½ or type-II hetero-NCs in which the electron and hole are spatially separated [241] (see Sect. 2.2; Fig. 3 above). Reduced rates of spontaneous radiative decay can be useful for applications such as in lasers or photodetectors, where spontaneous emission is not the desired decay pathway for charge carriers. The mechanism of radiative recombination in some QD materials such as Si or $CuInE_2$ is believed to involve at least one localized charge carrier [24, 32, 236, 242], and therefore cannot be expected to follow the trend predicted by Eq. (1). It is not yet clear how hetero-NCs with engineered electron and hole wavefunctions can be used to control radiative decay rates in QDs of materials such as Si or $CuInE_2$ [117].

The quantum efficiency η of NC emission is determined by the competition between the radiative decay rate γ_{rad} and all the possible non-radiative decay pathways with a combined rate γ_{nr}:

$$\eta = \frac{\gamma_{rad}}{\gamma_{rad} + \gamma_{nr}} \tag{4}$$

As discussed in Sect. 2.3 above, imperfections in the NC such as crystal defects or unsaturated chemical bonds on the surface have been identified as an important factor determining the quantum efficiency [123]. They provide "trap states" for charge carriers, i.e., energy levels within the bandgap where the charge carrier is spatially localized. Indeed, the quantum efficiency of NC emission improves when the NC surface is covered with a protective shell of high-bandgap material [13, 15, 16, 61, 74, 243–246], or when ligands saturate chemical bonds on the surface [16, 123, 247–251].

Generally, the quantum efficiency of different NCs within a single synthesis batch varies strongly. Some NCs have a high quantum efficiency (near 100 %), while others have a quantum efficiency near 0 %. The two subpopulations in a NC

ensemble are also known as the "bright fraction" and the "dark fraction" [251–256] (see Fig. 9). This means that within a single batch, some NCs have (almost) no non-radiative decay pathways, while in other NCs non-radiative decay is very likely. The dark fraction hardly contributes to the observed photoluminescence and, as a result, the photoluminescence decay measurements will reflect the dynamics of the bright NCs. This makes it possible that the photoluminescence decay curve for NC samples with ensemble quantum efficiencies well below 100 % are nearly single-exponential, with a time constant equal to the radiative lifetime of the NCs. High-quality NC batches are thus brighter not necessarily because non-radiative decay is

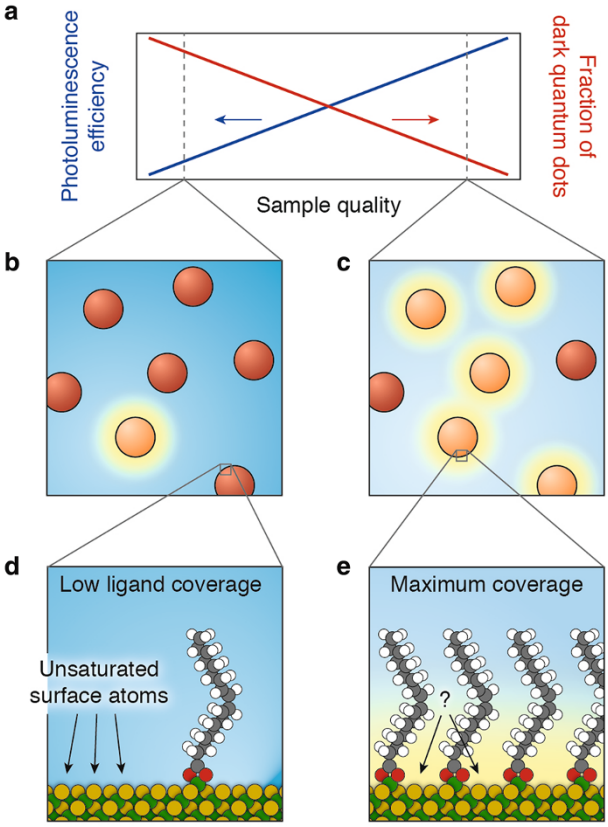

Fig. 9 The fraction of dark quantum dots in a sample. **a** With increasing quality of a QD sample, the photoluminescence efficiency improves (*blue line*). This happens not only because the brightness of each individual QD increases, but mainly because the number of completely dark QDs in the sample decreases (*red line*). **b** A low-quality sample contains many dark QDs and only a few bright ones. **c** A high-quality sample contains fewer dark QDs. **d** The surface of a dark CdSe QD: Cd (100) surface with a single $Cd(oleate)_2$ ligand attached, leaving many unsaturated surface atoms, which are believed to act as charge carrier traps enabling non-radiative recombination. **e** The sample quality improves when the QD surfaces are covered by ligands [251]. However, the maximum ligand coverage set by steric hindrance (~ 3 nm^{-2} for oleic acid) is not sufficient to saturate all surface atoms (~ 6 nm^{-2} for CdSe {100} or CdSe {111}) [123]. There are still unsaturated surface atoms, as highlighted with a *question mark*. Panels **d** and **e** were adapted from Ref. [123]

suppressed in each *individual* NC, but rather because the fraction of completely dark NCs in the ensemble is smaller. This is schematically depicted in Fig. 9a–c.

Despite over 20 years of research, the mechanisms of photoluminescence quenching by charge carrier trapping are still poorly understood. The simplest picture is that quenching can be suppressed by saturating chemical bonds of the surface atoms [15, 16, 61, 243–249, 251]. This can be achieved by overcoating the NC either by a shell of another semiconductor or by a ligand layer. For example, the photoluminescence quantum efficiencies of CdSe QDs can be increased to values as high as 85 % either by overcoating with CdS shells or by capping with primary alkylamines such as hexadecylamine. Computational studies have shown that linear chain alkylamines can form densely packed monolayers at the surface of CdSe NCs, saturating all the available surface Cd atoms [257]. Nevertheless, bright NCs can exist in a sample with low photoluminescence quantum efficiencies, low average surface quality and low average surface coverage by ligands (Fig. 9b, d). Many commonly used surface ligands, such as oleic acid, are bulky and can only saturate half of the available surface atoms because of steric hindrance [123]. This means that even the brightest NCs in an ensemble of oleic acid capped NCs have imperfect saturation of surface atoms. Clearly, additional factors affect the electronic structure of the NC surface, and charge carrier trapping. For example, trap states can be eliminated by surface relaxation and/or reconstruction in such a way that the dangling orbitals of neighboring cations and anions partially overlap, leading to a redistribution of electronic density that makes the surface auto-compensated (a process known as self-passivation or "self-healing") [258]. Surface- and global reconstruction has been observed for NCs of several compositions (e.g., CdSe, ZnSe) [259, 260], and shown to be affected by the nature and structure of the capping ligand monolayer [128, 261]. Nevertheless, it is currently unknown how the atomic structures, including surface ligands, of bright and dark NCs differ [262]. Some recent successes in correlated optical and electron microscopy have been reported, that can lead to more insight into the microscopic nature of quenching [222, 263, 264]. For example, a lower (time-average) brightness of NCs has been connected to stacking faults in the crystal structure or imperfections in surface coverage by a high-bandgap semiconductor shell [263]. The very dynamic nature of the NC surface and the strong interplay between capping ligands and the inorganic core [16] are also likely important factors determining charge carrier trapping. Unfortunately, the organic surface ligands are invisible in electron microscopy and can currently be investigated only on the ensemble level using infrared absorption [249, 265, 266], nuclear magnetic resonance spectroscopy [249, 267, 268], or neutron scattering [269, 270].

3.4 Blinking Dynamics on ms Timescales and Slower

Interestingly, the timescales relevant to the optical properties of semiconductor NCs extend to much longer than the radiative lifetime of the exciton. In this section, we do not discuss irreversible bleaching of NC luminescence due to, for example, oxidation [271], but only reversible physical phenomena encountered in NCs on timescales beyond the exciton radiative lifetime. These include not only

photoluminescence intermittency (blinking), but also photodimming and photobrightening, spectral diffusion, and delayed emission. We will first give a brief overview of experimental studies, and then discuss the microscopic nature of blinking and related processes, which is still largely unknown.

In 1996, Nirmal et al. [195] observed that the luminescence from NCs turns on and off intermittently on time scales from milliseconds up to many seconds (see Fig. 10a). This phenomenon, commonly known as "blinking", becomes apparent in studies on individual NCs, but is hidden in ensemble measurements on many NCs simultaneously. Nevertheless, blinking does have an adverse effect on the properties of NC ensembles, because there is always a fraction of NCs in the non-emissive state. Interestingly, because of the peculiar statistics of blinking, the fraction of non-emissive NCs can change in time under continued excitation, leading to reversible photodimming or photobrightening over time scales of many seconds (Fig. 10b) [272–274].

Blinking is observed in many different types of NCs, including QDs of CdSe [195], InP [275], CdTe [276], PbS [277], InAs [278], Pb-perovskites [279], as well as various hetero-NCs, and even in very different emitters such as organic dye molecules [280]. Methods to reduce blinking of NCs (i.e., to make random switches to a dark state less frequent) include surface protection using organic ligands [281] or an inorganic shell material [195, 282, 283], and also plasmonic enhancement of radiative decay [284]. This indicates that blinking involves slow changes on the surface of the QD that introduce non-radiative decay pathways. These can be either geometrical changes induced by ligand adsorption and desorption, or charge carrier trapping (for more discussion, see below).

A second phenomenon fundamental to semiconductor NCs but only observable in single-emitter measurements, is spectral diffusion (Fig. 10c). This entails that over time the emission spectrum of a NC shifts or jumps back and forth over the range of a few nanometers. Temporal variations in the peak emission wavelength are accompanied by, and correlated with, variations in the emission line width [285–288]. Most of the experiments into spectral diffusion were conducted at cryogenic temperatures [289–292], but the process occurs at room temperature, too [285–288]. A direct link between spectral diffusion and blinking was proposed, based on correlations between blinking events (on–off switches) and spectral shifts [290, 293]. At room temperature, typical time scales for spectral diffusion are milliseconds to seconds, but not shorter [294].

The statistics of blinking are peculiar. Typical duration distributions of bright and dark periods in an emission trace (as in Fig. 10a) are depicted in Fig. 10d. The durations are power-law distributed (with an exponential cut-off for the bright periods at long time scales) [295]. This means that a bright or dark period is most likely short (only a few milliseconds), but much longer periods of many seconds occur as well. The range of durations is much wider than it would be in case of exponential statistics. The power-law exponents are around 1.5 for most NCs, and independent or nearly independent of temperature [276], excitation intensity [276], and nature of the excitation laser (continuous wave or pulsed) [296]. Interestingly, the band-edge emission of semiconductor NCs contains a slow "delayed" component with power-law statistics, that extends over time scales from

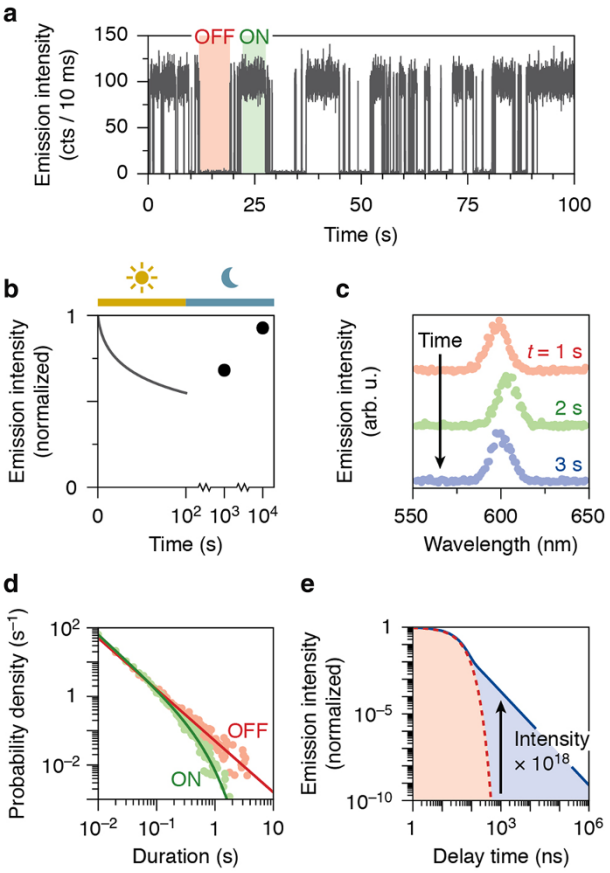

Fig. 10 Slow dynamics in semiconductor nanocrystals. **a** Under continued excitation, the emission from a typical individual NC turns on and off intermittently on time scales of milliseconds to many seconds. **b** If the durations of on and off periods have different distributions (see panel **d** for typical statistics), then the brightness of an ensemble of NCs can decrease under continued illumination as more NCs enter an off state. The brightness is restored in the dark. **c** The emission spectrum of an individual NC shifts back and forth over a few nanometers on time scales of seconds. **d** The distribution of on (*green*) and off (*red*) durations typically shows power-law statistics with exponents of approximately 1.5. The on statistics exhibit an exponential cut-off that depends on the excitation power. **e** The photoluminescence decay following pulsed laser excitation of NCs shows an exponential component due to radiative recombination of an electron–hole pair (*red*; see Sect. 3.3). On time scales longer than a few nanoseconds, the emission is dominated by a power-law component of delayed emission due to reversible charge carrier trapping (*blue*). All data in this figure are simulated

nanoseconds up to (at least) milliseconds [240, 256, 297] (Fig. 10e). This very slow emission is not trap emission due to recombination of a trapped and a delocalized charge carrier (see Sect. 2.3 above), because the emission wavelength is (nearly) identical to the band-edge emission. Instead, this emission component has been ascribed to reversible charge carrier trapping and detrapping, followed by emission [298]. Based on the similar statistics, a close relation between blinking and delayed emission has been suggested [240, 297].

The microscopic nature of blinking is, after 20 years, still under debate. Models must contain at least two ingredients: they must explain what makes a NC dark in the off state, and what causes the characteristic power-law statistics. Early on, Efros and Rosen [196] proposed the charging–discharging model, where the NC can become charged by the ejection of a photogenerated charge carrier. A neutral NC would correspond to the on state, while a charged NC is in the off state, where photoluminescence is quenched by Auger recombination (see Sect. 3.2). The initial model [196] proposed that charging could be due to Auger ejection of a charge carrier following the generation of a biexciton, but this would result in exponential statistics. Several adaptations for the charging–discharging model have been developed to account for the power-law statistics of blinking. These adapted models assume that the rate of charging and/or discharging varies in time, because of Coulomb blockade [299] or fluctuations in the geometry and surface structure of the NC [300], or because tunneling barriers for charge carrier trapping vary slowly in height and width [295].

The picture of Auger quenching in the off state has later been challenged, based on comparisons between the quenching rate of the biexciton state (due to Auger processes) and the off state [301]. However, such comparison assumes that Auger quenching in the off state is only due to the remaining charge carrier in the NC, while the ejected charge carrier does not play a role. Taking this role into account [193], may explain the discrepancies between biexciton and off state quenching. As an alternative to charging–discharging model, the multiple recombination center model was proposed in which structural changes in the NC geometry open and close pathways for trapping and non-radiative decay of charge carriers [302, 303]. These models also reproduce the power-law statistics of blinking. However, rapid non-radiative recombination is inconsistent with other experimental data, such as power-law delayed emission [240].

All existing models for blinking have one important weakness: they provide a mathematical description for blinking, but they lack a detailed microscopic (chemical) picture. In fact, it is surprising how little is established about blinking after 20 years of research, other than the statistics. A microscopic picture of blinking may eventually emerge from experiments combined with atomistic quantum mechanical calculations [264, 304] or from very challenging studies of correlated optical and time-resolved electron microscopy [305].

4 Summary and Outlook

The last three decades have witnessed a remarkable development in the colloidal synthesis of composition-, size-, and shape-controlled semiconductor NCs and hetero-NCs, allowing researchers to make materials with tailored physical–chemical and optoelectronic properties by exploiting nanoscale phenomena, such as quantum confinement and surface effects. These effects, and their impact on the properties of semiconductor NCs and hetero-NCs, were discussed in detail in Sect. 2.

The availability of high-quality colloidal nanomaterials has in turn lead to great advances in the fundamental understanding of their properties. In this review, we

focused on the excited-state dynamics in these nanomaterials, covering the whole range of relaxation processes spanning from the fs to the ms time scales: hot carrier relaxation (fs to ps), Auger decay of multi-carrier states (ps to ns), radiative decay (ns to μs), and photoluminescence intermittency (blinking), spectral diffusion, and delayed emission, which take place on time scales longer than ms. It is clear that the scientific community has a reasonably thorough understanding of many of the physical processes involved in the exciton formation and relaxation in semiconductor NCs and hetero-NCs, but there are still many poorly understood aspects and several knowledge gaps. As a result, a comprehensive theoretical framework capable of fully describing the exciton dynamics in semiconductor NCs and hetero-NCs has yet to emerge.

A particularly critical challenge is the understanding of the processes taking place at time scales longer than the radiative lifetime of the exciton, and the development of a detailed microscopic model that can relate these processes to chemical and structural transformations of the NC and/or its immediate vicinity. The understanding of the mechanisms underlying carrier trapping and photoluminescence quenching, and the role of capping ligands therein, is still fragmentary and merit a systematic and comprehensive investigation. Progress in this direction has been hampered by the lack of suitable tools, but many new techniques have appeared in recent years, and it is likely that further developments will make these issues amenable to experimental and computational investigation in the near future.

Another current limitation is that the large majority of the studies of the exciton dynamics in semiconductor NCs and hetero-NCs have been carried out on the prototypical case of CdSe and other Cd- and Pb-based compositions, while studies on emerging compositions such as InP, Cu chalcogenides and Si have been scarce. As a result, the latter class of nanomaterials is as yet poorly understood, despite their great potential as sustainable and less toxic alternatives to the conventional Cd- and Pb-based NCs and hetero-NCs. Recent advances in the synthesis of colloidal nanocrystals of these alternative compositions, and the growing interest that they have been attracting, will certainly lead to major efforts to close the gap in the understanding of their properties.

Acknowledgments FTR acknowledges financing by the Netherlands Organisation for Scientific Research (NWO): Rubicon Grant 680-50-1509.

References

1. Ekimov AI, Onuschchenko AA (1981) JETP Lett 34:345–348
2. Brus LE (1983) J. Chem. Phys. 79:5566–5571
3. Ekimov AI, Onuschchenko AA (1984) JETP Lett 40:1136–1138
4. Weller H, Koch U, Gutierrez M, Henglein A (1984) Ber. Bunsen. Phys. Chem. 88:649–656

5. Ekimov AI, Efros AL, Onushchenko AA (1985) Solid State Commun 56:921–924
6. Brus LE (1986) J. Chem. Phys. 90:2555–2560
7. Alivisatos AP, Harris AL, Levinos NJ, Steigerwald ML, Brus LE (1988) J. Chem. Phys. 89:4001–4011
8. Bawendi MG, Kortan AR, Steigerwald ML, Brus LE (1989) J. Chem. Phys. 91:7282–7290
9. Henglein A (1989) Chem Rev 89:1861–1873
10. Weller H (1993) Angew. Chem. Intl. Ed. Engl. 32:41–53
11. Murray CB, Norris DJ, Bawendi MG (1993) J Am Chem Soc 115:8706–8715
12. Katari JEB, Colvin VL, Alivisatos AP (1994) J Phys Chem 98:4109–4117
13. Hines MA, Guyot-Sionnest P (1996) J Phys Chem 100:468–471
14. Klimov VI, Ivanov SA, Nanda J, Achermann M, Bezel I, McGuire JA, Piryatinski A (2007) Nature 447:441–446
15. Talapin DV, Lee J, Kovalenko MV, Shevchenko EV (2010) Chem Rev 110:389–458
16. Donega CdM (2011) Chem Soc Rev 40:1512–1546
17. Zhao Y, Burda C (2012) Energy Environ Sci 5:5564–5576
18. Freeman R, Willner I (2012) Chem Soc Rev 41:4067–4085
19. Shirasaki Y, Supran G, Bawendi M, Bulović V (2012) Nat Photonics 7:13–23
20. Bucherl CN, Oleson KR, Hillhouse HW (2013) Curr. Opin. Chem. Eng. 2:168–177
21. Chen O, Zhao J, Chauhan VP, Cui J, Wong C, Harris DK, Wei H, Han HS, Fukumura D, Jain RK, Bawendi MG (2013) Nat Mater 12:445–451
22. Krumer Z, Pera SJ, van Dijk-Moes RJA, Zhao Y, de Brouwer AFP, Groeneveld E, van Sark WGJHM, Schropp REI, de Mello Donega C (2013) Sol Energy Mater Sol Cells 111:57–65
23. Stolle CJ, Harvey TB, Korgel BA (2013) Curr. Opin. Chem. Eng. 2:160–167
24. Kolny-Olesiak J, Weller H (2013) ACS Appl. Mater. Interfaces 5:12221–12237
25. Banin U, Ben-Shahar Y, Vinokurov K (2014) Chem Mater 26:97–110
26. Grim JQ, Manna L, Moreels I (2015) Chem Soc Rev 44:5897–5914
27. Knowles KE, Kilburn TB, Alzate DG, McDowall S, Gamelin DR (2015) Chem Commun 51:9129
28. Kovalenko MV, Manna L, Cabot A, Hens Z, Talapin DV, Kagan CR, Klimov VI, Rogach AL, Reiss P, Milliron DJ et al (2015) ACS Nano 9:1012–1057
29. Meinardi F, McDaniel H, Carulli F, Colombo A, Velizhanin KA, Makarov NS, Simonutti R, Klimov VI, Brovelli S (2015) Nat Nanotech 10:878
30. Silvi S, Credi A (2015) Chem Soc Rev 44:4275–4289
31. Wegner KD, Hildebrandt N (2015) Chem Soc Rev 44:4792–4834
32. van der Stam W, Berends AC, Donega CdM (2016) ChemPhysChem 17:559–581
33. Alivisatos AP (1996) J Phys Chem 100:13226–13239
34. Groeneveld E, Delerue C, Allan G, Niquet Y, de Mello Donega C (2012) J Phys Chem C 116:23160–23167
35. Koole R, Groeneveld E, Vanmaekelbergh D, Meijerink A, Donega CdM (2014) In: Donega CdM (ed) Nanoparticles: workhorses of Nanoscience, Ch. 2. Springer, Heidelberg
36. Efros AL, Rosen M, Kuno M, Nirmal M, Norris DJ, Bawendi MG (1996) Phys Rev B 54:4843–4856
37. Franceschetti A, Fu H, Wang LW, Zunger A (1999) Phys Rev B 60:1819–1829
38. Leung K, Pokrant S, Whaley KB (1998) Phys Rev B 57:12291–12301
39. Crooker SA, Barrick T, Hollingsworth JA, Klimov VI (2003) Appl Phys Lett 82:2793–2795
40. Labeau O, Tamarat P, Lounis B (2003) Phys Rev Lett 90:257404
41. Donega CdM, Bode M, Meijerink A (2006) Phys Rev B 74:085320
42. Wang H, de Mello Donega C, Meijerink A, Glasbeek M (2006) J Phys Chem B 110:733–737
43. Zhao Q, Graf PA, Jones WB, Franceschetti A, Li J (2007) Wang, Kim K. Nano Lett 7:3274–3280
44. Oron D, Aharoni A, de Mello Donega C, van Rijssel J, Meijerink A, Banin U (2009) Phys Rev Lett 102:177402
45. Schaller RD, Crooker SA, Bussian DA, Pietryga JM, Joo J, Klimov VI (2010) Phys Rev Lett 105:067403
46. Eilers J, van Hest J, Meijerink A, Donega CdM (2014) J Phys Chem C 118:23313–23319
47. Siebers B, Biadala L, Yakovlev DR, Rodina AV, Aubert T, Hens Z, Bayer M (2015) Phys Rev B 91:155304
48. Biadala L et al (2016) ACS Nano 10:3356–3364
49. Stroscio MA, Dutta M (2001) Phonons in Nanostructures. Cambridge University Press, New York
50. Klimov VI (2007) Annu Rev Phys Chem 58:635–673

51. Pandey A, Guyot-Sionnest P (2008) Science 322:929–932
52. Kambhampati P (2011) Acc Chem Res 44:1–13
53. Hannah DC, Dunn NJ, Ithurria S, Talapin DV, Chen LX, Pelton M, Schatz GC, Schaller RD (2011) Phys Rev Lett 107:177403
54. Henderson B, Imbusch GF (1989) Optical Spectroscopy of Inorganic Solids. Oxford University Press, Oxford
55. Cui J et al (2016) Nano Lett 16:289–296
56. Norris D, Efros A, Rosen M, Bawendi M (1996) Phys Rev B 53:16347–16354
57. Granados del Águila A, Jha B, Pietra F, Groeneveld E, de Mello Donega C, Maan JC, Vanmaekelbergh D, Christianen PCM (2014) ACS Nano 8:5921–5931
58. Donega CdM, Koole R (2009) J Phys Chem C 113:6511–6520
59. Moreels I, Lambert K, De Muynck D, Vanhaecke F, Poelman D, Martins JC, Allan G, Hens Z (2007) Chem Mater 19:6101
60. Ivanov SA, Piryatinski A, Nanda J, Tretiak S, Zavadil KR, Wallace WO, Werder D, Klimov VI (2007) J Am Chem Soc 129:11708–11719
61. Reiss P, Protière M, Li L (2009) Small 5:154–168
62. Halpert JE, Porter VJ, Zimmer JP, Bawendi MG (2006) J Am Chem Soc 128:12590
63. Zhong H, Scholes GD (2009) J Am Chem Soc 131:9170
64. Donega CdM (2010) Phys. Rev. B 81:165303
65. Pandey A, Guyot-Sionnest P (2007) J. Chem. Phys. 127:104710
66. Oron D, Kazes M, Banin U (2007) Phys. Rev. B 75:035330
67. Wijnen FJP, Blokland JH, Chin PTK, Christianen PCM, Maan JC (2008) Phys. Rev. B 78:235318
68. Biadala L, Louyer Y, Tamarat Ph, Lounis B (2009) Phys Rev Lett 103:037404
69. Groeneveld E, de Mello Donega C (2012) J Phys Chem C 116:16240–16250
70. Garcia-Santamaria F, Chen Y, Vela J, Schaller RD, Hollingsworth JA, Klimov VI (2009) Nano Lett 9:3482–3488
71. Dennis AM, Mangum BD, Piryatinski A, Park YS, Hannah DC, Casson JL et al (2012) Nano Lett 12:5545–5551
72. Rabouw FT et al (2013) Nano Lett 13:4884–4892
73. Diroll BT, Turk ME, Gogotsi N, Murray CB, Kikkawa JM (2016) Chem Phys Chem 17:759–765
74. Abel KA, Qiao H, Young JF, Van Veggel FCJM (2010) J Phys Chem Lett 1:2334–2338
75. Zhao Y, Riemersma C, Pietra F, Koole R, Donega CDM, Meijerink A (2012) ACS Nano 6:9058–9067
76. Brovelli S et al (2011) Nature Commun 2:280
77. Raino G, Stoferle T, Moreels I, Gomes R, Hens Z, Mahrt RF (2012) ACS Nano 6:1979–1987
78. Biadala L, Siebers B, Gomes R, Hens Z, Yakovlev DR, Bayer M (2014) J Phys Chem C 118:22309–22316
79. Granados del Aguila A, Groeneveld E, Maan JC, de Mello Donega de, Christianen PCM (2016) ACS Nano 10:4102–4110
80. Zhong X, Han M, Dong Z, White TJ, Knoll W (2003) J Am Chem Soc 125:8589–8594
81. Panda SK, Hickey SG, Waurisch C, Eychmuller A (2011) J Mater Chem 21:11550–11555
82. Groeneveld E, Witteman L, Lefferts M, Ke X, Bals S, van Tendeloo G, Donega CDM (2013) ACS Nano 7:7913–7930
83. Vaxenburg R, Lifshitz E (2012) Phys Rev B 85:075304
84. Park YS, Bae WK, Baker T, Lim J, Klimov VI (2015) Nano Lett 15:7319–7328
85. Petrov DV, Santos BS, Pereira GAL, de Mello Donega C (2002) J Phys Chem B 106:5325–5334
86. Bailey RE, Nie S (2003) J Am Chem Soc 125:7100–7106
87. Maikov GI, Vaxenburg R, Sashchiuk A, Lifshitz E (2010) ACS Nano 4:6547–6556
88. Regulacio MD, Han M (2010) Acc Chem Res 43:621–630
89. Zhang J, Yang Q, Cao H et al (2016) Chem Mater 28:618–625
90. Buonsanti R, Milliron DJ (2013) Chem Mater 25:1305–1317
91. Orlinskii SB, Schmidt J, Groenen EJJ, Baranov PG, de Mello Donega C, Meijerink A (2005) Phys Rev Lett 94:097602
92. Norris DJ, Efros AL, Erwin SC (2008) Science 319:1776–1779
93. Beaulac R, Schneider L, Archer PI, Bacher G, Gamelin DR (2009) Science 325:973–976
94. Bussian DA, Crooker SA, Yin M, Brynda M, Efros AL, Klimov VI (2009) Nature Mater 8:35–40
95. Chen D, Viswanatha R, Ong GL, Xie R, Balasubramaninan M, Peng X (2009) J Am Chem Soc 131:9333–9339

96. Eilers J, Groeneveld E, Donega CDM, Meijerink A (2012) J Phys Chem Lett 3:1663–1667
97. Sahu A, Kang MS, Kompch A, Notthoff C, Wills AW, Deng D, Winterer M, Frisbie CD, Norris DJ (2012) Nano Lett 12:2587–2594
98. Zhao Y, Rabouw FT, van Puffelen T, van Walree CA, Gamelin DR, de Mello Donega C, Meijerink A (2014) J Am Chem Soc 136:16533–16543
99. Schimpf AM, Knowles KE, Carroll GM, Gamelin DR (2015) Acc Chem Res 48:1929–1937
100. Barrows CJ, Chakraborty P, Kornowske LM, Gamelin DR (2016) ACS Nano 10:910–918
101. Franke D, Harris DK, Xie L, Jensen KF, Bawendi MG (2015) Angew Chem Int Ed 54:14299–14303
102. Dasog M, Kehrle J, Rieger B, Veinot JGC (2016) Angew. Chem. Int Ed 55:2322–2339
103. Roduner E (2006) Chem Soc Rev 35:583–592
104. Luther JM, Zheng H, Sadtler B, Alivisatos AP (2009) J Am Chem Soc 131:16851–16857
105. Grodzinska D, Pietra F, van Huis MA, Vanmaekelbergh D, de Mello Donega C (2011) J Mater Chem 21:11556–11565
106. Li H, Brescia R, Krahne R, Bertoni G, Alcocer MJP et al (2012) ACS Nano 6:1637–1647
107. Casavola M, Van Huis MA, Bals S, Lambert K, Hens Z, Vanmaekelbergh D (2012) Chem Mater 24:294–302
108. Groeneveld E, van Berkum S, van Schooneveld MM, Gloter A, Meeldijk JD, van den Heuvel DJ, Gerritsen HC, de Mello Donega C (2012) Nano Lett 12:749–757
109. Beberwyck BJ, Surendranath Y, Alivisatos AP (2013) J Phys Chem C 117:19759–19770
110. Gupta S, Kershaw SV, Rogach AL (2013) Adv Mater 25:6923–6944
111. Rivest JB, Jain PK (2013) Chem Soc Rev 42:89–96
112. Bouet C, Laufer D, Mahler B, Nadal B, Heuclin H, Pedetti S, Patriarche G, Dubertret B (2014) Chem Mater 26:3002–3008
113. Fayette M, Robinson RD (2014) J Mater Chem A 2:5965–5978
114. Ha D, Caldwell AH, Ward MJ, Honrao S, Mathew K, Hovden R, Koker MKA, Muller DA, Hennig RG, Robinson RD (2014) Nano Lett 14:7090–7099
115. Ott FD, Spiegel LL, Norris DJ, Erwin SC (2014) Phys Rev Lett 133:156803
116. Zhang D, Wong AB, Yu Y, Brittman S, Sun J, Fu A, Beberwyck B, Alivisatos AP, Yang PJ (2014) Am Chem Soc 136:17430–17433
117. van der Stam W, Bladt E, Rabouw FT, Bals S, Donega CDM (2015) ACS Nano 9:11430–11438
118. van der Stam W, Berends AC, Rabouw FT, Willhammar T, Ke X, Meeldijk JD, Bals S, Donega CdM (2015) Chem Mater 27:621–628
119. van der Stam W, Akkerman QA, Ke X, van Huis MA, Bals S, Donega CdM (2015) Chem Mater 27:283–291
120. De Trizio L, Gaspari R, Bertoni G, Kriegel I, Moretti L et al (2015) Chem Mater 27:1120–1128
121. de Trizio L, Manna L (2016) Chem Rev. doi:10.1021/acs.chemrev.5b00739
122. Wu H, Sato R, Yamaguchi A, Kimura M, Haruta M, Kurata H, Teranishi T (2016) Science 351:1306–1310
123. Boles MA, Ling D, Hyeon T, Talapin DV (2016) Nature Mater 15:141–153
124. Wuister SF, de Mello Donega C, Meijerink A (2004) J Phys Chem B 108:17393–17397
125. Koole R, Luigjes B, Tachiya M, Pool R, Vlugt TJH, de Mello Donegá C, Meijerink A, Vanmaekelbergh D (2007) J Phys Chem C 111:11208–11215
126. Frederick MT, Weiss EA (2010) ACS Nano 4:3195–3200
127. Jin SY, Harris RD, Lau B, Aruda KO, Amin VA, Weiss EA (2014) Nano Lett 14:5323–5328
128. Wuister SF, Donega CDM, Meijerink A (2004) J Am Chem Soc 126:10397–10402
129. Vanmaekelbergh D (2011) Nano Today 6:419–437
130. Kagan CR, Murray CB (2015) Nature Nanotech 10:1013–1026
131. Wang T, Zhuang J, Lynch J, Chen O, Wang Z, Wang X, LaMontagne D, Wu H, Wang Z, Cao YC (2012) Science 338:358–363
132. Miszta K, de Graaf J, Bertoni G, Dorfs D, Brescia R, Marras S, Ceseracciu L, Cingolani R, van Roij R, Dijkstra M, Manna L (2011) Nat Mater 10:872–876
133. Pietra F, Rabouw FT, Evers WH, Byelov DV, Petukhov AV, Donega CDM, Vanmaekelbergh D (2012) Nano Lett 12:5515–5523
134. Ye X, Chen J, Engel M, Millan JA, Li W, Qi L, Xing G, Collins JE, Kagan CR, Li J, Glotzer SC, Murray CB (2013) Nat Chem 5:466–473
135. Boneschanscher MP, Evers WH, Geuchies JJ, Altantzis T, Goris B, Rabouw FT, Van Rossum SAP, Van Der Zant HSJ, Siebbeles LDA, Van Tendeloo G, Swart I, Hilhorst J, Petukhov AV, Bals S, Vanmaekelbergh D (2014) Science 344:1377–1381

136. van der Stam W, Gantapara AP, Akkerman QA, Soligno G, Meeldijk JD, van Roij R, Dijkstra M, de Mello Donega C (2014) Nano Lett 14:1032–1037
137. van Anders G, Klotsa D, Karas AS, Dodd PM, Glotzer SC (2015) ACS Nano 9:9542–9553
138. Vanmaekelbergh D, van Vugt LK, Bakker HE, Rabouw FT, De Nijs B, van Dijk-Moes RJA, van Huis MA, Baesjou PJ, van Blaaderen A (2015) ACS Nano 9:3942–3950
139. Choi JJ et al (2011) J Am Chem Soc 133:3131–3138
140. Nagaoka Y, Chen O, Wang Z, Cao YC (2012) J Am Chem Soc 134:2868–2871
141. Wang Z, Schliehe C, Bian K, Dale D, Bassett WA, Hanrath T, Klinke C, Weller H (2013) Nano Lett 13:1303–1311
142. Goodfellow BW, Yu Y, Bosoy CA, Smilgies DM, Korgel BA (2015) J Phys Chem Lett 6:2406–2412
143. van der Stam W, Rabouw FT, Vonk SJW, Geuchies JJ, Ligthart H, Petukhov AV, Donega CDM (2016) Nano Lett 16:2608–2614
144. Pijpers JJH, Koole R, Evers WH, Houtepen AJ, Böhme S, Donega CDM, Vanmaekelbergh D, Bonn M (2010) J Phys Chem C 114:18866–18873
145. McDaniel H, Fuke N, Makarov NS, Pietryga JM, Klimov VI (2013) Nat Commun 4:2887
146. Jara DH, Yoon SJ, Stamplecoskie KG, Kamat PV (2014) Chem Mater 26:7221–7228
147. Pan Z, Mora-Sero I, Shen Q, Zhang H, Li Y, Zhao K, Wang J, Zhong X, Bisquert J (2014) J Am Chem Soc 136:9203–9210
148. Kagan C, Murray C, Bawendi M (1996) Phys Rev B 54:8633–8643
149. Konstantatos G, Huang C, Levina L, Lu Z, Sargent EH (2005) Adv Func Mater 15:1865–1869
150. Xu F et al (2011) ACS Nano 5:9950–9957
151. Shabaev A, Efros AL, Efros AL (2013) Nano Lett 13:5454–5461
152. Chou KF, Dennis AM (2015) Sensors 15:13288–13325
153. Klimov VI, McBranch DW (1998) Phys Rev Lett 80:4028–4031
154. Guyot-Sionnest P, Shim M, Matranga C, Hines M (1999) Phys Rev B 60:R1282–R2184
155. Wehrenberg BL, Wang C, Guyot-Sionnest P (2002) J Phys Chem B 106:10634–10640
156. Schaller RD et al (2005) Phys Rev Lett 95:196401
157. Tyagi P, Kambhampati P (2011) J Chem Phys 134:094706
158. Zhu H, Song N, Lian T (2011) J Am Chem Soc 133:8762–8771
159. Geigerat P et al (2015) ACS Nano 9:778–788
160. Spoor FCM et al (2016) ACS Nano 10:695–703
161. Makarov NS et al (2016) Nano Lett 16:2349–2362
162. Efros AL, Kharchenko VA, Rosen M (1995) Solid State Commun 93:281–284
163. Hendry E et al (2006) Phys Rev Lett 96:057408
164. Kilina SV, Kilin DS, Prezhdo OV (2009) ACS Nano 3:93–99
165. Rabouw FT et al (2015) ACS Nano 9:10366–10376
166. Schaller RD, Klimov VI (2004) Phys Rev Lett 92:186601
167. Ellingson RJ et al (2005) Nano Lett 5:865–871
168. Trinh MT et al (2008) Nano Lett 8:1713–1718
169. Pijpers JJH et al (2009) Nat Phys 5:814–881
170. Sandberg RL et al (2012) ACS Nano 6:9532–9540
171. Midgett AG et al (2013) Nano Lett 13:3078–3085
172. Cirloganu CM et al (2014) Nat Commun 5:4148
173. Beard MC et al (2007) Nano Lett 7:2506–2512
174. Schaller RD, Pietryga JM, Klimov VI (2007) Nano Lett 7:3469–3476
175. Nair G, Bawendi MG (2007) Phys Rev B 76:081304R
176. Ben-Lulu M, Mocatta D, Bonn M, Banin U, Ruhman S (2008) Nano Lett 8:1207–1211
177. Allan G, Delerue C (2006) Phys Rev B 73:205423
178. Semonin OE et al (2011) Science 334:1530–1533
179. Timmerman D, Izeddin I, Stallinga P, Yassievich IN, Gregorkiewicz T (2008) Nat Photonics 2:105–109
180. Bruhn B, Limpens R, Chung NX, Schall P, Gregorkiewicz T (2016) Sci Rep 6:20538
181. Achtstein AW et al (2016) Phys Rev Lett 116:116802
182. Jeong KS, Guyot-Sionnest P (2016) ACS Nano 10:2225–2231
183. Deng Z, Guyot-Sionnest P (2016) ACS Nano 10:2121–2127
184. Lutich AA et al (2010) Nano Lett 10:4646–4650
185. Krahne R et al (2011) Appl Phys Lett 98:063105

186. Wong JI et al (2014) ACS Nano 8:2873–2879
187. Galland C et al (2013) Nano Lett 13:321–328
188. Tisdale WA et al (2010) Science 328:1543–1547
189. Padilha LA et al (2011) ACS Nano 5:5045–5055
190. Galland C et al (2011) Nature 479:203–207
191. Polman A, Atwater HA (2012) Nat Mater 11:174–177
192. Allan G, Delerue C (2009) Phys Rev B 79:195324
193. Cohn AW, Schimpf AM, Gunthardt CE, Gamelin DR (2013) Nano Lett 13:1810–1815
194. Boehme SC et al (2015) Nano Lett 15:3056–3066
195. Nirmal M et al (1996) Nature 383:802–804
196. Efros AL, Rosen M (1997) Phys Rev Lett 78:1110–1113
197. Klimov VI et al (2000) Science 290:314–317
198. Ivanov SA et al (2004) J Phys Chem B 108:10625–10630
199. Klimov VI, Mikhailovsky AA, McBranch DW, Leatherdale CA, Bawendi MG (2000) Science 287:1011–1013
200. Park Y-S, Bae WK, Pietryga JM, Klimov VI (2014) ACS Nano 8:7288–7296
201. Vaxenburg R, Rodina A, Lifshitz E, Efros AL (2016) Nano Lett. doi:10.1021/acs.nanolett.6b00066
202. Istrate E et al (2008) J Phys Chem B 112:2757–2760
203. Kobayashi Y, Pan L, Tamai N (2009) J Phys Chem C 113:11783–11789
204. Robel I, Gresback R, Kortshagen U, Schaller RD, Klimov VI (2009) Phys Rev Lett 102:177404
205. Pijpers JJH, Milder MTW, Delerue C, Bonn M (2010) J Phys Chem C 114:6318–6324
206. Spinicelli P et al (2009) Phys Rev Lett 102:136801
207. Gomez DE, van Embden J, Mulvaney P, Fernée MJ, Rubinsztein-Dunlop H (2009) ACS Nano 3:2281–2287
208. Park Y-S, Bae WK, Padilha LA, Pietryga JM, Klimov VI (2014) Nano Lett 14:396–402
209. Zhang K, Chang H, Fu A, Alivisatos AP, Yang H (2006) Nano Lett 6:843–847
210. Jha PP, Guyot-Sionnest P (2009) ACS Nano 3:1011–1015
211. Cohn AW, Rinehart JD, Schimpf AM, Weaver AL, Gamelin DR (2014) Nano Lett 14:353–358
212. Schaller RD, Sykora M, Jeong S, Klimov VI (2006) J Phys Chem B 110:25332–25338
213. Nair G, Zhao J, Bawendi MG (2011) Nano Lett 11:1136–1140
214. Mangum BD, Ghosh Y, Hollingsworth JA, Htoon H (2013) Opt Express 21:7419–7426
215. Beyler AP et al (2014) Nano Lett 14:6792–6798
216. Bae WK et al (2013) Nat Commun 4:2661
217. Gao Y, Sandeep CSS, Schins JM, Houtepen AJ, Siebbeles LDA (2013) Nat Commun 4:2329
218. Vaxenburg R, Rodina A, Shabaev A, Lifshitz E, Efros AL (2015) Nano Lett 15:2092–2098
219. Hollingsworth JA (2013) Chem Mater 25:1318–1331
220. Qin W, Liu H, Guyot-Sionnest P (2014) ACS Nano 8:283–291
221. García-Santamaría F et al (2011) Nano Lett 11:687–693
222. Nasilowski M, Spinicelli P, Patriarche G, Dubertret B (2015) Nano Lett 15:3953–3958
223. Bae WK et al (2013) ACS Nano 7:3411–3419
224. Climente JI, Movilla JL, Planelles J (2012) Small 8:754–759
225. Cragg GE, Efros AL (2010) Nano Lett 10:313–317
226. Park Y-S et al (2011) Phys Rev Lett 106:187401
227. Zhao J, Chen O, Strasfeld DB, Bawendi MG (2012) Nano Lett 12:4477–4483
228. Norris DJ, Yao N, Charnock FT, Kennedy TA (2001) Nano Lett 1:3–7
229. Senden T, Rabouw FT, Meijerink A (2015) ACS Nano 9:1801–1808
230. Shabaev A, Rodina AV, Efros AL (2012) Phys Rev B 86:205311
231. Liu H, Guyot-Sionnest P (2010) J Phys Chem C 114:14860–14863
232. Justo Y et al (2013) J Phys Chem C 117:20171–20177
233. Li L et al (2011) J Am Chem Soc 133:1176–1179
234. Droseros N, Seintis K, Fakis M, Gardelis S, Nassiopoulou AG (2015) J Lumin 167:333–338
235. Van Driel AF et al (2005) Phys Rev Lett 95:236804
236. Dohnalová K et al (2013) Light Sci Appl 2:e47
237. Protesescu L et al (2015) Nano Lett 15:3692–3696
238. Lodahl P et al (2004) Nature 430:654–657
239. Kress SJP et al (2015) Nano Lett 15:6267–6275
240. Rabouw FT et al (2015) Nano Lett 15:7718–7725
241. Kim S, Fisher B, Eisler H-J, Bawendi M (2003) J Am Chem Soc 125:11466–11467

242. Knowles KE, Nelson HD, Kilburn TB, Gamelin DR (2015) J Am Chem Soc 137:13138–13147
243. Dabbousi BO et al (1997) J Phys Chem B 101:9463–9475
244. Peng X, Schlamp MC, Kadavanich AV, Alivisatos AP (1997) J Am Chem Soc 119:7019–7029
245. Talapin DV et al (2004) J Phys Chem B 108:18826–18831
246. Li L et al (2009) Chem Mater 21:2422–2429
247. Chen O et al (2011) J Am Chem Soc 133:17504–17512
248. Nag A et al (2012) J Am Chem Soc 134:13604–13615
249. Anderson NC, Hendricks MP, Choi JJ, Owen JS (2013) J Am Chem Soc 135:18536–18548
250. Gao Y, Peng X (2015) J Am Chem Soc 137:4230–4235
251. Busby E, Anderson NC, Owen JS, Sfeir MY (2015) J Phys Chem C 119:27797–27803
252. Ebenstein Y, Mokari T, Banin U (2002) Appl Phys Lett 80:4033
253. Donega CDM, Hickey SG, Wuister SF, Vanmaekelbergh D, Meijerink A (2003) J Phys Chem B 107:489–496
254. Brokmann X, Coolen L, Dahan M, Hermier JP (2004) Phys Rev Lett 93:107403
255. Pons T et al (2011) Small 7:2101–2108
256. Rabouw FT et al (2016) Nano Lett 16:2047–2053
257. Schapotschnikow P, Hommersom B, Vlugt TJH (2009) J Phys Chem C 113:12690–12698
258. Kahn A (1994) Surf Science 299:469
259. Lovingood DD, Achey R, Paravastu AK, Strouse GF (2010) J Am Chem Soc 132:3344–3354
260. Cadars S, Smith BJ, Epping JD, Acharya S, Belman N, Golan Y, Chmelka BF (2009) Phys Rev Lett 103:136802
261. Wuister SF, van Houselt A, Donega CDM, Vanmaekelbergh D, Meijerink A (2004) Angew Chem Int Ed 43:3029–3033
262. Kim D, Kim D-H, Lee J-H, Grossman JC (2013) Phys Rev Lett 110:196802
263. Orfield NJ, McBride JR, Keene JD, David LM, Rosenthal SJ (2014) ACS Nano 9:831–839
264. Orfield NJ et al (2016) ACS Nano 10:1960–1968
265. Nag A et al (2011) J Am Chem Soc 133:10612–10620
266. Cooper JK, Franco AM, Gul S, Corrado C, Zhang JZ (2011) Langmuir 27:8486–8493
267. Anderson NC, Owen JS (2013) Chem Mater 25:69–76
268. De Roo J et al (2014) J Am Chem Soc 136:9650–9657
269. Abel KA et al (2012) J Phys Chem C 116:3968–3978
270. Schindler T et al (2015) Langmuir 31:10130–10136
271. Van Sark WGJHM, Frederix PLTM, Van den Heuvel DJ, Gerritsen HC, Bol AA, van Lingen JNJ, Donega CDM, Meijerink A (2001) J Phys Chem B 105:8281–8284
272. Brokmann X et al (2003) Phys Rev Lett 90:120601
273. Chung I, Bawendi MG (2004) Phys Rev B 70:165304
274. Jensen RA, Coropceanu I, Chen Y, Bawendi MG (2015) J Phys Chem Lett 6:2933–2937
275. Kuno M et al (2001) Nano Lett 1:557–564
276. Shimizu KT et al (2001) Phys Rev B 63:205316
277. Peterson JJ, Krauss TD (2006) Nano Lett 6:510–514
278. Bischof TS, Correa RE, Rosenberg D, Dauler EA, Bawendi MG (2014) Nano Lett 14:6787–6791
279. Park Y-S, Guo S, Makarov NS, Klimov VI (2015) ACS Nano 9:10386–10393
280. Frantsuzov P, Kuno M, Jankó B, Marcus RA (2008) Nat Phys 4:519–522
281. Hohng S, Ha T (2004) J Am Chem Soc 126:1324–1325
282. Mahler B et al (2008) Nat Mater 7:659–664
283. Chen Y et al (2008) J Am Chem Soc 130:5026–5027
284. Ji B et al (2015) Nat Nanotechnol 10:170–175
285. Müller J et al (2005) Phys Rev B 72:205339
286. Gómez DE, Van Embden J, Mulvaney P (2006) Appl Phys Lett 88:154106
287. Dias EA, Grimes AF, English DS, Kambhampati P (2008) J Phys Chem C 112:14229–14232
288. Ihara T, Kanemitsu Y (2014) Phys Rev B 90:195302
289. Empedocles SA (1999) Bawendi MG 103:1826–1830
290. Neuhauser RG, Shimizu KT, Woo WK, Empedocles SA, Bawendi MG (2000) Phys Rev Lett 85:3301–3304
291. Plakhotnik T et al (2010) Phys Rev Lett 105:167402
292. Fernée MJ et al (2012) J Phys Chem Lett 3:1716–1720
293. Zhu Z, Marcus RA (2014) Phys Chem Chem Phys 16:25694
294. Marshall LF, Cui J, Brokmann X, Bawendi MG (2010) Phys Rev Lett 105:053005

295. Kuno M, Fromm DP, Hamann HF, Gallagher A, Nesbitt DJ (2001) J Chem Phys 115:1028–1040
296. Smyder JA et al (2014) Phys Chem Chem Phys 16:25723–25728
297. Sher PH et al (2008) Appl Phys Lett 92:101111
298. Jones M, Lo SS, Scholes GD (2008) Proc Natl Acad Sci 106:3011–3016
299. Verberk R, Van Oijen AM, Orrit M (2002) Phys Rev B 66:233202
300. Tang J, Marcus RA (2005) J Chem Phys 123:054704
301. Zhao J, Nair G, Fisher BR, Bawendi MG (2010) Phys Rev Lett 104:157403
302. Frantsuzov PA, Volkán-Kacsó S, Jankó B (2009) Phys Rev Lett 103:207402
303. Volkán-Kacsó S, Frantsuzov PA, Jankó B (2010) Nano Lett 10:2761–2765
304. Voznyy O, Sargent EH (2012) Phys Rev Lett 112:157401
305. Pennycook TJ, McBride JR, Rosenthal SJ, Pennycook SJ, Pantelides ST (2012) Nano Lett 12:3038–3042
306. Brittman S, Garnett EC (2016) J Phys Chem C 120:616–620
307. Boyd GD, Kasper H, McFee JH (1971) IEEE J Quant Electron 7:563–573

Top Curr Chem (Z) (2016) 374:73
DOI 10.1007/s41061-016-0073-8

REVIEW

Semiconductor Quantum Dots with Photoresponsive Ligands

Lorenzo Sansalone[1] · Sicheng Tang[1] · Yang Zhang[1] · Ek Raj Thapaliya[1] · Françisco M. Raymo[1] · Jaume Garcia-Amorós[1,2]

Received: 14 July 2016 / Accepted: 15 September 2016 / Published online: 28 September 2016

Abstract Photochromic or photocaged ligands can be anchored to the outer shell of semiconductor quantum dots in order to control the photophysical properties of these inorganic nanocrystals with optical stimulations. One of the two interconvertible states of the photoresponsive ligands can be designed to accept either an electron or energy from the excited quantum dots and quench their luminescence. Under these conditions, the reversible transformations of photochromic ligands or the irreversible cleavage of photocaged counterparts translates into the possibility to switch luminescence with external control. As an alternative to regulating the photophysics of a quantum dot via the photochemistry of its ligands, the photochemistry of the latter can be controlled by relying on the photophysics of the former. The transfer of excitation energy from a quantum dot to a photocaged ligand populates the excited state of the species adsorbed on the nanocrystal to induce a photochemical reaction. This mechanism, in conjunction with the large two-photon absorption cross section of quantum dots, can be exploited to release nitric oxide or to generate singlet oxygen under near-infrared irradiation. Thus, the combination of semiconductor quantum dots and photoresponsive ligands offers the opportunity to assemble nanostructured constructs with specific functions on the basis of electron

This article is part of the Topical Collection "Photoactive Semiconductor Nanocrystal Quantum Dots"; edited by Alberto Credi.

✉ Françisco M. Raymo
fraymo@miami.edu

✉ Jaume Garcia-Amorós
jgarciaamoros@ub.edu

[1] Laboratory for Molecular Photonics, Department of Chemistry, University of Miami, 1301 Memorial Drive, Coral Gables, FL 33146-0431, USA

[2] Grup de Materials Orgànics, Departament de Química Inorgànica I Orgànica (Secció de Química Orgànica), Institut de Nanociència i Nanotecnologia (IN2UB), Universitat de Barcelona, Martí i Franqués 1, 08028 Barcelona, Spain

or energy transfer processes. The photoswitchable luminescence and ability to photoinduce the release of reactive chemicals, associated with the resulting systems, can be particularly valuable in biomedical research and can, ultimately, lead to the realization of imaging probes for diagnostic applications as well as to therapeutic agents for the treatment of cancer.

Keywords Electron transfer · Energy transfer · Photocages · Photochromism · Quantum dots

1 Photophysical Properties of Semiconductor Quantum Dots

1.1 Comparison of Quantum Dots and Organic Dyes

Quantum dots (QDs) are one of the most interesting new materials that have emerged over the last two decades. The term "quantum dot" was coined by Yale physicist Mark Reed in 1988; however, they were first discovered in glass crystals by the Russian physicist Alexey Ekimov in 1981 and also noticed further in colloidal solutions by Louis E. Brus in 1985 at Bell Labs [1]. Semiconductor QDs are inorganic nanoparticles that tightly confine mobile charges, either negative electrons or positive electron holes, in all three spatial dimensions. Because the electrical charges are spatially confined at the nanoscale, QDs are endowed with unique properties, which fall between those of bulk semiconductors and those of discrete molecules.

Amongst the wide diversity of intriguing features of semiconductor QDs, their optical behavior is one of the most attractive. In fact, the photophysical properties of this amazing type of nanomaterial can be finely tuned by subtle modifications not only in their chemical composition but also in their shape and size [2–4]. On this basis, QDs have garnered significant attention in the fields of biology, chemistry, physics, and engineering as well as in a diversity of technological applications including transistors [5], solar cells [6], light-emitting devices [7], diode lasers [8, 9], quantum computing [10], and inkjet printing [11]. Furthermore, QDs have sparked great interest within photobiology and biomedicine, especially in the field of medical imaging [12]. Indeed, fluorescence microscopy and spectroscopy have become invaluable analytical tools in this area [13]. A wealth of imaging and sensing protocols for in vitro and in vivo applications have been devised on the basis of these convenient techniques. The amazing development of these methods, over the past few decades, has been, and continues to be, mainly a result of the tremendous progress in the basic understanding of the photophysical and recognition properties of organic molecules. Decades of investigations on the photophysical properties of organic dyes, in conjunction with the sophistication of chemical synthesis, have delivered an impressive palette of sensitive fluorophores. Recent investigations, however, suggest that the photophysical properties of semiconductor QDs can offer valuable solutions to the problems associated with conventional organic dyes [14–16].

Luminescent QDs offer several advantages over conventional all-organic fluorophores. Organic dyes, like rhodamine 6G (**1** in Fig. 1), generally absorb electromagnetic radiation (a in Fig. 1) and emit light in the form of fluorescence (c in Fig. 1) within very specific wavelength regions. Additionally, their emission bands are broad and asymmetric, in most instances, with often pronounced red tails (c in Fig. 1). In contrast, QDs exhibit broader absorption spectra and narrower emission peaks (b, d in Fig. 1, respectively). In fact, a single light source can be exploited to excite multiple QDs of different dimensions simultaneously to produce multiple emission bands resolved across the visible region [17]. Moreover, the energy gap between the valence and conduction bands of QDs can be regulated simply by adjusting their size and shape, for a given elemental composition. Such a level of structural control of the photophysical response (Fig. 2) possible with these inorganic nanomaterials cannot be replicated with their organic counterparts. For example, large CdSe QDs, with radius close to 10 nm, emit light at relatively long wavelengths to produce orange or red emission. By contrast, small CdSe QDs, with radius close to 1 nm, emit light at relatively short wavelengths to generate blue or green emission.

QDs also have a brighter emission than organic dyes and, therefore, offer the opportunity to achieve higher signal-to-noise ratios in imaging and sensing applications. Indeed, the product of molar absorption coefficient and luminescence quantum yield, the so-called brightness, of QDs is ca. 10- to 20-fold higher compared to that of conventional organic dyes. In addition, the continuous absorption spectra of QDs offer the opportunity to excite these nanoparticles at wavelengths far removed from their emission bands and, hence, allows the acquisition of fluorescence images with optimal contrast. Furthermore, the emissive inorganic core of semiconductor QDs can be encapsulated within a protective inorganic shell to enhance the luminescence quantum yield and minimize photobleaching.

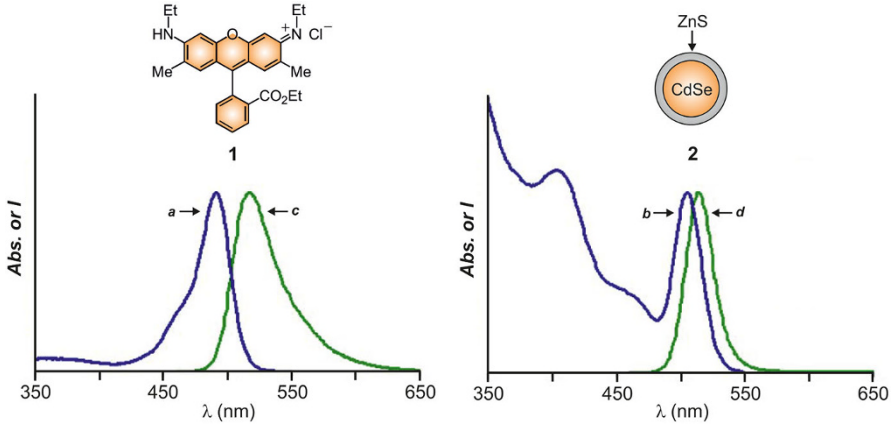

Fig. 1 Comparison of the absorption (*a* and *b*) and emission (*c* and *d*) spectra of rhodamine 6G (**1**, *a* and *c*), a conventional organic fluorophore, and a representative CdSe–ZnS core–shell QD (**2**, *b* and *d*) (Reproduced with permission from Physica E, 2004, © Elsevier Science Ltd.)

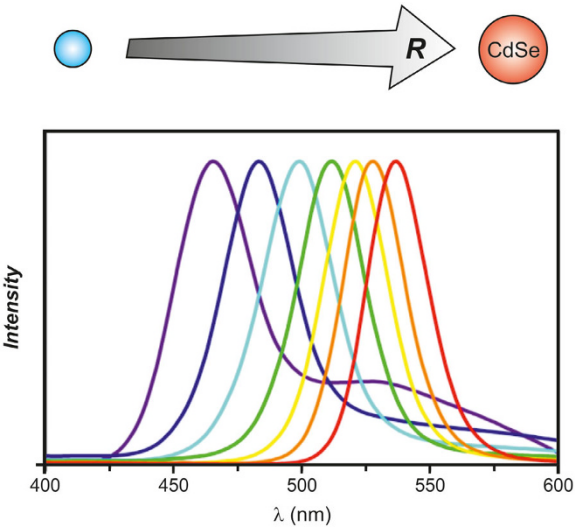

Fig. 2 Emission spectra of CdSe QDs with radius ranging from ca. 1 to 10 nm (Reproduced with permission from Materials, 2010, © MDPI.)

The inorganic nature of QDs also makes them more robust toward metabolic degradation and contributes to their longevity in vivo. In fact, in vivo imaging of thick specimens also benefits from the stability and brightness of QDs since the high absorption and autofluorescence of endogenous chromophores as well as light scattering from tissues can obscure the signal. Indeed, semiconductor QDs have allowed in vivo imaging of a variety of tissues of large animals, such as sentinel lymph nodes of pigs (1 cm deep) [18]. Moreover, the ability to produce QDs with emission bands resolved across the visible region of the electromagnetic spectrum allows the simultaneous tagging of distinct targets with emissive labels producing luminescence of different color and their tracking in parallel with the acquisition of fluorescence images. In fact, multiplex imaging schemes, based on QDs, might well become a powerful alternative to existing non-invasive imaging techniques, like magnetic resonance imaging, positron-emission tomography, X-ray and computing tomography, for diagnostic applications with high spatial and temporal resolutions. Although QDs offer many advantages over organic dyes, they also have several problems that must be addressed. In relation to their photophysical properties, QDs can have surface defects, which can affect the recombination of electrons and holes resulting in luminescence intermittence, the so-called blinking, and in a depressive effect on the emission intensity. Nevertheless, blinking can be minimized by having a protective shell around the emissive core. Some other disadvantages might appear when these systems are used for biomedical applications. QDs tend to aggregate within live cells and can therefore interfere with cellular processes and functions. Moreover, a major challenge lies in the need to promote the cellular internalization of QDs without killing the cells in the delivery process. Although QDs are in the nanometer range, bioconjugation with different molecules increases their size, complicating intracellular delivery. Finally, the potential toxicity of QDs is also a major concern. Their coating can be cytotoxic and high QD concentrations can

damage cells irreversibly. In addition, if the coating of the QDs is compromised, the leakage of heavy elements from the core can cause toxic effects. As a result, the gradual erosion of the shell may lead to undesirable reactions in vivo [19].

1.2 Electron Transfer with Quantum Dots

Electron and energy transfer processes can be designed to switch the luminescence of semiconductor QDs in response to molecular recognition events, offering the opportunity to implement valuable sensing schemes for biomedical applications. On the basis of these operating principles, the presence of target analytes can be transduced into detectable luminescence signals. These mechanisms resemble the operating principles of conventional fluorescent chemosensors and rely on the conjugation of the luminescent inorganic nanoparticles to sensitive organic ligands. The communication between the inorganic and organic components, in the form of an exchange of either electrons or energy upon excitation, then dictates the emissive behavior of the resulting assemblies.

QDs can exchange electrons with complementary acceptors or donors upon excitation. Indeed, photoinduced electron transfer is a process in which an electron is transferred from an electron-donating species (D) to an electron-accepting species (A) upon excitation. As a result of such redox reactions in the excited state, charge separation occurs to prevent the radiative deactivation of the excited species and suppress luminescence. In the case of QDs, the excited nanoparticles can either accept an electron from a donor or donate an electron to an acceptor and lose their ability to emit. In the first instance, the energy of the highest occupied molecular orbital (HOMO) of the donor (quencher) must be higher than that of the valence band of the QD. In the other case, the energy of the lowest unoccupied molecular orbital (LUMO) of the acceptor (quencher) must be lower than that of the conduction band of the QD. When these conditions are satisfied, the change in electronic configuration that accompanies the excitation of the QD is followed by the transfer of one electron either from the quencher to the excited QD or from the excited QD to the quencher (Fig. 3). Indeed, the electron-transfer process is exergonic in both instances with a free energy change (ΔG°) that can be estimated with Eq. (1).

$$\Delta G^0 = eE_{\mathrm{Ox}} - eE_{\mathrm{Red}} - \Delta E_{00} - \frac{e^2}{4\pi\varepsilon_0\varepsilon_{\mathrm{r}}d} \tag{1}$$

In this equation, e is the elementary charge, E_{Ox} is the redox potential of the species donating the electron, E_{Red} is the redox potential of the species accepting the electron, ΔE_{00} is the energy change associated with the electronic transition of the QD, ε_0 is the vacuum permittivity, ε_{r} is the dielectric constant of the medium, and d is the distance separating the QD from the quencher [20]. It is important to stress, however, that this equation was originally developed to estimate the free energy change for photoinduced electron transfer involving molecule-sized chromophores. Semiconductor QDs are significantly larger than their molecular counterparts and, in

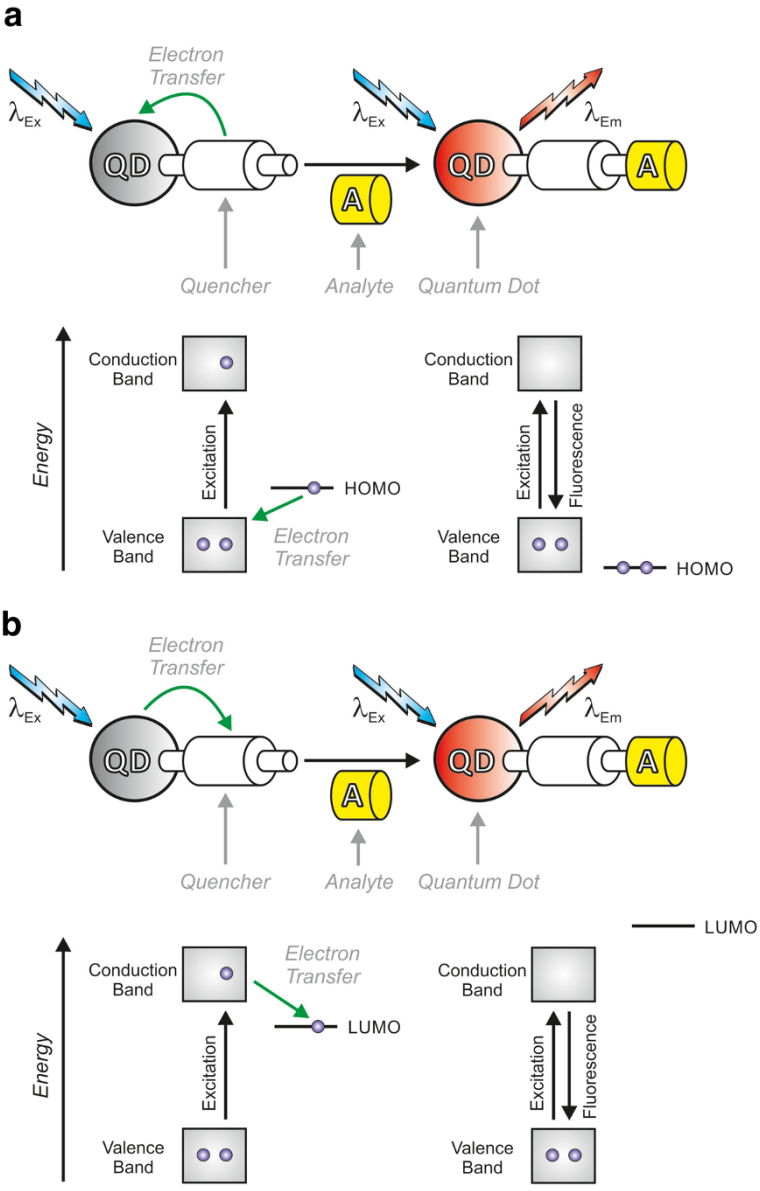

Fig. 3 Electron transfer either from the quencher to the excited QD (**a**) or vice versa (**b**) occurs in the absence of the analyte. In both instances, the association of the analyte with the receptor prevents electron transfer and the excited QD decays radiatively to the ground state

fact, the Bohr radii of their emissive cores can often extend well beyond any adsorbed molecular donors/acceptors, complicating the actual quantification of d.

The association of the quencher with a complementary analyte can be exploited to lower the HOMO energy and, hence, increase E_{Ox}. Alternatively, the recognition

event can be engineered to raise the LUMO energy and, thus, decrease E_{Red}. In both instances, these changes turn the electron transfer from exergonic to endergonic and switch the luminescence of the QDs from off to on. Thus, the switching of the photoinduced electron transfer driving force, on the basis of molecular recognition, can be exploited to regulate the emissive behavior of a QD.

1.3 Energy Transfer with Quantum Dots

Semiconductor QDs can transfer energy to one or multiple complementary acceptors upon excitation by means of the so-called Förster resonance energy transfer (FRET) process. The nanoparticle and the acceptor, however, need to be relatively close to each other for FRET to take place. Indeed, this process involves the nonradiative transfer of the electronic excitation energy of a donor fluorophore to a proximal acceptor. Specifically, FRET occurs efficiently over donor–acceptor distances ranging from 10 to 100 Å, a characteristic that has been widely exploited in the design of ligand binding assays. In addition to such short distances, FRET also requires spectral overlap between the donor emission (*a* in Fig. 4) and acceptor absorption (*b* in Fig. 4) [14, 21]. In fact, the magnitude of the spectral overlap ultimately dictates the magnitude of the distance at which FRET can occur efficiently (vide infra).

The rate (k_{FRET}) of FRET is related to the distance (r) between donor and acceptor according to Eq. (2), where τ_D is the lifetime of the donor excited state and R_0 is the Förster distance for the donor–acceptor pair. The latter parameter is the donor–acceptor separation at which the FRET efficiency (E) is equal to 50 %, according to Eq. (3), and can be estimated from the emission intensity measured for the donor without (F_D) and with (F_{DA}) the acceptor.

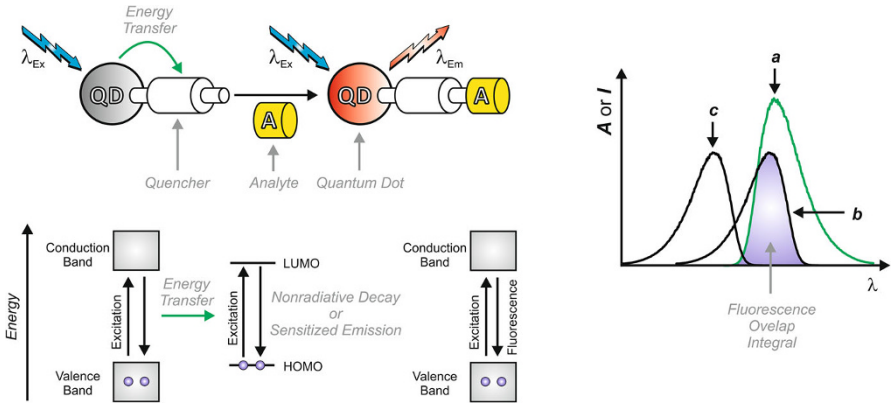

Fig. 4 Overlap between the emission band (*a*) of the QD and the absorption band (*b*) of the quencher permits the transfer of energy from the former to the latter upon excitation. The association of the analyte (*top left*) shifts the absorption band of the quencher (*c*), prevents energy transfer, and turns on the luminescence of the QD. The mechanism of the process is illustrated (*bottom left*)

$$k_{\mathrm{FRET}} = \frac{1}{\tau_{\mathrm{D}}}\left(\frac{R_0}{r}\right)^6 \tag{2}$$

$$E = 1 - \frac{F_{\mathrm{D}}}{F_{\mathrm{DA}}} = \frac{R_0^6}{R_0^6 + r^6} \tag{3}$$

The value of R_0 is related to the fluorescence quantum yield (Q_0) of the donor in the absence of the acceptor, the refractive index (n) of the solvent, Avogadro's number (N_{A}), the orientation factor (k^2), and the overlap integral (J), according to Eq. (4).

$$R_0^6 = \frac{9000\, Q_0 (\ln 10)\, k^2 J}{128 \pi^5 n^4 N_{\mathrm{A}}} \tag{4}$$

The value of J quantifies the spectral overlap between the bands associated with the emission of the donor and the absorption of the acceptor (overlap area, in purple, between a and b in Fig. 4). It can be estimated from the normalized emission of the donor (f_{D}) and the molar absorption coefficient (ε_{A}) of the acceptor measured over the wavelength (λ) range covered by the two bands with Eq. (5).

$$J = \int f_{\mathrm{D}}(\lambda)\ \varepsilon_{\mathrm{A}}(\lambda)\, \lambda^4\, \mathrm{d}\lambda \tag{5}$$

The value of k^2 quantifies the relative orientation of the transition moments of donor and acceptor and can vary from 0 to 4. If the two species exchanging energy are isotropically oriented, k^2 averages 2/3.

Molecular recognition events can be designed to alter the physical separation between a QD and an energy acceptor as well as their spectral overlap. Thus, the efficiency of energy transfer and the luminescence quantum yield of the nanoparticle can be engineered to vary with the supramolecular association of a specific substrate. Under these conditions, the presence of target analytes can be transduced into detectable luminescence signals. Conventional fluorescence assays, which measure the fluorescence intensity of bound dye labels, require separation of the unbound dyes before the extent of binding can be determined. FRET simplifies these assays because the binding is observed directly. When a donor is attached to one binding partner and an acceptor is attached to the other, the recognition of the two brings donor and acceptor close enough to allow FRET. In turn, the enhanced FRET efficiency provides a direct readout of the extent of binding (Fig. 4).

As mentioned above, there is a strong motivation for using QDs as donor groups in FRET experiments in place of conventional organic dye molecules. On one hand, the spectral properties of QDs can be finely tuned to match those of any desired acceptor molecule only by adjusting the QD size, without the need to change the whole chemical composition of the system. On the other hand, QDs also circumvent one of the main problems of conventional FRET, i.e., cross talk between the donor and acceptor emission, which is mainly caused by direct excitation of the acceptor, and spectral overlap between the donor and acceptor emission. As a result of this

phenomenon, noticeable background emission is generally produced, limiting the overall sensitivity of the assay. Importantly, and because of their broad absorption spectra, QDs can be excited efficiently at a wavelength that is far removed from the absorption spectrum of the acceptor, minimizing direct excitation. Also, the emission band of a QD is narrower and more symmetric than those organic dyes, making it much easier to distinguish the emission of the QD donor from that of the acceptor.

The applicability of the FRET formalism to QDs has been validated by many studies [22, 23]. It is usually assumed that k^2 is equal to 2/3 for QD donors because of their twofold degenerate (circular) transition dipole, the rotational freedom of proximal dyes, and the random assembly of those dyes to the QD surface. As donors, QDs are advantageous in that their narrow, continuously tunable emission (by size or composition) permits optimization of the spectral overlap integral, while also minimizing cross talk in measurements of donor and acceptor luminescence. Their broad absorption spectra also provide flexibility in the choice of excitation wavelength, so that direct excitation of an acceptor dye can be minimized. The other general advantages of QDs—their brightness, resistance to photobleaching, and more facile multiplexing—are also relevant to FRET configurations. Moreover, the large surface area of QDs permits the arraying of multiple acceptors per QD, thereby providing another mechanism to optimize FRET efficiencies. For the case of N equivalent acceptors around a central QD donor, Eq. (3) can be modified to Eq. (6), according to which FRET efficiency increases as the number of acceptors increases. Given the approximately spherical shape of QDs, such arrangements are easily accessed in real experiments. Furthermore, QDs are also excellent acceptors for certain classes of donors (e.g., lanthanides, chemiluminophores, and bioluminescent proteins) [14].

$$E_{\mathrm{FRET}} = \frac{NR_0^6}{NR_0^6 + r^6} \tag{6}$$

2 Quantum Dots with Photochromic Ligands

2.1 Spiropyrans

Photochromic molecules switch reversibly under optical control between distinct states, which differ in their ability to absorb electromagnetic radiation [24–27]. Typically, a photochromic transformation occurs upon illumination with ultraviolet light to cause pronounced changes in the visible region of the absorption spectrum. The photoresponsive character of these compounds and reversibility of their transformations have enabled the modulation of numerous molecular as well as macroscopic properties under optical stimulations. In particular, hybrid assemblies, combining the outstanding photophysical properties of inorganic nanocrystals and the unique photochemical behavior of organic photochromes, have been extensively studied in the last two decades with the ultimate goal of developing smart materials.

In this section, examples of such photoresponsive nanomaterials, consisting of QDs passivated with spiropyran ligands, are discussed.

At a given donor–acceptor distance, the efficiency of FRET depends predominantly on the spectral overlap between the emission of the donor and the absorption the acceptor. As a result, this parameter can be modulated reversibly relying on the pronounced changes in absorption associated with photochromic transformations. Specifically, spiropyrans (SPs) generally absorb at wavelengths shorter than 400 nm and isomerize reversibly to the merocyanines (MCs) upon ultraviolet illumination [28]. The photogenerated products absorb instead in the visible region with large molar absorption coefficients but revert either thermally or under visible illumination back to the original SP. These transformations can be exploited to generate reversibly a chromophore capable of accepting energy from a complementary QD and, therefore, modulate FRET efficiency.

SPs can be conveniently modified with aliphatic chains terminated by active esters, which can then be linked covalently to primary amino groups of biomolecules [29]. Specifically, this protocol was exploited to connect SPs to the maltose-binding protein (MBP) and, then, multiple copies of this labeled protein were conjugated to individual CdSe–ZnS core–shell QDs (Fig. 5). This particular protein has a C-terminal 5-HIS sequence and adsorbs on the ZnS shell of the QDs spontaneously because of the ability of the histidine tag of the biomolecule to coordinate the Zn atoms of the nanocrystal [30, 31]. The resulting construct emits at 550 nm upon excitation at 440 nm. Upon ultraviolet irradiation, the SP ligands connected to the QD switch to the corresponding MC with the concomitant

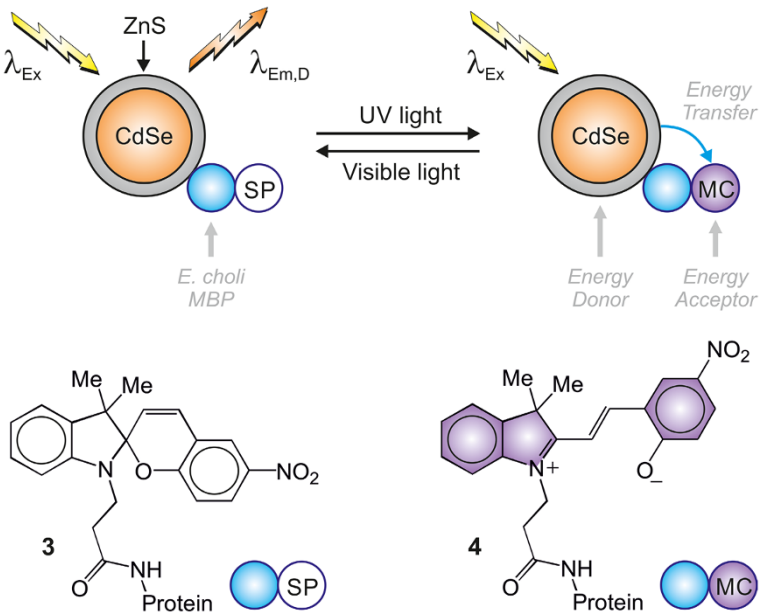

Fig. 5 Photoinduced and reversible interconversion of SP and MC ligands absorbed on the surface of a QD results in the modulation of the luminescence associated with the inorganic component

appearance of an intense absorption band around 550 nm. The significant overlap between the photogenerated absorption and the emission of the QDs activates energy transfer from the inorganic particle to the organic ligands upon excitation. As a consequence of the efficient transfer of excitation energy, the excited QDs deactivate nonradiatively and the luminescence decreases drastically. Upon illumination with visible light, the MC components revert back to the original SP form and the initial emission intensity is restored. In fact, alternating ultraviolet and visible inputs can be exploited to modulate the luminescence intensity of these QD–SP/MC constructs for multiple cycles.

Alternatively, SPs can be modified to allow their direct attachment to the surface of QDs without protein spacers [32]. These reactions are based on the affinity of sulfur-containing functional groups, i.e., disulfides or thiols, to adsorb on the ZnS shell of CdSe–ZnS core–shell QDs. In one instance, lipoic acid was conjugated to an SP in the form of compound **5** (Fig. 6). The dithiolane ring at the end of the aliphatic tail of **5** was chosen for its ability to bind the Zn centers of the QDs. After UV irradiation in dichloroethane, colorless isomer **5** switches to colored isomer **6** with the concomitant appearance of an intense absorption band in the visible region. The photogenerated isomer is thermally unstable and reverts back to the original state within a few seconds. The absorbance decay at 592 nm is indicative of first-

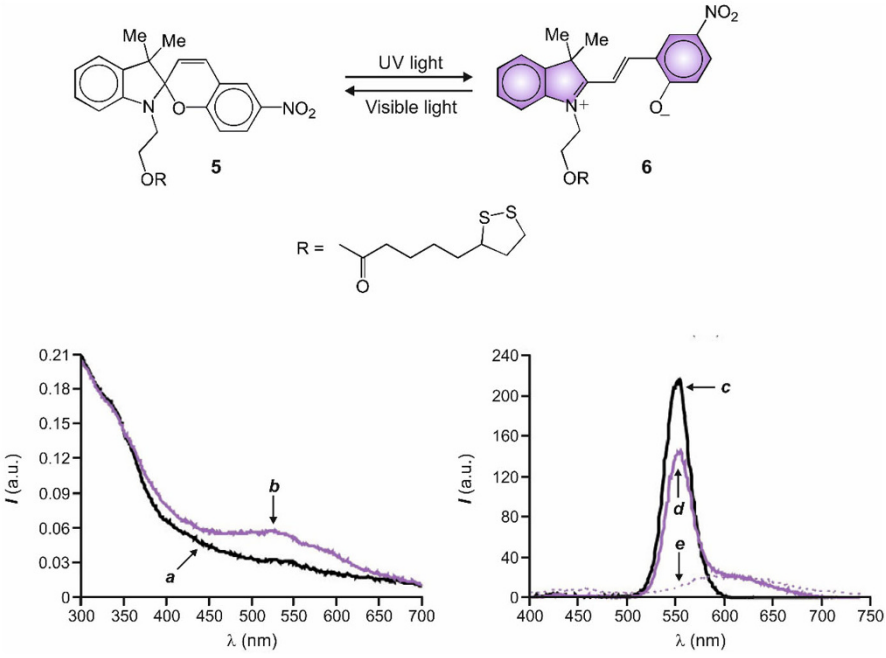

Fig. 6 Absorption spectra of a solution of CdSe–ZnS core–shell QDs (0.7 μM, dichloroethane, 20 °C) with **5** adsorbed on their surface before (*a*) and after (*b*) continuous irradiation (365 nm, 0.4 mW cm^{-2}, 10 min) and the corresponding (*c* and *d*) emission spectra ($\lambda_{Ex} = 380$ nm). Emission spectrum (*e*) of a solution of **5** (0.1 mM, dichloroethane, 20 °C, $\lambda_{Ex} = 380$ nm) after continuous irradiation (365 nm, 0.4 mW cm^{-2}, 10 min) (Reprinted with permission from Aust. J. Chem., 2006, © CSIRO Publishing)

order kinetics and suggests the lifetime of **6** to be ca. 25 s. Thus, the absorbance corresponding to the visible band of **6** can be modulated simply by turning an ultraviolet source on and off, offering the opportunity to control the ability of the photochromic component to accept energy from an excited QD.

The photochromism of **5** is retained after its adsorption on the surface of the QDs. Indeed, the characteristic band of **6** appears in the visible region (a, b in Fig. 6) upon UV illumination. This photoinduced transformation results in a significant decrease in the QD emission (c, d in Fig. 6) because of the ability of the MC ligands, photogenerated on the nanocrystal surface, to accept the excitation energy of the QDs. Consistently, the spectrum, recorded after the photoisomerization of the ligands, also shows a broad emission that was observed for **6** on its own (e in Fig. 6) and corresponds to the sensitized fluorescence of the energy acceptor. After the thermal isomerization of the MC ligands back to their SP state, the energy transfer pathway is suppressed and the original emission intensity of the QDs is fully restored. Interestingly, however, the adsorption of the photochromic components on the inorganic nanoparticles significantly slows the reisomerization kinetics and, in fact, the lifetime of MC increase to 250 s, under these conditions.

Similarly, mixing a thiol-containing SP (Fig. 7) with CdSe–ZnS core–shell nanoparticles at ambient temperature for 1 h in the dark can also produce QDs with photochromic ligands on their surface [33]. The adsorbed SP undergoes photoinduced ring opening under UV irradiation to give the corresponding MC form. Once again, the photogenerated isomer has a strong absorption in the visible region that significantly overlaps the QD emission. As a result of the optimal spectral overlap and close proximity of the two components, energy transfer occurs from the excited QD to the photogenerated MC with a concomitant decrease in luminescence intensity. The original emission is, however, restored after visible illumination to encourage the reisomerization of the MC ligands back to the SP form. These results demonstrate, yet again, that the photoinduced interconversion of the two states of

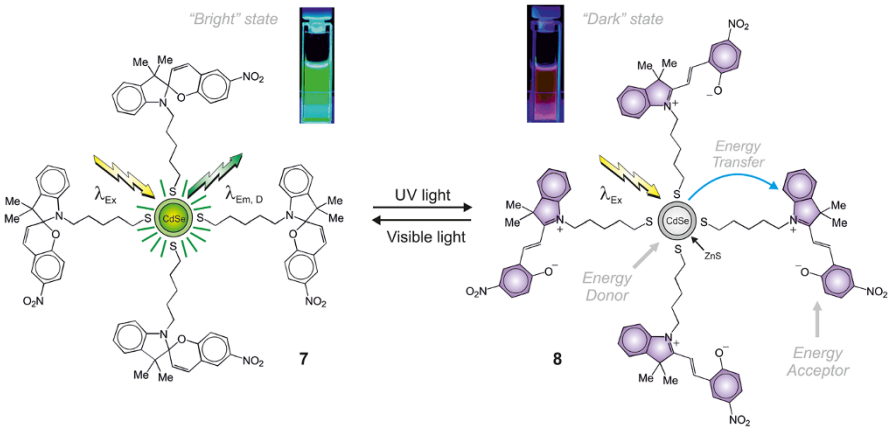

Fig. 7 Modulation of the luminescence intensity with the photochemical interconversion between the SP and MC forms of the photochromic ligands adsorbed on the surface of CdSe–ZnS core–shell QDs (Reprinted with the permission from J. Am. Chem. Soc., 2005, © American Chemical Society)

the photochromic component can be exploited to regulate the spectral overlap between the donor emission and the acceptor absorption with optical stimulations and, ultimately, photomodulate FRET efficiency.

2.2 Diarylethenes

Diarylethenes are members of another family of photochromic compounds that have been connected to QDs with the ultimate goal of modulating the luminescence of the inorganic nanoparticles under optical control [34–37]. In contrast to SP derivatives, which revert spontaneously from their photogenerated and colored state to their colorless form, diarylethenes are thermally stable and switch back to their initial form only under illumination at an appropriate wavelength [38]. Additionally, they are remarkable stable and generally tolerate multiple switching cycles without any significant photodegradation.

The outstanding photochromic performance of diarylethenes suggested the attachment of these photochromic compounds to the surface of CdSe–ZnS core–shell QDs (Fig. 8) [35]. Specifically, the treatment of preformed QDs with a diarylethene derivative with a terminal pyridyl anchoring group results in the adsorption of multiple photochromic ligands on the shell of the inorganic nanoparticles. In the resulting constructs, the diarylethene ligands retain their photochromic properties and can be interconverted between their colorless and colored forms by alternating ultraviolet and visible irradiation. The main absorption of the colored state significantly overlaps the emission of the QD, allowing the transfer of energy from the excited nanoparticle to the ligand. Additionally electron transfer from the colored form of the photochromic ligands to the excited QD is exergonic, according to Eq. (1). Both processes can lead to the nonradiative deactivation of the excited nanoparticles and the effective quenching of their luminescence. As a result, the photoinduced interconversion of **9** into **10** leads to a

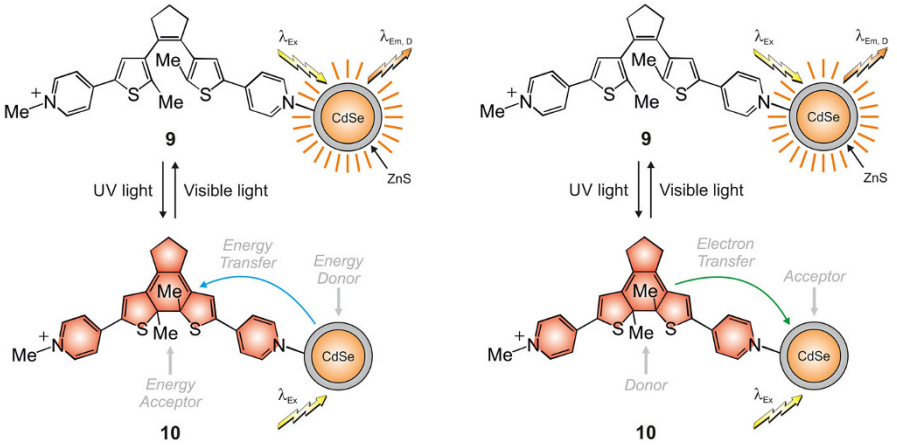

Fig. 8 Photoinduced interconversion of ring-open (**9**) and ring-closed (**10**) forms of diarylethene ligands adsorbed on CdSe–ZnS core–shell QDs and the associated FRET modulation

pronounced luminescence decrease and the photoinduced reisomerization of **10** back **9** restores the initial emission intensity.

Diarylethenes are relatively hydrophobic and QDs coated with **9** could be operated only in organic solvents [35]. In order to extend these operating principles

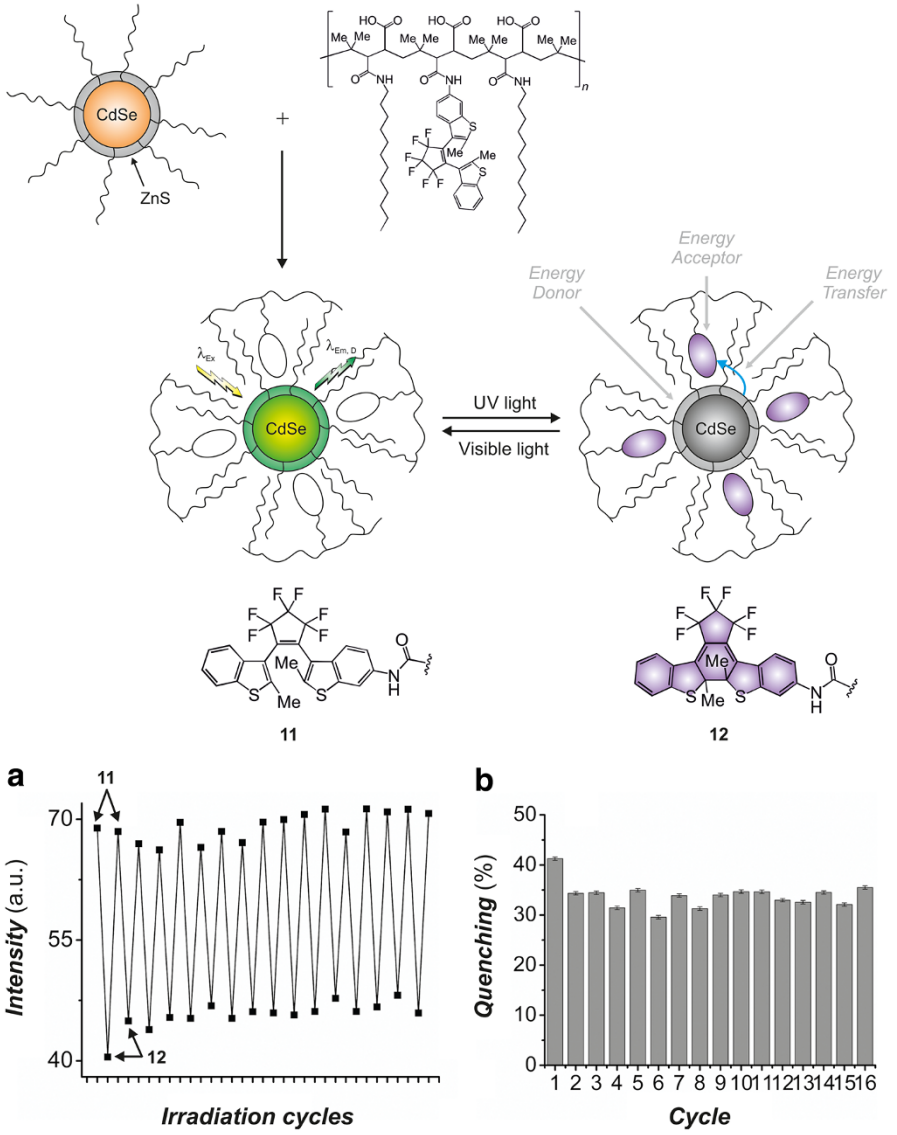

Fig. 9 Luminescence of QDs coated with an amphiphilic and photochromic polymer switches between high and low values with the state of the photochromic component because of efficient FRET from the excited inorganic components to the colored state of the diarylethene ligands. Luminescence intensity (**a**) and quenching efficiency (**b**) changes with alternating ultraviolet (340 nm, 1.0 mW cm^{-2}) and visible (545 nm, 5.8 mW cm^{-2}) pulses (60 s) (Adapted from ACS Nano, 2011, © American Chemical Society)

to water, QDs were capped instead with amphiphilic polymers with diarylethene components in their side chains (Fig. 9) [36]. The resulting QDs readily dissolve in aqueous solutions and, under these conditions, show a luminescence response to illumination similar to that observed for their hydrophobic counterparts. Once again, the diarylethene ligands can be interconverted between colorless and colored forms, by alternating ultraviolet and visible illumination, with the concomitant appearance and disappearance of an intense absorption band in the visible region. The absorption of the colored form significantly overlaps the emission of the QDs and, therefore, allows efficient FRET from the inorganic to the organic components upon excitation. As a result, the luminescence of the coated QDs is effectively quenched only when the diarylethene components are in their colored state. It follows that the emission of these nanostructured constructs can be switched for multiple cycles with excellent fatigue resistance simply by controlling the state of the photochromic components embedded in the polymer coating.

The behavior of this system was modeled taking into account a single QD donor and a polymer coating with a variable number of photochromic acceptors [36]. Interestingly, this analysis suggests the presence of two subsets of diarylethene photochromes, denoted as class 1 and 2. The photoisomerization of class 1 proceeds more efficiently than that of class 2, under UV irradiation, reaches a photostationary state of 2–4 %, and appears to be mostly responsible for quenching the QD luminescence. Class 2 interconverts only after prolonged UV illumination, reaches a photostationary state of 33 %, and has only a modest influence on FRET efficiency. Specifically, the FRET efficiency is 0.48 for class 1 and 0.007 for class 2. The different behavior of the two ligands subsets is, presumably, a consequence of distinct environments around the two subsets of photochromes. In fact, diarylethenes in class 1 are close to the QD surface (Fig. 10) and experience a relatively nonpolar environment, which facilitates photoisomerization. Additionally, their absorption transition moment appears to be predominantly perpendicular to the QD surface. Such an arrangement is, presumably, enhancing the orientation factor and, as a result, the FRET efficiency.

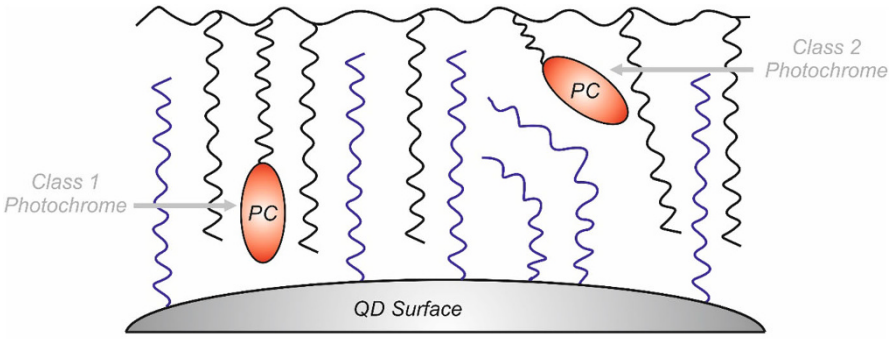

Fig. 10 Heterogeneity of distance and orientation of the photochromic (PC) components, i.e., the FRET acceptors, to the QD surface, i.e., the FRET donor (Adapted from ACS Nano, 2011, © American Chemical Society)

3 Quantum Dots with Photocaged Ligands

3.1 *ortho*-Nitrobenzyl Derivatives

Photocaged fluorophores switch from a nonemissive to an emissive state upon illumination at an appropriate activation wavelength and are particularly valuable probes for the investigation of biological samples [39]. In fact, fluorescence activation within a region of interest, under optical control, offers the opportunity to monitor the diffusion of a labeled target as well as to reconstruct fluorescence images with subdiffraction resolution [40–44]. The operating principles of such photoactivatable probes are generally based on the photoinduced cleavage of a quenching group from an organic fluorophore to transform a quenched into a non-quenched state. These switching mechanisms can also be adapted to control the luminescence of semiconductor QDs with the ultimate goal of developing probes with photoactivatable emission based on the superior photophysical properties of such inorganic nanoparticles.

ortho-Nitrobenzyl (ONB) groups have been used to cage organic fluorophores and activate their emission mostly relying on mechanisms based on photoinduced electron transfer [45–49]. Indeed, ONB groups cleave efficiently to form *ortho*-nitrosocarbonyl derivatives, under ultraviolet irradiation. This photolytic transformation can be exploited to separate an electron acceptor from a fluorescent chromophore and switch the emission of the latter on. Recently, this general design logic was extended to the optical control of QD luminescence [50, 51]. In one instance, CdTe–CdS core–shell QDs were coated with increasing amounts of ONB ligands, bearing a pair of thiol anchoring groups and a phosphate spacer (Fig. 11) [50]. The thiol groups ensure adsorption of the ligand on the QD shell, and the phosphate linker imposes aqueous solubility on the resulting assembly. The QDs coated with ONB ligands showed a significant reduction in luminescence (ca. 400-fold) compared to control nanoparticles lacking ONB groups (a–c in Fig. 12). Photoinduced electron transfer from the inorganic core to the ONB groups is responsible for the nonradiative deactivation of the excited QDs and the suppression of their emission. Upon ultraviolet illumination (365 nm, 2 mW mm^{-2}), **13**

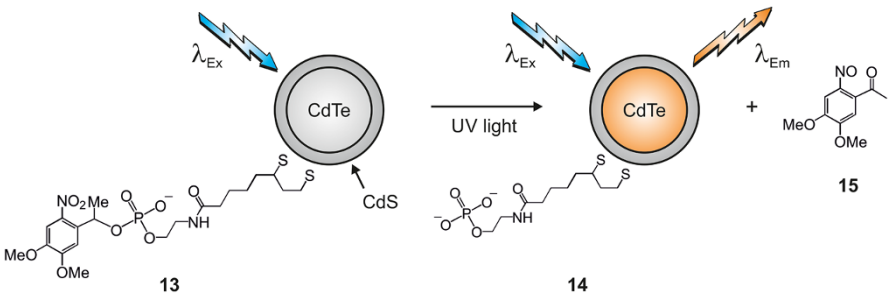

Fig. 11 Photoinduced separation of a QD from ONB ligands with the formation of the corresponding *ortho*-nitrosocarbonyl derivative (Adapted from J. Am. Chem. Soc., 2008, © American Chemical Society)

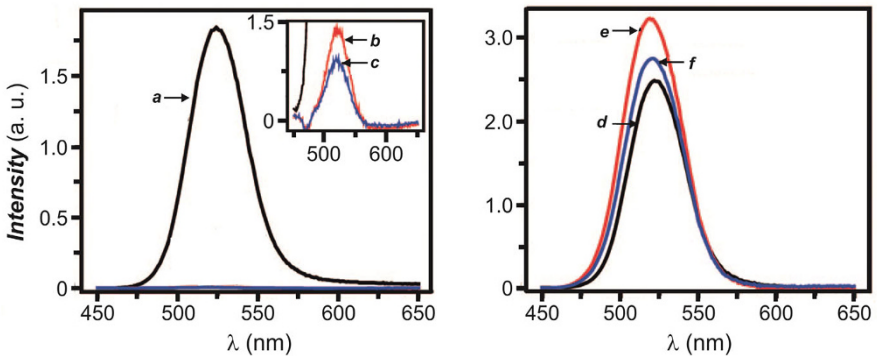

Fig. 12 Emission spectra (λ_{Ex} = 405 nm) of CdTe–CdS core–shell QDs without (*a*) and with different amounts (*b* and *c*) of ONB ligand **13**. Emission spectra of the very same QDs recorded after irradiation at 365 nm for 10 min (*d–f*) (Reprinted with permission from J. Am. Chem. Soc., 2008, © American Chemical Society)

switches to **14** and releases **15** (Fig. 11). The photoinduced separation of the electron acceptors from the inorganic component prevents quenching and activates the luminescence of the QDs (d–f in Fig. 12). Interestingly, the luminescence intensity after photolysis is slightly higher than that of the control QDs. In fact, illumination of the control nanoparticles, lacking the photocleavable quenchers, leads to a minor increase (1.3-fold) in luminescence intensity (a, d in Fig. 12). Presumably, photoinduced annealing of surface traps is responsible for these effects.

Alternatively, photocleavable ONB groups can be attached to CdSe–ZnS core–shell QDs coated with hydrophilic polymeric ligands to control their luminescence with optical stimulations (Fig. 13) [52]. In this instance, two batches of QDs with different diameter and, hence, resolved emission bands were synthesized and coated with polymer **16**. This polymer incorporates multiple thiol anchoring groups, to encourage adsorption on the QD shell, and multiple hydrophilic oligo(ethylene glycol) chains, to impose aqueous solubility on the coated QDs. Additionally, some of the hydrophilic side chains have terminal carboxylic acids to allow the coupling of organic chromophores to the water-soluble QDs. One of the two QD batches was reacted with 2-nitrobenzylamine to couple multiple ONB groups to the polymer coating and then mixed in excess with the unreacted batch. The emission spectrum (a in Fig. 13) of the resulting mixture shows two resolved bands for the two sets of quantum dots. One of them corresponds to QDs with small diameter, low concentration, and no ONB ligands on their surface. The other is associated with QDs with large diameter, high concentration, and ONB ligands on their surface. Upon ultraviolet illumination, the ONB ligands cleave from the surface of the large QDs and the corresponding emission band increases in intensity significantly (b in Fig. 13), while the one associated with the small QDs lacking the ONB ligands remains almost unaffected. If the very same experiment is repeated swapping the role of the two batches of QDs, a similar luminescence enhancement is observed (c and d in Fig. 13). Specifically, the ONB groups were connected to the small QDs in this instance and only the emission band at short wavelengths increases with

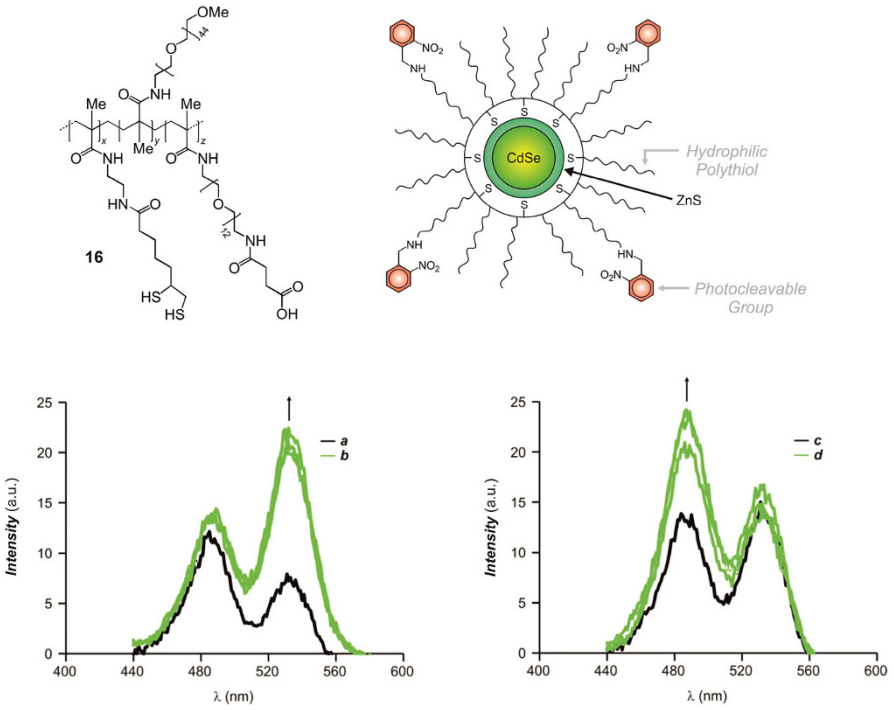

Fig. 13 Emission spectra of mixtures (PBS, pH 7.4, 25 °C, $\lambda_{Ex} = 420$ nm) of two sets of CdSe–ZnS core–shell QDs, both coated with **16** but differing in core diameter, recorded after conjugation of 2-nitrobenzylamine to the set emitting at long (*a*) or short (*c*) wavelengths and after further ultraviolet irradiation for 5, 10, and 15 min (*b* and *d*). The concentrations of the quantum dots emitting at short wavelengths are 0.1 (*a* and *b*) and 1.8 μM (*c* and *d*) and those of the ones emitting at long wavelengths are 0.8 (*a* and *b*) and 5.6 μM (*c* and *d*) (Reprinted with permission from J. Am. Chem. Soc., 2012, © American Chemical Society)

illumination as a result. These observations indicated that the illumination conditions have negligible influence on QDs lacking the ONB groups, irrespectively of their size. By contrast, the luminescence of the QDs functionalized with ONB groups increases with irradiation because of the photoinduced cleavage of such electron acceptors away from the nanoparticle surface.

These operating principles can also be exploited to switch QD luminescence under optical control within the intracellular environment. Specifically, the incubation of Chinese hamster ovary (CHO) cells with one batch of QDs coated with ONB groups results in the internalization of the nanoparticles. The corresponding phase-contrast image (Fig. 14a) clearly reveals the contour of individual cells, which, however, cannot be observed in the luminescence-only counterpart (Fig. 14b) because of the low luminescence of the QDs coated with the quenching ONB units. After ultraviolet illumination, the emission intensity of the internalized QDs increased significantly and the stained cells become visible in both phase-contrast and luminescence-only images (Fig. 14c, d).

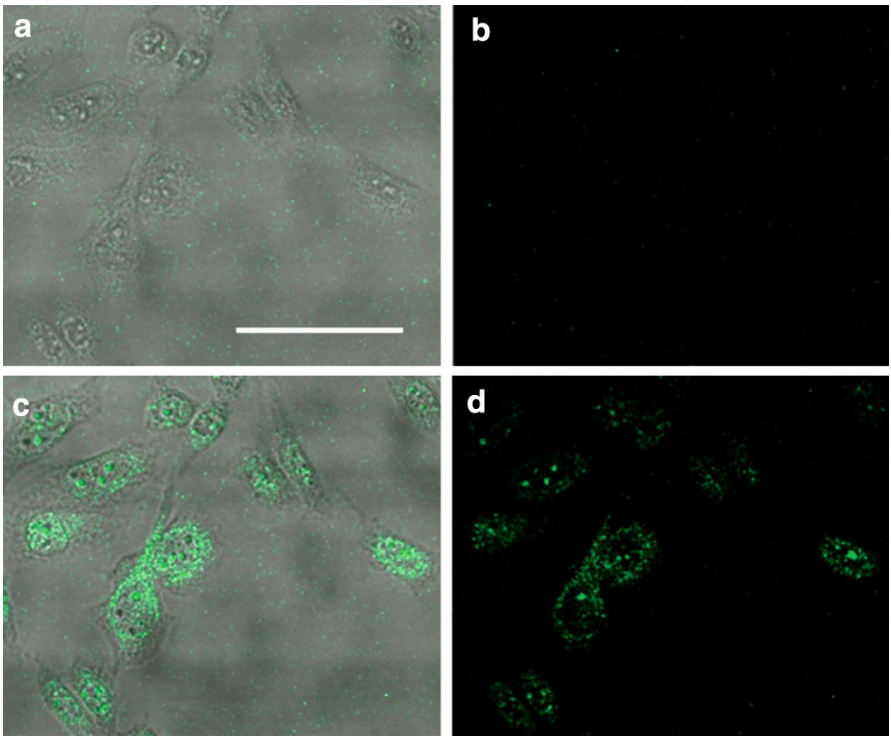

Fig. 14 Phase-contrast (**a**, **c**) and luminescence (**b**, **d**) images (800 nm, *scale bar* 50 μm), recorded before (**a**, **b**) and after (**c**, **d**) irradiation (365 nm, 0.4 mW cm^{-2}, 30 min), of CHO cells incubated with CdSe–ZnS core–shell QDs (30 nM), coated with **16** and conjugated to 2-nitrobenzylamine, for 3 h (Reprinted with permission from J. Am. Chem. Soc., 2012, © American Chemical Society)

3.2 Photocaged Nitric Oxide

Nitric oxide (NO) is a gas at physiological temperature (37 °C) and a free radical having an unpaired electron in a π* antibonding molecular orbital [53, 54]. NO is sufficiently nonpolar to freely diffuse through the cell membrane and elicits its effect far from the site of production or release. Once considered a toxic pollutant with no physiological importance, it took almost two decades to elucidate the biochemical implications of NO and these seminal investigations culminated with the assignment of the Nobel Prize in Physiology and Medicine to Louis J. Ignarro, Ferid Murad, and Robert F. Furchgott [55–57]. The role of NO in several physiological and pathophysiological processes related to the immune response, smooth muscle vascular tone control, neuronal communication, gene regulation, and cancer biology is now well recognized [58]. Indeed, promising therapeutic applications for NO are actively being explored [59–61].

Several compounds have already been developed with the ultimate goal of delivering NO in the human body [62, 63]. In this context, light can be a particularly convenient stimulation to control the delivery of such therapeutic agents in a

specific location of the body at a given time [64]. In fact, the photoinduced release of NO from appropriate biocompatible precursors, in combination with the outstanding photophysical properties of semiconductor QDs, is especially promising [65]. Such inorganic nanocrystals can be designed to absorb effectively exciting photons at wavelengths with optimal penetration depths in biological samples (650–900 nm, [66]) and transfer their excitation energy to ligands adsorbed on their surface that can then release NO.

The sensitization of NO release with QDs was first reported in 2007 by Peter C. Ford [67]. In this seminal study, *trans*-Cr^{III}(cyclam)$(ONO)_2^+$ (**18** in Fig. 15) was the photocaged NO ligand. This compound is a weakly absorbing species, but the rate of NO production can be enhanced significantly with the aid of an antenna chromophore. For this purpose, a solution of water-soluble CdSe–ZnS core–shell QDs, passivated with dihydrolipoic acid (**17**), was treated with increasing amounts of **18**. Quenching of QD luminescence was observed (a and b in Fig. 15) and ascribed to the electrostatic adsorption of the cationic metal complexes on the anionic QDs surface. Indeed, the adsorption of the metal complexes on the nanocrystals promotes FRET, quenches the luminescence of the latter, and encourages the release of NO from the former (c and d in Fig. 15) [68]. The mechanism responsible for the photoinduced release of NO is illustrated in the diagram of Fig. 16 [69]. The excited QD transfers energy to the quartet excited state of **18** (^{4}CrONO in Fig. 16). Intersystem crossing then populates a reactive doublet state (^{2}CrONO in Fig. 16), which finally releases NO. Furthermore, the efficiency of the overall process can be enhanced further by varying the structure of the

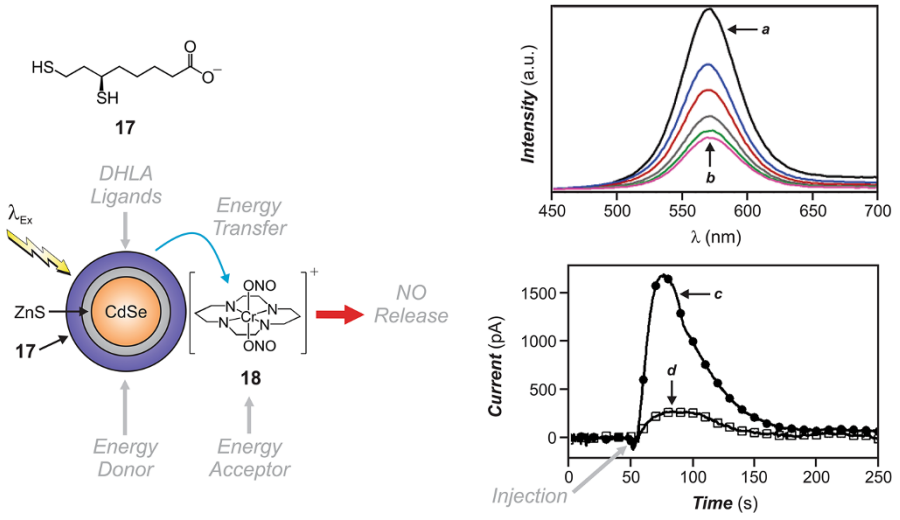

Fig. 15 Excitation of CdSe–ZnS core–shell QDs coated with dihydrolipoic acid (**17**) is followed by energy transfer to the metal complex (**18**), adsorbed on the nanocrystal surface, and release of NO. *Top right* Emission spectra (λ_{Ex} = 366 nm) of QDs (130 nM) in phosphate buffer, showing luminescence quenching with increasing concentrations of **18** from 0 (*a*) to 630 μM (*b*). *Bottom right* Amperometric detection of NO released from **18** with (*c*) and without (*d*) QDs upon excitation (Adapted with permission from J. Am. Chem. Soc., 2007, © American Chemical Society)

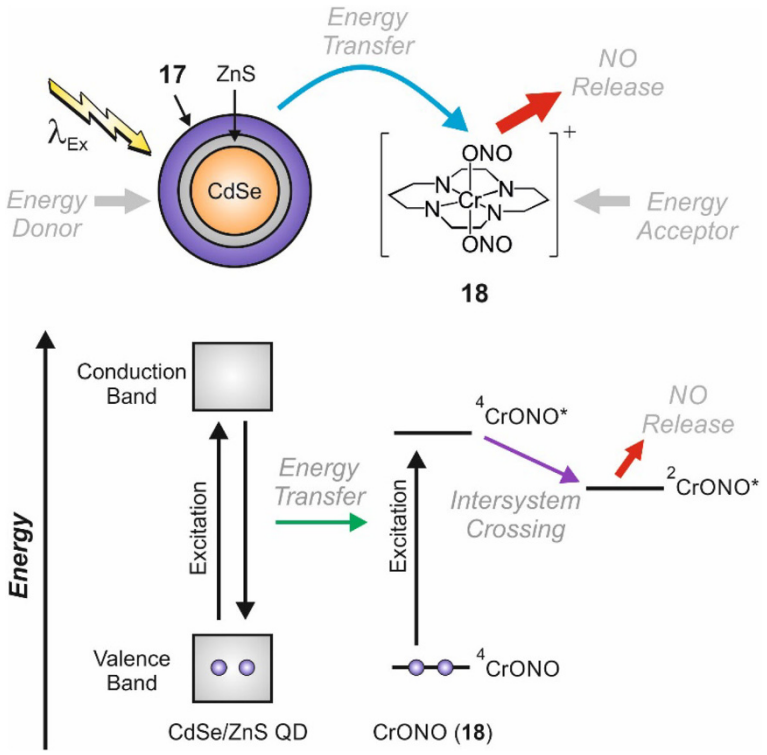

Fig. 16 Mechanism responsible for the photoinduced release of NO (CrONO represents **18**) (Adapted with permission from J. Am. Chem. Soc., 2007, © American Chemical Society)

macrocycle around the metal cation and the nature of its counterion as well as by adjusting the size and elemental composition of the QD in order to optimize the overlap between donor emission and acceptor absorption [69].

A related study focused on the synthesis of water-soluble CdTe QDs, passivated with mercaptopropionic acid (**19**), that were used to sensitize the nitrosyl ruthenium complex *cis*-[Ru(NO)(4-ampy)$(bpy)_2$]-$(PF_6)_3$ (**20**) (bpy is 2,2′-bipyridine, and 4-ampy is aminopyridine) and photogenerate NO [70]. Irradiation of a solution containing both species at 530 nm generated an eightfold increase of NO release, compared to the irradiation of just the ruthenium–nitrosyl complex (Fig. 17).

The addition of increasing amounts of **20** to a solution of QDs resulted in significant luminescence quenching. However, there is little or no overlap between the QD emission and the Ru-NO absorption; thus, a mechanism other than FRET must be responsible for quenching. In fact, the absorption spectrum of the mixture of the two components is significantly different from the sum of those of the separate species. A new absorption band appears at 457 nm in the spectrum of the mixture, as a result of the adsorption of **20** on the QD surface in the ground state with the formation of the adduct shown in Fig. 18. Presumably, electron transfer

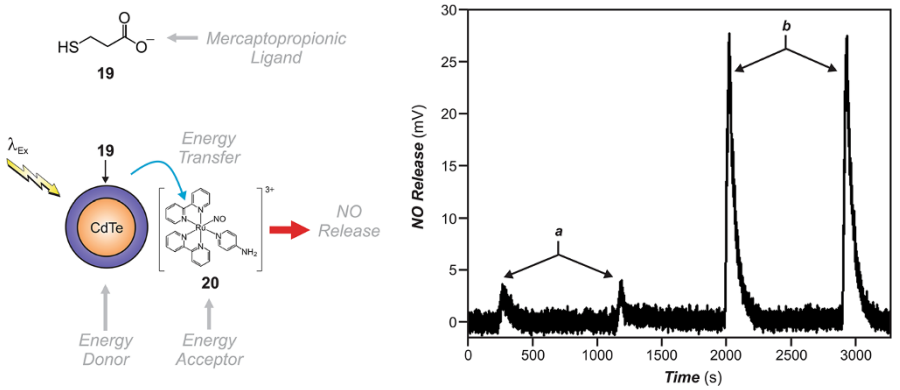

Fig. 17 Amperometric detection of NO in a solution of *cis*-[Ru(NO)(4-ampy)(bpy)$_2$]-(PF$_6$)$_3$ (**20**), before (*a*) and after (*b*) adding CdTe QDs, upon irradiation at 530 nm for 30 s in citric buffer (Adapted with permission from *J. Phys. Chem. A*, 2014, © American Chemical Society)

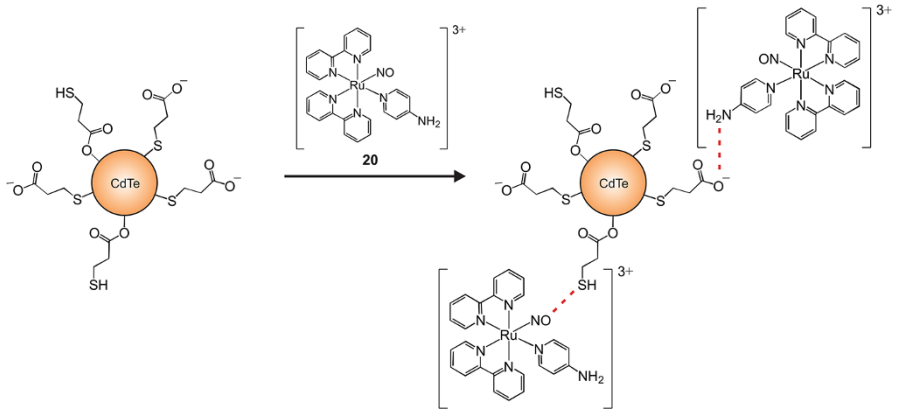

Fig. 18 Adsorption of **20** on the surface of CdTe QDs passivated with **19** (Adapted from J. Phys. Chem. A, 2014, © American Chemical Society)

from the excited CdTe core to the adsorbed ruthenium center is responsible for luminescence quenching and for the sensitization of the NO release.

The photoinduced release of NO was also achieved with nanoparticles composed of positively charged chitosan nanospheres that encapsulate glutathione-capped Ag_2S QDs and have Roussin's black salt (RBS) electrostatically adsorbed on their surface (Fig. 19) [71]. The inorganic core of the resulting construct absorbs at 794 nm and emits at 963 nm and, therefore, offers the opportunity to acquire images relying exclusively on near-infrared radiation. The RBS components can be irradiated at 488 nm to photogenerate NO. Interestingly, the luminescence core and photoresponsive ligands do not interfere with each other and can be operated in parallel to allow the simultaneous acquisition of images and NO release (Fig. 20). Furthermore, the introduction of a Mn(II)-doped ZnS QD within the chitosan nanospheres, in place of the Ag_2S core, can be exploited to shift the wavelength,

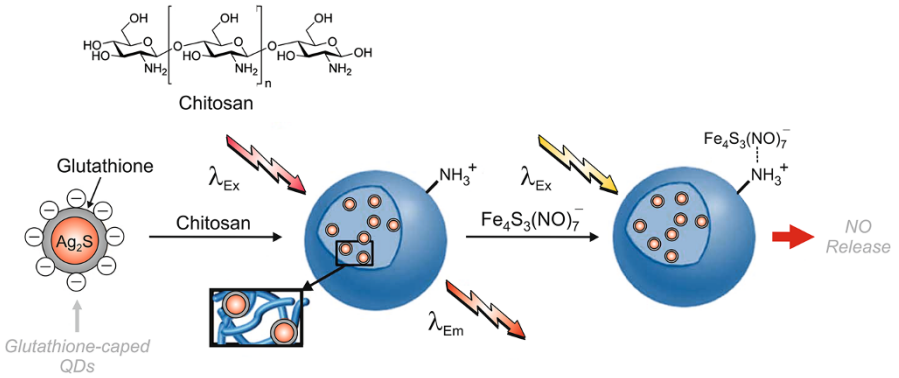

Fig. 19 Assembly of chitosan nanospheres with an emissive Ag_2S core and RBS electrostatically adsorbed on their surface (Adapted with permission from Analyst, 2014, © Royal Society of Chemistry)

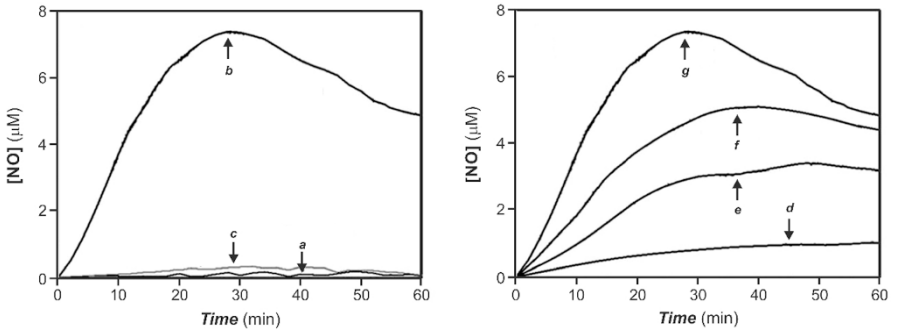

Fig. 20 Amperometric detection of NO in a solution of the nanospheres illustrated in Fig. 19 without irradiation (*a*) and with irradiation at either 488 (*b*) or 758 nm (*c*). Amperometric detection of NO in the same solution under irradiation at 488 nm with increasing power: 2 (*d*), 5 (*e*), 7 (*f*), and 10 W (*g*) (Reproduced with permission from Analyst, 2014, © Royal Society of Chemistry)

required to induce the release of NO, to 1160 nm. In fact, Mn(II)-doped QDs were found to exhibit orange emission (586 nm) when excited by two-photon absorption with relatively long wavelengths. Such an upconversion mechanism effectively allows the production of the therapeutic agent under near-infrared illumination [72].

A similar system was constructed to photoinduce the release of NO within cancer cells [73, 74]. It is based on the electrostatic absorption of RBS on the surface of Mn^{2+}-doped ZnSe QDs, passivated with glutathione. Two-photon excitation of the inorganic core at 1130 nm results in the efficient transfer of energy to RBS with the concomitant release of NO (Fig. 21). Incubation of HeLa cells with this particular system results in the cellular internalization of the photoresponsive construct. Subsequent illumination of the stained cells at 1130 nm encourages the intracellular release NO and, as a result, induces cell mortality.

As an alternative to transition metal complexes, nitrosothiols can be exploited to photoinduce the release of NO upon excitation of a conjugated QD [75]. The very first nitrosothiol to be synthesized, as early as in 1909, was nitrosothiophenol [76].

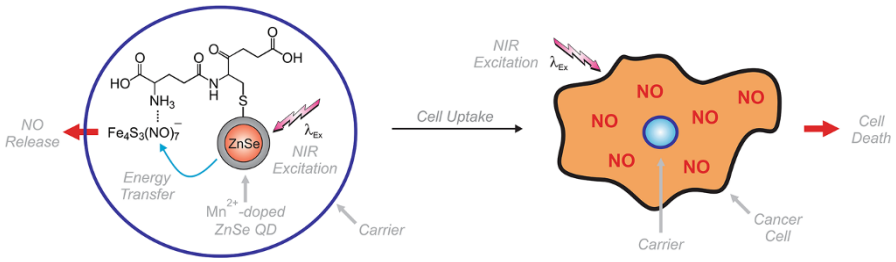

Fig. 21 Near-infrared excitation of Mn^{2+}-doped ZnSe QDs encourages the transfer of energy to RBS, electrostatically absorbed on the nanoparticle surface, and the intracellular release of NO (Adapted from Mat. Chem. Phys., 2015, © Elsevier)

Since then, the relative instability of this class of compounds and their tendency to release NO has been extensively investigated [62, 77]. Specifically, heat, UV radiation, metal ions, oxidants, thiols, and seleno compounds can all promote the cleavage of the S–NO bond with the release of NO. One of the most studied nitrosothiols is *S*-nitrosoglutathione (GSNO) [78]. Irradiation of GSNO leads to the formation of NO and thiyl radicals. In an oxygen-deprived environment, the radicals react directly with GSNO to form a disulfide adduct and NO. In oxygenated environments, peroxidation of GS•, followed by reaction with an additional GSNO molecule, takes place with release of NO instead (Fig. 22).

The first construct, combining QDs and nitrosothiols, was originally designed to photoinduce the generation of singlet oxygen [75]. *S*-Nitrosocysteine was adsorbed on the surface of TiO_2 nanotubes, doped with PbS QDs, in five synthetic steps (Fig. 23). Irradiation of the final assembly with a photoreactor, producing radiation at wavelengths longer than 600 nm, produced reactive oxygen species (ROS) and NO simultaneously. Indeed, excitation of the TiO_2 nanotubes, followed by electron transfer in the excited state, is responsible for generating ROS [79], while excitation of the PbS QDs sensitizes the release of NO from *S*-nitrosocysteine. Reaction of ROS with NO ultimately leads to the formation of singlet oxygen that can be detected with an appropriate trapping agent, namely sodium 1,3-cyclohexadiene-1,4-diethanoate.

Multifunctional and photoresponsive constructs, based on the photophysical properties of glutathione-capped Ag_2S QDs, were also assembled relying on *S*-nitrosopenicillamine (Fig. 24) [80, 81]. Excitation of the inorganic core at 808 nm results in intense emission at 990 nm, offering the opportunity to acquire images relying exclusively on near-infrared radiation. These illumination conditions have no influence on the nitrosothiol and do not result in the formation of NO. Its direct

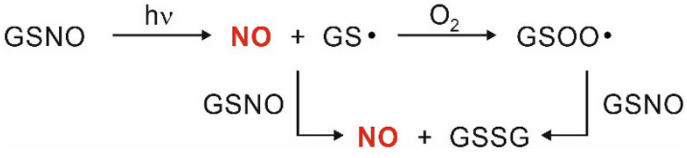

Fig. 22 Photoinduced decomposition of GSNO with the release of NO

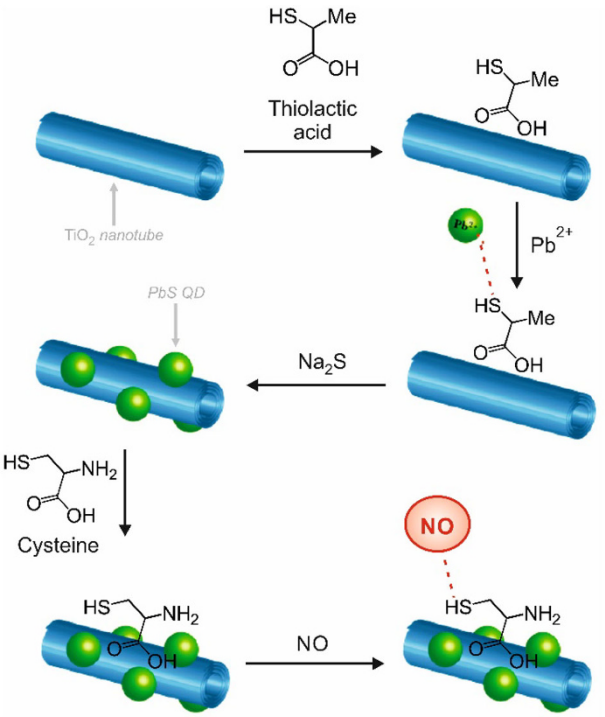

Fig. 23 Five-step assembly of *S*-nitrosocysteine on the surface of TiO_2 nanotubes (*blue cylinders*) doped with PbS QDs (*green spheres*) (Adapted from J. Am. Chem. Soc., 2011, © American Chemical Society)

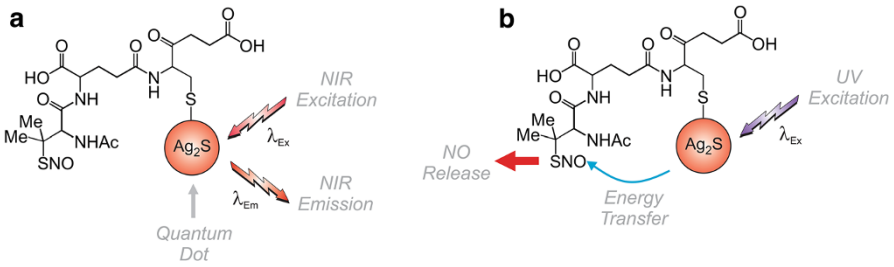

Fig. 24 Adsorption of *S*-nitrosopenicillamine on the surface of Ag_2S QDs results in the formation of a photoresponsive construct capable of producing fluorescence (**a**), under near-infrared illumination and releasing NO (**b**), under UV illumination (Adapted with permission from ACS Appl. Mater. Interfaces, 2013, © American Chemical Society)

excitation at 365 nm, however, causes the cleavage of the S–NO bond and the formation of NO. Thus, this particular construct can be used to photoinduce cytotoxic effects, while simultaneously imaging the specimens.

Nitroanilines are also valuable building blocks to assemble constructs capable of photoinducing the release of NO [82]. A trifluoromethane substituent, however, must be introduced in one of the two *ortho* positions, relative to the nitro group, to

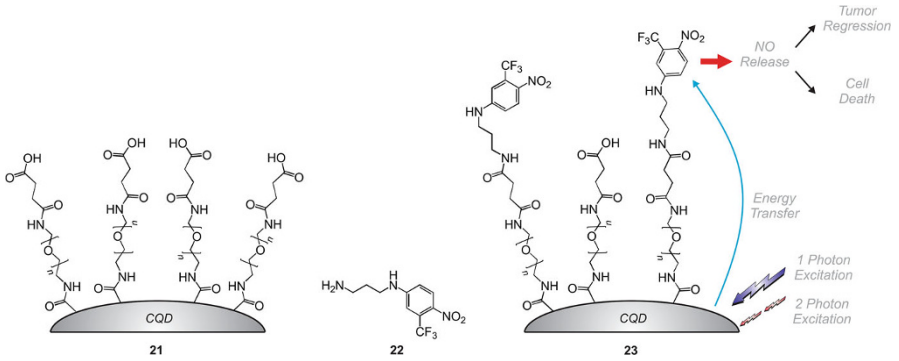

Fig. 25 Carboxylic acids on the surface of carbon QDs are coupled to the primary amino group of **22**. One- or two-photon excitation of the QD within the resulting assembly transfers energy to the connected nitroanilines and induces the release of NO in the intracellular environment (Adapted from Chem. Comm., 2015, © Royal Society of Chemistry)

impose a twisted geometry on it and allow NO release upon excitation [83]. When this structural requirement is satisfied, this relatively simple organic chromophore can be connected to carbon QDs and permit the one- or two-photon uncaging of NO [84]. Specifically, the primary amino group of **22** can be coupled to carboxylic acid groups at the termini of oligo(ethylene glycol) chains adsorbed on the surface of carbon QDs (Fig. 25). Either one-photon excitation of the QDs at 350 nm or their two-photon excitation at 800 nm results in the efficient transfer of energy to the appended nitroanilines, which then release NO. This mechanism for NO photorelease can also be replicated in the intracellular environment. In particular, incubation of HeLA cells with these photoresponsive constructs and subsequent illumination of the cells at 800 nm lead to the two-photon excitation of the QD, transfer of energy to the nitroaniline ligands, and intracellular release of NO ultimately to induce cell mortality.

4 Conclusions and Perspectives

The outstanding photophysical properties of inorganic QDs, in conjunction with the photochemical response of appropriate organic ligands anchored to their surface, can be exploited to assemble nanostructured constructs with photoresponsive functions. In the resulting assemblies, the inorganic component is designed to exchange either an electron or energy with the organic counterparts upon excitation. Under these conditions, the electronic character of the ligands controls the fate of the QD excited state and, hence, the luminescence intensity and lifetime. Specifically, only one of the interconvertible states of a photochromic ligand can be engineered to accept the excitation energy of a QD and quench its luminescence as a result. On the basis of these operating principles, the photoinduced and reversible interconversion of the photochromic ligands, generally in the form of diarylethene or spiropyran derivatives, translates into the modulation of the QD

luminescence. Similarly, electron donors can be connected to the outer shell of a QD with photocleavable linkers in order to quench the luminescence on the inorganic component. The photoinduced cleavage of the spacer, generally in the form of *ortho*-nitrobenzyl derivatives, connecting the two separates the organic quenchers from the inorganic emitter and switches luminescence on irreversibly. In fact, nanostructured constructs with photoswitchable luminescence can be realized with this choice of components and quenching mechanisms. In turn, the ability to switch luminescence with optical stimulations is particularly valuable to monitor dynamic events in biological samples and reconstruct images with subdiffraction resolution of these specimens.

A significant limitation of the present mechanisms to photoswitch QD luminescence, however, is that unitary quenching efficiencies can hardly be achieved. As a result, the emission intensity generally switches from a low to a high value, or vice versa, with the photochemical transformation of the ligands adsorbed on the luminescent nanoparticle. It follows that the ratio between the latter and the former values, the so-called contrast ratio, is relatively modest in most instances, complicating the possible implementation of imaging schemes that require detection at the single-emitter level. Additionally, the photoinduced conversion of the ligands has negligible, if any, influence on the absorption properties of the emissive QD. As a consequence, the *selective* excitation of the photoswitched QDs, in the presence of their nonswitched counterparts, is impossible, preventing the realization of imaging protocols that demand the selective bleaching of the switched probes after their detection. Thus, future research efforts must be directed to the identification of operating principles to photoswitch QD luminescence with infinite contrast ratio, while drastically altering the absorption spectrum of the emissive inorganic core. Should these challenging objectives be achieved, QDs with photoswitchable luminescence might well become the probe of choice for a diverse range of imaging applications.

The mechanisms developed so far to control the photophysical properties of a QD with the photoinduced transformation of appropriate ligands can be adapted to sensitize the photochemical conversion of the latter components relying on the excitation dynamics of the former. In particular, the transfer of energy from a QD to a photoactive ligand can be exploited to populate the excited state of the latter and induce a photochemical reaction. In this context, the large two-photon absorption cross sections of QD are especially valuable and can be exploited to induce the release of a therapeutic agent, generally in the form of nitric oxide or singlet oxygen, under near-infrared illumination. Furthermore, these operating principles can be reproduced in the intracellular environment to induce cell mortality under optical control and can evolve into a promising tool for the treatment of cancer.

The transition from experiments in model cell lines to therapeutic applications in living organisms, however, remains more than a challenge. The potential toxic effects of the heavy metals that compose the emissive core of most QDs are of concern. Even in the presence of protective inorganic shells and passivating organic layers, metal cations might eventually leak out of these nanostructured constructs over relatively long time scales. Additionally, the biodistribution of such photoresponsive assemblies, their potential accumulation in specific organs, the

rates of their clearance from the organism, and their immediate and long-term effects all remain unclear. Detailed investigations aimed at elucidating these effects are very much needed, together with fundamental studies directed to the identification of alternative elemental compositions for the emissive core of QDs. Only then can the integration of semiconductor QDs and photoresponsive ligands eventually lead to valuable therapeutic tools with long-term implications in biomedical research.

Acknowledgments The National Science Foundation (CHE-1049860) is acknowledged for financial support.

References

1. Graham-Rowe D (2008) Nat Photonics 3:307–309
2. Tartakovskii A (2012) Quantum dots: optics, electron transport and future applications. Cambridge University Press, Cambridge
3. Masumoto Y, Takagahara T (2002) Semiconductor quantum dots. Physics, spectroscopy and applications. Springer-Verlag, Heidelberg
4. Woggon U (2013) Optical properties of semiconductor quantum dots. Springer-Verlag, Heidelberg
5. Karmakar S (2014) Fabrication, modeling and application. Novel three-state quantum dot gate field effect transistor. Springer, New Delhi
6. Wu J, Wang ZM (2014) Quantum dot solar cells. Springer, New York
7. Wang ZM (2012) Quantum dot devices. Springer, New York
8. Ustinov VM, Zhukov AE, Egorov AY, Maleev NA (2003) Quantum dot lasers. Oxford University Press, Oxford
9. Rafailov EU, Cataluna MA, Avrutin EA (2011) Ultrafast lasers based on quantum dot structures: physics and devices. Wiley-VCH, Weinheim
10. Stolze J, Suter D (2004) Quantum computing. Wiley-VCH, Weinheim
11. Hoath SD (2016) Fundamentals of inkjet printing. Wiley-VCH, Weinheim
12. Grumezescu AM (2016) Nanobiomaterials in medical imaging. Applications of nanobiomaterials. Elsevier, Oxford
13. Lakowicz JR (2006) Principles of fluorescence spectroscopy. Springer, New York
14. Algar Russ W, Kim H, Medintz IL, Hildebrandt N (2014) Coord Chem Rev 263–264:65–85
15. Wegner DK, Hildebrandt N (2015) Chem Soc Rev 44:4792–4834
16. Resch-Genger U, Grabolle M, Cavaliere-Jaricot S, Nitschke R, Nann T (2008) Nat Methods 5:763–775
17. Chan WCW, Maxwell DJ, Gao X, Bailey RE, Han M, Nie S (2002) Curr Opin Biotech 13:40–46
18. Kim S, Lim YT, Soltesz EG, De Grand AM, Lee J, Nakayama A, Parker AJ, Mihaljevic T, Laurence RG, Dor DM, Cohn LH, Bawendi MG, Frangioni JV (2004) Nat Biotech 22:93–97
19. Hardman R (2006) Environ Health Perspect 114:165–172
20. Kavarnos GJ (1993) Fundamentals of photoinduced electron transfer. Wiley-VCH, Weinheim
21. Willard DM, Van Orden A (2003) Nat Materials 2:575–576
22. Medintz IL, Mattoussi H (2009) Phys Chem Chem Phys 165:17–45
23. Algar WR, Tavares AJ, Krull UJ (2010) Anal Chim Acta 673:1–25
24. Bouas-Laurent H, Durr H (2001) Pure Appl Chem 73:639–665
25. Crano JC, Guglielmetti RJ (1999) Organic photochromic and thermochromic compounds: main photochromic families. Springer, Berlin
26. Crano JC, Guglielmetti RJ (2006) Organic photochromic and thermochromic compounds: physico-chemical studies, biological applications, and thermochromism. Springer, Berlin
27. Durr H, Bouas-Laurent H (1990) Photochromism: molecules and systems. Elsevier, Amsterdam
28. Klajn R (2014) Chem Soc Rev 43:148–184
29. Medintz IL, Trammell SA, Mattoussi H, Mauro JM (2004) J Am Chem Soc 126:30–31
30. Medintz IL, Clapp AR, Mattoussi H, Goldman ER, Fisher B, Mauro JM (2003) Nat Mater 2:630–638
31. Medintz IL, Goldman ER, Lassman ME, Mauro JM (2003) Bioconjugate Chem 14:909–918

32. Tomasulo M, Yildiz I, Raymo FM (2006) Aust J Chem 59:175–178
33. Zhu L, Zhu M-Q, Hurst JK, Li ADQ (2005) J Am Chem Soc 127:8968–8970
34. Giordano L, Jovin TM, Irie M, Jares-Erijman EA (2002) J Am Chem Soc 124:7481–7489
35. Erno Z, Yildiz I, Gorodetsky B, Raymo FM, Branda NR (2010) Photochem Photobiol Sci 9:249–253
36. Díaz SA, Menéndez GO, Etchehon MH, Giordano L, Jovin TM, Jares-Erijman EA (2011) ACS Nano 5:2795–2805
37. Diaz SA, Gillanders F, Jares-Erijman EA, Jovin TM (2015) Nat Commun 6 6036:1–11
38. Irie M, Fukaminato T, Matsuda K, Kobatake S (2014) Chem Rev 114:12174–12277
39. Raymo FM (2013) Phys Chem Chem Phys 15:14840–14850
40. Huang B, Bates M, Zhuang X (2009) Ann Rev Biochem 78:993–1016
41. Fernández-Suárez M, Ting AY (2008) Nat Rev Mol Cell Biol 9:929–943
42. Heilemann MJ (2010) Biotech. 149:243–251
43. Banala S, Maurel D, Manley S, Johnsson K (2012) ACS Chem Biol 7:289–293
44. Zhang Y, Swaminathan S, Tang S, Garcia-Amorós J, Boulina M, Captain B, Baker JD, Raymo FM (2015) J Am Chem Soc 137:4709–4719
45. Zhao Y, Zheng Q, Dakin K, Xu K, Martínez ML, Li WH (2004) J Am Chem Soc 126:4653–4663
46. Ellis-Davies GCR (2007) Nat Methods 4:619–628
47. Shao Q, Xing B (2010) Chem Soc Rev 39:2835–2846
48. Yu CYY, Kwok RTK, Mei J, Hong Y, Chen S, Lam JWY, Tang BZ (2014) Chem Commun 50:8134–8136
49. Shaban Ragab S, Swaminathan S, Garcia-Amorós J, Captain B, Raymo FM (2015) New J Chem 39:1570–1573
50. Gang Han TM, Ajo-Franklin C, Cohen BE (2008) J Am Chem Soc 130:15811–15813
51. Miesch C, Emrick T (2014) J Coll Interf Sci 425:152–158
52. Impellizzeri S, McCaughan B, Callan JF, Raymo FM (2012) J Am Chem Soc 134:2276–2283
53. Wink DA, Grisham MB, Mitchell JB, Ford P (1996) Methods Enzymol 268:12–31
54. Davis KL, Martin E, Turko IV, Murad F (2001) Annu Rev Pharmacol Toxicol 41:203–206
55. Murad F (1999) Angew Chem Int Ed 38:1856–1868
56. Furchgott RF (1999) Angew Chem Int Ed 38:1870–1880
57. Ignarro LJ (1999) Angew Chem Int Ed 38:1882–1892
58. Seabra AB, Duran N (2010) J Mater Chem 20:1624–1637
59. Sonveaux P, Jordan BF, Gallez B, Feron O (2009) Eur J Cancer 45:1352–1369
60. Cheng H, Wang L, Mollica M, Re AT, Wu S, Zuo L (2014) Cancer Lett 353:1–7
61. Huerta S (2015) Future Sci OA 1(1):FS044-1–9
62. Keefer LK, Nims RW, Davies KM, Wink DA (1996) Methods Enzymol 268:281–293
63. Wang PG, Xian M, Tang X, Wu X, Wen Z, Cai T, Janczuk AJ (2002) Chem Rev 102:1091–1134
64. Schloßbauer A, Sauer AM, Cauda V, Schmidt A, Engelke H, Rothbauer U, Zolghadr K, Leonhardt H, Bräuchle C, Bein T (2012) Adv Healthcare Mater 1:316–320
65. Ford PC (2013) Nitric Oxide 34:56–64
66. Jacques SL (2013) Phys Med Biol 58:R37–R61
67. Neuman D, Ostrowsky AD, Absalonson RO, Strouse GF, Ford PC (2007) J Am Chem Soc 129:4146–4147
68. Neuman D, Ostrowsky AD, Mikhailovsky AA, Absalonson RO, Strouse GF, Ford PC (2008) J Am Chem Soc 130:168–175
69. Burks PT, Ostrowski AD, Mikhailovsky AA, Chan EM, Wagenknecht PS, Ford PC (2012) J Am Chem Soc 134:13266–13275
70. Franco LP, Cicillini AS, Biazzotto JC, Schiavon MA, Mikhailovsky A, Burks P, Garcia J, Ford PC, da Silva RS (2014) J Phys Chem A 118:12184–12191
71. Tan L, Wan A, Zhu X, Li H (2014) Analyst 139:3398–3406
72. Tan L, Wan A, Zhu X, Li H (2014) Chem Commun 50:5725–5728
73. Xu Z, Wu Z, Sun J, Gui RJ (2015) Mat Chem Phys 162:286–290
74. Jin H, Gui R, Sun J, Wang Y (2016) Anal Chim Acta 922:48–54
75. Ratanatawanate C, Chyao A, Balkus KJ Jr (2011) J Am Chem Soc 133:3492–3497
76. Tasker HS, Jones HO (1909) J Chem Soc 95:1910–1918
77. Williams DLH (1996) Chem Commun 1085–1091
78. Singh SP, Wishnok JS, Keshive M, Deen WM, Tannenbaum SR (1996) Proc Natl Acad Sci 93:14428–14433
79. Ratanatawanate C, Tao Y, Balkus KJ Jr (2009) J Phys Chem C 113:10755–10760

80. Tan L, Wan A, Li H (2013) ACS Appl Mat Interf 5:11163–11171
81. Tan L, Wan A, Li H (2013) Langmuir 29:15032–15042
82. Callari FL, Sortino S (2008) Chem Commun 1971–1973
83. Caruso EB, Petralia S, Conoci S, Giuffrida S, Sortino S (2007) J Am Chem Soc 129:480–481
84. Fowley C, McHale AP, McCaughan B, Fraix A, Sortino S, Callan JF (2015) Chem Commun 51:81–84

Top Curr Chem (Z) (2016) 374:65
DOI 10.1007/s41061-016-0066-7

REVIEW

Interfacing Luminescent Quantum Dots with Functional Molecules for Optical Sensing Applications

Serena Silvi[1] · Massimo Baroncini[1] · Marcello La Rosa[1] · Alberto Credi[2]

Received: 6 May 2016 / Accepted: 17 August 2016 / Published online: 31 August 2016

Abstract Semiconductor quantum dots possess unique size-dependent electronic properties and are of high potential interest for the construction of functional nanodevices. Photoinduced electron- and energy-transfer processes between quantum dots and surface-bound molecular species open up attractive routes to implement chemical switching of luminescence, which is at the basis of luminescence sensing. In this article, we discuss the general principles underlying the rational design of this kind of multicomponent species. Successively, we illustrate a few prominent examples, taken from the recent literature, of luminescent chemosensors constructed by attaching molecular species to the surface of quantum dots.

Keywords Chemosensor · Energy transfer · Electron transfer · Luminescence · Nanocrystal · Nanoscience

This article is part of the Topical Collection "Photoactive Semiconductor Nanocrystal Quantum Dots"; edited by Alberto Credi.

✉ Serena Silvi
serena.silvi@unibo.it

✉ Alberto Credi
alberto.credi@unibo.it

[1] Dipartimento di Chimica "G. Ciamician", Università di Bologna, via Selmi 2, 40126 Bologna, Italy

[2] Dipartimento di Scienze e Tecnologie Agro-alimentari, Università di Bologna, viale Fanin 44, 40129 Bologna, Italy

1 Introduction

Quantum dots (QDs) are crystals of semiconductor materials comprising from some hundreds to a few thousands of atoms, with a spherical shape and a diameter typically ranging between 1 and 15 nm. They exhibit peculiar optical and electronic properties; in particular, they are strongly luminescent [1–3]. Since their discovery in the early 1980s [4, 5] and the development of solution-based preparation methods affording an accurate size control [6], it became clear that these particles represent a valid alternative to molecular species for luminescence applications [7, 8]. Indeed, as soon as chemical synthesis methods became available, QDs were introduced for use in bioimaging and diagnostics [9]. The interest in QDs as alternatives to organic dyes has increased dramatically, as witnessed by the number of research papers, reviews [10–16], and books [17–20] dealing with such nanomaterials.

Quantum dots were initially prepared by materials physicists with epitaxial or lithographic techniques for basic studies on quantum confinement [4]. Chemical synthesis methods, which have become of widespread use [21–24], rely on the controlled growth of the crystals in the presence of molecular species (capping ligands) that can form a monolayer on the crystal surface [25–27]. Such a layer has a few important functions: (i) it covers the surface, thus preventing further growth of the crystal, (ii) it prevents inter-particle aggregation, (iii) it regulates the solubility of the QDs, and (iv) it affects the optical and electronic properties of the nanocrystals. Hence, it should be emphasized that QDs dispersed in solution consist in fact of an inorganic crystal core coated by a shell of organic molecular ligands. Indeed, the reliable construction of such nanocrystal-molecule hybrids and a deep understanding of the physical and chemical aspects of nanocrystal-molecule interactions are essential for extending the basic knowledge on these fascinating systems and foster the design of QDs tailored for specific technological applications [28].

Optical chemosensors offer the possibility of a sensitive, rapid, and reproducible determination of a wide range of analytes using simple and cheap instrumentation. The modular construction of multicomponent molecular sensors based on changes in the absorption or, more frequently, the emission of light, has been extensively investigated in the past four decades [29]. Since as discussed above the surface of QDs is usually covered with molecular species, such nanoparticles can be used as scaffolds for the development of multicomponent nanoscale devices for sensing applications.

In this regard, QD-based systems possess a number of advantages in comparison with earlier all-organic sensors [7]. For example, more sensitive measurements can be made by taking advantage of the intense absorption, large emission quantum yield, and high photostability of QDs. Their color tunability, combined with a small Stokes shift, a broad absorption spectrum, and a sharp emission band, have enabled multiplexed optical sensing. Such techniques allow the determination of several different parameters with a single measurement by using color-coding, and are of interest for nanoscience and biotechnology applications [30]. QDs are also superior to organic dyes in experiments that require two-photon excitation with near-infrared light, such as in vivo tests [31]. Last but not least, the rich surface chemistry of nanocrystals can be exploited to endow these luminophores with specific

(bio)chemical properties. It is therefore not surprising that a lot of attention is being dedicated to quantum dots as components of luminescent sensors [20, 32–37].

In this article, we will describe hybrids composed of semiconductor nanocrystals attached to functional molecular units, in which the interplay between the QD and molecular components is exploited to perform luminescence sensing of a variety of ionic and molecular analytes. We will focus on systems containing either bare core or type-I core–shell nanocrystals because they represent the vast majority of QD-based luminescent sensors.

It should be noted that chemical or physical interactions of the analyte directly with the QD surface can affect the photophysical properties of the nanocrystal, thus enabling the use of bare QDs for luminescent sensing [38]. Such an approach, however, will not be discussed here because it appears to be limited to a few small ions or molecules capable of reacting directly with the QD surface. Similarly, we will not consider the use of bare QDs as sensors of temperature and pressure.

In the first part of the paper, we will briefly illustrate the fundamental physico-chemical properties of quantum dots and describe the methodologies for the chemical modification of their surface. Successively, the processes that can be exploited to obtain chemical switching of luminescence (that is, signal transduction) in nanocrystals–molecule conjugates will be discussed. In the next sections, we will illustrate such concepts by describing examples taken from the recent literature, subdivided according to the type of process at the basis of the optical transduction of the analytical signal. The selected case studies are intended to give an overview comprising different systems and analyte categories. Finally, the limitations and perspectives of optical sensing with QD-molecule hybrids will be critically presented.

2 Size-Dependent Optoelectronic Properties

In a semiconductor, upon absorption of a photon with energy equal or larger than the band gap, an electron is excited from the valence to the conduction band and a hole is left in the valence band (Fig. 1). Such an electron–hole pair is called an exciton, and is stabilized by the electrostatic attraction between the opposite charges. The extension of the exciton wavefunction over the crystal lattice is expressed by the Bohr radius; for example, the Bohr radius for excitons in CdSe is about 5 nm. When the size of the semiconductor particle approaches the exciton Bohr radius, quantum confinement effects come into play and the optical and electrical properties of the material become dependent on its physical dimension [1–5, 39]. Under these conditions, the band structure of the semiconductor changes into discrete levels, and the energy difference between the highest occupied level and the lowest unoccupied level widens as the particle size decreases, following in many cases the behavior expected for an electron inside a three-dimensional box.

The absorption spectrum of QDs is characterized by a sharp band on the low-energy side, corresponding to population of the first exciton state exhibiting a strong oscillator strength, often referred to as the bright state. For the reasons described above, the maximum wavelength and intensity of this band depend on the particle

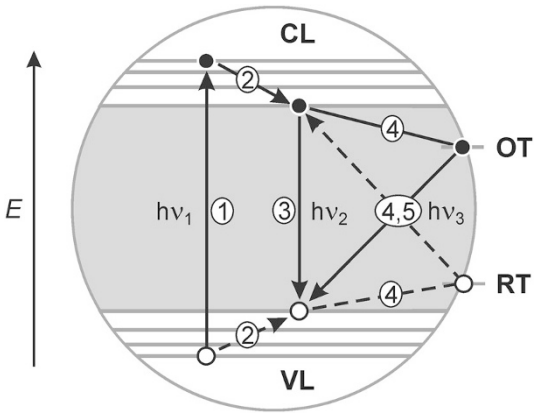

Fig. 1 Schematic representation of electronic transitions in a semiconductor nanocrystal. *Full* and *dashed lines* represent transitions of electrons and holes, respectively. Legend of symbols: *VL* valence levels, *CL* conduction levels, *RT* reducing surface trap, *OT* oxidizing surface trap. Legend of processes: *1* light excitation ($h\nu_1$), *2* thermal relaxation of the excited electron and hole, *3* band edge luminescence ($h\nu_2$), *4* nonradiative recombination mediated by surface states, *5* luminescence involving surface states ($h\nu_3$)

size (Fig. 2), while its width and shape reflect the size distribution of the QDs. Indeed, owing to their large molar absorption coefficients in the UV–visible region, quantum dots can be effectively excited in a wide spectral range and with low intensity light.

In direct band gap semiconductors[1] such as CdS, CdO, CdSe, ZnS, ZnSe, GaAs and InP, the recombination of the exciton leads to the emission of a photon (process 3 in Fig. 1). QDs of these materials show a very intense luminescence that occurs with a remarkably narrow spectral profile: the typical full width at half maximum (fwhm) is on the order of 30 nm, i.e., less than 1000 cm^{-1} for an emission band peaking at 550 nm. The emission energy can be tuned in a spectral region ranging from the UV to the IR, by choosing the chemical composition (i.e., the band gap of the bulk material) and the diameter of the particles. A frequently used semiconductor to make QDs for optical applications is CdSe, because the size modulation of its band gap enables to accurately adjust the emission maximum across the visible region (Fig. 2).

It has to be highlighted that the surface of the nanocrystals must be appropriately passivated in order to have efficient emission; otherwise, the charge carriers would be likely trapped in surface states and undergo nonradiative recombination (Fig. 1). As a matter of fact, the presence of surface states, originating from the dangling bonds of the surface atoms, crystal defects and/or impurities, have a profound influence on the spectroscopic and redox properties of QDs [17–20]. The luminescence quantum yield can be improved by coating the nanocrystal with a layer of another semiconductor material having a larger bandgap. QDs of this type are known as type-I core–shell systems and

[1] Direct band gap semiconductors are those in which the minimum energy state in the conduction band and the maximum energy state in the valence band have the same momentum.

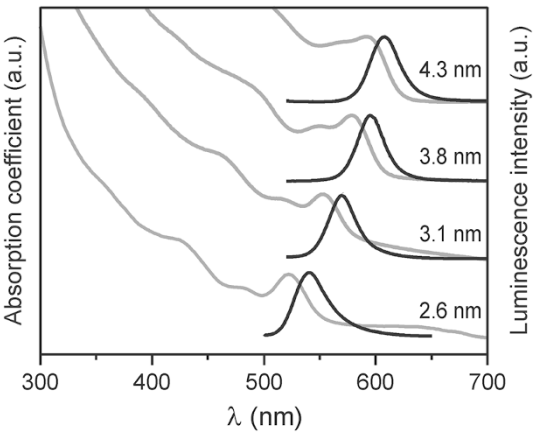

Fig. 2 Absorption and luminescence spectra ($CHCl_3$, room temperature) of CdSe QDs of different size capped with tris-*n*-octylphosphineoxide (TOPO) and *n*-hexadecylamine (HDA) ligands. Excitation was performed at $\lambda = 480$ nm. The spectra are vertically offset for clarity

have become very popular, the prototypical case being that of CdSe–ZnS core–shell QDs [40, 41], which are commercially available in various sizes. Not surprisingly, the majority of the studies reported in the literature, and those described here, are based on CdSe–ZnS QDs.

In type-I core–shell QDs, because of the alignment of the respective valence and conduction band levels, both the electron and the hole generated upon light excitation are confined in the core; thus, the optoelectronic properties of these QDs are solely determined by the core composition and size and are almost unaffected by the shell thickness. Other band alignments afford heterojunctions with different properties. In type-II nanocrystals (e.g., CdSe–CdTe [42]) the two charge carriers are localized in different parts of the particle—either the core or the shell—forming a spatially indirect exciton. Quasi type-II (or type $I^{1/2}$) nanocrystals also exist, in which one of the charge carriers is delocalized over the entire particle whereas the other one is confined in one part; for example, in CdSe-CdS core–shell QDs [43] the electron is delocalized while the hole is localized in the core. The optoelectronic properties of type-II and quasi type-II QDs depend on both the core diameter and the shell thickness, as well as on the chemical nature of the core and shell materials. Because all the examples presented here refer to shell-free or type-I core–shell QDs, a detailed discussion of type II or quasi type-II QDs is beyond the scope of this article. Interested readers can refer to specific references [12, 40–44].

Other important properties of QDs include their relatively long luminescence lifetimes and the remarkable photobleaching resistance, in particular for type-I core–shell systems. In fact, QDs are more suitable than molecular fluorophores in single-particle detection or in applications that require irradiation with high intensities and/or long periods.

3 Synthesis and Surface Modification

Most common methods for the synthesis of QDs involve the reaction of inorganic precursors in apolar organic solvents, in the presence of molecular ligands that form a coating layer on the surface of the nanoparticle (Fig. 3a) [17–25]. As mentioned above, a shell of another semiconductor with a larger band gap can be deposited onto the surface of the core nanocrystal in order to improve its optical properties [40]. Such methods enable an excellent control over size, shape, composition and homogeneity of the nanocrystals, whose surface is typically covered with alkylphosphine, alkylamine and/or alkanethiol ligands. These highly hydrophobic particles can be successively transferred into aqueous solutions by, e.g., incorporation in a polymer shell or in micelles [45]. Methods for the direct synthesis of semiconductor nanocrystals in water have also been developed [46, 47].

It is worth noting that the preparation protocols of QDs differ from traditional molecular syntheses as they are very sensitive to conditions and often exhibit reproducibility issues or strong dependence on the quality of the precursors and solvents [14, 35, 48]. It should also be considered that molecules are precisely defined objects in terms of composition and structure, whereas nanocrystals are, at best, monodisperse. This means that additional standardization efforts, considering the statistics due to populations of different sizes and hence of electronic properties, are required. Moreover, researchers should be aware of the fact that in materials chemistry reproducing results may not be straightforward. Nevertheless, lower limits of detection than with molecular sensors may be reached owing to the outstanding photophysical properties of semiconductor nanocrystals.

The nature of the interaction between the surface of the nanocrystals and the head group of the ligand plays a crucial role in determining the photophysical properties and the charge-transfer behavior of the QDs. A description of this interaction derived from the covalent bond classification method originally developed for transition metal complexes [49] has been recently proposed [27, 50, 51]. According to this model, the ligands can be subdivided into L-type (two-electron donors, neutral Lewis bases), X-type (one-electron donors), and Z-type (two-electron acceptors, Lewis acids). L-type ligands donate their lone pair to a surface metal atom, thus establishing a dative bond; examples are amines, phosphines and phospine oxides. X-type ligands are typically monovalent anions that bind positively charged sites at the QD surface; formally, this situation corresponds to a normal covalent bond between a ligand atom and a surface atom both possessing one unpaired electron. Examples of X-type surfactants are carboxylates, phosphonates, and thiolates. While both L- and X-type ligands bind to electron poor surface sites, Z-type ligands behave as Lewis acids and interact with electron rich sites such as chalcogenide anions in metal chalcogenide nanocrystals.

The binding of most ligands to the nanoparticle surface is dynamic; this is an important point because it allows the exchange of the ‘native’ ligands (i.e., those attached to the surface during the synthesis of the nanocrystal) with other surfactants bearing different functionalities. For example, biological applications require an engineering of the QD surface so that the particles are soluble in water. Some

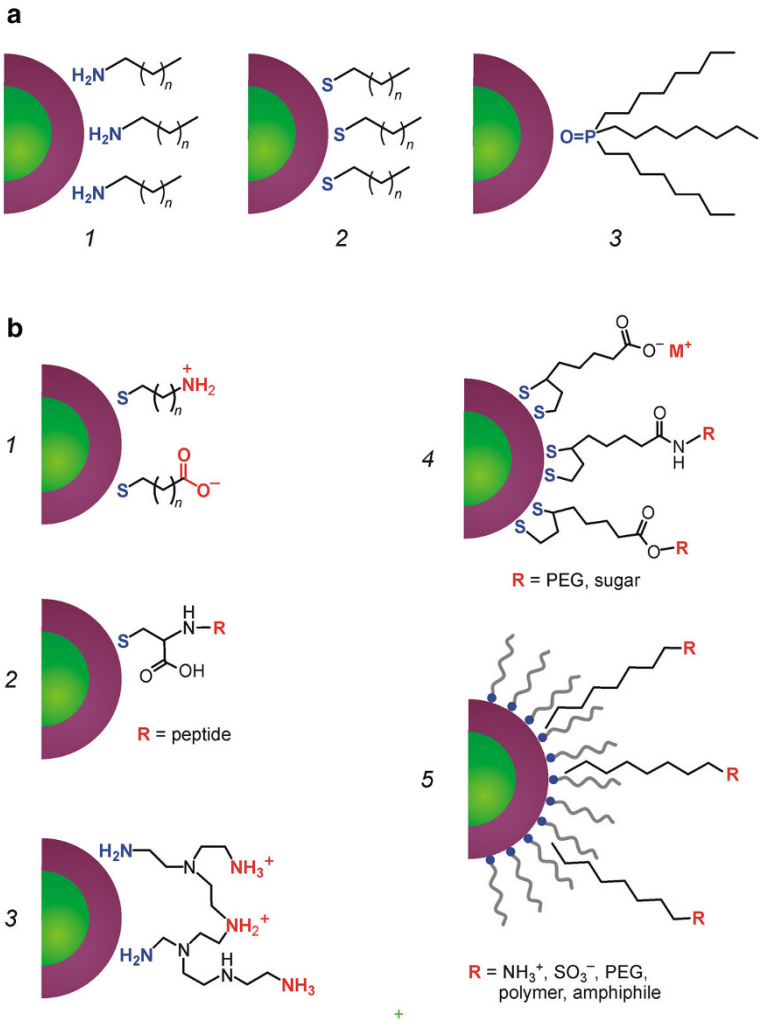

Fig. 3 Schematic representation of core (*green*)-shell (*magenta*) QDs with different surface ligands. **a** Hydrophobic QDs with alkylamines (*1*), alkanethiols (*2*) and tris-*n*-octylphosphineoxide (TOPO, *3*) capping ligands. **b** Hydrophilic QDs obtained by ligand exchange with mercaptoammonium or mercaptocarboxylic derivatives (*1*), cysteine-modified peptides (*2*), polyamines (*3*), and 1,2-dithiolane (lipoic acid) derivatives (*4*). Type *5* particles are obtained by encapsulation of hydrophobic QDs by self-assembly with amphiphilic cations, anions or polymers (*PEG* polyethylene glycol)

strategies developed to make water-soluble QDs are illustrated in Fig. 3 [32, 52, 53]. These routes can also be applied to decorate QDs with functional molecular units via the covalent or non-covalent attachment of such units to the water-solubilizing ligands. Chemically functionalized QDs soluble in organic solvents can also be prepared, usually by replacing the native ligands with suitably functionalized molecular ligands.

Methodologies for surface modification can exhibit drawbacks such as degradation of the optical or electronic properties, particle aggregation, or poor stability of the molecular coating. A common issue for these strategies is the increase of the final size of the nanoparticles, posing limitations to their use in some biological applications. It was shown, however, that compact and biocompatible QDs could be obtained by capping the nanocrystals with ligands consisting of a 1,2-dithiolane anchor, a short polyethylenglycol (PEG) chain and an amine or carboxylate terminus [54].

Macromolecular ligands with multiple thiol groups, poly(ethylene glycol) chains, and reactive functional units appended to a common polymeric backbone have also been proposed [55]. The thiol groups displace the native hydrophobic ligands of the QD and afford a stable anchoring of the polymers onto the nanocrystal surface; the poly(ethylene glycol) chains impose hydrophilic character, and the reactive groups enable the conjugation with other molecular units. CdSe–ZnS QDs coated with such polymeric ligands exhibited valuable properties in terms of stability over a broad pH range, water solubility and luminescence quantum yield, and showed a hydrodynamic diameter on the order of 15 nm [55].

Recently, simple and flexible methods for the chemical [56] or photochemical [57] activation of 1,2-dithiolane ligands to exchange the native capping ligands of QDs have proven effective for producing nanoparticles with tailor-made chemical properties.

In general, bare QDs possess a limited value as luminescent sensors because their photophysical properties are not affected by the presence of analytes in the surrounding medium (with the exception of some metal ions that can exchange with those on the nanocrystal surface, as mentioned in the Introduction). This is particularly true for strongly emissive QDs, i.e., those that can afford high sensitivity in luminescent measurements. In fact, large emission quantum yield values are brought about by an efficient passivation of the surface of the nanocrystals (by an inorganic shell and/or the monolayer of capping ligands), thus rendering them insensitive to the surrounding environment (e.g., pH, O_2). Hence, a strategy to implement a sensing response with QDs is to combine them with chemosensitive molecular components.

Indeed, a thorough investigation and selection of appropriate functional molecules allows the design of tailor-made nanoconjugates, wherein the QD-molecule electronic communication can be tuned by the presence of the analyte. In a different approach, the functional ligands and the nanocrystals do not communicate, and their respective spectroscopic properties remain unchanged and independent in the nanoassembly. In this case, the nanoparticles can serve as scaffolds for the chemosensors, and can also provide a luminescent signal that can be useful as an internal reference for ratiometric sensing.

4 Modular Design of Photoactive QD-Molecule Conjugates

A luminescent chemosensor is a molecular switch in which one (or more) input signal(s), coded for by a change in the analyte(s) concentration, produces a change in a luminescence output [29, 63]. To follow a modular approach in the design of a luminescent switch, three components are required: (i) a luminophore (L), that is, a unit capable of emitting light upon photoexcitation, (ii) a quencher (Q) capable of preventing the luminophore emission by some mechanism, and (iii) a control component that, in response to external stimulation, can modify the behavior of the quencher. In a luminescent chemosensor (Fig. 4), the control component is a receptor (R) that can recognize the target analyte (A). The basis of the sensing mechanism is that the ability of the quencher component to alter the emission of the luminophore is influenced by the binding of the analyte to the receptor [29]. In many cases, the quenching and control functions can be performed by the same chemical component. In the scheme shown in Fig. 4, the quenching process is switched off when the analyte becomes bound to the receptor, giving rise to a 'turn on' luminescence response (i.e., the luminescence intensity is directly proportional to the analyte concentration). 'Turn off' sensors, in which the luminescence intensity is inversely proportional to the analyte concentration, can also be designed.

Taking advantage of the flexible choice of molecular components, based on well-known spectroscopic and redox properties, a large variety of supramolecular luminescent sensors have been obtained by applying such modular approaches [29, 58]. In principle, the very same approaches can be extended to the construction of systems containing both molecular and nanocrystal components [59–61]. Indeed, QDs possess suitable optical and electronic features to become involved in luminescence-quenching phenomena.

The light-induced transfer of electrons or electronic energy between connected molecular components are widely used mechanisms to afford the modulation of luminescence intensity in supramolecular (multicomponent) systems [62, 63]. These processes are thermodynamically allowed if the energy levels of the components are correctly positioned relatively to one another, as schematized in Figs. 5 and 6. For example, if the QD is close to a molecular electron acceptor A exhibiting a LUMO level at a lower energy than that of the conduction band edge, a photoinduced

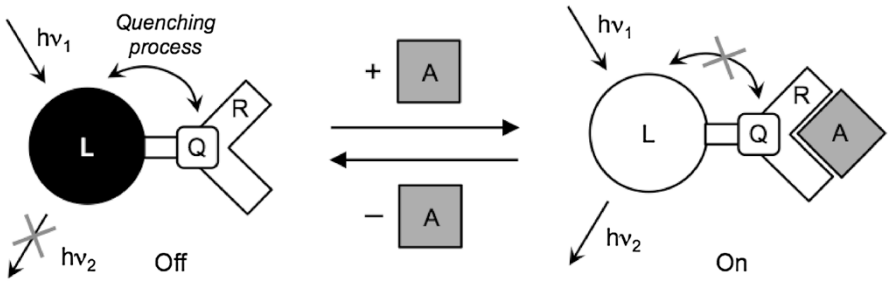

Fig. 4 Scheme of the analyte-modulated 'turn on' photoluminescence response in a luminophore-quencher-receptor multicomponent chemosensor

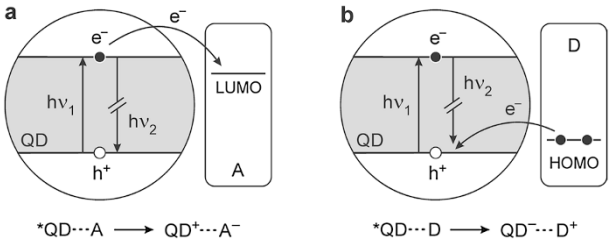

Fig. 5 Schematization of **a** electron transfer from a photoexcited QD to an electron acceptor *A*, and **b** electron transfer from an electron donor *D* to a photoexcited QD. Adapted by permission from Ref. [61]. Copyright 2014 Elsevier

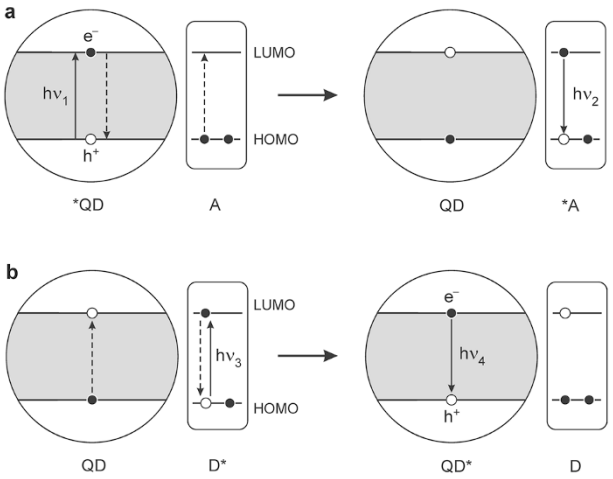

Fig. 6 Schematization of dipole–dipole energy transfer (FRET) **a** from a photoexcited QD to a molecular energy acceptor (*A*), and **b** from a photoexcited molecular energy donor (*D*) to a QD. The energy-transfer process may give rise to photosensitized emission of the energy acceptor component ($h\nu_2$ for **a**, $h\nu_4$ for **b**). Adapted by permission from Ref. [61]. Copyright 2014 Elsevier

electron transfer from the QD to the electron acceptor can occur and the luminescence of the nanocrystal is consequently quenched (Fig. 5a). Conversely, if the nanocrystal is in contact with an electron donor D possessing a HOMO level at an energy higher than that of the valence band edge, an electron transfer from the molecular donor to the photoexcited QD (or, with an alternative explanation, a hole transfer from the QD valence band to the molecular HOMO) can take place (Fig. 5b).

Another common process is electronic energy transfer between the nanocrystal and a nearby molecular species. In the case of QD-molecule conjugates, energy transfer usually obeys to the Förster (dipole–dipole) mechanism, which is frequently referred to as fluorescence resonance energy transfer (FRET, Fig. 6). In most QD-molecule hybrids the electronic energy is transferred from the photoexcited QD to the molecular chromophore, according to the scheme shown in Fig. 5a [32]. Systems exhibiting energy transfer in the opposite direction (from a photoexcited

molecule to the QD, Fig. 6b) are less common [8] because the photosensitized luminescence of the nanocrystal ($h\nu_4$ in Fig. 6b) may not be easily observed. This is because the intense and broad absorption spectrum of the QD usually prevents a selective, substantial excitation of the attached molecule.

As discussed in "Size-dependent optoelectronic properties", in type-I core–shell nanocrystals such as CdSe–ZnS QDs, the spectroscopic and electronic properties are determined by the core (e.g., CdSe) [12, 40, 41]. Because of the larger band gap of the shell material (e.g., ZnS) and the offset of its valence and conduction bands, the shell levels are not directly involved in energy- or electron-transfer processes. Hence, the models shown in Figs. 5 and 6, which are strictly valid for bare core nanocrystals, can also be adopted to interpret the behavior of type-I QDs [32–34, 59–61]. The presence of the shell, whose thickness is typically on the order of a few atomic layers, does not affect the thermodynamics of energy or electron transfer in a type-I QD-molecule system but it can influence the kinetics due to the increased donor–acceptor distance and the different smoothing effect exerted on the electron and hole wavefunctions [64, 65]. The situation is totally different for type-II and quasi type-II nanocrystals, in which the shell levels play an active role in electron-transfer processes (see, e.g., Ref. [66]).

A thorough discussion of energy- and electron-transfer mechanisms is beyond the scope of this work and can be found elsewhere [63, 67]. Generically speaking, one can say that the rate of these processes depends on various parameters of the partners such as their spectral features, distance, electronic coupling, and spin properties. If one or more of these parameters is affected by external stimulation, a switching behavior can be obtained. Conventional formalisms for the interpretation of energy- and electron-transfer processes between molecules have been successfully applied to nanoparticles [68, 69], and several examples of luminescent sensors based on the interplay between quantum dots and surface-bound functional molecular species have been reported [32–37]. Representative examples, subdivided according to the nature of the QD-molecule interplay producing the sensing response, are described in the next sections and are summarized in Table 1.

5 Sensors Based on Photoinduced Electron Transfer

Excited-state electron-transfer processes between the nanocrystals and functional ligands have been exploited for sensing purposes. As discussed in the previous section, the occurrence of such processes depends on the relative position of the electronic energy levels of the nanocrystal with respect to those of the molecular orbitals of the ligand. For this reason, electrochemical investigations on the nanohybrids components can help in designing and investigating photoinduced electron transfer processes.

Mews and coworkers reported on CdTe and CdSe nanocrystals functionalized with ligands consisting of a 1,10-phenanthroline moiety directly linked to azacrown ethers (Fig. 7) [70]. Upon replacement of the native capping ligands with a phenanthroline-azacrown ether ligand, the QD luminescence is quenched because of electron transfer from the phenanthroline HOMO, filling the hole left in the valence

Table 1 Overview of the examples reported in the main text

Transduction mechanism	QD	Functional ligand	Analyte/target	Role of QD	References
Electron transfer	CdSe CdTe	1,10-Phenanthroline-azacrown ether	Ba^{2+}	Electron acceptor	[70]
	CdSe	Urea derivative	CO_3^{2-}	Electron donor	[71]
	CdSe–ZnS	3-Mercaptopropionic acid-lucigenin complex	Cl^-	Electron donor	[72]
	CdSe–ZnS	Peptide–dopamine	H^+	Electron donor	[75]
Energy transfer	CdSe–ZnS	Amphiphilic polymer-squaraine	H^+	Energy donor	[79]
	CdTeSe–ZnS	Carbocyanine derivative	H^+	Energy donor	[80]
	CdSe–ZnS CdSeTe–ZnS	Polymer-biotin	Streptavidin-Terbium complexes	Energy acceptor	[81]
	CdSe–ZnS	Pd-porphyrin derivative	O_2	Energy donor	[82]
	CdSe	Pyrene or anthracene derivative	O_2 or bisphenylethynyl-anthracene	Energy donor	[83]
No interaction	CdSe–ZnS	Pyrene derivative	O_2	Internal reference	[85]

band of the photoexcited QD. The luminescence intensity of the nanohybrids can be modulated by Ba^{2+} ions in a way that depends on the dimensions (2.5 or 3 nm) and on the composition of the nanocrystals. In particular, it was observed that for CdSe (both 2.5 and 3 nm in diameter) and CdTe (2.5 nm) nanoconjugates, the luminescence intensity is suppressed by addition of Ba^{2+} ions.

The behavior of the larger CdTe nanohybrids is significantly different, as the photoluminescence intensity strongly increases after the addition of Ba^{2+} ions. Electrochemical studies on the isolated components were used to evaluate the redox levels involved in the electron-transfer processes. In particular, the anodic voltammetric peaks are related to the valence band of the QDs or the HOMO level of the ligands. The addition of Ba^{2+} ions, which are complexed by the azacrown ether units, makes the oxidation of the phenanthroline moiety more difficult by lowering its HOMO level. Cyclic voltammetry experiments performed on the nanocrystals samples point out that only for larger CdTe nanoparticles the valence band levels lies above the HOMO level of the complexed ligands, thus preventing electron transfer.

An analogous approach, but with an electron-transfer process taking place in the opposite direction, is at the basis of carbonate anion sensing in QD-urea

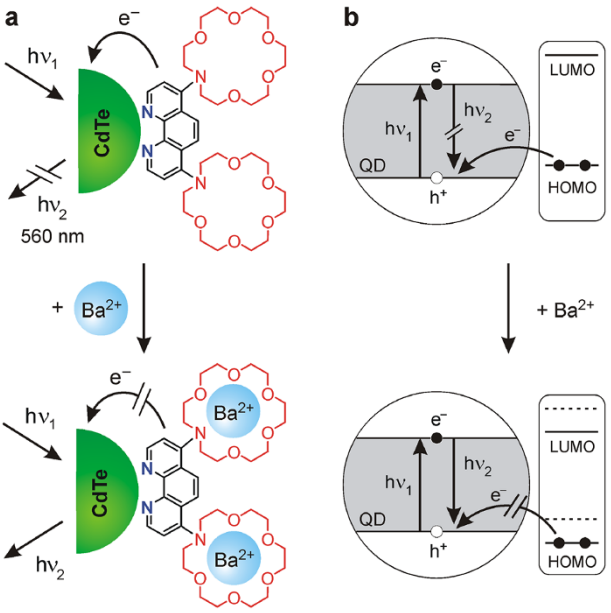

Fig. 7 Schematic representation (**a**) and simplified energy-level diagram (**b**) of the luminescent sensing of Ba^{2+} ions with CdTe QDs functionalized with phenanthroline-azacrown ether ligands [70]

nanohybrids [71]. Native tris-*n*-octylphosphineoxide (TOPO) capping molecules on the surface of CdSe quantum dots are exchanged with thiol-type ligands containing a urea group as recognition site for anions. The luminescence of the nanohybrids is quenched by the functional ligands, most likely because of an electron transfer from the photoexcited QD to the chemisorbed ligand. Complexation of CO_3^{2-} anions by the ureidic moiety of the ligand switches on the luminescence of the nanocrystals. Two possible mechanisms can be responsible for the recovery of the luminescence: (i) inhibition of the photoinduced electron transfer as the reduction potential of the ligands is shifted to more negative potential as a consequence of anion complexation, or (ii) rigidification of the ligand induced by binding of the analyte. This nanoconjugate exhibits remarkable selectivity for CO_3^{2-} in comparison with several competing anions (halides, nitrate, nitrite, HPO_4^{2-}, $H_2PO_4^-$, HCO_3^-, HSO_4^-).

A chloride ion sensor was developed based on photoinduced electron transfer from QD to lucigenin, a fluorescent Cl^- sensor [72]. CdSe–ZnS QDs capped with hexadecylamine were modified with 3-mercaptopropionic acid to impart hydrophilicity to the nanocrystals and negative charge on their surface. Lucigenin is an acridinium dication that can interact electrostatically with the negatively charged QDs. In the supramolecular nanoconjugate, both QD and lucigenin emissions are quenched and their lifetimes are shorter with respect to the separated components, because of the photoinduced electron transfer process from the semiconductor nanocrystal to the ligand (Fig. 8). In presence of Cl^- ions, a further decrease of lucigenin emission and an enhancement of QD luminescence were

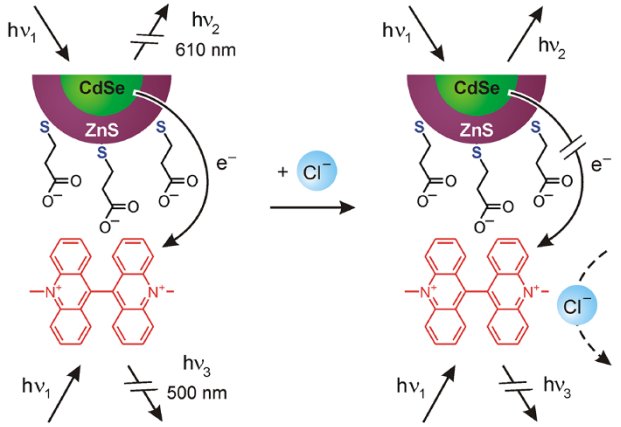

Fig. 8 Schematic representation of chloride sensing based on photoinduced electron transfer in adducts composed of CdSe–ZnS QDs and lucigenin molecules [72]

detected. Lucigenin is a well-known chloride sensor [73] that detects Cl^- via collisional quenching [74]; concomitantly, this process prevents electron transfer from QD to lucigenin, causing the recovery of the QD emission. The same trend is exhibited by the luminescence lifetimes of both components: the average lifetimes of QD and lucigenin emissions increase and decrease, respectively. The ratio of these average lifetimes showed a linear response versus chloride concentration, thus forming the basis for ratiometric sensing. The selectivity of the nanosensor was also tested, and the QD emission showed a negligible response toward several anions (sulphate, sulphite, nitrate, nitrite, phosphate, acetate, $HClO_4^-$, HCO_3^-). Finally, the QD-lucigenin conjugate was tested in simulated physiological samples and for fluorescence lifetime imaging applications, showing a promising applicability of the system [72].

A QD-dopamine bioconjugate was realized [75] for in vitro and intracellular pH sensing. Dopamine and related quinones are well-known electron acceptors in biological environments [76, 77]. These systems undergo a coupled two electrons-two protons transfer process, as dopamine is oxidized to quinone by O_2, generating H_2O_2. A cyclic voltammetry investigation on dopamine demonstrates a linear dependence of the reduction potential on pH: namely, on increasing pH, oxidation to quinone is more favorable. The reduced hydroquinone form is a poorer electron acceptor with respect to quinone, therefore the extent of photoinduced electron transfer can be tuned by changing the pH. CdSe–ZnS nanocrystals of different sizes (radius = 28.0, 30.2 and 33.8 Å) were functionalized with increasing amounts of dopamine-labeled peptides, and the pH dependence of QD emission was investigated (Fig. 9).

At low pH, the dopamine is in the reduced hydroquinone form, which produces only marginal quenching of the QD emission. As pH increases, ambient O_2 oxidizes dopamine to quinone, which is an electron acceptor and significantly quenches the QD emission. The QD quenching increases as a function of the dopamine/QD ratio, and decreases as a function of QD dimensions (Fig. 10). Notably, the quenching

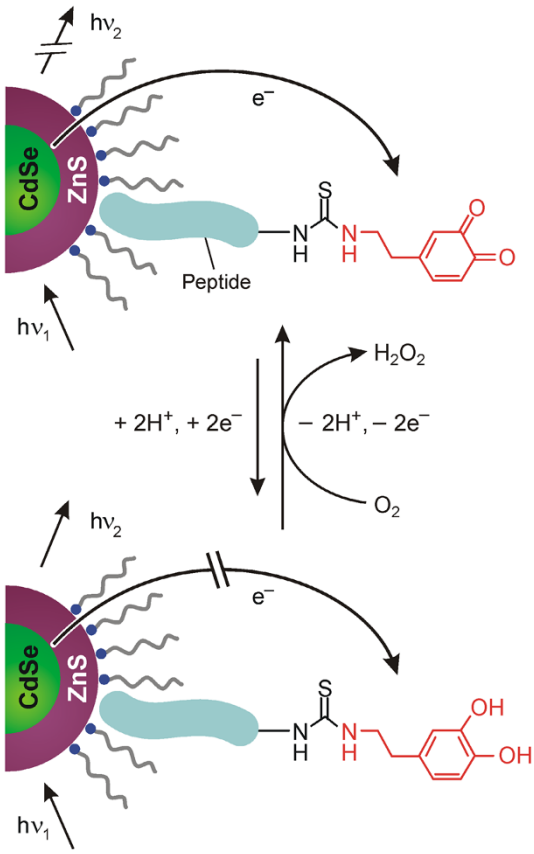

Fig. 9 Schematic representation of peptide–dopamine species assembled on the surface of CdSe–ZnS QDs [75]. The pH-dependent oxidation of hydroquinone to quinone triggered by ambient O_2 modulates the electron-transfer efficiency and is exploited to sense pH in aqueous solution and biological environments

efficiency of QD shows a linear dependence from pH similar to that exhibited by the reduction potential of dopamine. The sensing ability of the nanohybrids were also investigated in an intracellular environment. Cells were injected with the QD-dopamine conjugates at pH = 6.5 and the growth medium was switched to basic pH in presence or absence of nystatin, a drug that induces pore formation in membranes allowing only H^+/OH^- ions to be exchanged with the extracellular environment. A quenching of cytoplasmic QD luminescence in the presence of nystatin was observed as equilibrium was reached between the cytosolic pH and the surrounding medium.

6 Sensors Based on Photoinduced Energy Transfer

Several examples are available of quantum dot sensors derivatized with functional molecules based on energy-transfer processes, either from the QD to the chromophore or in the reverse direction. Another reason (besides those mentioned in "Modular design of photoactive QD-molecule conjugates") why QDs are

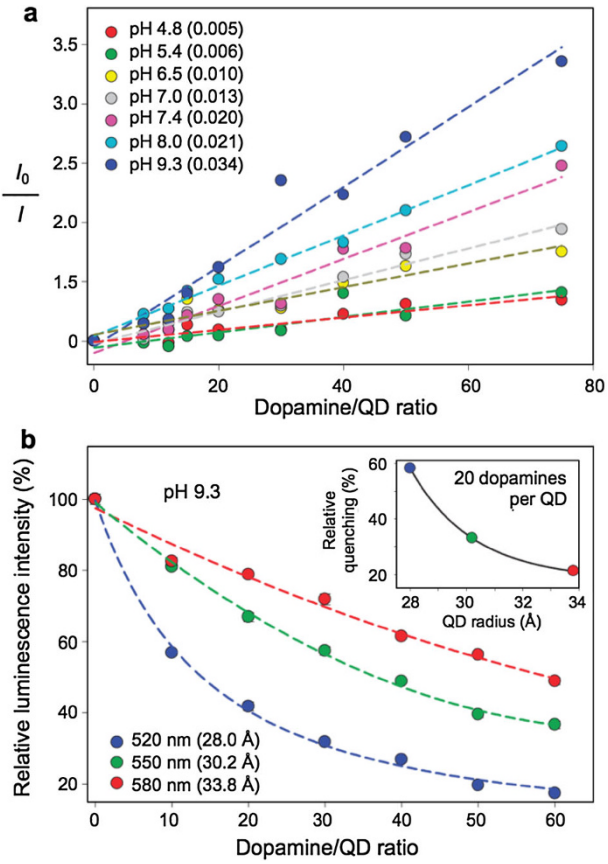

Fig. 10 **a** Plot of the luminescence quenching ratio (I_0/I) as a function of the dopamine/QD ratio for different pH values. The *values* in *parenthesis* are the slopes derived for each data set, showing that the quenching versus ratio increases upon increasing pH. **b** Plot of the normalized luminescence intensity as a function of the dopamine/QD ratio for QDs of different size at pH 9.3. The *inset* shows the normalized luminescence intensity versus the QD size for hybrids containing 20 dopamine species per QD. Adapted by permission from Ref. [75]. Copyright 2010 Nature Publishing Group

inefficient energy acceptors when organic fluorophores are used as donors is the unfavorable competition between the fast radiative decay of the donor and the relatively slow non-radiative energy transfer process [78].

Examples of QD-molecule conjugate pH sensors were reported, wherein the absorption profile of the chromophores depends on the pH. As the energy-transfer efficiency is determined by the extent of spectral overlap between the QD emission and the functional chromophore absorption, pH-dependent spectral shifts of the dye absorption affect the energy-transfer efficiency. Moreover, in order to avoid any interference in the measurement of pH, the surface ligands should not display any pH sensitivity.

The first ratiometric quantum dot pH sensor was based on CdSe–ZnS nanocrystals encapsulated within an amphiphilic polymer, upon which a squaraine

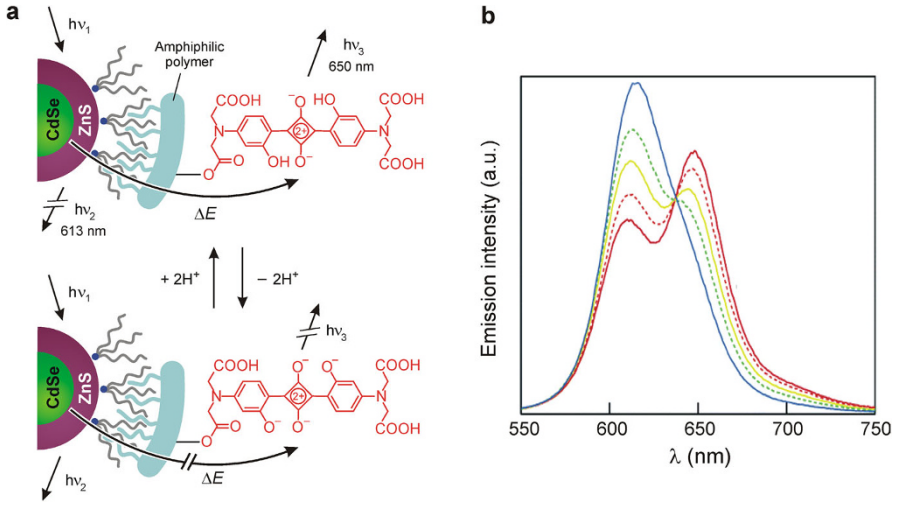

Fig. 11 **a** Scheme of a luminescent pH sensor composed of CdSe–ZnS QDs functionalized with a pH-sensitive squaraine. **b** Emission spectra of the QD-squaraine conjugate at different pH values (H_2O, $\lambda_{exc} = 380$ nm): 6.0 (*red solid line*); 7.0 (*orange dotted line*); 8.0 (*yellow solid line*); 9.0 (*green dotted line*); 10 (*blue solid line*). Adapted by permission from Ref. [79]. Copyright 2006 American Chemical Society

dye was conjugated (Fig. 11) [79]. The QD emission overlaps with the squaraine absorption, which is pH dependent: in particular the absorption band of the dye at $\lambda > 600$ nm is suppressed at basic pH. Therefore the spectral overlap between the squaraine absorption and the nanocrystal emission decreases on increasing the pH. Overall, the emission profile of the QD-squaraine conjugate shows a dependence on the pH of the environment, which is intrinsically ratiometric (Fig. 11).

At low pH values, the absorption band of the dye matches the emission band of the QD; the energy transfer is efficient, the QD luminescence is quenched, and the emission spectrum of the nanohybrid is dominated by the band of the squaraine dye. At high pH values, the spectral overlap is small, the energy transfer is inefficient, and the emission spectrum shows only the QD band.

The pH-triggered modulation of the overlap of QD and chromophore emission and absorption spectra was also exploited in CdTeSe–ZnS nanocrystals conjugated with near infrared (NIR) fluorescent probes [80]. These probes are particularly valuable for sensing in biological environment, as NIR light has the maximum depth of penetration in tissues. Moreover, the regulation of pH is relevant for most cellular processes, therefore its measurement has a crucial biological importance. Coupling organic dyes with inorganic semiconductor nanocrystals has the advantages of (i) overcoming the limitations of organic NIR chromophores, in particular their photostability and the limited pH-response of luminescence lifetime, and (ii) exploiting the excellent photophysical properties of QDs and the pH sensitivity of NIR organic dyes.

A carbocyanine dye exhibits an absorption maximum in the NIR (750 nm) at low pH and in the visible (520 nm) at high pH. CdTeSe–ZnS nanocrystals with emission

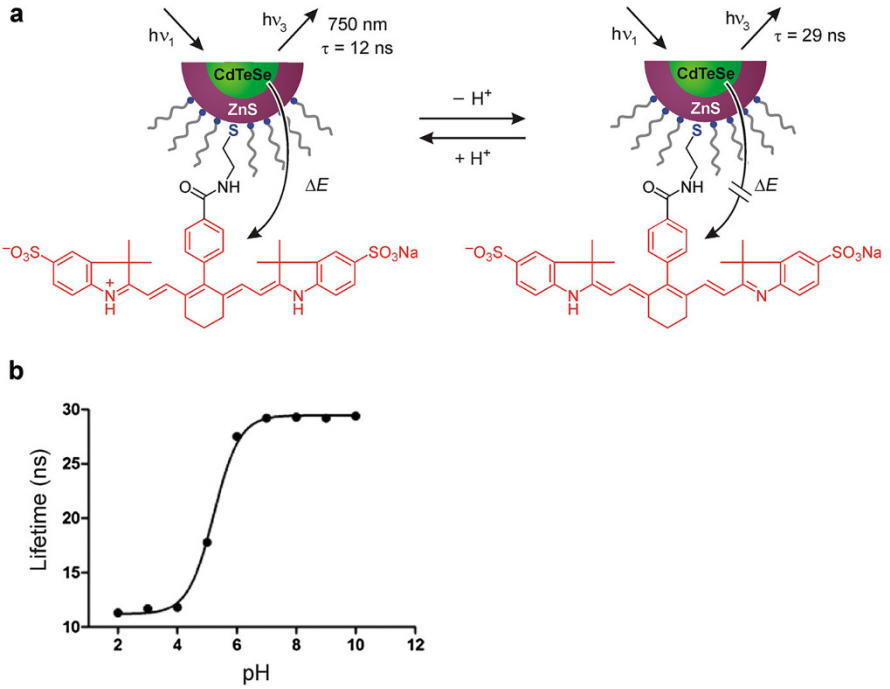

Fig. 12 **a** Representation of a hybrid composed of QD ($\lambda_{em} = 750$ nm) and carbocyanine dye components; the mechanism at the basis of the pH-dependent luminescence lifetime is also shown. **b** Plot of the luminescence lifetime as a function of pH and sigmoidal fit of the data points. Adapted by permission from Ref. [80]. Copyright 2012 American Chemical Society

at 750 nm functionalized with the carbocyanine dye (Fig. 12a) exhibit excellent spectral overlap with the chromophore absorption in the NIR at acidic pH. Efficient energy transfer from the QD to the carbocyanine is responsible for the quenching of the luminescence of the nanocrystals at low pH values. On increasing pH, the carbocyanine NIR absorption decreases and the QD luminescence is restored (Fig. 12a). Luminescence lifetime measurements confirmed the same pH response, with a decrease from 29 ns (pH $>$ 7) to 12 ns (pH $<$ 5). A sigmoidal plot of luminescence lifetime versus pH was reported, in agreement with the pH response of the dye and with a pK_a of 5.2 (Fig. 12b).

The pH-dependent shift of the absorption maximum of the carbocyanine can be exploited to accomplish ratiometric sensing. CdTeSe–ZnS QDs with emission at 560 nm exhibit good spectral overlap with the chromophore absorption in the visible at basic pH (Fig. 13a). The efficiency of energy transfer and the luminescence lifetime in the nanoconjugate increases on increasing pH, and the plot of emission lifetime as a function of pH exhibits a sigmoidal transition with a pK_a of 5.5 (Fig. 13b). As the two nanoconjugates display a complementary response to pH changes, their combination would allow ratiometric pH sensing.

QDs could also play the role of acceptors in energy-transfer processes, by virtue of their large absorption coefficient in a wide spectral region. It has been

demonstrated that inorganic semiconductor nanocrystals are efficient energy acceptors in combination with long-lived lanthanide-based donors [81]. Five different surface-biotinylated QDs were coupled with a luminescent Terbium complex conjugated to streptavidin for demonstrating the feasibility of

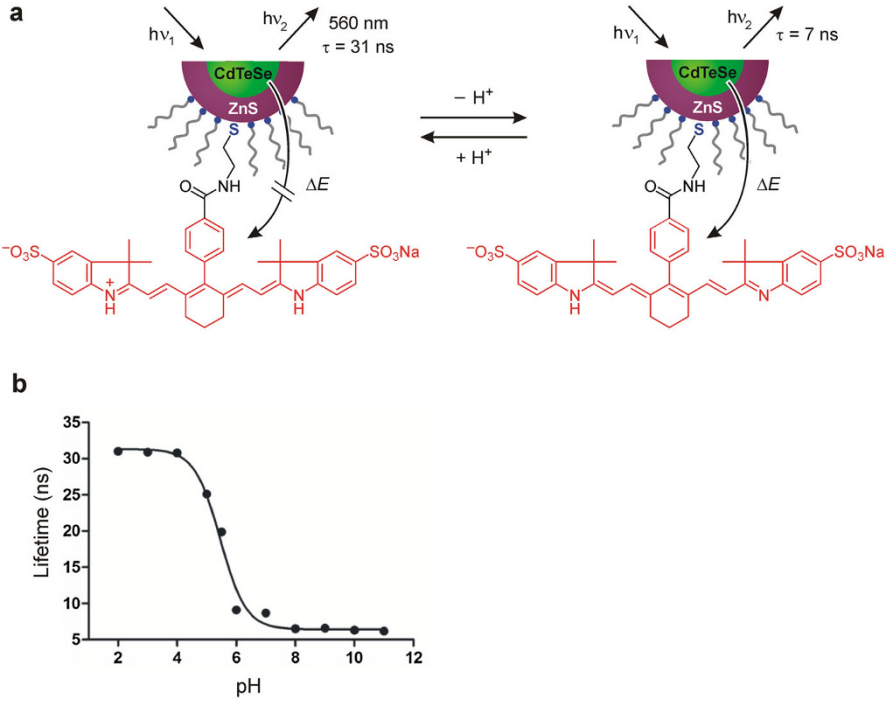

Fig. 13 **a** Representation of a hybrid composed of QD ($\lambda_{em} = 560$ nm) and carbocyanine dye components; the mechanism at the basis of the pH-dependent luminescence lifetime is also shown. **b** Plot of the luminescence lifetime as a function of pH and sigmoidal fit of the data points. Adapted by permission from Ref. [80]. Copyright 2012 American Chemical Society

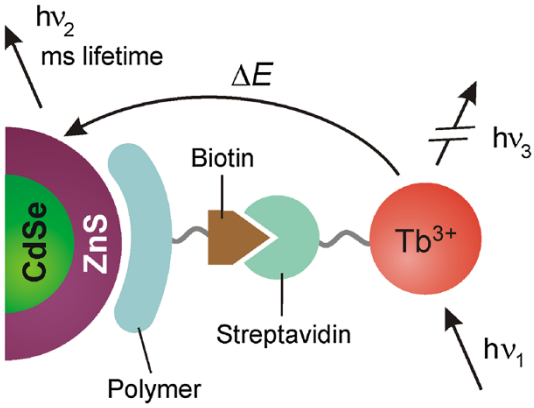

Fig. 14 A nanohybrid consisting of a surface-biotinylated QD bound to a terbium complex-streptavidin conjugate. Upon light excitation of the lanthanide complex in the UV, energy is transferred to the QD, thus resulting in luminescence quenching of Tb and the appearance of a long-lived QD luminescence with millisecond decay times

ultrasensitive multiplexed diagnostics (Fig. 14). CdSe–ZnS or CdSeTe–ZnS nanocrystals were selected with emission maxima at 529, 565, 604, 653, and 712 nm, in order to fit within the gaps of the terbium complex emission bands. Key requisites of this system are the symmetric bandwidth of the nanocrystals and the well-separated emission bands of the Tb complex.

On addition of the biotinylated QDs to a solution of streptavidin labeled with the terbium complex, the long-lived photosensitized QD emission increased, whereas the luminescence intensity of the terbium complex decreased (Fig. 14). Measurements were performed both on the single QD-Tb complex nanoconjugate, and on the mixture of all the five biotinylated QD samples. In this case, the parallel (i.e., multiplexed) measurement of the concentration of the five conjugates was possible. On increasing the QD-ligand ratio, five different emission bands arising from the photosensitized long-lived QD emission grew out of the Tb emission spectrum (Fig. 15). The limit of detection of this technique was found to be lower than picomolar, both for single and multiplexed measurements. A significant advantage of this approach is that the long-lived Tb luminescence allows time-gated detection, which leads to suppression of autofluorescence and fluorescence from directly excited QDs.

Energy transfer can also be exploited in a different approach for sensitizing the emission of a sensor, without playing an active role in the sensing process. In such a strategy, QDs serve as antennas for light absorption: upon selective excitation of the nanocrystals the energy is transferred to the analyte-sensitive ligand, which, on its turn, emits light. In particular, QDs exhibit large two-photon absorption cross

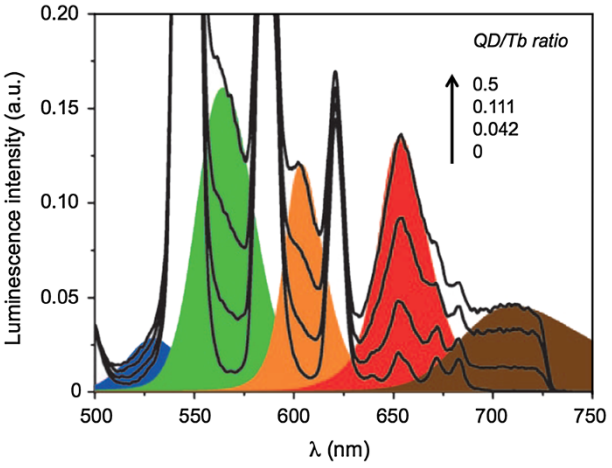

Fig. 15 Luminescence spectra for increasing concentration ratios of biotinylated QDs/streptavidin-conjugated Tb complex (aqueous borate buffer, $\lambda_{exc} = 320$ nm). The time-gated detection (50–450 μs) enabled the suppression of background autofluorescence of the biological species and QD emission arising from direct excitation. The spectra are normalized ($I = 1.0$ a.u.) to the 545 nm peak of the Tb complex; the figure shows a magnified view of the spectral region of interest. The steady-state emission spectra of the different QDs employed are displayed as superimposed colored curves ($\lambda_{em} = 529$ nm, *blue*; 565 nm, *green*; 604 nm, *orange*; 653 nm, *red*; 712 nm, *brown*). Adapted by permission from Ref. [81]. Copyright 2010 Wiley-VCH

section, thus allowing excitation in the NIR window, which, as mentioned above, is particularly attractive for biological applications.

As oxygen is an analyte of biological interest, near-IR excitation and detection are valuable features of sensors for imaging of live tissues. Thus, QDs are versatile platforms for building supramolecular oxygen sensing assemblies. Oxygen sensing commonly exploits the efficient quenching of molecular phosphorescence (that is, emission from a triplet excited state) by ground state oxygen ($^3O_2$); by monitoring phosphorescence intensity or lifetime of the sensor, the amount of O_2 can be quantified. Good candidates for developing this strategy are platinum and palladium porphyrins, because of their strong and long-lived phosphorescence in the 650–800-nm range. Nevertheless, as the two-photon absorption cross section of Pd-porphyrins is low, they must be coupled with an antenna.

Pd porphyrins with *meso*-pyridyl substituents were self-assembled on the surface of CdSe core–shell QDs [82], selected in order to display an emission profile overlapped with the absorption band of the Pd porphyrins (Fig. 16). The quantum yield of phosphorescence of Pd porphyrins increases up to four times when bound to the QD, as a result of FRET from the nanocrystals to the ligands. This effect is even more pronounced under two-photon excitation at 800 nm: the absorption cross section of QDs is four orders of magnitude greater than that of the porphyrin and the porphyrin emission in the nanoconjugate exhibit an up to tenfold increase. The lifetime of triplet emission of the porphyrins assembled on the surface of the nanocrystals increased of three orders of magnitude (from hundreds of nanoseconds to hundreds of microseconds) on going from aerated to deaerated conditions, both under one- and two-photon excitation.

Dexter-type triplet–triplet energy transfer from QDs to functional ligands was recently observed [83]. The advantage of using semiconductor nanocrystals in this process relies also on the close spacing of excited-state energy levels (1–15 meV)

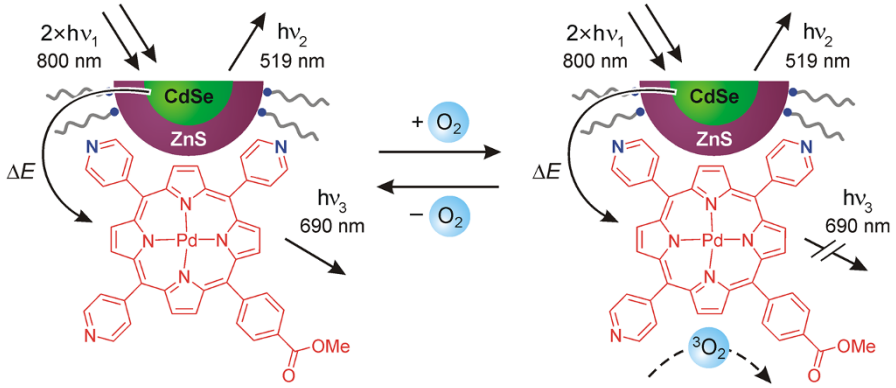

Fig. 16 Representation of a QD-Pd porphyrin nanohybrid in which the QD acts as a two-photon antenna for NIR excitation [82]. The insensitivity of the QD emission towards dioxygen provides an internal reference signal to establish a ratiometric response to O_2

[84] with respect to the large and energy-consuming singlet–triplet energy gap of molecular sensitizers.

CdSe QDs with a diameter of 2.4 nm were functionalized with 9-anthracenecarboxylic acid or 1-pyrenecarboxylic acid (Fig. 17) [83]. These nanocrystals exhibited the typical sharp luminescence band ($\lambda_{max} = 515$ nm) arising from band edge recombination, and a broad red-shifted feature (λ_{max} ca. 700 nm) due to trap state emission. Triplet levels derived from these exciton states possess an energy suitable for triplet–triplet energy transfer to the ligand (A_1) adsorbed on the surface of the semiconductor nanocrystals. Upon excitation of the QDs at 505 nm, the luminescence of the functionalized nanocrystals is quantitatively quenched. Ultrafast transient absorption spectroscopy measurements performed on the conjugates showed that the decay of the QD excited state occurs on a timescale coinciding with the growth of the $T_1 \rightarrow T_n$ transition of 9-anthracenecarboxylic acid, thus confirming the triplet exciton migration from the semiconductor nanocrystal to the molecular acceptor. The same results, but with different kinetics, were obtained with 1-pyrenecarboxylic acid.

Further energy transfer from the long-lived triplets localized on the QD ligands to suitable acceptors (A_2) by collisional encounters in solution was demonstrated. Indeed, the nanoconjugate could either photosensitize the production of $^1O_2$, as evidenced by the characteristic phosphorescence of the latter at 1277 nm, or transfer the electronic energy to another triplet acceptor, 2-chlorobisphenylethynylanthracene (CBPEA). The transient absorption spectrum of the QD-anthracene (or pyrene) conjugate in presence of CBPEA shows the absorption spectrum of the anthracene (or pyrene) triplet at short delay times, and the absorption spectrum of ^{3}CBPEA at longer delay times. These results demonstrate the feasibility of a general strategy in which quantum dots can photosensitize a range of processes relevant for applications in optoelectronics, solar energy conversion, and medicine.

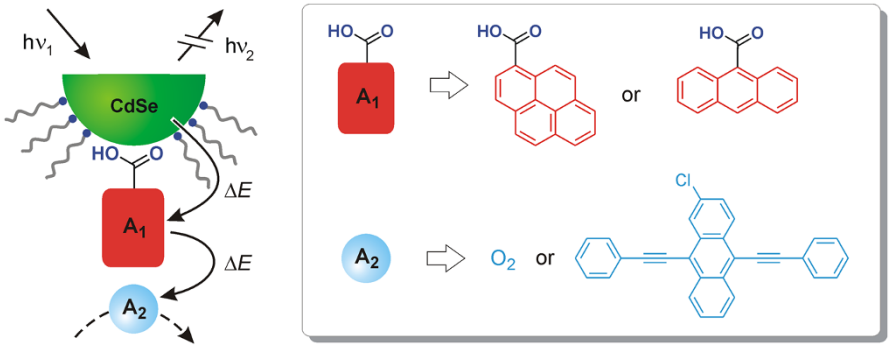

Fig. 17 Schematic representation of nanohybrids composed of CdSe QDs and surface-adsorbed organic molecules acting as triplet energy acceptors (A_1) [83]. Triplet–triplet energy transfer from the organic ligands to secondary molecular acceptors (A_2) freely diffusing in solution is also shown

7 Sensors Based on Spectroscopically Independent Components

As discussed in "Synthesis and surface modification", the insensitivity of the QD emission to most environmental parameters, like O_2 concentration and pH, can be exploited to design sensors in which the nanocrystals provide a scaffold for anchoring the sensing molecules and generate a constant emission that can serve as an internal intensity standard for ratiometric sensing. An example of such a system is the ratiometric oxygen sensor schematized in Fig. 18 [85].

CdSe–ZnS core–shell QDs were functionalized with a pyrenyl moiety attached to an imidazole surface docking unit. The absorption spectrum of the nanohybrid is a linear combination of the molecular components; also the emission spectrum obtained exciting both QD and pyrene exhibit the spectral feature of the separated components. Investigation of lifetimes and excitation spectra suggests that energy transfer is inefficient in this assembly. The luminescence spectrum of the QD-pyrene conjugate is affected by the presence of oxygen, and the two emission bands exhibit a different response to O_2 concentration (Fig. 19). In particular the pyrene type emission is quenched by O_2 following the Stern–Volmer relation, whereas the QD emission is unaffected by the presence of oxygen. Therefore the emission of QD can be used as an internal standard for normalizing the response signal of the pyrene moiety, thus forming the basis for a ratiometric sensor. In the present system, the emission signals originating from the QD and functional sensing ligands are fully independent from one another. This chromophore orthogonality offers a different functioning from related QD-chromophore nanoconjugates, and removes one of the energetic conditions associated with FRET systems.

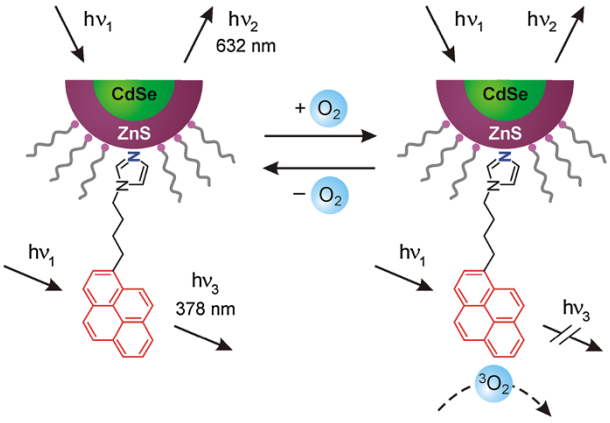

Fig. 18 Schematic representation of the luminescence response of CdSe–ZnS QDs, capped with TOPO and pyrenyl units towards molecular oxygen [85]

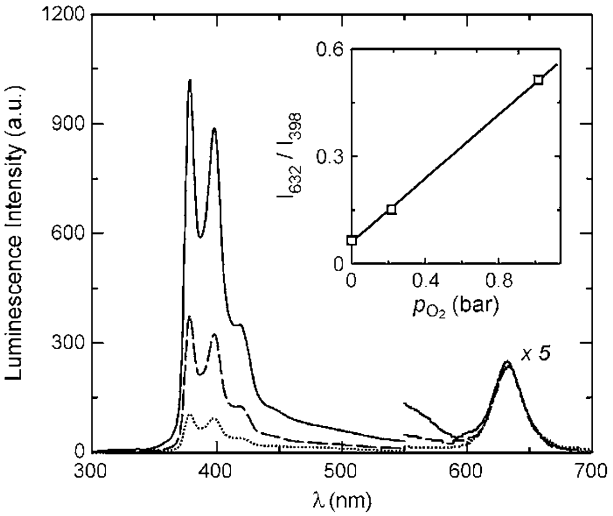

Fig. 19 Luminescence spectra ($\lambda_{exc} = 275$ nm) of the QD-pyrene nanohybrids in chloroform as a function of the oxygen pressure: 0 (*continuous line*), 0.213 (*dashed line*), and 1.013 (*dotted line*) bar. The *inset* shows the linear correlation between the ratiometric photoluminescence response (calculated as the QD-to-pyrene emission intensity ratio) and the O_2 partial pressure. Adapted from Ref. [85] with permission from The Royal Society of Chemistry

8 Conclusions

The use of quantum dots with predetermined optical properties and tailor-made surface for the construction of sensing nanodevices is gaining increasing attention. These systems are interesting because of their modular design and the presence of a luminescence signal, arising from the inorganic nanocrystal, which can be affected by surface-attached chemosensitive molecular species by exploiting electron- or energy-transfer mechanisms.

To this aim, semiconductor nanocrystals have revealed more appropriate than organic dyes, because of their peculiar size-dependent photophysical properties and excellent photostability, combined with the possibility of playing as scaffolds for arranging functional molecular units on their surface. In the past few years, strategies to control and improve the chemical and physical properties of QDs (including solubility, long-term stability and biocompatibility) while maintaining a size of a few nanometers and preserving their outstanding optical and electronic properties have become available.

Despite these advances, however, further experimental and computational investigations are needed because some chemical and physical properties of semiconductor nanocrystals are not completely clear yet. It should be highlighted that the lack of reproducibility which characterizes the preparation of quantum dots, the irregular behavior of their surface, and the artifacts connected with their characterization hamper significantly the rational design and preparation of QD-based systems. Finally, the toxicity of the nanocrystals and the environmental problems arising from the use of cadmium-based compounds need to be carefully

evaluated before QD sensors can find real-world applications [86, 87]. Only a multidisciplinary research effort can address all these stimulating challenges and ultimately enable a full technological exploitation of such fascinating nanodevices.

Acknowledgments Financial support from the Italian Ministry of Education, University and Research (PRIN 2010CX2TLM "InfoChem"), the Université Franco-Italienne (Vinci programme) and the University of Bologna is gratefully acknowledged.

References

1. Bawendi MG, Steigerwald ML, Brus LE (1990) Ann Rev Phys Chem 41:477–496
2. Efros AL, Rosen M (2000) Ann Rev Mater Sci 30:475–521
3. Alivisatos AP (1996) Science 271:933–937
4. Efros AL (1982) Sov Phys Semicond 16:772–775
5. Brus LE (1983) J Chem Phys 79:5566–5571
6. Murray CB, Norris DJ, Bawendi MG (1993) J Am Chem Soc 115:8706–8715
7. Resch-Genger U, Grabolle M, Cavaliere-Jaricot S, Nitschke R, Nann T (2008) Nat Methods 5:763–775
8. Hötzer B, Medintz IL, Hildebrandt N (2012) Small 8:2297–2326
9. Michalet X, Pinaud FF, Bentolila LA, Tsay JM, Doose S, Li JJ, Sundaresan G, Wu AM, Gambhir SS, Weiss S (2005) Science 307:538–544
10. Talapin DV, Lee JS, Kovalenko MV, Shevchenko EV (2010) Chem Rev 110:389–458
11. Kamat PV, Tvrdy K, Baker DR, Radich JG (2010) Chem Rev 110:6664–6688
12. de Mello Donegá C (2011) Chem Soc Rev 40:1512–1546
13. Doane TL, Burda C (2012) Chem Soc Rev 41:2885–2911
14. Amelia M, Lincheneau C, Silvi S, Credi A (2012) Chem Soc Rev 41:5728–5743
15. Shirasaki Y, Supran GJ, Bawendi MG, Bulović V (2013) Nat Photon 7:13–23
16. Fernée MJ, Tamarat P, Lounis B (2014) Chem Soc Rev 43:1311–1337
17. Schmid G (2004) Nanoparticles: from theory to applications. Wiley, Weinheim
18. Klimov VI (2005) Semiconductor and metal nanocrystals. Dekker, New York
19. Rogach AL (2008) Semiconductor nanocrystal quantum dots. Springer, Vienna
20. Callan JF, Raymo FM (2013) Quantum dot sensors: technology and commercial applications. Pan Stanford Publishing, Singapore
21. Yin Y, Alivisatos AP (2005) Nature 437:664–670
22. de Mello Donegá C, Liljeroth P, Vanmaekelbergh D (2005) Small 1:1152–1162
23. Park J, Joo J, Kwon SG, Jang Y, Hyeon T (2007) Angew Chem Int Ed 46:4630–4660
24. Das A, Snee PT (2016) ChemPhysChem 17:598–617
25. Green M (2010) J Mater Chem 20:5797–5809
26. Morris-Cohen AJ, Malicki M, Peterson MD, Slavin JWJ, Weiss EA (2013) Chem Mater 25:1155–1165
27. Boles MA, Ling D, Hyeon T, Talapin DV (2016) Nat Mater 15:141–153
28. Credi A (2012) New J Chem 26:1925–1930
29. de Silva AP, Gunaratne HQN, GunnlaugssonT Huxley NAJM, McCoy CP, Rademacher JT, Rice TE (1997) Chem Rev 97:1515–1566
30. Hildebrandt N (2011) ACS Nano 5:5286–5290
31. Larson DR, Zipfel WR, Williams RM, Clark SW, Bruchez MP, Wise FW, Webb WW (2003) Science 300:1434–1436
32. Somers RC, Bawendi MG, Nocera DG (2007) Chem Soc Rev 3:579–591
33. Raymo FM, Yildiz I (2007) Phys Chem Chem Phys 9:2036–2042
34. Freeman R, Willner I (2012) Chem Soc Rev 41:4067–4085
35. Petryayeva E, Algar WR, Medintz IL (2013) Appl Spectr 67:215–252
36. Tyrakowski CM, Snee PT (2014) Phys Chem Chem Phys 16:837–855
37. Silvi S, Credi A (2015) Chem Soc Rev 44:4275–4289
38. Chen Y, Rosenzweig Z (2002) Anal Chem 74:5132–5138
39. Norris DJ, Efros AL, Rosen M, Bawendi MG (1996) Phys Rev B 53:16347–16354

40. Reiss P, Protière M, Li L (2009) Small 5:154–168
41. Chaudhuri RG, Paria S (2012) Chem Rev 112:2373–2433
42. Kim S, Fisher B, Eisler HJ, Bawendi M (2003) J Am Chem Soc 125:11466–11467
43. Talapin D, Koeppe R, Gotzinger S, Kornowski A, Lupton J, Rogach A, Benson O, Feldmann J, Weller H (2003) Nano Lett 3:1677–1681
44. Rabouw FT, de Mello Donega C. Top Curr Chem (**in press**)
45. Palui G, Aldeek F, Wang W, Mattoussi H (2015) Chem Soc Rev 44:193–227
46. Lesnyak V, Gaponik N, Eychmüller A (2013) Chem Soc Rev 42:2905–2929
47. Ulusoy M, Jonczyk R, Walter JG, Springer S, Lavrentieva A, Stahl F, Green M, Scheper T (2016) Bioconjugate Chem 27:414–426
48. Wang F, Tang R, Kao JLF, Dingman SD, Buhro WE (2009) J Am Chem Soc 131:4983–4994
49. Green MLH (1995) J Organomet Chem 500:127–148
50. Anderson NC, Hendricks MP, Choi JJ, Owen JS (2013) J Am Chem Soc 135:18536–18548
51. Owen J (2015) Science 347:615–616
52. Medintz IL, Uyeda HT, Goldman ER, Mattoussi H (2005) Nat Mater 4:435–446
53. Erathodiyil N, Ying JY (2011) Acc Chem Res 44:925–935
54. Liu W, Howarth M, Greytak AB, Zheng Y, Nocera DG, Ting AY, Bawendi MG (2008) J Am Chem Soc 130:1274–1284
55. Yildiz I, Deniz E, McCaughan B, Cruickshank SF, Callan JF, Raymo FM (2010) Langmuir 26:11503–11511
56. Avellini T, Lincheneau C, La Rosa M, Pertegas A, Bolink HJ, Wright IA, Constable EC, Silvi S, Credi A (2014) Chem Commun 50:11020–11022
57. Palui G, Avellini T, Zhan N, Pan F, Gray D, Alabugin I, Mattoussi H (2012) J Am Chem Soc 134:16370–16378
58. Baly B, Ling J, de Silva AP (2015) Chem Soc Rev 44:4203–4211
59. Yildiz I, Tomasulo M, Raymo FM (2008) J Mater Chem 18:5577–5584
60. Medintz IL, Mattoussi H (2009) Phys Chem Chem Phys 11:17–45
61. Avellini T, Lincheneau C, Vera F, Silvi S, Credi A (2014) Coord Chem Rev 263–264:151
62. Credi A (2014) Chem Soc Rev 43:3995–4270 **(themed issue on photochemistry of supramolecular systems and nanostructured assemblies)**
63. Balzani V, Credi A, Venturi M (2008) Molecular devices and machines—concepts and perspective for the nano world. Wiley, Weinheim
64. Zhu H, Song N, Lian T (2010) J Am Chem Soc 132:15038–15045
65. Kaledin AL, Lian T, Hill CL, Musaev DG (2015) J Phys Chem B 119:7651–7658
66. Zeng P, Kirkwood N, Mulvaney P, Boldt K, Smith TA (2016) Nanoscale 8:10380–10387
67. Lakowicz JR (2006) Principles of fluorescence spectroscopy, 3rd edn. Springer, New York
68. Clapp AR, Medintz IL, Mattoussi H (2006) ChemPhysChem 7:47–57
69. Aldeek F, Ji X, Mattoussi H (2013) J Phys Chem C 117:15429–15437
70. Völker J, Zhou X, Ma X, Flessau S, Lin H, Schmittel M, Mews A (2010) Angew Chem Int Ed 49:6865–6868
71. Han C, Cui Z, Zou Z, Tian SD, Li H (2010) Photochem Photobiol Sci 9:1269–1273
72. Ruedas-Rama MJ, Orte A, Hall EAH, Alvarez-Pez JM, Talavera EM (2012) Analyst 137:1500–1508
73. Huber C, Klimant I, Krause C, Werner T, Mayr T, Wolfbeis OS (2000) Fresenius J Anal Chem 368:196–202
74. Huber C, Krause C, Werner T, Wolfbeis OS (2003) Microchim Acta 142:245–253
75. Medintz L, Stewart MH, Trammell SA, Susumu K, Delehanty JB, Mei BC, Melinger JS, Blanco-Canosa JB, Dawson PE, Mattoussi H (2010) Nat Mater 9:676–684
76. Laviron E (1984) J Electroanal Chem 164:213–227
77. Wraight CA (2004) Front Biosci 9:309–337
78. Clapp AR, Medinitz L, Fisher BR, Anderson GP, Mattoussi H (2005) J Am Chem Soc 127:1242–1250
79. Snee PT, Somers RC, Nair G, Zimmer JP, Bawendi MG, Nocera DG (2006) J Am Chem Soc 128:13320–13321
80. Tang R, Lee H, Achilefu S (2012) J Am Chem Soc 134:4545–4548
81. Geissler D, Charbonnière LJ, Ziessel RF, Butlin NG, Löhmansröben H-G, Hildebrandt N (2010) Angew Chem Int Ed 49:1396–1401
82. Lemon CM, Karnas E, Bawendi MG, Nocera DG (2013) Inorg Chem 52:10394–10406
83. Mongin C, Garakyaraghi S, Razgoniaeva N, Zamkov M, Castellano FN (2016) Science 351:369–372

84. Scholes GD (2014) Adv Funct Mater 13:1039–1043
85. Amelia M, Lavie-Cambot A, McClenaghan ND, Credi A (2011) Chem Commun 47:325–327
86. Bottril M, Green M (2011) Chem Commun 47:7039–7050
87. Ye L, Yong KT, Liu L, Roy I, Hu R, Zhu J, Cai H, Law WC, Liu J, Wang K, Liu J, Liu Y, Hu Y, Zhang X, Swihart MT, Prasad PN (2012) Nat Nanotech 7:453–458

Top Curr Chem (Z) (2016) 374:53
DOI 10.1007/s41061-016-0056-9

REVIEW

Light-Harvesting Antennae Based on Silicon Nanocrystals

Francesco Romano[1] · Yixuan Yu[2] · Brian A. Korgel[2] · Giacomo Bergamini[1] · Paola Ceroni[1,3]

Received: 24 May 2016 / Accepted: 13 July 2016 / Published online: 28 July 2016

Abstract Silicon (Si) nanocrystals are relatively strong light emitters, but are weak light absorbers as a result of their indirect band gap. One way to enhance light absorption is to functionalize the nanocrystals with chromophores that are strong light absorbers. By designing systems that enable efficient energy transfer from the chromophore to the Si nanocrystal, the brightness of the nanocrystals can be significantly increased. There have now been a few experimental systems in which covalent attachment of chromophores, efficient energy transfer and significantly increased brightness have been demonstrated. This review discusses progress on these systems and the remaining challenges.

Keywords Quantum dots · Luminescence · Brightness · Energy transfer · Indirect band gap semiconductor

This article is part of the Topical Collection "Photoactive Semiconductor Nanocrystal Quantum Dots"; edited by "Alberto Credi".

✉ Brian A. Korgel
korgel@che.utexas.edu

✉ Paola Ceroni
paola.ceroni@unibo.it

[1] Department of Chemistry "G. Ciamician", University of Bologna, Via Selmi 2, 40126 Bologna, Italy

[2] Department of Chemical Engineering, Texas Materials Institute, Center for Nano- and Molecular Science and Technology, The University of Texas at Austin, Austin, TX 78712, USA

[3] Centro Interuniversitario per la Conversione Chimica dell'Energia Solare (SOLAR-CHEM), Unità di Bologna, Bologna, Italy

1 Introduction

1.1 Working Principle of a Light-Harvesting Antenna

An antenna for light harvesting (Fig. 1) is an organized multi-component system in which many chromophoric units absorb the incident light and then channel the excitation energy to a common acceptor component. Light-harvesting antennae are not just a human invention. In green plants, chlorophylls collect an enormous amount of solar energy and redirect it as electronic excitation energy to reaction centers, where subsequent conversion into redox chemical energy takes place [1].

The first requirement for a light-harvesting antenna is, of course, its capacity to absorb light. Another essential property of the light absorbing units is their chemical and photochemical stability. An efficient antenna effect can only be obtained in multichromophoric arrays suitably organized in the dimensions of time, energy, and space. Each component has to absorb the incident light and the excited state so obtained (donor) has to transfer electronic energy to a nearby component (acceptor), before undergoing radiative or nonradiative deactivation (organization in the time dimension). In order for energy transfer to occur, the energy of the acceptor excited state (or exciton in the case of a nanocrystal acceptor) has to be lower or, at most, equal to the energy of the excited state of the donor (organization in the energy dimension). Finally, the successive donor-to-acceptor energy-transfer steps must result in an overall energy-transfer process leading the excitation energy towards a selected component of the array (organization in the space dimension). The occurrence of energy transfer requires electronic interactions and therefore the rate of energy transfer decreases with increasing separation between the donor units A and the acceptor B (Fig. 1).

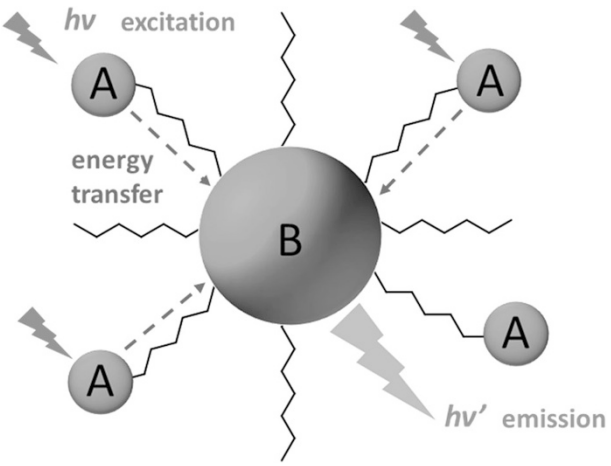

Fig. 1 General representation of an antenna system composed of multiple chromophoric units *A* around the acceptor component *B*

Different antenna systems are evaluated by considering the efficiency of the successive energy transfer steps that take place after light absorption occurs. For example, with reference to Fig. 1, light absorption by a number of components A is followed by energy transfer to a common luminescent component B. The sensitized emission quantum yield of B, Φ_{sens}, is a product of the emission quantum yield of B by its direct excitation, Φ_B, and the efficiency η_{et} of energy transfer from the electronic excited state of A to B:

$$\Phi_{sens} = \eta_{et}\Phi_B \quad (1)$$

Clearly, the quantum yield of the sensitized emission of B cannot be larger than the quantum yield of the emission obtained upon direct excitation of B.

An "amplification factor" has been used [2, 3], referring to the ratio of the intensity of the sensitized emission of B to the intensity obtained upon direct excitation of B. The use of this factor can be misleading since it depends on the experimental conditions that are employed. A more representative measure of the performance of a light harvesting antenna—and directly relevant for practical applications—is the brightness:

$$\text{brightness} = \varepsilon(\lambda_{ex})\,\Phi_{sens} \quad (2)$$

where ε (λ_{ex}) is the molar absorption coefficient of the antenna at the excitation wavelength (where light is absorbed by A) and Φ_{sens} is the sensitized emission as defined in Eq. (1). With higher brightness, lower concentrations of the antenna are needed to observe a detectable emission.

In the last 15 years, much attention has been devoted to the design and synthesis of artificial antennae for different applications, such as photochemical conversion of solar energy [4, 5], signal amplification in luminescent sensors [6], organic light-emitting diodes [7, 8], and energy upconversion processes [9]. Most artificial antennae investigated in the past have been designed based on dendrimers [10–13], which enable the organization of many photoactive units within a restricted space with some control over their placement within the architecture, namely the periphery, branches or core. Other nanostructures have also been investigated: for example, zeolites [14], polymers [15, 16], G-quartet nanostructures [17], and DNA [18, 19].

1.2 Silicon Nanocrystals as Scaffolds for Light-Harvesting Antennae

Silicon (Si) nanocrystals are an emerging new class of luminescent probes [20–23] that can play a dual role of scaffold and luminescent acceptor unit to build light-harvesting antennae. Their photoluminescence can be tuned from the visible to the near-infrared spectral region by changing their size [20, 21, 24]. Although they have excellent emission properties, Si nanocrystals are weak light absorbers due to the indirect nature of the band gap of silicon [25, 26]. This limits the luminescence brightness of Si nanocrystals, and the photon energy required for photoexcitation is usually significantly higher than the peak emission energy. For example, Si nanocrystals with peak light emission at 800 nm are usually excited with light of

wavelength 400 nm to achieve reasonable emission signal. To enhance the light absorption, Si nanocrystals can be decorated with a surface layer containing light-absorbing chromophores that funnel excitation energy to the Si core; this is the working principle of a molecular light-harvesting antenna. Although a large body of literature exists detailing energy transfer between more conventional light-emitting colloidal semiconductor nanocrystals, e.g. CdSe, and various fluorophores [27, 28], up to now, only a few studies, which will be described in Sect. 3, have examined energy transfer as a means to induce light emission from Si nanocrystals.

Some key aspects of using Si nanocrystals as the light-emitters are: (1) silicon is an earth-abundant and non-toxic element [29], (2) the surface passivation, necessary to prevent oxidation and to get a stable dispersion, is robust due to the covalent bond between silicon and the protecting layer [30, 31], and (3) luminescence is long-lived [32–35] (hundreds of microseconds, compared to tenths of nanoseconds for standard quantum dots)[1] enabling time-gated detection [36] for easy subtraction of the autofluorescence of biological samples.

2 Synthesis of Functionalized Silicon Nanocrystals and Relation to Their Optical Properties

Approaches for the synthesis and surface functionalization of colloidal silicon nanocrystals have been recently reviewed in the literature [20, 37, 38]. Only the synthetic procedures that have been used to obtain light-harvesting antennae are described here, with particular emphasis on the resulting optical properties.

Broadly speaking, two approaches have been explored to make Si nanocrystals functionalized with light-absorbing chromophores/antenna. One approach is to generate hydrogen-terminated Si nanocrystals that are subsequently linked to an alkene-functionalized chromophore by hydrosilylation [32, 39–43]. A second reported approach has grafted chromophores to pendant amines on ligand-stabilized Si nanocrystals [44].

Figure 2 illustrates one effective approach for generating ligand-stabilized crystalline Si nanocrystals with relatively uniform and *synthetically-tunable* size. This method, introduced by Veinot and coworkers [45], involves the thermal decomposition of hydrogen silsesquioxane (HSQ, $[HSiO_{3/2}]_n$) to obtain Si nanocrystals embedded in SiO_2. Etching the oxide matrix with HF yields free-standing H-terminated Si nanocrystals, which can be capped by a thermally-promoted hydrosilylation reaction with an alkene. Korgel and coworkers [46, 47] have shown that this method can yield light-emitting Si nanocrystals that are sufficiently uniform to create superlattices. To functionalize the nanocrystals with a chromophore, the hydrosilylation reaction is carried out in the presence of a mixture of alkene and alkene-functionalized chromophore [32, 42, 43]. Locritani, et al. [32] found that Si nanocrystals could not be capped with pure chromophore and that a

[1] Luminescent intensity decay is dependent on the synthetic methodology employed and contrasting results about the correlation between dimension and emission properties (energy and lifetime) are found in the literature (see Sect. 2) [24, 62].

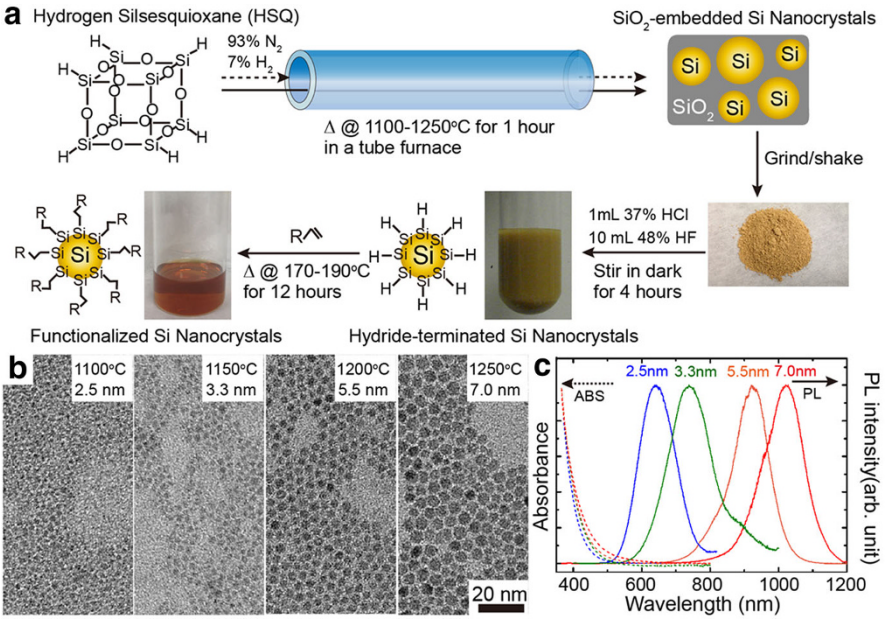

Fig. 2 **a** Synthetic route for generating colloidal Si nanocrystals. **b** TEM images of organic ligand-capped Si nanocrystals generated using the method described in (**a**), demonstrating the relatively uniform size of the nanocrystals and the ability to adjust the average diameter. **c** Optical absorbance and photoluminescence emission spectra for the Si nanocrystals imaged by TEM in (**b**), exhibiting the expected size-dependent emission energy

mixture of alkene and alkene-terminated chromophores was needed to obtain solvent-dispersable, light-emitting Si nanocrystals functionalized with the chromophores.

Wang and Xu [41] synthesized their Si nanocrystals using an approach similar to the one described in Fig. 2, but, instead of starting with HSQ, they began by oxidizing $HSiCl_3$ with water at −78 °C to obtain an HSQ-like precursor material that was then thermally degraded into oxide-embedded Si nanocrystals. These nanocrystals were used to obtain H-terminated Si nanocrystals for subsequent hydrosilylation. Alternatively, Sommer et al. [39] and Groenewegen, et al. [40] began with Si nanocrystals generated by the gas-phase process developed by Wiggers and coworkers [48]. The Si nanocrystal starting material had oxidized surfaces and required an HF etch to generate H-terminated Si nanocrystals, which were used for chromophore addition by hydrosilylation. One drawback of both of those methods was the broad size distribution of the Si nanocrystals that were obtained.

Rosso-Vasic et al. [44] used an entirely different approach to generate their Si nanocrystals. They carried out a room-temperature arrested precipitation, similar to the route first described by Tilley and co-workers [49]. They "reduced" $SiCl_4$ with $LiAlH_4$ in a mixture of toluene and THF in the presence of the surfactant, tetraoctylammonium bromide (TOAB) [50]. (Note that at room temperature, the

addition of $LiAlH_4$ to $SiCl_4$ actually results in the hydrogenation product of SiH_4, which is a gas and thermally stable at room temperature and *pyrophoric*—this type of reaction should be carried out with extreme care.) The TOAB-stabilized material was then reacted with an alkylamine in the presence of a hydrosilylation catalyst, $PtCl_6^{2-}$ [44]. Rosso-Vasic et al. [44] describe the resulting product as Si nanocrystals coated with covalently-bonded alkyl-amines. The amines were then reacted with the chromophore via an amine-*N*-hydroxysuccinimidyl ester coupling reaction to yield the final luminescent product. Although the only materials characterization data provided in ref [44] are optical absorbance and photoluminescence spectra and the quality of the materials cannot be assessed, this method is known to produce Si materials that luminesce in the blue part of the spectrum with relatively short emission lifetimes (tenths of nanoseconds), which is different from the Si nanocrystals made by the high-temperature decomposition of HSQ or the gas-phase approaches, which tend to emit in the orange-to-near infrared wavelength range with significantly longer emission lifetimes (hundreds of microseconds) [24]. Veinot and coworkers [51] have attributed similar blue light emission to the incorporation of nitrogen species as a dopant into the Si nanocrystal core, which might be considered as a possibility here, or the light emission might be associated in some way with oxidized Si species [52].

Since the optical properties of Si nanocrystals can depend on factors such as size uniformity, crystallinity, purity, and oxidation, it is usually best to characterize the materials using a few different techniques [24]. For estimating the nanocrystal size, transmission electron microscopy (TEM) is a powerful tool, but it only provides the ability to measure the size of a small number of nanocrystals. Small angle X-ray scattering (SAXS) measurements of Si nanocrystal dispersions provide a statistical average of the size and uniformity of the nanocrystals. Si nanocrystal samples should always be characterized by X-ray diffraction (XRD) to ensure that the materials are crystalline and have bulk-like diamond cubic crystal structure. One emerging aspect of Si nanocrystal crystallinity is that the smallest nanocrystals (ca. 2 nm diameter) can exhibit significant amounts of orientational bond disorder, which might influence the optical properties of the materials [53]. For characterizing the nanocrystal surfaces, Fourier transform infrared (FTIR) spectroscopy is a useful technique for observing hydrocarbon species and hydrogenated Si on the nanocrystal surface, but is not particularly effective at determining the extent of surface oxidation. For this, another important characterization technique, X-ray photoelectron spectroscopy (XPS), should be used. XPS can provide a detailed analysis of the extent of oxidation on the Si nanocrystal surface [24]. Not only can zero valent Si be observed—to ensure that the nanocrystals are indeed made of Si^0—but the various oxidized Si species can also be determined, i.e., Si^{1+}, Si^{2+}, Si^{3+} and Si^{4+}. Covalent Si–C species on the surface is also observable by XPS. Since the light emission of Si nanocrystals is influenced by surface oxide, XPS data is very informative for helping interpret the observed optical properties of chromophore-functionalized Si nanocrystals.

3 Examples of Si Nanocrystal-based Light-Harvesting Antennae

This section provides examples of Si nanocrystal antennae presented in order of decreasing energy of the lowest absorption band of the appended chromophore. Examples in which chromophores and silicon nanocrystals are not covalently bound, but a physical mixture is prepared (see, e.g. [54, 55]) are not discussed in the following since there is no control over the distance between donor and acceptor and the energy transfer efficiency and brightness vary significantly depending on the preparation procedure and concentration.

Alkyl chains that are covalently bound to the Si nanocrystal (SiNC) surface do not affect the optical properties of Si nanocrystals, while other functional groups, such as halides or nitrogen linked to the silicon surface, can significantly change the photophysical properties of the SiNC [56, 57]. In some cases, the attachment of a chromophore via a short and conjugated bridge also leads to a change of the optical features by charge transfer interactions with silicon [58, 59]. The following only presents examples in which the authors investigated the photoinduced energy transfer processes from the chromophores to the SiNC or vice versa, and not only a change of the emission properties of the nanocrystals upon direct excitation of the silicon core.

3.1 UV Absorbing Dyes

Figure 3 is a schematic representation of water-soluble 2- and 4-vinylpyridine-terminated SiNCs with sizes between 2 and 3 nm [39]. For these studies, SiNCs were made by a low-pressure microwave plasma-induced decomposition of silane and then etched in an ethanolic HF solution before carrying out a thermal hydrosilylation reaction with vinylpyridine ligands. The functionalized SiNCs were reported to emit in the blue-green spectral region with emission quantum yields around 30 %. Femtosecond transient absorption spectroscopy evidenced an ultrafast (<1 ps) energy transfer process from an initially photogenerated interfacial charge-transfer state to the conduction band levels of the SiNCs. However, excitation was performed at 387 nm, where vinylpyridine is not absorbing light; the authors attribute the absorption in this spectral range to a charge-transfer transition between the pyridine and the SiNCs. On the other hand, the excitation spectrum performed at

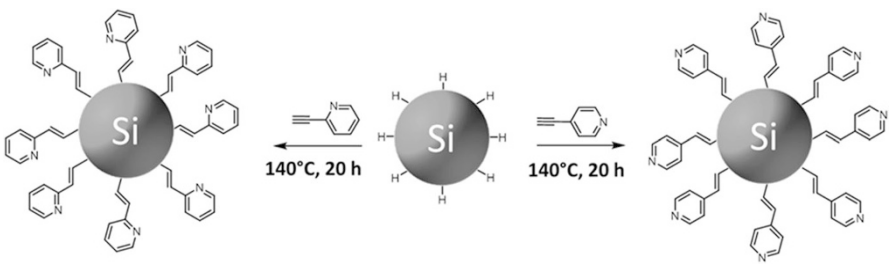

Fig. 3 Schematic representation of 2-vinylpyridine and 4-vinylpyridine-terminated SiNCs [39]

the SiNC emission shows only a modest contribution from the vinylpyridine chromophore, which points to a rather inefficient energy transfer process.

The same authors [40] also investigated the photophysical properties of 3-vinylthiophene-terminated SiNCs (Fig. 4) with sizes between 2 and 3 nm, synthesized by the same approach as described above. These nanocrystals emit blue light with maximum at 460 nm, and an emission quantum yield of ~23 %. Photoexcitation with 150-fs pump pulses at 387 nm leads to a transient absorption band with maximum at 450 nm, ascribed to the population of the lowest singlet excited state S_1 of 3-vinylthiophene via two-photon absorption. Subsequent ultrafast excitation energy transfer or electron transfer to conduction band states of the Si core was assumed by monitoring the rise dynamics of transient absorption transitions of conduction-band electrons. The hypothesis of 2-photon absorption of 3-vinylthiophene upon excitation at 387 nm was not supported by a similar behavior of the free chromophore under the same experimental conditions, since immediate photodegradation of the chromophore yielded a brown precipitate. In the present example, the authors could not discriminate between energy and electron transfer processes.

Anthracene was used to decorate the SiNC surface (Fig. 5): H-terminated silicon nanocrystals (ca. 5 nm average diameter) obtained by thermal disproportionation of $(HSiO_{1.5})_n$ at 1150 °C were reacted with 9-vinylanthracene by thermal hydrosililation at 156 °C in mesitylene [41]. Upon excitation of the anthracene chromophore at

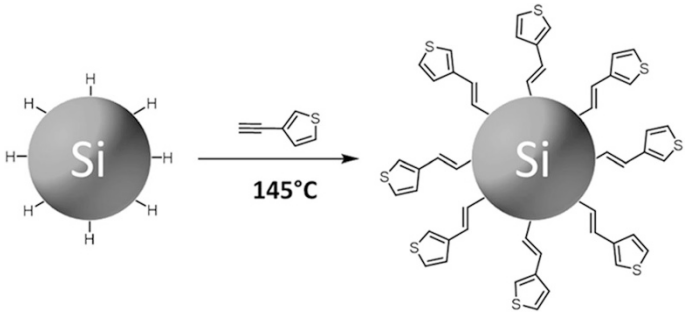

Fig. 4 Schematic representation of 3-vinylthiophene-terminated SiNC synthesis [40]

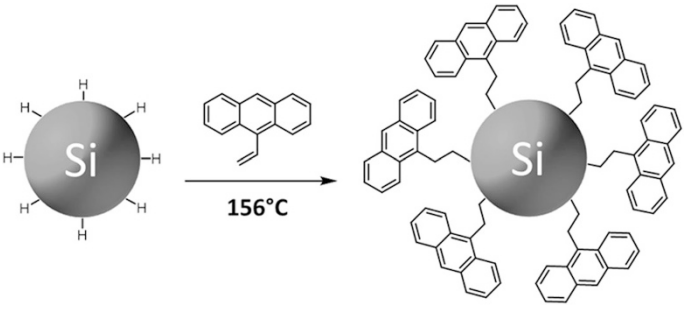

Fig. 5 Schematic representation of 9-ethylanthracene-terminated SiNC synthesis [41]

360 nm, dual-emission has been observed with peaks centered at 431 and 824 nm, corresponding to the anthracene and SiNC luminescence, respectively. The peak at the longer wavelength is very similar to that observed for a sample of SiNC passivated by reaction with non-chromophoric 1-decene. On the other hand, the fluorescence properties of the anthracene are modified by the covalent attachment to the nanocrystals: the emission maximum is blue-shifted by 10 nm and the lifetime is longer (7.35 ns) compared to the starting 9-vinylanthracene, suggesting a coupling effect between the chromophore and the SiNC core. Therefore, in the present case, the chromophore properties are modified by the coupling to the nanocrystals, but no quenching of the anthracene fluorescence is evidenced, as demonstrated by the longer lifetime of the bound anthracene (data of the emission quantum yields are not reported). Therefore, this system does not work as a light-harvesting antenna.

Two other examples of SiNC decorated with UV absorbers have recently been reported by some of us [32, 42]. The two systems contain the same pyrene chromophore and differ by the length of the alkyl chain (C_3 or C_{11}) connecting the chromophore to the silicon core (Fig. 6). Both systems are based on two families of SiNCs with different diameters (ca. 3 and 5 nm) synthesized by thermal decomposition of hydrogen silsesquioxane (see Sect. 2 and Fig. 2 for more details). Hereafter, the samples will be named as $\mathbf{Si_{\mathit{x}nm}C_3Py}$ and $\mathbf{Si_{\mathit{x}nm}C_{11}Py}$ ($x = 3$ or 5 corresponds to the average diameter in nm) for the short and long chain, respectively, and $\mathbf{Si_{\mathit{x}nm}}$ are the reference nanocrsytals passivated only with 1-dodecene.

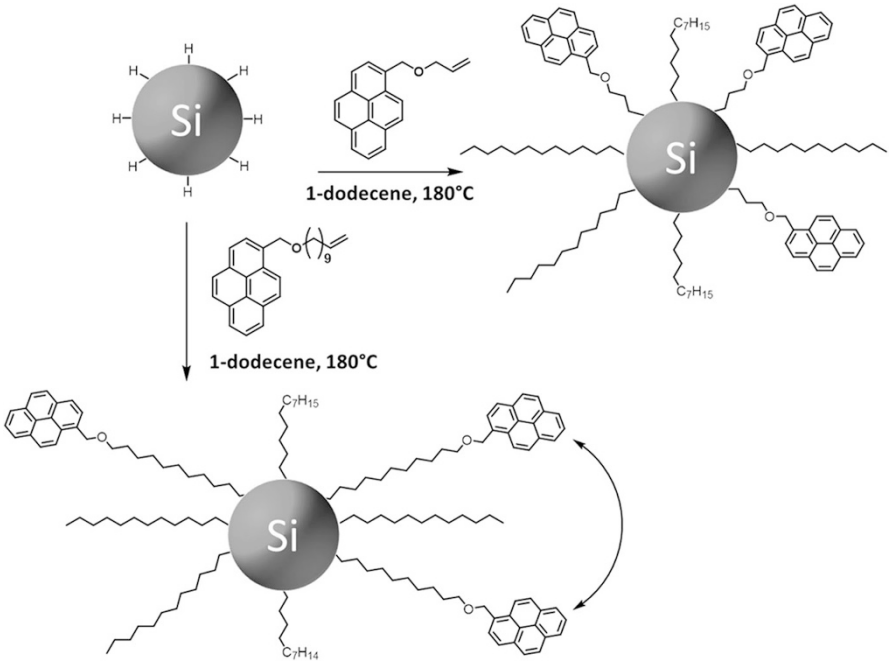

Fig. 6 Representation of SiNC co-passivated with 1-dodecene and pyrene units [32, 42]

The absorption spectra of toluene dispersions of **$Si_{3nm}C_3Py$** and **$Si_{5nm}C_3Py$** (red curves in Fig. 7a, c) are the superposition of the unstructured absorption profile characteristic of SiNCs (blue curves in Fig. 7a, c) and the structured absorption band of the pyrene chromophore in the 300–350 nm region (Fig. 7a, c, black dotted lines). This result demonstrates that no ground-state interaction takes place between the organic chromophore and the inorganic silicon core. On the basis of the molar absorption coefficients of pyrene and the SiNCs [24], the average number of pyrene chromophores per nanocrystals are estimated to be: 8 and 60 pyrene units per **$Si_{3nm}C_3Py$** and **$Si_{5nm}C_3Py$**, respectively. The emission spectra of the **$Si_{xnm}C_3Py$** samples (Fig. 7b, d) show pyrene fluorescence at 390 nm. Moreover, the characteristic silicon core emission at 635 and 970 nm is observed for **$Si_{3nm}C_3Py$** and **$Si_{5nm}C_3Py$**, respectively: lifetimes are of the order of hundreds of μs in both cases.

In order to study the photoinduced energy transfer processes, emission spectra were measured with excitation wavelengths of either 378 or 345 nm to selectively photoexcite the SiNC core or the pyrene units. The pyrene emission band at 400 nm is largely quenched for both the **$Si_{3nm}C_3Py$** and **$Si_{5nm}C_3Py$** samples, as also confirmed by lifetime measurements, and a sensitized emission of the silicon core is

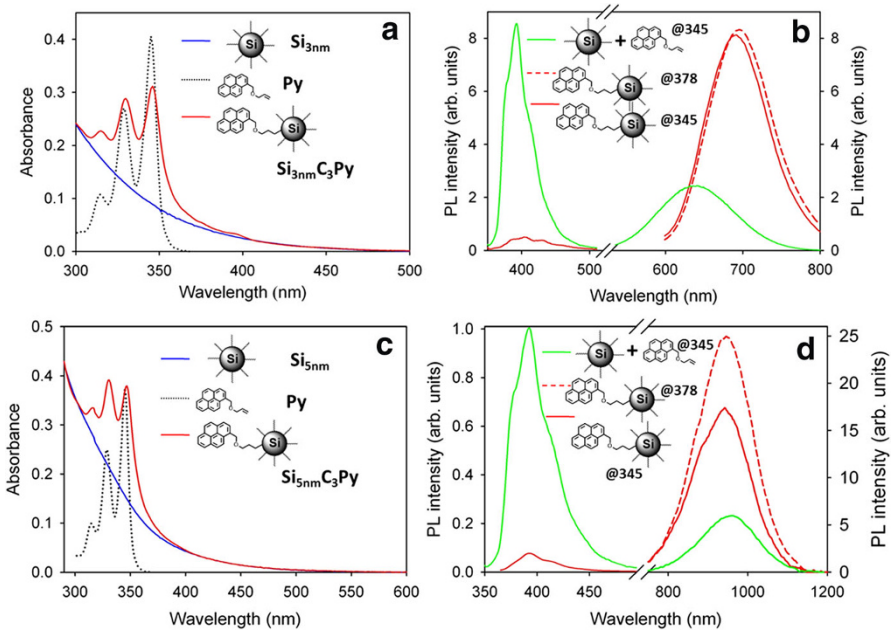

Fig. 7 Absorbance spectra of (**a**) 3 and (**c**) 5 nm diameter **Si_{xnm}** (*blue*), **$Si_{xnm}C_3Py$** (*red line*), and pyrene model compound (Py, *black dotted line*) in air-equilibrated toluene. Emission spectra of (**b**) 3 and (**d**) 5 nm diameter **$Si_{xnm}C_3Py$** (*solid red line*, $\lambda_{ex} = 345$ nm; *dashed red line*, $\lambda_{ex} = 378$ nm) and optically matched solutions of free pyrene mixed with **Si_{xnm}** in the appropriate ratio (*green lines*, $\lambda_{ex} = 345$ nm) in air-equilibrated toluene. In (**b**, **d**), the *y*-axis on the *left* corresponds to the pyrene-related emission, and the *y*-axis on the *right* corresponds to the SiNC-related emission Adapted from ref [32]

observed. From the analysis of these results, the estimated energy transfer efficiencies are 95 and 65 % for **$Si_{3nm}C_3Py$** and **$Si_{5nm}C_3Py$**, respectively [32]. The excitation spectra, measured by detecting only the long-wavelength and long-lived emission from the Si nanocrystals, exhibit a peaked pyrene-related band, demonstrating the occurrence of the energy transfer process.

The effect of the distance between the pyrene chromophore and the Si nanocrystal core on the energy transfer efficiency has been studied in detail in the systems **$Si_{x nm}C_{11}Py$** [42]. The optical properties of **$Si_{x nm}C_{11}Py$** dispersed in toluene at room temperature were compared to those of the corresponding alkyl functionalized nanocrystals (**$Si_{x nm}$**) and to those of **$Si_{x nm}C_3Py$**. As described for the previous example, from the absorption spectra, it was possible to estimate that there are, on average, 3.5 and 50 pyrene chromophores attached to each 3 and 5 nm nanocrystal, respectively. Upon excitation of the pyrene chromophores of **Si_{3nm}-$C_{11}Py$** at 345 nm, a very weak pyrene emission is observed with maximum at 390 nm (solid red line in Fig. 8), resulting in a quenching efficiency of 90 %. Moreover, the shape of the emission band is different from that of pyrene: **$Si_{3nm}C_{11}Py$** displays a shoulder at 470 nm, which is typical of an excimer emission [60]. The excimer emission was not present for the shorter chain **$Si_{x nm}C_3Py$** (Fig. 7b, d) since, in that case, the pyrene chromophores are embedded within the dodecyl ligand layer on the nanocrystals. On the other hand, the longer C_{11} tether places the **Py** units far enough away from the dodecene monolayer that an electronically excited pyrene can interact with a nearby pyrene in the ground state. The estimated energy transfer efficiencies were 70 % for **$Si_{3nm}C_{11}Py$** and 30 % for

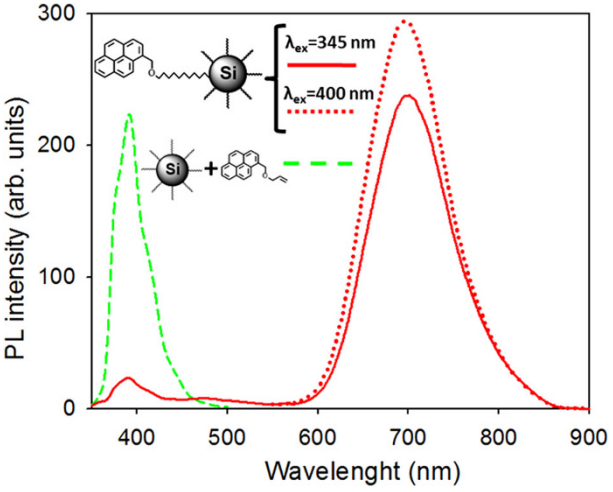

Fig. 8 Emission spectra of **$Si_{3nm}C_{11}Py$** in air-equilibrated toluene, recorded with two different excitation wavelengths (*solid red line*, $\lambda_{ex} = 345$ nm; *dotted red line*, $\lambda_{ex} = 400$ nm) to photoexcite either the pyrene or the silicon core, respectively. The measurements were made with the dispersion concentration adjusted to optically match the amount of absorbed light under each excitation condition. For comparison, the emission spectrum for a mixture of SiNC and Py in the proper ratio is shown as a *dashed green line* ($\lambda_{ex} = 345$ nm). Adapted from Ref. [42]

$Si_{5nm}C_{11}Py$. The sensitization efficiency is lower than that observed for the **$Si_{xnm}C_3Py$** because of the longer average distance between pyrene and Si core which slows down the energy transfer process. On the other hand, the quenching efficiency of pyrene is only slightly lower than in **$Si_{xnm}C_3Py$** because, in the case of **$Si_{xnm}C_{11}Py$**, the radiative decay of the fluorescent pyrene monomer excited state competes not only with the intramolecular non-radiative decay and the energy transfer process but also with excimer formation.

The observation of excimer formation for pyrene units in **$Si_{xnm}C_{11}Py$** indicates that the **Py** is exposed significantly to the surroundings and it is well known that pyrene interacts strongly with carbon allotropes by π–π stacking [61]. Starting from these premises, the interactions between **$Si_{xnm}C_{11}Py$** and C_{60}, carbon nanotubes and graphene have been explored. Titration of a **$Si_{xnm}C_{11}Py$** toluene solution with C_{60} leads to a decrease in SiNC emission and a concomitant decrease of the lifetime. The linearity of the Stern–Volmer plot— i.e. the ratio of the lifetimes in the absence (τ_0) and presence of C_{60} (τ) as a function of C_{60} concentration—suggests a dynamic quenching process: [60] **$Si_{3nm}C_{11}Py$** interacts with C_{60} only in the excited state and not in the ground state.

Upon addition of single-walled carbon nanotubes (SWCNTs) to a sample of **$Si_{3nm}C_{11}Py$** in air-equilibrated toluene, the emission intensity of the silicon core at 700 nm decreases with no change of the corresponding lifetime. This result is in line with a static quenching [60], in which the **$Si_{3nm}C_{11}Py$** and SWCNTs are associated in the ground state thanks to π–π stacking. Further confirmation of the ground state interaction is provided by high-resolution TEM and scanning transmission high-angle annular dark field analyses, which show that nanocrystals are preferentially located on the SWCNTs rather than on the carbon film-coated copper grid.

To investigate the interaction of **$Si_{3nm}C_{11}Py$** with graphene, a graphene film grown by chemical vapor deposition (CVD) was soaked in a solution of the nanocrystal. The nanocrystals form a uniformly dispersed monolayer of nanoparticles, without the formation of thick aggregates (Fig. 9a). The emission of **$Si_{3nm}C_{11}Py$** is significantly lower in intensity on the graphene layer, as evidenced by both the emission spectrum and the wide-field luminescence image reported in Fig. 9b. The different emission intensity registered on quartz and graphene is ascribed to a quenching mechanism from the SiNC to the graphene. The luminescence lifetimes registered on quartz and graphene are similar, as expected for a static quenching (see previous discussion on SWCNT).

3.2 Visible Absorbing Dyes

Blue-emitting amine-terminated SiNC (average diameter = 1.6 nm) were functionalized by a Ru(II) polypyridine complex (Fig. 10) using standard amine-*N*-hydroxysuccinimidyl ester coupling reaction conditions [44]. Si nanoparticles were synthesized by reduction of silicon halides (Sect. 2) and protected by amine-terminated alkyl chains attached by a Pt-catalysed reaction. The distance between the dye and the Si core is controlled by different alkyl chain lengths ($-C_3H_6$, $-C_6H_{12}$, and $-C_{11}H_{22}$). These SiNCs exhibit an additive absorption of both constituents, silicon core and Ru(II) complex. The emission spectra consist of two

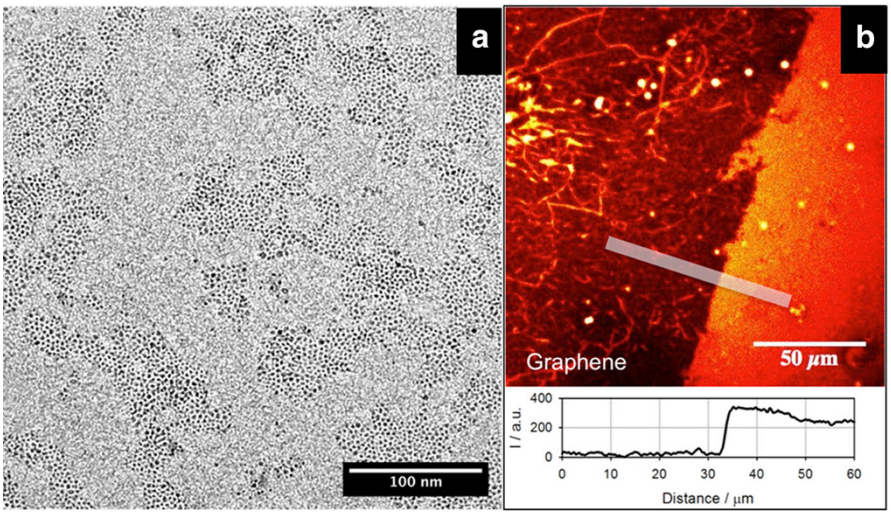

Fig. 9 **a** Low-magnification TEM micrographs of $\mathbf{Si_{3nm}C_{11}Py}$ deposited on CVD graphene. **b** Wide-field luminescence microscope image of $\mathbf{Si_{3nm}C_{11}Py}$ deposited on quartz and graphene-coated quartz. The image shows the graphene film edge. **c** Emission intensity profile registered by wide-field luminescence microscopy along the *white line* in (**a**). Reprinted with permission from Mazzaro et al. [42] copyright 2015, American Chemical Society

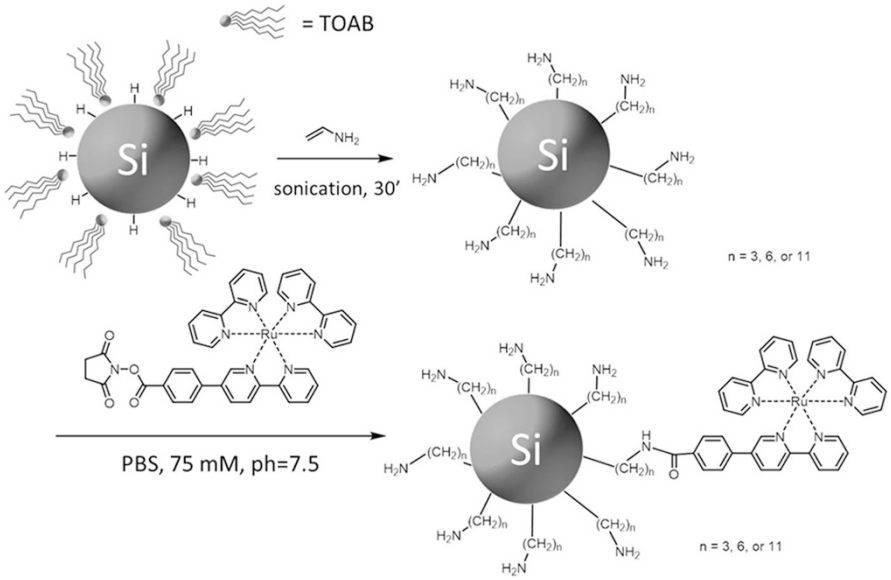

Fig. 10 Amine-terminated SiNC co-functionalized with a Ru(II) polypyridine complex [44]

distinct peaks upon excitation at 360 nm: one in the blue part (centered at ~460 nm, typical of SiNCs produced by this synthetic approach) and one in the red part of the optical spectrum (~630 nm, typical of the Ru(II) complex). The

emission of the SiNCs around 460 nm is quenched to a lower degree when the distance between the SiNC and the Ru(II) complex is longer and the sensitization of the complex at 630 nm is concomitantly reduced, as expected. By steady-state and time-resolved emission measurements, the efficiency of energy transfer was estimated to be 55, 18 and 8 % upon increasing the length of the alkyl spacer from $–C_3H_6$ to $–C_{11}H_{22}$. Assuming a Förster-type mechanism of energy transfer [60] and fixed distances between the SiNC core and the Ru(II) center, the calculated Förster distance R_0 is 28 Å. On the basis of this value, and using the distances between the center of the nanocrystal and the Ru(II) ion for R, the calculated energy transfer rates show a much stronger dependence over the distance, compared to the observed experimental trend. As suggested by the authors, this deviation can be attributed to the actual distance between the two chromophores, which is shorter than the calculated one because of the flexibility of alkyl chain linkers.

Two families of silicon nanocrystals with different average diameters of 3 and 5 nm have been decorated with a mixed capping layer of dodecyl and Zn(II) tetraphenylporphyrin (Fig. 11) [43]. This example is reported to demonstrate the photoinduced interaction between the organic chromophores and the silicon core to obtain a visible light-harvesting antenna exhibiting a long-lived emission in the near-infrared (NIR) spectral region. The choice of the chromophore was dictated by the excellent photophysical properties of zinc porphyrins, which are fluorescent and strongly absorbing in the visible region.

The synthesis of the two families of SiNCs (3 nm and 5 nm) was made via thermal disproportionation of hydrogen silsesquioxane (see Sect. 2 and Fig. 2 for more details), followed by thermal hydrosilylation with dodecene and Zn(II) tetraphenylporphyrin appended with an alkene group (**P** in Fig. 11), hereafter called $\mathbf{Si_{xnm}P}$. The absorption spectra of the two systems show the typical porphyrin bands at 426 and 560 nm superimposed onto the characteristic tail of the silicon core. This demonstrates that there is no significant interaction between porphyrin and silicon core in the ground state. On the basis of the molar absorption coefficients, the number of porphyrin units attached to each Si nanocrystal can be estimated in 1 and 10 porphyrins per nanocrystal for $\mathbf{Si_{3nm}P}$ and $\mathbf{Si_{5nm}P}$, respectively. The investigated hybrid materials contain two luminescent units: the porphyrin chromophore, which

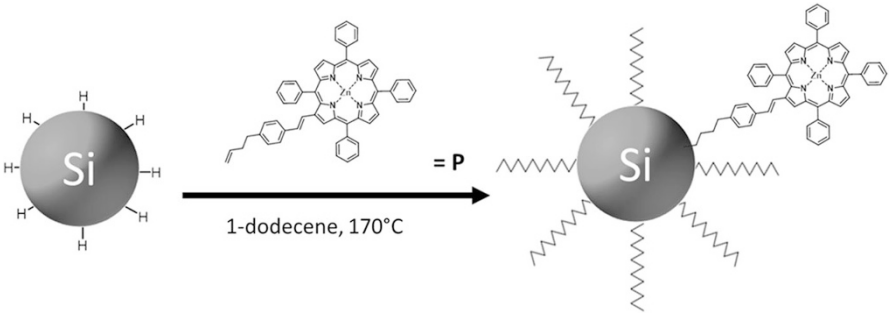

Fig. 11 Synthetic procedure for the SiNC co-passivated with tetraphenylporphyrin-Zn(II) and 1-dodecene [43]

is characterized by a structured fluorescence band with maximum at 604 and 655 nm, and the silicon core with emission peaks at 650 nm ($\mathbf{Si_{3nm}}$) and 920 nm ($\mathbf{Si_{5nm}}$). Intramolecular energy transfer experiments carried out for a toluene dispersion of $\mathbf{Si_{3nm}P}$ were not easy to rationalize because of the superposition of the two emission bands. However, the shortening of the lifetime of the fluorescent excited state of porphyrin (from 2.4 ns for the free dye to 1.2 ns for $\mathbf{Si_{3nm}P}$) evidenced the presence of a quenching process with ca. 50 % efficiency. Upon excitation at 427 nm, where most of the light is absorbed by the porphyrin (Soret band), $\mathbf{Si_{5nm}P}$ exhibits two emission bands: one with maximum at 655 nm typical of the porphyrin fluorescence and one peaking at 905 nm due to the SiNC emission. The intensity decay at 655 nm exhibits a lifetime of 1.2 ns, shorter than that of the free **P** (2.3 ns). This result is in agreement with the quenching of the emission quantum yield. The excitation spectrum of $\mathbf{Si_{5nm}P}$ shows the typical excitation band of the porphyrin peaked at 425 nm superimposed on the tail of the SiNCs. It has been observed that the emission quantum yield of the SiNC in the NIR is lower for $\mathbf{Si_{5nm}P}$ (0.08) compared to $\mathbf{Si_{5nm}}$ (0.42). This decrease can be due to the presence of a larger number of defects in the presence of the bulky porphyrin chromophores or to an additional quenching process, such as photoinduced electron transfer, but the authors could not discriminate between these two hypotheses. In the same paper, functionalization with another porphyrin dye is reported and the photophysical behavior is very similar with the results reported above [43].

4 Conclusions

Chromophores can be covalently attached to SiNCs to enhance their light absorption, and energy transfer from photoexcited chromophores to SiNCs has now been confirmed in at least a few different systems [32, 42, 43]. Chromophores have been attached to SiNCs without significant degradation of their optical properties, and strong enhancements in luminescence brightness have been observed. One challenge is now to obtain a deeper insight into the mechanism of energy transfer between the chromophores and the silicon core, in order to study the distance-dependence for systems in which dyes and SiNCs are held at a fixed distance by a rigid linker or by encapsulating in a rigid innocent matrix. This deeper understanding will enable the construction of more efficient light-harvesting antennae. Another outstanding challenge is then to design chromophores with strong light absorption near the absorption edge of the nanocrystals in order to minimize the apparent Stokes shift between the photoexcitation wavelength and the emission wavelength. This is important for in vivo biological imaging applications that might require photoexcitation with red or NIR light (as opposed to blue or green).

Acknowledgment We gratefully acknowledge the European Commission ERC Starting Grant (PhotoSi, 278912).

References

1. Blankenship RE (2002) Molecular mechanisms of photosynthesis. Blackwell, Oxford
2. Serin JM, Brousmiche DW, Fréchet JMJ (2002) A FRET-based ultraviolet to near-infrared frequency converter. J Am Chem Soc 124:11848–11849. doi:10.1021/ja027564i
3. Miller RA, Presley AD, Francis MB (2007) Self-assembling light-harvesting systems from synthetically modified tobacco mosaic virus coat proteins. J Am Chem Soc 129:3104–3109. doi:10.1021/ja063887t
4. Frischmann PD, Mahata K, Wurthner F (2013) Powering the future of molecular artificial photosynthesis with light-harvesting metallosupramolecular dye assemblies. Chem Soc Rev 42:1847–1870. doi:10.1039/C2CS35223K
5. Puntoriero F, Sartorel A, Orlandi M et al (2011) Photoinduced water oxidation using dendrimeric Ru(II) complexes as photosensitizers. Coord Chem Rev 255:2594–2601. doi:10.1016/j.ccr.2011.01.026
6. Voegtle F, Gestermann S, Kauffmann C et al (2000) Coordination of Co2 + ions in the interior of poly(propylene amine) dendrimers containing fluorescent dansyl units in the periphery. J Am Chem Soc 122:10398–10404
7. Hwang S-H, Moorefield CN, Newkome GR (2008) Dendritic macromolecules for organic light-emitting diodes. Chem Soc Rev 37:2543–2557. doi:10.1039/B803932C
8. Tang M-C, Tsang DP-K, Chan MM-Y et al (2013) Dendritic luminescent Gold(III) complexes for highly efficient solution-processable organic light-emitting devices. Angew Chem Int Ed 52:446–449. doi:10.1002/anie.201206457
9. Ceroni P (2011) Energy up-conversion by low-power excitation: new applications of an old concept. Chem Eur J 17:9560–9564. doi:10.1002/chem.201101102
10. Balzani V, Bergamini G, Ceroni P, Marchi E (2011) Designing light harvesting antennas by luminescent dendrimers. New J Chem 35:1944–1954. doi:10.1039/C1NJ20142E
11. Balzani V, Ceroni P, Maestri M, Vicinelli V (2003) Light-harvesting dendrimers. Curr Opin Chem Bio 7:657–665. doi:10.1016/j.cbpa.2003.10.001
12. Li W-S, Aida T (2009) Dendrimer porphyrins and phthalocyanines. Chem Rev 109:6047–6076. doi:10.1021/cr900186c
13. Ceroni P, Credi A, Venturi M (2014) Light to investigate (read) and operate (write) molecular devices and machines. Chem Soc Rev 43:4068. doi:10.1039/c3cs60400d
14. Calzaferri G (2012) Nanochannels: hosts for the supramolecular organization of molecules and complexes. Langmuir 28:6216–6231. doi:10.1021/la3000872
15. Leem G, Morseth ZA, Puodziukynaite E et al (2014) Light harvesting and charge separation in a π-conjugated antenna polymer bound to TiO_2. J Phys Chem C 118:28535–28541. doi:10.1021/jp5113558
16. Winiger CB, Li S, Kumar GR et al (2014) Long-distance electronic energy transfer in light-harvesting supramolecular polymers. Angew Chem Int Ed 53:13609–13613. doi:10.1002/anie.201407968
17. Pu F, Wu L, Ran X et al (2015) G-quartet-based nanostructure for mimicking light-harvesting antenna. Angew Chem Int Ed 54:892–896. doi:10.1002/anie.201409832
18. Woller JG, Hannestad JK, Albinsson B (2013) Self-assembled nanoscale DNA–porphyrin complex for artificial light harvesting. J Am Chem Soc 135:2759–2768. doi:10.1021/ja311828v
19. Garo F, Häner R (2012) A DNA-based light-harvesting antenna. Angew Chem Int Ed 51:916–919. doi:10.1002/anie.201103295
20. McVey BFP, Tilley RD (2014) Solution synthesis, optical properties, and bioimaging applications of silicon nanocrystals. Acc Chem Res 47:3045–3051. doi:10.1021/ar500215v
21. Mastronardi ML, Henderson EJ, Puzzo DP, Ozin GA (2012) Small silicon, big opportunities: the development and future of colloidally-stable monodisperse silicon nanocrystals. Adv Mater 24:5890–5898. doi:10.1002/adma.201202846
22. Gonzalez CM, Iqbal M, Dasog M et al (2014) Detection of high-energy compounds using photoluminescent silicon nanocrystal paper based sensors. Nanoscale 6:2608–2612. doi:10.1039/C3NR06271F
23. Yi Y, Zhu G, Liu C et al (2013) A label-free silicon quantum dots-based photoluminescence sensor for ultrasensitive detection of pesticides. Anal Chem 85:11464–11470. doi:10.1021/ac403257p

24. Hessel CM, Reid D, Panthani MG et al (2012) Synthesis of ligand-stabilized silicon nanocrystals with size-dependent photoluminescence spanning visible to near-infrared wavelengths. Chem Mater 24:393–401. doi:10.1021/cm2032866
25. Hodes G (2007) When small is different: some recent advances in concepts and applications of nanoscale phenomena. Adv Mater 19:639–655. doi:10.1002/adma.200601173
26. Kovalev D, Diener J, Heckler H et al (2000) Optical absorption cross sections of Si nanocrystals. Phys Rev B 61:4485–4487
27. Algar WR, Kim H, Medintz IL, Hildebrandt N (2014) Emerging non-traditional Förster resonance energy transfer configurations with semiconductor quantum dots: investigations and applications. Coord Chem Rev 263–264:65–85. doi:10.1016/j.ccr.2013.07.015
28. Medintz IL, Mattoussi H (2009) Quantum dot-based resonance energy transfer and its growing application in biology. Phys Chem Chem Phys 11:17–45. doi:10.1039/B813919A
29. Enghag P (2004) Encyclopedia of the Elements: technical data-history-processing-applications. In: Encyclopedia of the Elements: Technical Data - History - Processing - Applications. Wiley, Weinheim
30. Buriak JM (2014) Illuminating silicon surface hydrosilylation: an unexpected plurality of mechanisms. Chem Mater 26:763–772. doi:10.1021/cm402120f
31. Kelly JA, Henderson EJ, Veinot JGC (2010) Sol-gel precursors for group 14 nanocrystals. Chem Commun 46:8704–8718. doi:10.1039/C0CC02609C
32. Locritani M, Yu Y, Bergamini G et al (2014) Silicon nanocrystals functionalized with pyrene units: efficient light-harvesting antennae with bright near-infrared emission. J Phys Chem Lett 5:3325–3329. doi:10.1021/jz501609e
33. Rowland CE, Hannah DC, Demortière A et al (2014) Silicon nanocrystals at elevated temperatures: retention of photoluminescence and diamond silicon to β-silicon carbide phase transition. ACS Nano 8:9219–9223. doi:10.1021/nn5029967
34. Zhou Z, Brus L, Friesner R (2003) Electronic structure and luminescence of 1.1- and 1.4-nm silicon nanocrystals: oxide shell versus hydrogen passivation. Nano Lett 3:163–167. doi:10.1021/nl025890q
35. Beard MC, Knutsen KP, Yu P et al (2007) Multiple exciton generation in colloidal silicon nanocrystals. Nano Lett 7:2506–2512. doi:10.1021/nl071486l
36. Gu L, Hall DJ, Qin Z et al (2013) In vivo time-gated fluorescence imaging with biodegradable luminescent porous silicon nanoparticles. Nat Commun 4:2326. doi:10.1038/ncomms3326
37. Cheng X, Lowe SB, Reece PJ, Gooding JJ (2014) Colloidal silicon quantum dots: from preparation to the modification of self-assembled monolayers (SAMs) for bio-applications. Chem Soc Rev 43:2680. doi:10.1039/c3cs60353a
38. Dasog M, Kehrle J, Rieger B, Veinot JGC (2015) Silicon nanocrystals and silicon-polymer hybrids: synthesis, surface engineering, and applications. Angew Chem Int Ed. doi:10.1002/anie.201506065
39. Sommer A, Cimpean C, Kunz M et al (2011) Ultrafast excitation energy transfer in vinylpyridine terminated silicon quantum dots. J Phys Chem C 115:22781–22788. doi:10.1021/jp206495j
40. Groenewegen V, Kuntermann V, Haarer D et al (2010) Excited-state relaxation dynamics of 3-vinylthiophene-terminated silicon quantum dots. J Phys Chem C 114:11693–11698. doi:10.1021/jp100266w
41. Wang G, Ji J, Xu X (2014) Dual-emission of silicon quantum dots modified by 9-ethylanthracene. J Mater Chem C 2:1977. doi:10.1039/c3tc32318h
42. Mazzaro R, Locritani M, Molloy JK et al (2015) Photoinduced processes between pyrene-functionalized silicon nanocrystals and carbon allotropes—SI. Chem Mater 27:4390–4397. doi:10.1021/acs.chemmater.5b01769
43. Fermi A, Locritani M, Carlo D et al (2015) Light-harvesting antennae based on photoactive silicon nanocrystals functionalized with porphyrin chromophores. Faraday Discuss 00:1–15. doi:10.1039/c5fd00098j
44. Rosso-Vasic M, DeCola L, Zuilhof H (2009) Efficient energy transfer between silicon nanoparticles and a Ru-polypyridine complex. J Phys Chem C 113:2235–2240. doi:10.1021/jp804623w
45. Hessel CM, Henderson EJ, Veinot JGC (2006) Hydrogen silsesquioxane: a molecular precursor for nanocrystalline Si-SiO_2 composites and freestanding hydride-surface-terminated silicon nanoparticles. Chem Mater 18:36139–36146. doi:10.1021/cm602803
46. Yu Y, Bosoy CA, Hessel CM et al (2013) Silicon nanocrystal superlattices. ChemPhysChem 14:84–87. doi:10.1002/cphc.201200738
47. Yu Y, Bosoy CA, Smilgies DM, Korgel BA (2013) Self-assembly and thermal stability of binary superlattices of gold and silicon nanocrystals. J Phys Chem Lett 4:3677–3682. doi:10.1021/jz401964s

48. Knipping J, Wiggers H, Rellinghaus B et al (2004) Synthesis of high purity silicon nanoparticles in a low pressure microwave reactor. J Nanosci Nanotechnol 4:1039–1044. doi:10.1166/jnn.2004.149
49. Tilley RD, Warner JH, Yamamoto K et al (2005) Micro-emulsion synthesis of monodisperse surface stabilized silicon nanocrystals. Chem Commun (Camb). doi:10.1039/b416069j
50. Rosso-Vasic M, Spruijt E, Van Lagen B et al (2008) Alkyl-functionalized oxide-free silicon nanoparticles: synthesis and optical properties. Small 4:1835–1841. doi:10.1002/smll.200800066
51. Dasog M, Yang Z, Regli S et al (2013) Chemical insight into the origin of red and blue photoluminescence arising from freestanding silicon nanocrystals. ACS Nano 7:2676–2685. doi:10.1021/nn4000644
52. Tsybeskov L, Vandyshev JV, Fauchet PM (1994) Blue emission in porous silicon: oxygen-related photoluminescence. Phys Rev B 49:7821–7824
53. Petkov V, Hessel CM, Ovtchinnikoff J et al (2013) Structure-properties correlation in Si nanoparticles by total scattering and computer simulations. Chem Mater 25:2365–2371. doi:10.1021/cm401099q
54. Liu N, Chen H-Z, Chen F, Wang M (2008) Förster resonance energy transfer from poly(9-vinyl carbazole) to silicon nanoparticles in their composite films. Chem Phys Lett 451:70–74. doi:10.1016/j.cplett.2007.11.057
55. Erogbogbo F, Chang C-W, May J et al (2012) Energy transfer from a dye donor to enhance the luminescence of silicon quantum dots. Nanoscale 4:5163. doi:10.1039/c2nr31003a
56. Dasog M, De Los Reyes GB, Titova LV et al (2014) Size vs surface: tuning the photoluminescence of freestanding silicon nanocrystals across the visible spectrum via surface groups. ACS Nano 8:9636–9648. doi:10.1021/nn504109a
57. Dohnalová K, Gregorkiewicz T, Kůsová K (2014) Silicon quantum dots: surface matters. J Phys: Condens Matter 26:173201. doi:10.1088/0953-8984/26/17/173201
58. Li Q, He Y, Chang J, Wang L, Chen H, Tan Y-W, Wang H, Shao Z (2013) Surface-modified silicon nanoparticles with ultrabright photoluminescence and single-exponential decay for nanoscale fluorescence lifetime imaging of temperature. J Am Chem Soc 135:14924–14927
59. Zhou T, Anderson RT, Li H et al (2015) Bandgap tuning of silicon quantum dots by surface functionalization with conjugated organic groups. Nano Lett 15:3657–3663. doi:10.1021/nl504051x
60. Balzani V, Ceroni P, Juris A (2014) Photochemistry and photophysics: concepts, research, applications. Wiley, Weinheim
61. Star A, Liu Y, Grant K, Ridvan L, Stoddart JF, Steuerman DW, Diehl MR, Boukai A, Heath JR (2003) Noncovalent side-wall functionalization of single-walled carbon nanotubes. Macromolecules 36:553–560. doi:10.1021/ma021417n
62. Ondic L, Kusova K, Ziegler M et al (2014) A complex study of the fast blue luminescence of oxidized silicon nanocrystals: the role of the core. Nanoscale 6:3837–3845. doi:10.1039/C3NR06454A

Top Curr Chem (Z) (2016) 374:48
DOI 10.1007/s41061-016-0049-8

REVIEW

Luminescent Rare-earth-based Nanoparticles: A Summarized Overview of their Synthesis, Functionalization, and Applications

Alberto Escudero[1,2] · Carolina Carrillo-Carrión[3] · Mikhail V. Zyuzin[1] · Wolfgang J. Parak[1,3]

Received: 15 March 2016 / Accepted: 24 June 2016 / Published online: 19 July 2016

Abstract Rare-earth-based nanoparticles are currently attracting wide research interest in material science, physics, chemistry, medicine, and biology due to their optical properties, their stability, and novel applications. We present in this review a summarized overview of the general and recent developments in their synthesis and functionalization. Their luminescent properties are also discussed, including the latest advances in the enhancement of their emission luminescence. Some of their more relevant and novel biomedical, analytical, and optoelectronic applications are also commented on.

Keywords Luminescence · Nanoparticles · Rare earths · Synthesis · Bioimaging · Biosensing

1 Introduction, Chemical Composition, Luminescent Properties

Rare-earth (RE)-based nanoparticles (NPs) constitute one type of luminescent materials available in the literature. RE-based nanophosphors exhibit important advantages compared with the other available luminescent materials due to their lower toxicity, photostability, high thermal and chemical stability, high

This article is part of the Topical Collection "Photoactive Semiconductor Nanocrystal Quantum Dots", edited by "Alberto Credi".

✉ Alberto Escudero
alberto.escudero@csic.es

[1] AG Biophotonik, Fachbereich Physik, Philipps-Universität Marburg, Renthof 7, 35037 Marburg, Germany

[2] Instituto de Ciencia de Materiales de Sevilla, CSIC, Universidad de Sevilla, C. Américo Vespucio 49, E-41092 Seville, Spain

[3] CIC biomaGUNE, Paseo Miramón 182, E-20009 San Sebastian, Spain

luminescence quantum yield, and sharp emission bands [1]. These nanophosphors usually consist of a host inorganic matrix doped with luminescent lanthanide (Ln) cations. The final characteristic properties of the nanophosphors are highly influenced by both the inorganic matrix and the dopant. Fluoride matrices are used due to their low vibrational energies, which minimize the quenching of the exited state of the Ln cations and result in a higher quantum efficiency of luminescence [2–4]. Phosphate-based matrices attract interest for their high biocompatibility and good biodegradability [5]. Other matrices such as vanadates, molybdates, and wolframates are used to enhance the global luminescent emission of the materials [6, 7], and some silicate-based matrices are appropriate for the production of persistent luminescent NPs [8, 9]. The election of the Ln cation or cations determines the final luminescent properties of the material. Luminescence is expected for most of the Ln^{3+} cations, but in practice most of the studies are focused on Eu^{3+}, Tb^{3+}/Ce^{3+}, Dy^{3+}, and Nd^{3+} cations, which produce red, green, yellow/orange luminescence, and near-infrared luminescence, respectively [10–14]. These cations are examples of the so-called downconversion (DC) luminescence (i.e. conventional Stokes type), in which higher energy photons are converted into lower energy photons. High research attention is attracted by upconverting nanoparticles (UCNPs), in which the sequential absorption of two or more photons leads to the emission of light at shorter wavelengths than the excitation wavelength (i.e. anti-Stokes type emission), which means that near infrared long-wavelength excitation radiation is converted into shorter visible wavelengths [15, 16]. Different mechanisms of upconversion luminescence have been reported for lanthanide-based materials. Excited-state absorption occurs for singly doped upconversion materials, and is based on a successive two-photon absorption of appropriate energy. Such absorption takes place via an excited metastable level, and the relaxation from the excited to the original ground state produces the upconversion luminescence. Such processes are highly inefficient, and low concentration of lanthanide dopants are normally required [17]. Much higher efficiencies (but still quite low) are observed in energy-transfer processes, in which an absorbing sensitizer cation and an emitting activator cation are required. Er^{3+}, Tm^{3+}, and Ho^{3+} codoped with Yb^{3+} are commonly used as upconverting luminescent cation pairs. Yb^{3+} normally acts as a sensitizer cation, given its large absorption cross-section and the resonance of its $^2F_{7/2} \rightarrow {}^2F_{5/2}$ transition with many f–f transition of other lanthanide cations [18]. After the absorption and energy transfer processes, the upconversion luminescence appears in the active cations by different mechanisms, including excited-state absorption, successive energy transfer, cross-relaxation upconversion, cooperative sensitization, and cooperative luminescence [19].

The main disadvantage of Ln-doped NPs is their relatively low global intensity luminescence, caused by the low absorptions of the parity forbidden Ln^{3+} 4f–4f transitions, and constituting a serious limitation for their use for different applications [20]. Different energy transfer schemes from the host materials to the Ln cations are employed to enhance the global luminescence of downconverting lanthanide-doped NPs, which include the use of vanadate or oxyfluoride matrices [21–25]. Despite their highly scientific interest, extremely low upconversion efficiencies (in the range of 10^{-5} to 1 %) are normally observed for UCNPs, which

depend also on the excitation laser power density, and on the material, size, and surface structure of the NPs [26–28]. Core/shell nanostructures, which minimize the surface quenching effects [29–32], as well as the association with organic near-infrared (NIR) dyes, which can alleviate the inherently weak and narrow near-infrared absorption of the Ln ions [33], are used to enhance the luminescence of such materials. However, laser excitation sources are still required to study these particles.

In this article the more recent and common methods of synthesis of luminescent NPs based on RE will be briefly summarized, as well as the different existing functionalization strategies. Some of their imaging, sensing, and optoelectronic applications based on their fluorescent properties will also be mentioned. For a deeper and more detailed description, some excellent reviews can be found in the recent literature [18, 19, 34–39].

2 Synthesis of Uniform Luminescent Nanoparticles

Thermal decomposition [40], coprecipitation [2, 41], cation exchange [42], and hydro (solvo) thermal synthesis have become popular routes for the preparation of monodisperse Ln-doped luminescent NPs. Among the latter routes, a general synthesis strategy based on a phase transfer and separation mechanism occurring at the interfaces of the liquid, solid, and solution (LSS) phases during the synthesis normally produces small Ln-doped inorganic NPs with a narrow particle size distribution, a high luminescence efficiency, and a high phase purity [43]. These syntheses are carried out in organic solvents (such as oleic or linoleic acids, ethanol, octadecene, eicosene, trioctylamine) in the presence of additives such as sodium oleate, sodium linoleate, trioctylphosphine oxide (TOPO), and stearic acid at high temperatures (200–400 °C) [44–46]. However, the hydrophobic nature of the resulting NPs requires a further step of surface modification to make them water-dispersible. Water-dispersible NPs with controlled size and shape can be synthesized by recently reported methods based on homogeneous precipitation in polyol-based solvents at moderate temperatures (120–180 °C). These strategies include an optimization of the different reaction parameters, such as solvents (including mixtures of them), precursors, concentrations, temperature, and presence of additives. Many different luminescent and uniform Ln-doped inorganic NPs, including fluorides [47–50], phosphates [51–54], and vanadates [23, 25] have been reported. Microwave-assisted methods in both water and polyol-based solvents have also been described, resulting in much shorter reaction times [55, 56]. Some examples of monodispersed Ln-doped NPs are shown in Fig. 1.

Recently, laser ablation of micrometric-sized powder Ln-doped particles has been used to produce Ln-doped NPs with a great control of their size and monodispersity [57].

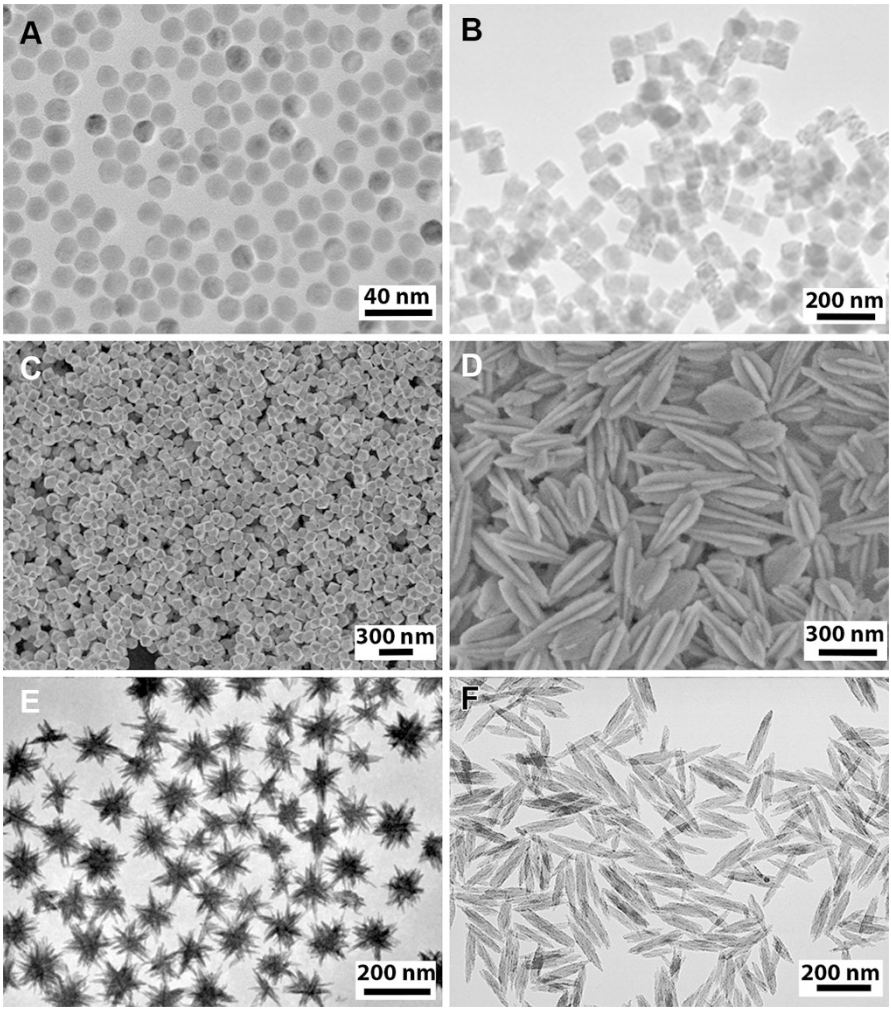

Fig. 1 **a** Ho^{3+}, Yb^{3+}-doped $NaGdF_4$ NPs synthesized in oleic acid and 1-octadecene at 340 °C. Taken from [46]. **b** Eu^{3+}-doped $GdPO_4$ nanocubes synthesized in butylene glycol at 120 °C, taken from [51]. **c** Eu^{3+}-doped α-BiO_yF_{3-2y} NPs with octahedral morphology synthesized in diethyleneglycol–water at 120 °C. Taken from [22]. **d** Dy^{3+}-doped $GdPO_4$ particles with a lance-shaped morphology synthesized in ethylene glycol–water at 180 °C. Taken from [52]. **e** Eu^{3+}-doped $BiPO_4$ nanostars synthesized in ethylene glycol-water in the presence of sodium citrate at 120 °C. Taken from [53]. **f** Eu^{3+}-doped calcium hydroxyapatite nanospindles synthesized in water at 180 °C in the presence of PAA. Taken from [55]

3 Functionalization and Colloidal Stability

A functionalization process is especially required for the biomedical use of NPs, and it is mandatory for non-water-dispersible NPs. Functionalization not only increases the colloidal stability of the NPs by introducing electrostatic and/or steric repulsions [58], but also provides anchors for adding functional ligands of biomedical interest such as antibodies, peptides, proteins, and some anticancer drugs [59]. Ligand exchange,

polymer encapsulation, and silica encapsulation are common strategies used for the stabilization in water of native hydrophobic NPs. In the ligand exchange method, the original hydrophobic ligands are completely displaced by hydrophilic ligands (i.e. PEG-type and polymeric ligands, and anions such as citrate and BF_4^-) on the NP surface [60, 61]. Ligand exchange methods typically offer NPs with smaller hydrodynamic diameters but suffer (for most NP materials) from limited colloidal stability. Polymer coating yields NPs that are very colloidally stable, but that normally show larger hydrodynamic radii [62]. In this strategy, the hydrophobically capped NPs are overcoated with amphiphilic polymers such as poly(isobutylene-*alt*-maleic anhydride) modified with dodecylamine (PMA), and its modifications with 4-(aminomethyl)pyridine (Py-PMA), and polyethylene glycol (PEG-PMA) [60, 63–66]. The hydrophobic portion of the polymer intercalates with the hydrophobic ligands on the NP surface, leaving the hydrophilic portion of the polymer exposed to solution [62]. Treatments with acids [67] or with excess of ethanol under ultrasonication [68] have also been used to remove the hydrophobic organic coating of the NPs, and the oleic acid ligands on the NPs can be oxidized with the Lemieux-von Rudloff reagent, yielding water-dispersible carboxylic acid-functionalized NPs [69].

The most convenient strategy of functionalization of hydrophilic Ln-doped NPs is the so-called one-pot synthesis, in which the functionalizing agent acts as an additive during the synthesis process. In some cases, their presence plays also a key role in the final morphology of the particles [55]. One-pot synthesis of luminescent Ln-doped NPs with aminocaproic and citric acid [70], poly-ethylenimine (PEI) [71] and poly acrylic acid (PAA) [23, 25, 49] have been recently reported in the literature. Functionalization of Ln-doped NPs can also be carried out in a second step with agents such as dextran-based polymers [23, 48]. The layer-by-layer (LbL) approach, which is based on the electrostatic deposition of layers of polyelectrolytes with alternating charge on the surface of the particles [72], has also been used for the functionalization of RE fluoride [60, 73] and vanadate NPs [74]. However, NPs functionalized in a second step normally show a worse colloidal stability when compared with the one-pot synthesized NPs [74]. Silica-shell encapsulation (i.e. the growth of a silica shell around the NP) is used to functionalize both hydrophobic and hydrophilic NPs [75]. The reverse microemulsion method can be applied for hydrophobic NPs [76], whereas the standard Stöber procedure is used for hydrophilic NPs, which in some cases do have to be previously stabilized with agents such as polyvinylpyrrolidone (PVP) of PEG-based ligands [77, 78]. This functionalization process shows some advantages, given the SiO_2 high biocompatibility and possible further surface chemistry, which can be used to link different molecules of biomedical interest. A summary of some possible functionalization strategies is shown in Fig. 2.

4 Bioimaging Applications

Both downconverting and upconverting Ln-doped NPs can be used for fluorescent bioimaging applications. The features of such particles are highly influenced by their optical and luminescent properties, as previously reported [1]. Ln-doped NPs show some advantages when compared with other available luminescent

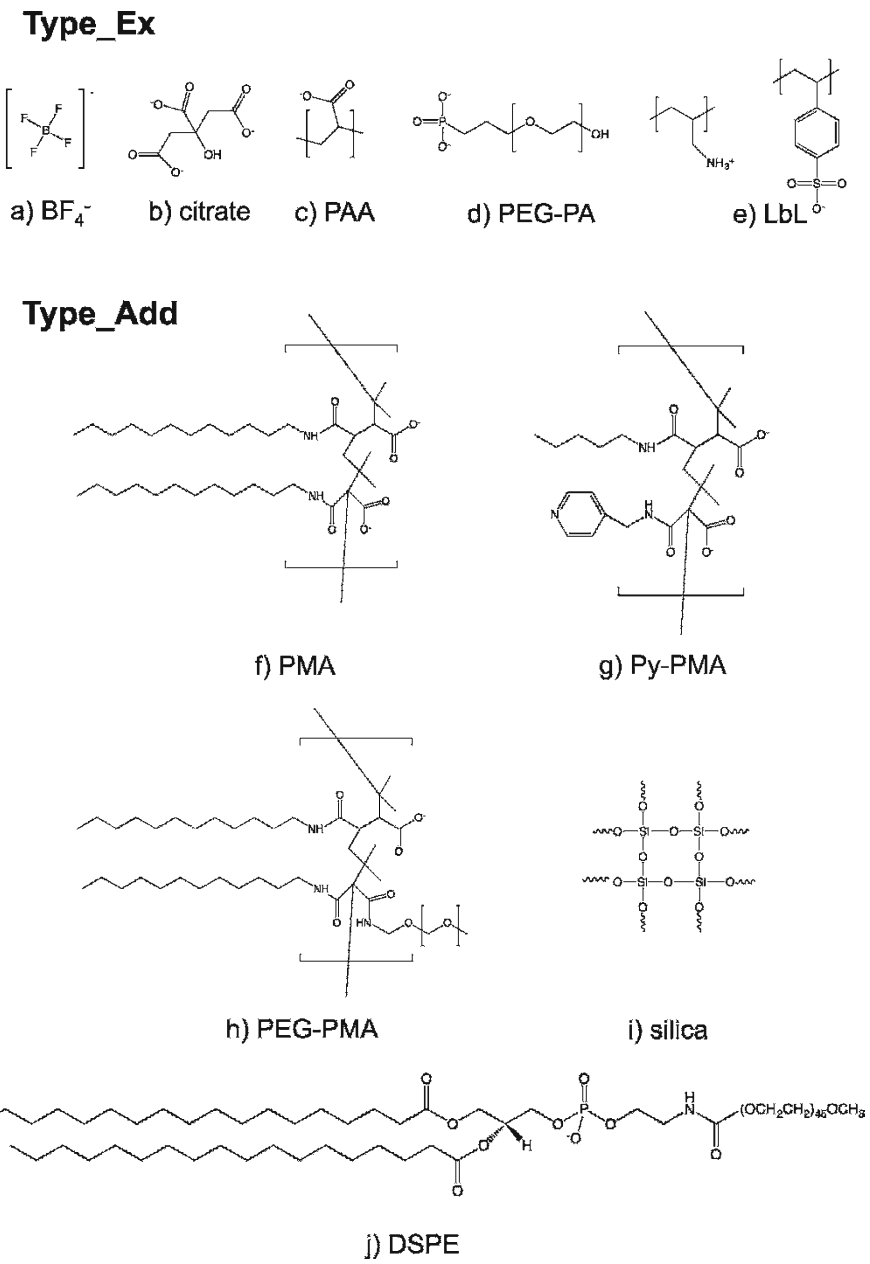

nanomaterials, such as their low photobleaching, nonblinking (i.e. they do not show intermittent emission), high efficiencies (for downconversion of NPs), possibility of multifunctional and multimodal imaging, and sharp emission lines, which prevents possible interferences [19]. Moreover, they can even be used for long-term imaging due to their photostability [79]. The sharp and specific bands of the direct excitation

◀ **Fig. 2** Overview of general strategies for surface modification of Ln-doped NPs. The modifications can be classified into two categories: **a–e** ligand exchange methods (Type_Ex); **f–j** addition of an amphiphilic layer or silica coating (Type_Add). Examples of Type_Ex modifications include coating with: **a** tetrafluoroborate (BF_4^-); **b** trisodium citrate (citrate); **c** poly(acrylic acid) (PAA); **d** poly(ethylene-oxide)-10-OH with a terminal phosphate ester (PEG-PA); **e** layer-by-layer coating (LbL) with poly(allylamine hydrochloride) (PAH) and poly(sodium 4-styrenesulfonate) (PSS) on an initial citrate layer. Examples of Type_Add modifications are coating with: **f** poly(isobutylene-*alt*-maleic anhydride) modified with dodecylamine (PMA); **g** poly(isobutylene-*alt*-maleic anhydride) modified with pentylamine and 4-(aminomethyl)pyridine (Py-PMA); **h** the same as **f** but with further modification with α-methoxy-ω-amino poly(ethylene glycol)-1200 (PEG-PMA); **i** silica coating with a shell thickness of ~5 nm (silica); **j** 1,2-distearoyl-*sn*-glycero-3-phospho-ethanolamine-*N*-[methoxy(poly-ethylene glycol)-2000] (ammonium salt) (DSPE). Taken from [60] with modifications

of the Ln-doped NPs constitute, however, a limitation, since specific equipment and appropriate laser wavelengths for the excitation are normally required. The main disadvantage of the use of Ln-doped NPs for fluorescent bioimaging applications relies on their low global luminescent emission. For the DC nanophosphors, the direct excitation of the Ln^{3+} cations (which normally consists of narrow and low absorbance bands, the more intense occurring at 393 nm for Eu^{3+}, 349 and 366 nm for Tb^{3+}, and 349 nm for Dy^{3+}) is normally not enough to produce intense luminescence. As mentioned above, this can be overcome though an indirect excitation through the matrix, but ultraviolet excitations radiations are still required, which in some ways can be harmful for the cells.

Recently, Eu^{3+}, Bi^{3+} codoped $REVO_4$ (RE = Y, Gd) NPs have been proposed for in-vitro fluorescent bioimaging applications (Fig. 3). The incorporation of Bi^{3+} into the $REVO_4$ structure shifts the original absorption band corresponding to the vanadate toward longer wavelengths, yielding nanophosphors excitable by near-ultraviolet and visible light [74]. More studies can be found in the literature regarding UCNPs, since the use of near-infrared light for excitation avoids photodamage and background fluorescence in biological systems, and enables a higher penetration depth into biological tissue, despite their very low quantum yield efficiencies [38]. These features make them highly attractive for luminescent bioimaging applications, both in vitro and in vivo [80–84] (Fig. 4).

5 Sensing and Analytical Applications

Application of Ln-doped NPs for sensing can be roughly divided into two classes: one is the directly observed luminescence from the Ln-doped NPs, and the other is based on energy transfer, and/or reabsorption processes, including fluorescence resonance energy transfer (FRET) and lanthanide-based resonance energy transfer (LRET).

An important feature of Ln-doped NPs for using their direct intrinsic fluorescence is that they present multiple emission lines, which allows ratiometric measurements because normally some of them are analytically sensitive, while others are insensitive and serve as reference signals [85]. In other cases, the emission corresponding to the Ln^{3+} can be considered as insensitive, and the functionalization of the NPs with fluorophores whose intensity is affected by the presence of the

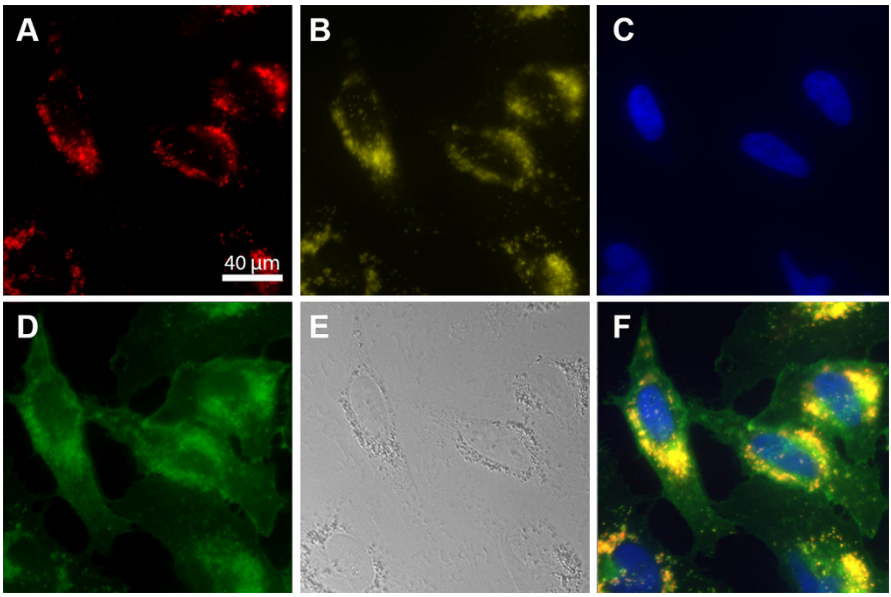

Fig. 3 Fluorescence images of HeLa cells incubated with Eu^{3+}, Bi^{3+}-doped YVO_4 NPs for 24 h. **a** *Red* channel, NPs ($\lambda_{ex} = 340 \pm 26$ nm; $\lambda_{em} > 600$ nm); **b** *yellow* channel, lysosomes; **c** *blue* channel, cell nuclei; **d** *green* channel, cell membranes; **e** transmission image, and **f** merged image. The fluorescent signal of **b**, **c**, and **d** occurs due to immunostaining of cells with organelle-specific reagents. Taken from [74]

analyte allows the design of other ratiometric sensors [74]. FRET is an energy-transfer process between an excited donor fluorophore and a ground-state acceptor fluorophore in close proximity (approximately 1–20 nm). Due to their small size, lanthanide complexes (mostly based on Eu^{3+} and Tb^{3+}) are often used in FRET-based assays [86, 87]. Small Ln-doped NPs (generally with sizes below 30 nm) can also be coupled with organic fluorophores, metallic NPs, or quantum dots for FRET/

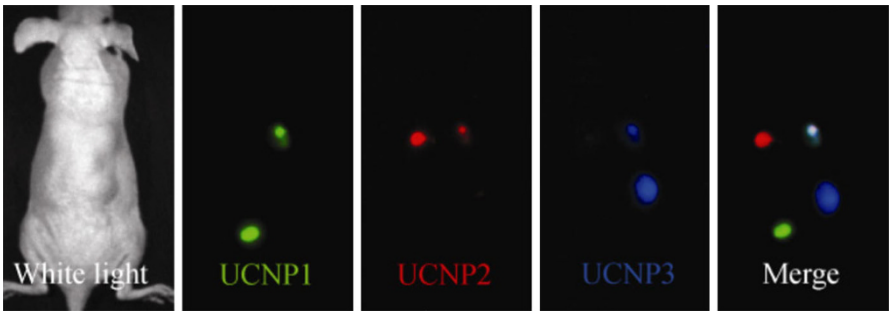

Fig. 4 *Left* **a** *white light* image of a mouse subcutaneously injected with different Er^{3+}, Yb^{3+}-doped $NaYF_4$ UCNPs; the rest of the images: in-vivo multicolour images of a nude mouse subcutaneously injected with different UCNPs solutions. Taken from [81]

LRET-based sensing approaches, where Ln-doped NPs are typically the donor unit [88–91]. For providing selective detection towards a specific analyte (e.g. biomolecules, ions, gas molecules), the NPs have to be functionalized with suitable groups/motifs that have a recognition capability of the target analyte. For example, a single-stranded DNA has been used as Hg^{2+}-capturing element in the development of a method for determining Hg^{2+} ions based on a FRET mechanism between Tm^{3+}, Yb^{3+}-doped $NaYF_4$ UCNPs as energy donor and a DNA intercalating dye (SYBR Green I) as energy acceptor [92]. As the SYBR has a strong absorbance overlapping with the blue emission of the UCNPs, in the presence of Hg^{2+} ions there is a simultaneous decrease of the blue emission of the UCNPs and an increase of SYBR green emission. By monitoring the ratio of the acceptor emission to the donor emission, the Hg^{2+} ion can be detected at levels as low as 0.06 nM. This system allows for not only determining the concentration of Hg^{2+} but also monitoring changes in the distribution of Hg^{2+} in living cells by upconversion of luminescence bioimaging.

In-vivo pH sensing by an energy transfer mechanism has been carried out with Er^{3+}, Yb^{3+}-doped β-$NaYF_4$ UCNPs functionalized with polyglutamic porphyrin–dendrimers. In this case, the green and red emission bands of the UCNPs are attenuated differently depending on the protonation state of the porphyrin [93].

The sensitive and specific interaction between avidin and biotin has been used for the detection and quantification of fluorescein isothiocyanate (FITC)-labeled avidin with biotinylated NPs. In this case, the increase in the emission of the FITC at the expense of the Ln^{3+} was correlated to the amount of FITC-labeled avidin, with a detection limit up to 3.0 nM [94]. Dissolution-enhanced luminescent bioassays (DELBA) with ultra-small Ln-based NPs have been recently proposed for the detection of tumor biomarkers due to their relatively high stability and greater flexibility for bioconjugation. In this case, the NP size is a key factor, since ultra-small NPs minimize the interference with the antigen–antibody binding processes [95], while larger nanoprobes based on lanthanide-chelate-embedded polystyrene or silica NPs have a tendency to agglomerate and swell in aqueous solution [96]. After an appropriate functionalization, often based on the well-known specific interaction between avidin and biotin, the NPs are able to recognize the analyte. The addition of an enhancer solution containing high chelating and sensitizing additives dissolves the NPs, releases the Ln^{3+} cations, and finally, highly luminescent lanthanide complexes (also called lanthanide luminescent micelles) are formed. This strategy has been used for the ultrasensitive in-vitro detection of carcinoembryonic antigen (CEA) [97], and prostate-specific antigens [98].

By using Au NPs as an acceptor instead of a fluorophore, the detection of trace amounts of avidin has been reported. In this system the selective and sensitive avidin–biotin interaction is responsible for bringing together the avidin-modified Er^{3+}, Yb^{3+}-doped $NaYF_4$ NPs used as donor and the biotinylated-Au NPs, whose strong absorption at $\sim$541 nm matches well with the green emission of the Ln-doped NPs, and therefore an effective FRET process occurs [99]. An important advantage of this approach is its potential to be extended to wherever the avidin–biotin system functions, for example to study protein-protein interactions, ligand-receptor interactions, the formation of DNA duplexes, and so on.

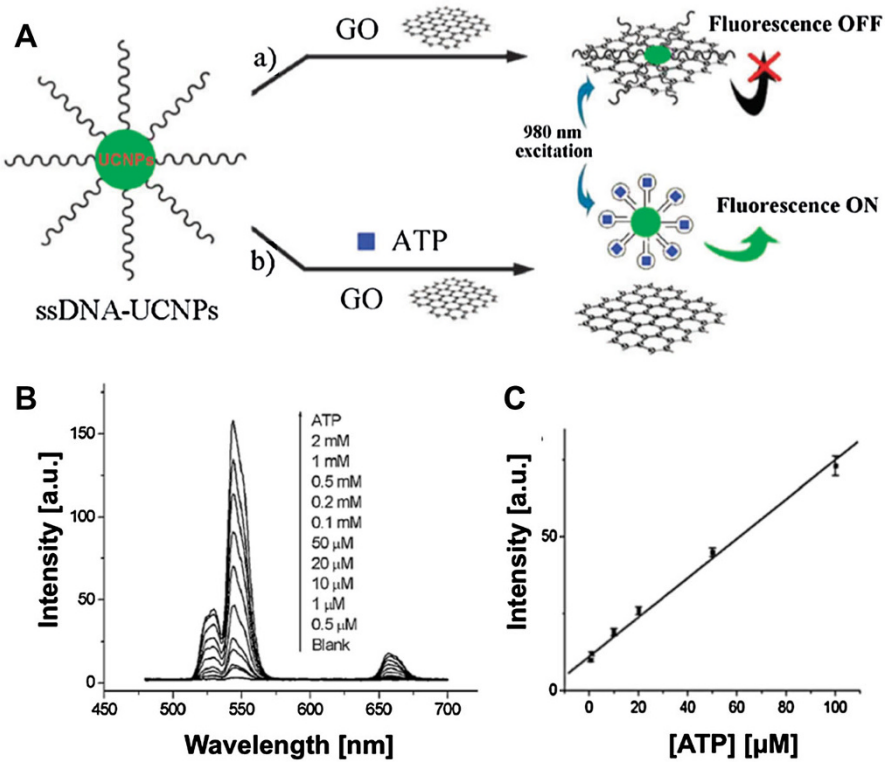

Fig. 5 **a** Scheme of the upconversion fluorescence resonance energy transfer between ssDNA-UCNPs and GO for ATP sensing. **b** Upconversion fluorescence spectra of the UCNPs-GO FRET aptasensor in the presence of 0–2 mM ATP. **c** Plot of upconversion fluorescence intensity at 547 nm vs. ATP concentration. Taken from [100]

Looking for a higher efficiency of the FRET process, and thus a higher sensitivity of the method, Liu et al. proposed the use of graphene oxide (GO) as an efficient acceptor, since it completely quenches the visible emissions of the Ln-doped NPs due to their strong absorption [100]. After quenching the emission from single-stranded DNA-functionalized Er^{3+}, Yb^{3+}-doped $NaYF_4$ UCNPs by their adsorption on the surface of GO, their fluorescence can be recovered by addition of adenosine triphosphate (ATP) (Fig. 5). ATP causes the desorption of the ssDNA-NPs from the GO as consequence of the formation complexes of ATP with the ssDNA (designed as adenosine triphosphate-specific aptamer), resulting in the decreased quenching efficiency and enhanced upconversion fluorescence, which is proportional to the ATP concentration. This aptasensor design can be further extended for sensing other kinds of molecules.

Semiconductor QDs have also been combined with UCNPs in FRET configurations. The superiority of QDs as acceptors owes to the fact that they have broad excitation bands and size-tuneable emission wavelength, and thus the upconversion wavelength of the UCNP–QD couple may be continuously adjusted. Combining Tm^{3+}, Yb^{3+}-doped $NaYF_4$ UCNPs as the energy donor and the CdTe QDs as the

energy acceptor, the determination of lead ions in human serum with a detection limit of 80 nM has been achieved [101]. Such a low detection limit is possible thanks to the use of the NIR-laser as excitation source, which is capable of overcoming self-luminescence from serum excitation with visible light.

A FRET process is not only possible between two NPs, but also between the emission bands of RE NPs and an enzyme absorbance band. Tm^{3+}, Yb^{3+}-doped Gd_4O_2S UCNPs have been used to monitor the redox state of a flavoenzyme (PETNR, pentaerythritol tetranitrate reductase) [102]. Due to a variation in the absorbance profile of the flavin core of the enzyme upon reduction/oxidation, the FRET between the donor/acceptor units can effectively be turned 'on' or 'off' by changing the redox state of PETNR. The presence of two bands separated by over 300 nm allowed the ratiometric signaling of this process.

The multiplexing capabilities of Ln-doped NPs have been also demonstrated by using different UCNPs excited with the same IR laser. The simultaneous detection of two types of pathogenic bacteria (Salmonella Typhimurium and Staphylococcus aureus) was carried out by means of aptamer-conjugated Er^{3+}, Yb^{3+}, and Tm^{3+}, Yb^{3+}-doped $NaYF_4$ UCNPs [103].

Interestingly, Ln-doped UCNPs can also be used as nanothermometers based on the strong temperature dependence of the fluorescence intensities from two emitting levels of lanthanides [104, 105]. This principle has been exploited for monitoring temperature changes in living cells, which is of particular interest for the investigation of enzyme reactions and sub-cellular processes [106]. Wolfbeis et al. studied temperature sensing using UCNPs of varying size and RE dopants recently [107]. They found that the core–shell structured hexagonal 2 % Er^{3+}, 20 % Yb^{3+}-doped $NaYF_4$/$NaYF_4$ UCNPs were more suitable for temperature sensing because their higher brightness allowed resolving temperature differences of less than 0.5 °C in the physiological range between 20 and 45 °C [107].

6 Optoelectronic Applications

Because of their unique optical properties, Ln-doped materials are also widely used for optoelectronic applications, which include laser sources [108], fiber-optic communication [109], light-emitting diodes and solid-state lightening [110, 111], and color display devices [112]. These properties have been extensively studied in bulk materials since the last century, and nowadays the design and the study of the properties and applications of the nanostructured materials attract wide research interest. In particular, Ln-doped semiconductor nanostructures open up the possibilities for photonic/electronic integration and cheap CMOS-compatible optical sources, while efficient solid-state lighting based on Ln-doped nanostructures are increasingly playing a role in new green technologies [113].

Some Ln-doped NPs are used as color and white light-emitting materials. For the latter, both the selection of appropriate host matrices, which should be able to excite the Ln cations after one single wavelength absorption, and the optimization of the Ln contents, which can also absorb and transfer energy between them, are demanded. Examples of Ln-doped white light-emitting NPs are Dy^{3+}, Eu^{3+}-doped

ZrO_2 [114], Dy^{3+}-doped yttria stabilized zirconia (YSZ) [115], and Dy^{3+}, Tb^{3+}, Eu^{3+}-doped $GdPO_4$ [52].

Ln-doped NPs are also used to improve the energy conversion efficiency in solar cells by overcoming both of the two primary loss mechanisms in solar cells. Such mechanisms are related to the absorption of photons with larger or lower energy than the bandgap of the solar cell, reducing their efficiency in practice. On one hand, DC NPs can absorb UV photons and re-emit them at longer wavelengths, where the solar cell exhibits a significantly better response [116]. For example, Eu^{3+}, Bi^{3+}-doped YVO_4 NPs have been used in Si-based solar cells to reduce the thermalization of charge carriers caused by the absorption of high-energy photons [117]. On the other hand, UCNPs are used to transform low-energy photons into higher energy photons that can be used by the solar cells, and thus significantly enhance the efficiency of the photovoltaic device [118]. Er^{3+}, Yb^{3+}-doped $NaYF_4$ NPs, one of the most studied fluorides, has been used with this objective [119]. In some cases, UCNPs are also associated with organic dyes [120].

7 Concluding Remarks and Future Outlook

Current and widely used strategies for synthesis and functionalization of RE-based NPs have been discussed, and some recent advances in their imaging, sensing, and optoelectronic applications have been mentioned. Even when the synthesis in organic media, normally in the presence of additives such as oleic acid, provides a powerful tool for the production of highly monodispersed NPs, the hydrophobic character of the resulting NPs requires the development of new synthesis routes yielding homogeneous, uniform, and water-dispersible NPs. The use of polyol-based solvents in homogeneous precipitation reactions at moderate temperatures has partially overcome this disadvantage, although reported NP sizes are larger (>40 nm). New synthesis methods yielding Ln-doped NPs with different shapes and sizes for many systems are still in demand, as well as universal functionalization strategies for hydrophilic NPs, as the layer-by-layer approach. Apart from the synthesis and functionalization perspectives, the main disadvantage of Ln-based NPs continues to be their relatively low emission intensity. Even when the indirect excitation with codoped inorganic matrices for downconverting NPs and core/shell structures for upconverting NP have demonstrated notable improvements, new strategies to enhance their luminescence are still demanded.

Acknowledgments This work was supported by a Junta de Andalucía (Spain) Talentia Postdoc Fellowship, co-financed by the European Union's Seventh Framework Programme, Grant agreement No. 267226, and by the European Commission (Grant FutureNanoNeeds to WJP). CCC acknowledges the Spanish Ministry of Economy and Competitiveness for a Juan de la Cierva—Incorporacion contract.

References

1. Wang G, Peng Q, Li Y (2011) Acc Chem Res 44:322
2. Stouwdam JW, van Veggel FCJM (2002) Nano Lett 2:733
3. Lage MM, Righi A, Matinaga FM, Gesland JY, Moreira RL (2004) J Phys Condens Matter 16:3207

4. Yan RX, Li YD (2005) Adv Funct Mater 15:763
5. Epple M, Ganesan K, Heumann R, Klesing J, Kovtun A, Neumann S, Sokolova V (2010) J Mater Chem 20:18
6. Gupta BK, Rathee V, Narayanan TN, Thanikaivelan P, Saha A, Govind, Singh SP, Shanker V, Marti AA, Ajayan PM (2011) Small 7:1767
7. Kaczmarek AM, Van Deun R (2013) Chem Soc Rev 42:8835
8. Maldiney T, Richard C, Seguin J, Wattier N, Bessodes M, Scherman D (2011) ACS Nano 5:854
9. Maldiney T, Lecointre A, Viana B, Bessière A, Bessodes M, Gourier D, Richard C, Scherman D (2011) J Am Chem Soc 133:11810
10. Richardson FS (1982) Chem Rev 82:541
11. Liping L, Minglei Z, Wenming T, Xiangfeng G, Guangshe L, Liusai Y (2010) Nanotechnology 21:195601
12. Eliseeva SV, Bunzli J-CG (2010) Chem Soc Rev 39:189
13. Riedinger A, Zhang F, Dommershausen F, Rocker C, Brandholt S, Nienhaus GU, Koert U, Parak WJ (2010) Small 6:2590
14. Pandey A, Roy MK, Pandey A, Zanella M, Sperling RA, Parak WJ, Samaddar AB, Verma HC (2009) IEEE Trans NanoBioscience 8:43
15. Wang F, Liu X (2009) Chem Soc Rev 38:976
16. Zhou B, Shi B, Jin D, Liu X (2015) Nat Nano 10:924
17. Auzel F (2004) Chem Rev 104:139
18. Haase M, Schäfer H (2011) Angew Chem Int Ed 50:5808
19. Zhou J, Liu Q, Feng W, Sun Y, Li F (2015) Chem Rev 115:395
20. Wisser MD, Chea M, Lin Y, Wu DM, Mao WL, Salleo A, Dionne JA (2015) Nano Lett 15:1891
21. Núñez N, Sabek J, García-Sevillano J, Cantelar E, Escudero A, Ocaña M (2013) Eur J Inorg Chem 2013:1301
22. Escudero A, Moretti E, Ocaña M (2014) CrystEngComm 16:3274
23. Núñez NO, Rivera S, Alcántara D, de la Fuente JM, García-Sevillano J, Ocaña M (2013) Dalton Trans 42:10725
24. Abdesselem M, Schoeffel M, Maurin I, Ramodiharilafy R, Autret G, Clément O, Tharaux P-L, Boilot J-P, Gacoin T, Bouzigues C, Alexandrou A (2014) ACS Nano 8:11126
25. Núñez NO, Zambrano P, García-Sevillano J, Cantelar E, Rivera-Fernández S, de la Fuente JM, Ocaña M (2015) Eur J Inorg Chem 2015:4546
26. Boyer J-C, van Veggel FCJM (2010) Nanoscale 2:1417
27. Mialon G, Türkcan S, Dantelle G, Collins DP, Hadjipanayi M, Taylor RA, Gacoin T, Alexandrou A, Boilot J-P (2010) J Phys Chem C 114:22449
28. Ostrowski AD, Chan EM, Gargas DJ, Katz EM, Han G, Schuck PJ, Milliron DJ, Cohen BE (2012) ACS Nano 6:2686
29. Shao W, Chen G, Damasco J, Wang X, Kachynski A, Ohulchanskyy TY, Yang C, Ågren H, Prasad PN (2014) Opt Lett 39:1386
30. Yin W, Zhou L, Gu Z, Tian G, Jin S, Yan L, Liu X, Xing G, Ren W, Liu F, Pan Z, Zhao Y (2012) J Mater Chem 22:6974
31. Punjabi A, Wu X, Tokatli-Apollon A, El-Rifai M, Lee H, Zhang Y, Wang C, Liu Z, Chan EM, Duan C, Han G (2014) ACS Nano 8:10621
32. Dantelle G, Calderón-Villajos R, Zaldo C, Cascales C, Gacoin T (2014) ACS Appl Mater Interfaces 6:22483
33. Zou W, Visser C, Maduro JA, Pshenichnikov MS, Hummelen JC (2012) Nat Photon 6:560
34. Gnach A, Bednarkiewicz A (2012) Nano Today 7:532
35. Liu Y, Tu D, Zhu H, Chen X (2013) Chem Soc Rev 42:6924
36. Liu Y, Tu D, Zhu H, Ma E, Chen X (2013) Nanoscale 5:1369
37. Dong H, Du S-R, Zheng X-Y, Lyu G-M, Sun L-D, Li L-D, Zhang P-Z, Zhang C, Yan C-H (2015) Chem Rev 115:10725
38. Sedlmeier A, Gorris HH (2015) Chem Soc Rev 44:1526
39. Zheng W, Huang P, Tu D, Ma E, Zhu H, Chen X (2015) Chem Soc Rev 44:1379
40. Boyer J-C, Vetrone F, Cuccia LA, Capobianco JA (2006) J Am Chem Soc 128:7444
41. Yi GS, Chow GM (2006) Adv Funct Mater 16:2324
42. Dong C, van Veggel FCJM (2009) ACS Nano 3:123
43. Wang X, Zhuang J, Peng Q, Li Y (2005) Nature 437:121
44. Wang F, Deng R, Liu X (2014) Nat Protocols 9:1634

45. Zhengquan L, Yong Z (2008) Nanotechnology 19:345606
46. Naccache R, Vetrone F, Mahalingam V, Cuccia LA, Capobianco JA (2009) Chem Mat 21:717
47. Quintanilla M, Nunez NO, Cantelar E, Ocana M, Cusso F (2011) Nanoscale 3:1046
48. Rodríguez-Liviano S, Núñez NO, Rivera-Fernández S, de la Fuente JM, Ocaña M (2013) Langmuir 29:3411
49. Nuñez NO, García M, García-Sevillano J, Rivera-Fernández S, de la Fuente JM, Ocaña M (2014) Eur J Inorg Chem 2014:6075
50. Becerro AI, González-Mancebo D, Cantelar E, Cussó F, Stepien G, de la Fuente JM, Ocaña M (2016) Langmuir 32:411
51. Rodríguez-Liviano S, Becerro AI, Alcántara D, Grazú V, de la Fuente JM, Ocaña M (2013) Inorg Chem 52:647
52. Becerro AI, Rodríguez-Liviano S, Fernández-Carrión AJ, Ocaña M (2013) Cryst Growth Des 13:526
53. Becerro AI, Criado J, Gontard LC, Obregón S, Fernández A, Colón G, Ocaña M (2014) Cryst Growth Des 14:3319
54. Becerro AI, Ocana M (2015) RSC Adv 5:34517
55. Escudero A, Calvo ME, Rivera-Fernández S, de la Fuente JM, Ocaña M (2013) Langmuir 29:1985
56. Rodríguez-Liviano S, Aparicio FJ, Rojas TC, Hungría AB, Chinchilla LE, Ocaña M (2012) Cryst Growth Des 12:635
57. Gemini L, Hernández MC, Kling R (2016) Proc. SPIE 9722:972205
58. Pellegrino T, Kudera S, Liedl T, Muñoz Javier A, Manna L, Parak WJ (2005) Small 1:48
59. Thanh NTK, Green LAW (2010) Nano Today 5:213
60. Wilhelm S, Kaiser M, Wurth C, Heiland J, Carrillo-Carrion C, Muhr V, Wolfbeis OS, Parak WJ, Resch-Genger U, Hirsch T (2015) Nanoscale 7:1403
61. Dong A, Ye X, Chen J, Kang Y, Gordon T, Kikkawa JM, Murray CB (2011) J Am Chem Soc 133:998
62. Zhang F, Lees E, Amin F, Rivera_Gil P, Yang F, Mulvaney P, Parak WJ (2011) Small 7:3113
63. Li L-L, Zhang R, Yin L, Zheng K, Qin W, Selvin PR, Lu Y (2012) Angew Chem Int Edn 51:6121
64. Jiang G, Pichaandi J, Johnson NJJ, Burke RD, van Veggel FCJM (2012) Langmuir 28:3239
65. Deng M, Tu N, Bai F, Wang L (2012) Chem. Mat. 24:2592
66. Carrillo-Carrión C, Parak WJ (2016) J Colloid Interface Sci
67. Bogdan N, Vetrone F, Ozin GA, Capobianco JA (2011) Nano Lett 11:835
68. Wang M, Liu J-L, Zhang Y-X, Hou W, Wu X-L, Xu S-K (2009) Mater Lett 63:325
69. Chen Z, Chen H, Hu H, Yu M, Li F, Zhang Q, Zhou Z, Yi T, Huang C (2008) J Am Chem Soc 130:3023
70. Cooper DR, Kudinov K, Tyagi P, Hill CK, Bradforth SE, Nadeau JL (2014) Phys Chem Chem Phys 16:12441
71. Chen YC, Huang SC, Wang YK, Liu YT, Wu TK, Chen TM (2013) Chem Asian J 8:2652
72. Sukhorukov GB, Donath E, Davis S, Lichtenfeld H, Caruso F, Popov VI, Möhwald H (1998) Polym Adv Technol 9:759
73. Wang L, Yan R, Huo Z, Wang L, Zeng J, Bao J, Wang X, Peng Q, Li Y (2005) Angewandte Chemie Int Edn 44:6054
74. Escudero A, Carrillo-Carrión C, Zyuzin MV, Ashraf S, Hartmann R, Núñez NO, Ocaña M, Parak WJ (2016) Nanoscale 8:12221
75. Guerrero-Martínez A, Pérez-Juste J, Liz-Marzán LM (2010) Adv Mater 22:1182
76. Hu H, Xiong L, Zhou J, Li F, Cao T, Huang C (2009) Chem Eur J 15:3577
77. Gai S, Yang P, Li C, Wang W, Dai Y, Niu N, Lin J (2010) Adv Funct Mater 20:1166
78. Mader HS, Link M, Achatz DE, Uhlmann K, Li X, Wolfbeis OS (2010) Chem Eur J. 16:5416
79. Gargas DJ, Chan EM, Ostrowski AD, Aloni S, Altoe MVP, Barnard ES, Sanii B, Urban JJ, Milliron DJ, Cohen BE, Schuck PJ (2014) Nat Nano 9:300
80. Sun L, Ge X, Liu J, Qiu Y, Wei Z, Tian B, Shi L (2014) Nanoscale 6:13242
81. Cheng L, Yang K, Zhang S, Shao M, Lee S, Liu Z (2010) Nano Res 3:722
82. Chen G, Shen J, Ohulchanskyy TY, Patel NJ, Kutikov A, Li Z, Song J, Pandey RK, Ågren H, Prasad PN, Han G (2012) ACS Nano 6:8280
83. Wong H-T, Tsang M-K, Chan C-F, Wong K-L, Fei B, Hao J (2013) Nanoscale 5:3465
84. Wu X, Zhang Y, Takle K, Bilsel O, Li Z, Lee H, Zhang Z, Li D, Fan W, Duan C, Chan EM, Lois C, Xiang Y, Han G (2016) ACS Nano 10:1060
85. Gorris HH, Ali R, Saleh SM, Wolfbeis OS (2011) Adv Mater 23:1652

86. Geißler D, Linden S, Liermann K, Wegner KD, Charbonnière LJ, Hildebrandt N (2014) Inorg Chem 53:1824
87. Qiu X, Hildebrandt N (2015) ACS Nano 9:8449
88. Tang Ya, Hu J, Elmenoufy AH, Yang X (2015) ACS Appl Mater Interfaces 7: 12261
89. Hemmer E, Quintanilla M, Légaré F, Vetrone F (2015) Chem Mat 27:235
90. Chen H, Guan Y, Wang S, Ji Y, Gong M, Wang L (2014) Langmuir 30:13085
91. Mattsson L, Wegner KD, Hildebrandt N, Soukka T (2015) RSC Adv 5:13270
92. Kumar M, Zhang P (2010) Biosens Bioelectron 25:2431
93. Esipova TV, Ye X, Collins JE, Sakadžić S, Mandeville ET, Murray CB, Vinogradov SA (2012) Proc Natl Acad Sci 109:20826
94. Liu Y, Zhou S, Tu D, Chen Z, Huang M, Zhu H, Ma E, Chen X (2012) J Am Chem Soc 134:15083
95. Rainò G, Stöferle T, Park C, Kim H-C, Topuria T, Rice PM, Chin I-J, Miller RD, Mahrt RF (2011) ACS Nano 5:3536
96. Johanna V, Tero S (2014) Methods Appl Fluoresc 2:012001
97. Zhou S, Zheng W, Chen Z, Tu D, Liu Y, Ma E, Li R, Zhu H, Huang M, Chen X (2014) Angew Chem Int Ed 53:12498
98. Xu J, Zhou S, Tu D, Zheng W, Huang P, Li R, Chen Z, Huang M, Chen X (2016) Chem Sci 7:2572
99. Saleh SM, Ali R, Hirsch T, Wolfbeis OS (2011) J Nanoparticle Res 13:4603
100. Liu C, Wang Z, Jia H, Li Z (2011) Chem Commun 47:4661
101. Xu S, Xu S, Zhu Y, Xu W, Zhou P, Zhou C, Dong B, Song H (2014) Nanoscale 6:12573
102. Harvey P, Oakland C, Driscoll MD, Hay S, Natrajan LS (2014) Dalton Trans 43:5265
103. Duan N, Wu S, Zhu C, Ma X, Wang Z, Yu Y, Jiang Y (2012) Anal Chim Acta 723:1
104. Wu K, Cui J, Kong X, Wang Y (2011) J Appl Phys 110:053510
105. Li D, Wang Y, Zhang X, Yang K, Liu L, Song Y (2012) Optics Commun 285:1925
106. Vetrone F, Naccache R, Zamarrón A, Juarranz de la Fuente A, Sanz-Rodríguez F, Martinez Maestro L, Martín Rodriguez E, Jaque D, García Solé J, Capobianco JA (2010) ACS Nano 4: 3254
107. Sedlmeier A, Achatz DE, Fischer LH, Gorris HH, Wolfbeis OS (2012) Nanoscale 4:7090
108. Liu X, Wang Y, Wang J, Zhang E, Xiong L, Zhao W (2009) Lasers & Electro Optics & The Pacific Rim Conference on Lasers and Electro-Optics, 2009. CLEO/PACIFIC RIM '09. Conference on p 1
109. Zhou P, Wang X, Ma Y, Lü H, Liu Z (2012) Laser Phys 22:1744
110. Sayed FN, Grover V, Sudarsan V, Pandey BN, Asthana A, Vatsa RK, Tyagi AK (2012) J Colloid Interface Sci 367:161
111. Nathan CG, Kristin AD, Ram S (2013) Annu Rev Mater Res 43:481
112. Li Y, Zhang J, Luo Y, Zhang X, Hao Z, Wang X (2011) J Mater Chem 21:2895
113. Than ETTY (2012) Rare Earth Nanotechnology. Pan Stanford Publishing Pte. Ltd., Singapore
114. Das S, Yang C-Y, Lu C-H (2013) J Am Ceram Soc 96:1602
115. Soares MRN, Soares MJ, Fernandes AJS, Rino L, Costa FM, Monteiro T (2011) J Mater Chem 21:15262
116. Klampaftis E, Ross D, McIntosh KR, Richards BS (2009) Solar Energy Mater Solar Cells 93:1182
117. Huang CK, Chen YC, Hung WB, Chen TM, Sun KW, Chang WL (2013) Prog Photovolt Res Appl 21:1507
118. Naccache R, Vetrone F, Capobianco JA (2013) ChemSusChem 6:1308
119. Yuan C, Chen G, Prasad PN, Ohulchanskyy TY, Ning Z, Tian H, Sun L, Agren H (2012) J Mater Chem 22:16709
120. Yuan C, Chen G, Li L, Damasco JA, Ning Z, Xing H, Zhang T, Sun L, Zeng H, Cartwright AN, Prasad PN, Ågren H (2014) ACS Appl Mater Interfaces 6:18018

Top Curr Chem (Z) (2016) 374:42
DOI 10.1007/s41061-016-0041-3

REVIEW

Recent Progress in Quantum Dot Based White Light-Emitting Devices

Liang Su[1] · Xiaoyu Zhang[1] · Yu Zhang[1] · Andrey L. Rogach[2]

Received: 7 April 2016 / Accepted: 27 May 2016 / Published online: 14 June 2016

Abstract Colloidal semiconductor quantum dots (QDs) have been widely employed as components of white light-emitting diodes (WLEDs) due to their excellent optical properties (highly saturated emission color, high luminescence quantum yield) as well as thermal and chemical stability. Much effort has been devoted to realize efficient QD-based WLEDs, including the synthesis of superior luminescent nanomaterials with excellent stabilities, and the design of advanced devices structures. In this paper, after introducing photometric parameters of the contemporary QD-based WLEDs, we highlight the recent progress in these devices grouped according to three main mechanisms for white light generation: optical excitation, direct charge carrier injection, and Förster resonance energy transfer. The methods to generate white light, the design of QD emitters and QD-based devices, as well as their fabrication techniques are considered, and the key scientific and technological challenges in the QD-based WLEDs are highlighted. Novel light-emitting materials for WLEDs such as carbon-based nanoparticles are also considered.

This article is part of the Topical Collection "Photoactive Semiconductor Nanocrystal Quantum Dots"; edited by "Alberto Credi".

✉ Yu Zhang
yuzhang@jlu.edu.cn

✉ Andrey L. Rogach
andrey.rogach@cityu.edu.hk

[1] State Key Laboratory on Integrated Optoelectronics, College of Electronic Science and Engineering, Jilin University, Changchun 130012, China

[2] Department of Physics and Materials Science, Centre for Functional Photonics (CFP), City University of Hong Kong, Kowloon, Hong Kong

Keywords Nanocrystals · Quantum dots · Light emitting devices · Down-conversion · Charge injection · FRET

1 Introduction

The emission of exhaust gases constitutes a serious health problem, which is currently being tackled by searching for green energy sources; this is closely related to a strong push towards energy savings in various fields. Lighting consumes almost 20 % of the total electric energy used worldwide [1], and saving electric energy and improving its efficiency are particular appealing in this area. One parameter used to evaluate the energy efficiency of light sources is their luminous efficiency (LE), defined as lumens divided by input electrical power (W), where lumen is the optical power of the emitted light perceived by the human eye. Among the present mainstream light sources, incandescent bulbs reach an excellent color rendering index (CRI) of 100, which is the best value equal to that of sunlight, while their LE is rather low (15 lm/W). As a consequence, fluorescent lamps with higher LE of about 80 lm/W are prevalent nowadays for indoor lighting. However, there are some drawbacks with this class of light source: their CRI is low (80, causing poor ability of color rendition), and a prevailing blue component in their white light spectrum hurts human eyesight. Sources for outdoor lighting, such as street, stadium or construction sites, are high intensity discharge lamps, with both LE and CRI comparable to those of fluorescent lamps.

Solid-state lighting in the form of white-light-emitting diodes (WLEDs) has drawn much attention in laboratories and industries throughout the world due to their attractive LE of above 200 lm/W [2–5], which is better than double the efficiency of fluorescent lamps. In addition to their appealing luminous efficiency, WLEDs offer some other advantages over conventional light sources, such as small volume, light weight, sturdiness and durability. There are two major designs for WLEDs: single-chip and multi-chip. In multi-chip WLEDs, white light is created by combining three LED chips with red, green and blue color. This design provides high CRI; however, the fabrication technique is complex and costly as each LED chip requires a power source and an external detector as well as a feedback system owing to their different degradation rates. Scarcity of highly efficient material systems suitable for use in green LEDs is also a challenge [6]. Unlike multi-chip counterparts, single-chip WLEDs employ phosphors deposited on an electrically pumped LED that emits blue or ultraviolet (UV) light. In such phosphor-converted WLED (pc-WLED) [7–11], phosphors absorb part of the excitation light and re-emit photons with longer wavelengths, which should ideally add up to a white light. The light conversion process may cause energy losses due to re-absorption, scattering, thermal quenching, and photo-bleaching. In order to meet the conditions for a warm white light with high CRI and high luminous efficiency of optical radiation, ideal phosphors should satisfy the following criteria: (1) strong absorption of UV or blue light but weak absorption of light with longer wavelengths; (2) high photoluminescence quantum yield (PL QY); (3) large Stokes shift; (4) high photochemical and thermal stability; (5) narrow emission bandwidth in the red part of the spectrum; (6) small granule size. Colloidally grown quantum dots (QDs) possess

many of those desirable characteristics, including a size/composition tunable emission color, high PL QY, strong absorption of blue and UV light, small size, reasonable photochemical stability, and narrow red emission bandwidth. Solution processibility of QDs and the availability of fabrication techniques to process them into thin films (spin-casting, transfer printing, inkjet printing, etc.) are useful to realize WLEDs with large area and flexibility. QDs can be employed as phosphors in QDs converted WLEDs (QDC-WLEDs), but also excited electrically to generate white light. In the latter design, electrons and holes are injected directly to QD emitters of different sizes, where they recombine producing different emission colors, which then mix together to generate white light. To date, reports on QD-based electroluminescent WLEDs (EL-WLEDs) are rather limited, but monochromatic QD-based electroluminescent LEDs have already reached the performance characteristics of the state-of-the-art organic light-emitting diodes (OLEDs). The third approach to produce white light is realized in so-called Förster resonance energy transfer (FRET) assisted LEDs: these combine quantum wells (QWs) and QDs, where excitons formed in QWs are non-radiatively transferred to QDs and then recombine.

Consequently, in this review, we focus on recent developments in these three types of WLEDs. The methods to generate white light, the design of QD emitters and QD-based devices, as well as their fabrication techniques will be considered. We start with a brief introduction to the basic parameters used to characterize the light properties of WLEDs.

2 Photometric Characteristics of WLEDs

Commission International de L'Eclairage (CIE) coordinates (x, y) are used to indicate the color of a light source perceived by the human eye. For example, (0.33, 0.33) is the ideal value for white light. CRI is a quantitative measure of the ability of

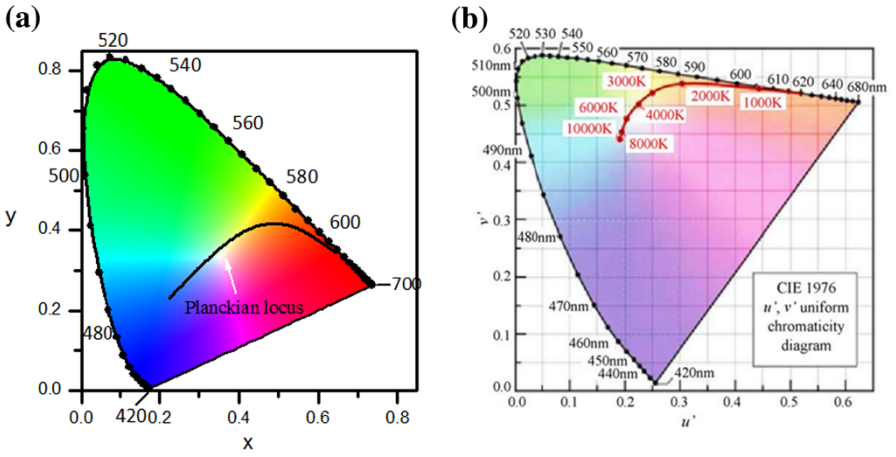

Fig. 1 **a** Planckian locus shown in the (x, y) chromaticity diagram. **b** Chromaticity diagram (u, v) along with the Planckian locus [14]

a light source to reproduce the colors of illuminated objects in comparison to an ideal or natural light source. CRI ranges from 0 to 100, where 100 represents the best color rendering ability. When CIE coordinates of a light source fall on the Planckian locus, as shown in Fig. 1a, the corresponding blackbody radiation temperature of coordinates represents its color temperature (CT). When the coordinates do not fall on the Planckian locus, the correlated color temperature (CCT) is used to define the CT of light sources. CCT is calculated by transforming the (x, y) coordinates to (u, v) by using Eqs. (1) and (2) [12], and by determining the CT of the closest point of the Planckian locus to the light source on the (u, v) uniform chromaticity diagram (Fig. 1b). The luminous efficacy of optical radiation (LER) indicates the relative optical power of emitted spectra perceived by the human eye compared to the emitted total optical power, thus its unit is lumen per optical Watt. On the other hand, luminous efficiency (LE) represents the same with respect to electrical power. LER and LE are calculated using Eqs. (3) and (4) [13], respectively, where $s(\lambda)$ is optical spectral density, $V(\lambda)$ is eye sensitivity function.

$$u' = \frac{4x}{-2x + 12y + 3} \tag{1}$$

$$v' = \frac{9y}{-2x + 12y + 3} \tag{2}$$

$$\mathrm{LER} = (683\mathrm{lm/W_{opt}}) \frac{\int V(\lambda)s(\lambda)\mathrm{d}\lambda}{\int s(\lambda)\mathrm{d}\lambda} \tag{3}$$

$$\mathrm{LE} = (683\mathrm{lm/W_{opt}}) \frac{\int V(\lambda)s(\lambda)\mathrm{d}\lambda}{P_{\mathrm{elect}}} \tag{4}$$

3 QD-Based Down-Conversion WLEDs

3.1 WLEDs Based on Combinations of Conventional Phosphors and QDs

Since the first commercialization of pc-WLED constructed by the combination of a blue InGaN LED chip with yellow-emitting $Y_3Al_5O_{12}:Ce^{+3}$ (YAG:Ce) phosphors [7], these devices have received increasing attention. Such pc-WLEDs have the advantages of a simple fabrication process and low cost, but their CRI lies mostly in the range of 75–80 because of the absence of the red spectral component. A widely employed method used to address this issue is to integrate combinations of green and red phosphors on blue LEDs [9, 10]. Unfortunately, the emission spectra of conventional red-emitting phosphors are strongly broadened towards the deep red region, where human eyes have weak visual response, consequently leading to low LER, which is unfavorable when high quality warm white light (high CRI and high LER) is required. Therefore, red-emitting QDs with high PL QY and narrow emission bandwidth were considered as a possible red color component. Jang et al.

[15] combined green-emitting $Sr_3SiO_5:Ce^{3+},Li^{3+}$ phosphor co-doped with Pr^{3+}, and red-emitting CdSe QDs, which, excited by blue LEDs led to WLEDs with high CRI of 90 but low LE of 14 lm/W, which was related mostly to the relatively low PL QY of core-only CdSe QDs. By replacing CdSe QDs with CdSe/ZnSe core/shell QDs with high PL QY of 70 %, a WLED with CRI of 85, and higher LE of 27 lm/W was fabricated [16]. Similarly, Shen et al. [17] fabricated a WLED based on a InGaN blue LED combined with blends of YAG:Ce,Gd phosphors and CdSe/ZnS QDs in a weight ratio of 1:1. This WLED showed CRI of 90, LE of 80 lm/W comparable to the fluorescent lamps and CIE coordinates of (0.3283, 0.3156), which satisfied the commercial criteria of application. Chung et al. [18] integrated green and red emitting CdSe/ZnS QDs into $Ca_2BO_3Cl:Eu^{2+}$ phosphor as color conversion materials in combination with blue InGaN LED to achieve white light with CRI of 84 and warm CCT of 4055 K.

Besides CdSe-based QDs, red-emitting InP QDs were also employed. Jeong and co-workers [19] demonstrated a WLED fabricated by integrating yellow YAG:Ce phosphors and red emitting InP/ZnS/ZnSe core/multi-shell QDs on a blue LED chip, with resulting CRI of 84. Kim et al. [20] used highly luminescent InP/GaP/ZnS QDs with PL QY of 85 %, and integrated them into YAG:Ce-based white LEDs, which resulted in high LE of 54.7 lm/W, CRI of 81, CCT of 7864 K and CIE coordinates of (0.30, 0.28).

For CdSe- and InP-based WLEDs, self-absorption, due to the small Stokes shift (defined as an energy shift between the lowest energy peak in the absorption spectrum and the corresponding emission peak), would result in undesired energy losses, which decrease the energy conversion efficiency. This issue could be overcome by employing QDs with large Stokes shift, such as $CuInS_2$ (CIS) or ZnCuInS (ZCIS) core/shell QDs, and some doped QDs. Aboulaich et al. [21] employed red color CIS/ZnS QD converters deposited on the surface of YAG:Ce–

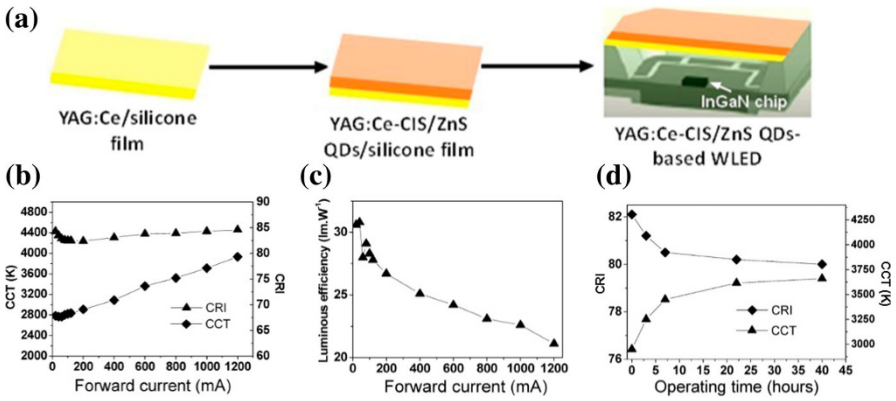

Fig. 2 **a** Schematics of fabrication of layered yellow-emitting $Y_3Al_5O_{12}:Ce^{+3}$ (YAG:Ce)- and $CuInS_2$ (CIS)/ZnS quantum dot (QD)-based white light-emitting diodes (WLED). **b** Corrected color temperature (CCT), color rendering index (CRI) and **c** luminous efficiency (LE) of WLEDs as a function of forward current; **d** temporal evolution of CRI and CCT for a WLED operated at 200 mA for a duration of up to 40 h. Reproduced with permission from [21], © 2013 American Chemical Society

silicone film (Fig. 2a). These WLEDs showed CCT rising from 2784 to 3934 K, and LE dropping from 30.6 to 21.1 lm/W with increasing applied current from 20 to 1200 mA (Fig. 2b), along with CRI values exceeding 80 (Fig. 2c). Stability tests of these WLEDs operated at 200 mA for 40 h revealed that both CRI and CCT experienced an initial drop but remained constant after 7 h of operation (Fig. 2d), suggesting that the layered structure of the yellow- and red-emitting components could be a good solution to achieve stable warm WLED, especially when high current density is applied. Different from separately layered films, the blends of the same materials have also been employed to generate white light with CRI of 86 and

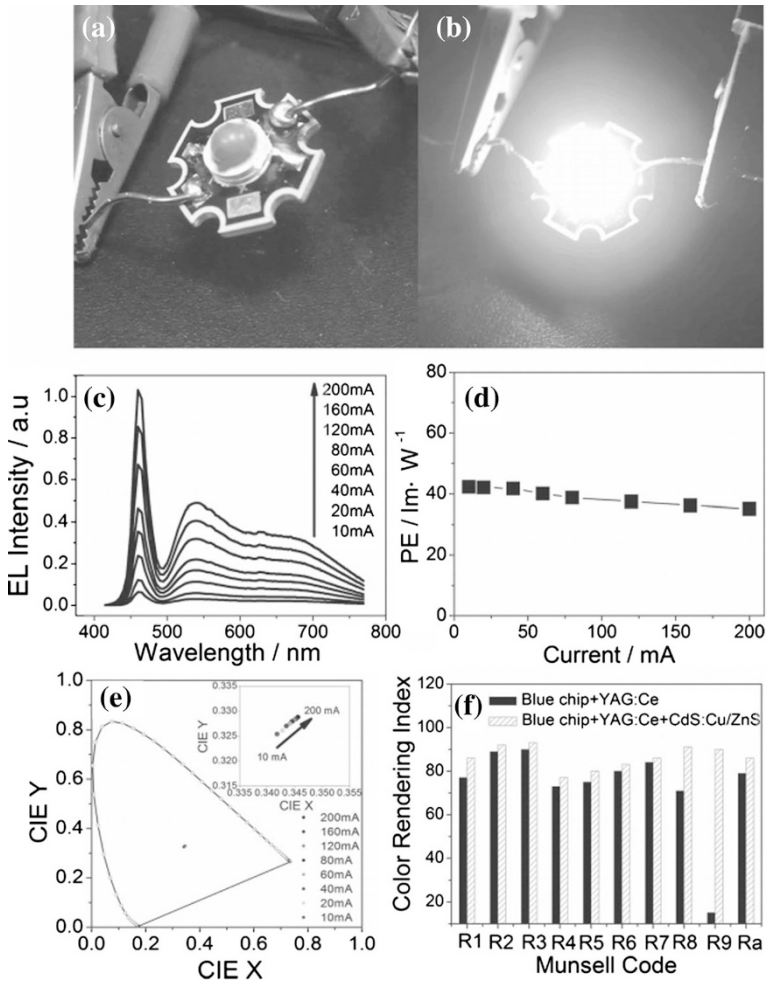

Fig. 3 Photographs of **a**, **b** WLED based on YAG:Ce phosphors and CdS:Cu/ZnS QDs operated at 120 mA, with their **c** electroluminescent (EL) spectra, **d** LE and **e** Commission International de L'Eclairage (CIE) color coordinates under different forward bias currents. **f** Comparison of CRI of such WLED and a WLED based on solely commercial YAG:Ce phosphor, operated at 120 mA. Reproduced with permission from [27], © 2012 Wiley InterScience

LE of 43.7 lm/W at the forward current of 20 mA [22]. For achieving better color rendition ability, green Eu^{2+}-doped silicate was incorporated with the combination of red CIS/ZnS QDs and yellow YAG:Ce phosphors, with the resulting WLEDs reaching CRI as high as 92 [23]. Chuang et al. [24] combined highly luminescent orange- and red-emitting CIS/ZnS QDs with a green-emitting $Ba_2SiO_4:Eu^{2+}$ phosphor, with the resulting WLEDs showing high CRI of 90, as well as LE of 36.7 lm/W.

Doped QDs represent another kind of light-emitting materials with little or even zero self-quenching due to the large Stokes shift. Kim et al. [25] synthesized Mn-doped $Zn_{1-x}Cd_xS$:Mn/ZnS QDs with PL QY gradually increasing from 14 % to 30 % upon decrease of the Zn content in the core. Their WLEDs utilizing the red-emitting CdS:Mn/ZnS QDs deposited on top of a blue LED, showed a low CRI of 62 because of the deficiency of the green–yellow spectrum, while addition of yellow-emitting YAG:Ce phosphor improved the CRI towards 85 [26]. Sun and co-workers [27] synthesized a red-emitting Cu-doped CdS:Cu/ZnS core/shell QDs with PL QY of 40–50 %, high photochemical and thermal stability, and little absorption of green–yellow light, which were combined with YAG:Ce^{3+} phosphor on a blue LED chip to produce WLED with a high CRI of 90, slightly decreased LE and little changed CIE coordinates around (0.3449, 0.3282) under an increasing forward bias current from 10 mA to 200 mA (Fig. 3). Using similar QDs, Xuan et al. reported a WLED from a combination of red-emitting Cu-doped CdS:Cu/ZnS QDs, yellow-emitting YAG:Ce^{3+} phosphor, green-emitting LuAG:Ce phosphor and blue LED chips, showing high CRI of 90, LE of 45 lm/W, and CCT of 6591 K under the forward bias current of 40 mA [28]. These WLED exhibited good color stability with unchanged CIE color coordinates of (0.3155, 0.3041) under different forward bias currents.

3.2 All-QD Based WLEDs

The performance of WLEDs based on the combination of yellow–green color phosphors with red emitting QDs has already satisfied the criteria for commercial lighting applications. However, issues of scattering, reflection and refraction, as consequences of the large granule size (scale of micrometer) of conventional phosphors, may alter the emitted light quality and prohibit further improvement of LE. There are some adverse factors related to the use of phosphors, such as their complex synthetic process, patent control, as well as difficulties in controlling the granule size, dispersibility in polymer matrices, and deposition of uniform films. The nanometer-scale size of QDs makes them easily dispersable in epoxy resin or silicone, and it is rather straightforward to deposit uniform films with decreased effects of scattering, reflection and refraction. Intense efforts have thus been focused on fabrication of all QD-based WLEDs. Chen et al. [29] demonstrated that combinations of green- and red-emitting CdSe/ZnS QDs with blue InGaN LED chips result in WLEDs with CRI of 91 and CIE coordinates of (0.33, 0.33). Nizamoglu et al. [30, 31] conducted a series of investigations on all CdSe/ZnS QD-based WLEDs, including the effects of type, concentration and film thicknesses of QDs on tuning the output color properties (CIE coordinates, CCT and CRI), as well

as conducting performance comparison between layer by layer assembled QD-based WLEDs and blended ones. As mentioned above, it is difficult to obtain warm white light with both high CRI (>90) and high LER (>380 lm/W) for pc-WLEDs, due to the phosphors' broad emission tail toward the deep-red part of the spectrum where the eye is not sensitive, thus decreasing LER. But, such cases could be alleviated in all-QD-based WLEDs. Nizamoglu et al. [4, 32] integrated appropriate combinations of CdSe/ZnS QDs in blue LEDs and demonstrated warm white light with both high LER (>300 lm/W) and high CRI up to 90. Adam et al. [33] incorporated three colored (red, yellow, green) CdSe/ZnS QDs in borax-based mixed crystals, acting as color converters to demonstrate a warm WLED with CCT of 2720 K, high CRI of 91.1 and high LER of 341 lm/W. In these WLEDs, core/shell QDs with a high PL QY (i.e., CdSe/ZnS or CdSe/CdS) are typically employed, in order to increase the LE of devices. Strain effects at the core–shell interface in such structures may, however, deteriorate resistance of QDs to moisture and oxygen [34], thus decreasing their stability during long-term operation in ambient conditions. Numerous efforts have thus been devoted to optimizing the structure of core/shell QDs with the aim of improving both their photo- and thermal-stability, as well as PL QY, including

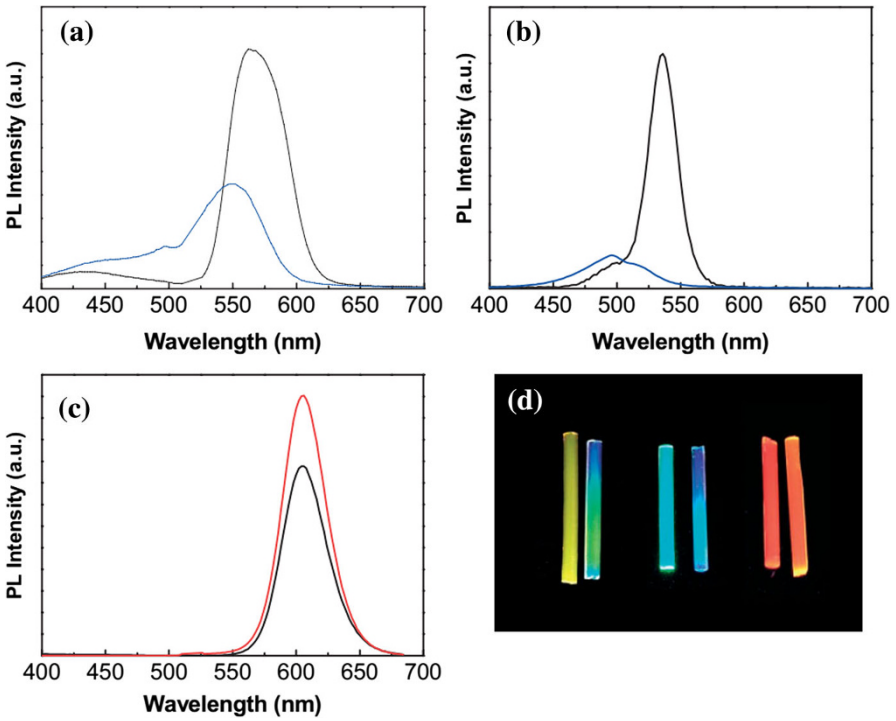

Fig. 4 Photoluminescence (PL) spectra of polymer composites with **a** CdSe QDs (*black* initial, *blue* 144 h UV-exposed), **b** CdSe/ZnS QDs (*black* initial, *blue* 144 h UV-exposed), and **c** CdSe/CdS/ZnS QDs (*black* initial, *red* 330 h UV-exposed). **d** A photograph of the QD–polymer composites excited at 365 nm. From *left* to *right* CdSe QDs, initial and 144 h, CdSe/ZnS QDs, initial and 144 h, CdSe/CdS/ZnS QDs, initial and 330 h. Reproduced with permission from [35], © 2007 Wiley InterScience

design of strain-graded core/shell interfaces (CdSe/CdS/ZnS [35], CdSe/ZnSe/ZnS [36], CdTe/CdSe/CdS/ZnS [37]), as well as alloyed QDs (ZnCdSe [38], CdZnSeS [39], CdSe/CdS/CdZnS/ZnS [40], CdZnS/ZnS [41, 42]) As compared to CdSe/ZnSe core/shell QDs, the CdSe/ZnSe/ZnS core/multi-shell QDs were found to have improved crystallinity of the ZnS outer shell, and thus a PL QY of 80 % [36]. CdTe/CdSe/CdS/ZnS core/multi-shell QDs showed reversible thermal quenching at 100 °C with no thermal degradation [37]. Jang and co-workers [35] conducted comparative stability studies among CdSe QDs, CdSe/ZnS core/shell QDs and CdSe/CdS/ZnS core/multishell QDs, which were all encapsulated in epoxy resin. The PL intensity of CdSe/CdS/ZnS QDs–epoxy composite even improves after 330 h UV exposure, while other QDs showed significantly reduced brightness and blue-shifted emission wavelength (Fig. 4). The same group synthesized multi-shell structured green-emitting CdSe/ZnS/CdSZnS QDs and red-emitting CdSe/CdS/ZnS/CdSZnS QDs with PL QY in the range of 70–90 %, and combined them with blue LEDs to realize WLEDs with LE of 41 lm/W and color reproducibility of 100 % compared to the NTSC color space [43]. These WLEDs were successfully integrated into a 46-inch LCD TV panel, demonstrating an excellent color gamut (Fig. 5a). EQEs of monochrome green and red QD-LEDs reached up to 72 % and 34 %, respectively, and these LEDs maintained their initial efficiency for longer than 2200 h under ambient conditions (Fig. 5b). Their half-life has been estimated to be over 15,000 h, reaching timespans that mobile displays usually guarantee.

As already mentioned above, InP based core/shell nanocrystals with a tunable emission range covering the whole visible spectrum are alternative candidates to CdSe-based QDs, and have also been employed in all QD-based WLEDs. Red-, yellow-, and bluish-green-emitting InP/ZnS core/shell QDs were mixed together and coated on a blue LED chip, producing white light with a CRI of 89 [44]. In another related work, red and green InP/ZnS core/shell QD-based WLEDs provided a color gamut as high as 87 % relative to NTSC triangle standard [45]. As for CIS

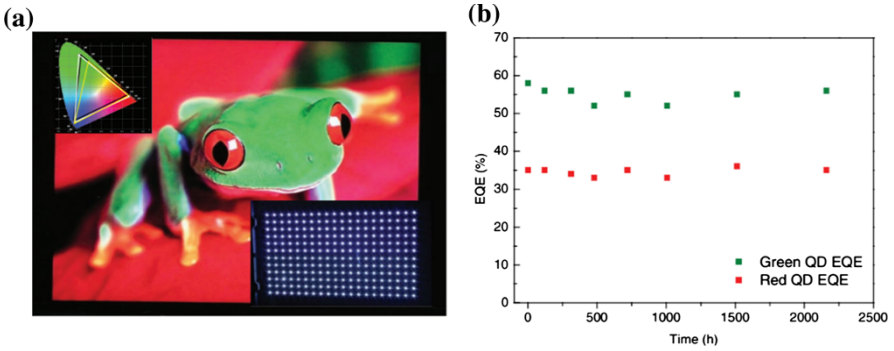

Fig. 5 **a** Display image of a 46-inch LCD TV panel and a quarter of the WLED backlights where the WLED was prepared by integrating the blends of *red* CdSe/CdS/ZnS/CdSZnS QDs and *green* CdSe/ZnS/CdSZnS QDs on a *blue* LED (*lower right inset*). *Color triangles* of the QD-LED (*white*) and the phosphor-LED (*yellow*) compared to NTSC1931 (*black*) are provided in the *upper left inset*. **b** Emission quantum yields (EQYs) of the monochrome QD-LEDs over long-term operation. Reproduced with permission from [43], © 2010 Wiley InterScience

QD-based WLEDs, they often possess good color rendition ability with only one type of CIS QDs as color converters because of their broad emission bandwidth in the yellow–green part of the spectrum. Song et al. [46] realized WLEDs fabricated from highly luminescent yellow CIS/ZnS core/shell QDs deposited on blue LED chip. The performance of these devices has been characterized as a function of forward current varying from 5 mA to 100 mA, showing CIE coordinates of (0.334–0.348, 0.273–0.291), CRI of 72–75, and CCT of 4447–5380 K (Fig. 6). In addition, a high LE of 63.4 lm/W and light conversion efficiency of 74.7 % were achieved at a forward current of 20 mA. In another work, the same group used CuInGaS/ZnS QDs as highly efficient yellow converters to fabricate WLEDs with CRI of 71–72, and LE of 69.1–75.0 lm/W at a forward current of 20 mA [47]. Most recently, Park et al. [48] reported WLEDs based on the combination of blue LED chips and bright yellow–green emitting CIS/ZnS/ZnS core/multi-shell QDs, demonstrating LE of 80.3 lm/W, CRI of 73, and CCT of 6140 K. High LE values of CIS QD-based devices is related to the large Stokes shift of these QDs, resulting in a nearly-zero self-absorption. As discussed above for the case of the YAG:Ce-based WLEDs, however, there is much room for improvement of these devices in terms of CRI, from the similar reason of the existing deficiency for yellow–green emitting CIS QD-converted WLEDs in the red part of spectrum. Song et al. [47]

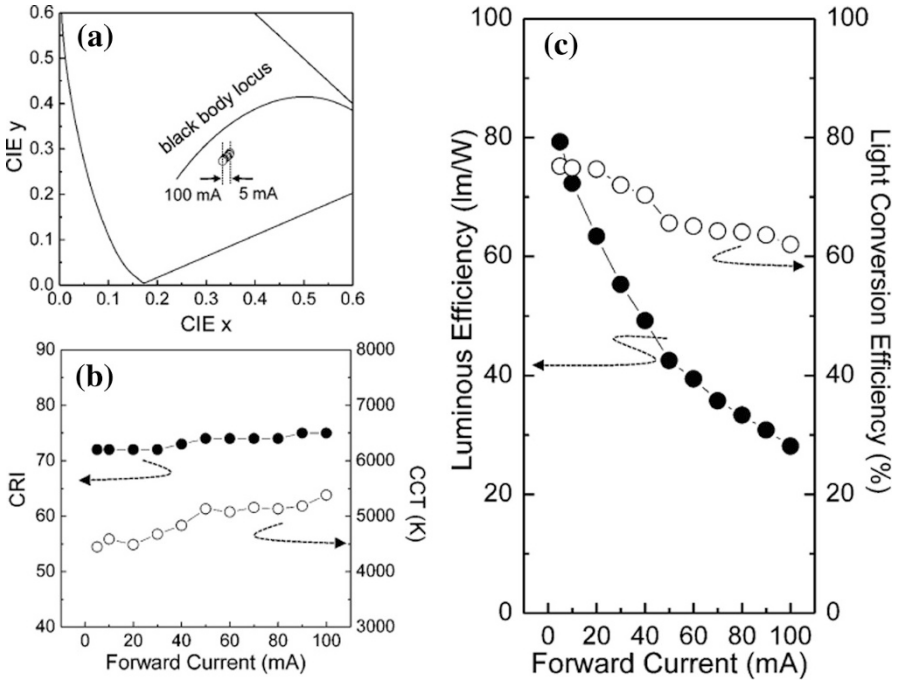

Fig. 6 Variations of **a** CIE color coordinates, **b** CRI/CCT, and **c** LE/light conversion efficiency of white QD-LED fabricated from yellow–green emitting CIS/ZnS QDs as a function of forward current from 5 mA to 100 mA. Reproduced with permission from [46], © 2012 American Chemical Society

achieved CRI of 76–78 using blends of two types of QDs—$CuIn_{0.3}Ga_{0.7}S/ZnS$ and CIS/ZnS—as color converters. Chung et al. [49] employed red and yellow–green emitting ZnCuInS QDs as color conversion materials, and reached CRI of 84.1. Chen et al. [50] fabricated WLEDs based on green and red color emitting CIS-based QDs, which exhibited high CRI of 95, LE of 70 lm/W, and tunable CCT of 4600–5600 K. Recently, Yuan et al. [51] reported efficient WLEDs with high CRI up to 96, LE of 70–78 lm/W and CCT of 3800–5760 K constructed by integrating red and green Cu doped ZnInS/ZnS QDs on blue LEDs. It was demonstrated that negligible energy transfer occurred between Cu-doped QDs, which was consistent with the small spectral overlap between QD emission and absorption.

For the devices discussed above, QDs are usually blended physically with silicone or epoxy resin directly, followed by thermal curing. Several concerns arise with this kind of processing in terms of the commonly used long-chain hydrophobic surface capping ligands of QDs. Incompatibility between the polymer (i.e., silicone and epoxy resin) and the often hydrophobic surface of QDs may give rise to agglomeration of QDs, resulting in energy transfer between smaller and larger QDs and in scattering problems, thus decreasing the LE. Long-chain carbon ligands impede the complete polymerization of resin, which leads to local softening after the thermal curing process and reduces its mechanical stability. In order to minimize such issues, the hydrophobic ligands of QDs can be replaced with oligomeric or polymeric ligands containing functional anchor moieties (such as thiols, amines, or carboxylicgroups) which increase their miscibility with the polymer matrix [52]. Another common method is to protect QDs with an optically transparent barrier material such as silica, forming QDs-silica composite [53–62]. In the work of Ziegler et al. [53], SiO_2-coated red emitting InP/ZnS QDs were produced, showing excellent compatibility between the silica shell and silicone resin, thus forming homogeneous, stable, and transparent QDs-silicone composites. Jun et al. [60] fabricated a strongly luminescent and photostable CdSe/CdS/ZnS QD-silica monolith (QDSM) that was homogeneously doped with up to 12 vol% QD, using

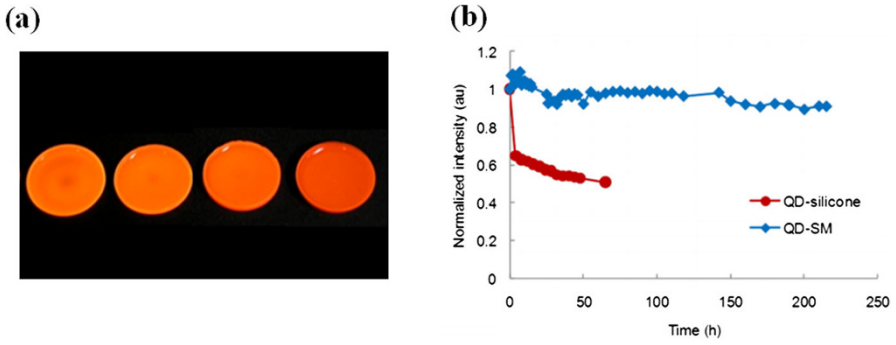

Fig. 7 **a** Photographs of red light-emitting QD-silica monoliths (QDSM) with various concentrations of QDs in the silica matrix (*left* to *right*: 0.12 vol%, 0.6 vol%, 1.2 vol%, 4.8 vol%, and 12 vol%) under UV light. **b** Changes in the emission intensities of the CdSe/CdS/ZnS QDSM, and the same bare QD in silicone matrix during the operation with a high-power UV LED (peak at 400 nm, ~1 W, driving current 350 mA). Reproduced with permission from [60]

6-mercaptohexanol for the surface ligand exchange and propylamine as a catalyst for the silica sol–gel condensation (Fig. 7a). This composite material maintained the initial PL after thermal curing at 100 °C, and exhibited strong photostability against high-power UV radiation (1 W) for at least 200 h (Fig. 7b). A WLED made from those separately prepared green and red QDSM, exhibited LE of 47 lm/W and CIE coordinate at (0.23, 0.21) suitable for a backlight application. Jang et al. [58] dip-coated uniform hybrid double layers consisting of polyvinylpyrrolidone (PVP) as an adhesion layer and sol–gel-derived silica as a gas barrier layer on QDs-PMMA, thus realizing a remote-type WLED equipped with a silica-barrier-coated QD plate, displaying an excellent device stability with LE of 60–61 lm/W, along with stable white light qualities regardless of the operating time at a current input of 20 mA. Zhou et al. [63]. incorporated red-emitting CdSe/ZnS QDs into silica microspheres in order to prevent aggregation, photo-degradation by oxygen and moisture, and incompatibility between QDs and the encapsulating matrix. They integrated these luminescent microspheres with YAG:Ce yellow phosphors, resulting in WLEDs with CIE coordinates changing only slightly from (0.3402, 0.3405) under 10 mA to (0.3339, 0.3335) under 200 mA, which indicated high quality white light and high color stability under varying currents. These WLEDs demonstrated an excellent LE of up to 142.5 lm/W at 10 mA. The LE decreased by about 19 % from 142.5 lm/W at 10 mA to 116 lm/W at 200 mA while the CCT increased from 5171 K to 5430 K under the same alteration conditions, revealing good operational stability.

3.3 Carbon Dot/QD Based WLEDs

Carbon-based nanoparticles, which are commonly classified into carbon dots (CDs) and graphene quantum dots (GQDs), which were first discovered during the purification of single-walled carbon nanotubes through electrophoresis in 2004 [64], possess a number of attractive characteristics, such as high colloidal solubility, robust chemical inertness, facile surface modification, and high resistance to photo-bleaching [65]. They have recently seen extended use as components of WLEDs. Chen's group used blue-emitting CDs, synthesized by a plasma-induced method utilizing acrylamide as the precursor, in combination with red and green CdTe QDs as color converters to produce WLEDs with CRI of 87, LE of 30 lm/W and CIE coordinates of (0.38, 0.36) [66]. The same group also reported warm WLEDs with CIE coordinates of (0.34, 0.35), fabricated by a combination of yellow-emitting CDs and a blue GaN LED chip [67]. Sun et al. [68] demonstrated WLEDs based on blends of blue-emitting CDs with red- and green-emitting ZnCuInS QDs, achieving a high CRI up to 93 and tunable CCT from 3825 to 6452 K. They also combined blue-emitting CDs with red- and green-emitting polymer dots to generate white light with an even higher CRI (up to 96) and widely tunable CCT (from 2805 to 7786 K) [69]. Flexible, free-standing and transparent CD-incorporating ionogels have been shown to achieve a full-color emission tunability under fixed single excitation wavelength [70]; a similar concept was later explored towards fabrication of all CD-based WLEDs [71].

GQDs also received attention in the field of WLEDs. Liu et al. [72] reported an easy method of fabricating a GQD–agar composite (Fig. 8a, b) exhibiting excellent optical stability and no luminescence quenching. It was deposited on blue LED chips to produce WLEDs (Fig. 8c, d) with LE of 42.2 lm/W and a light conversion efficiency of 61.1 %, with the latter value being stable for over 100 h under continuous operation (Fig. 8g).

3.4 WLEDs Based on Dual-Color-Emitting and White-Emitting QDs

In previous sections, we considered methods for white light generation based on combinations of separate light emitting materials, such as yellow phosphors, or red and green emitting QDs deposited on blue LED chips; or by integrating red, green and blue emitting QDs on a UV LED. In all these composites, slight variations in

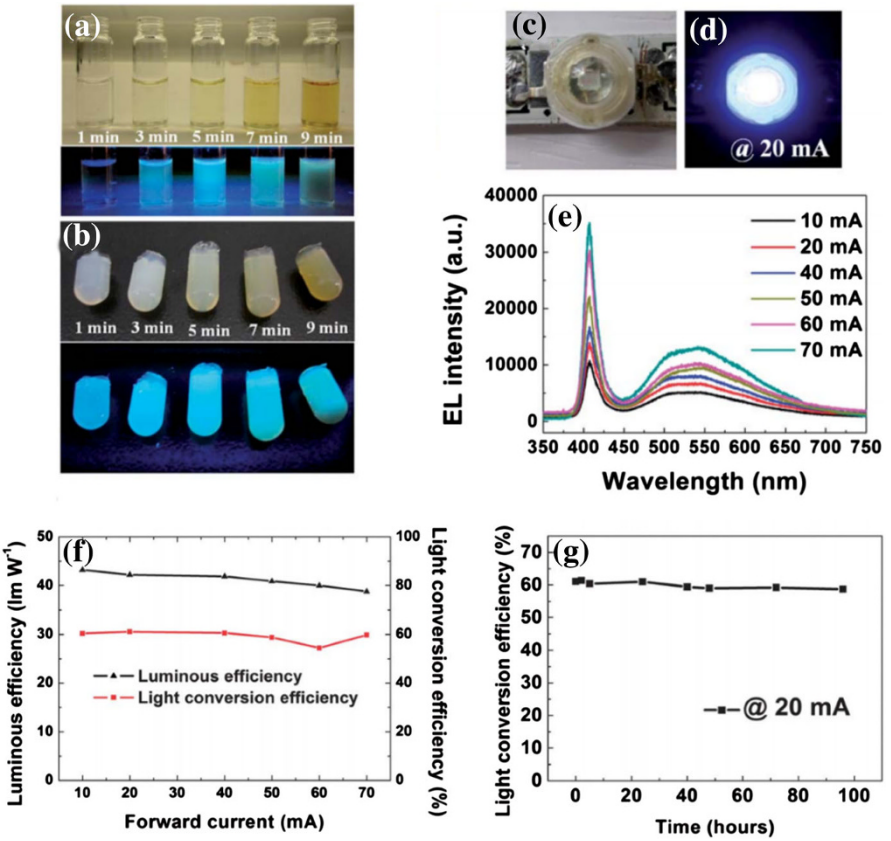

Fig. 8 Fluorescence images of **a** graphene quantum dot (GQD) solutions and **b** GQD–agar composites. Photograph of the GQD-based WLEDs **c** without and **d** with biased current. **e** EL spectra of the WLED under various forward currents, **f** LE and light conversion efficiency against forward currents. **g** Light conversion efficiency of the WLED operated at 20 mA as a function of time. Reproduced with permission from [72], © 2012 Royal Society of Chemistry

concentration and/or film thickness of QDs would change the device properties, such as CIE coordinates and CCT. Moreover, when QDs with different colors are mixed together, or their different color-emitting films are layered separately as color converters, different degradation rates of those QDs may change the emission spectrum over time, thereby leading to undesirable changes in photometric performances of WLEDs. In order to avoid such issues, QDs able to emit multi-color emission from the same entity have been designed. Such multi-color emitting QDs can be categorized into dual-emitting and white light-emitting QDs. In the emission spectrum of the former, two distinct colors appear, while the emission spectrum of the latter is broad and covers the whole visible spectral region. Both these QDs have been employed in WLEDs, as detailed below.

Nizamoglu et al. [73] realized WLEDs by depositing dual color (green and red)-emitting CdSe/ZnS/CdSe core/shell/shell QDs on a blue InGaN/GaN LED, with CIE of (0.36, 0.30), LER of 278 lm/W, CCT of 3929 K, and CRI of 75.1. Such QDs suffered from a rather strong self-absorption, which could be minimized by a proper structural QD design as recently demonstrated by Sapra et al. [74]. As already mentioned above, doped dual-emitting QDs with little, or even zero, self-absorption offer great potential for WLEDs. Zhang et al. [75] developed a dual-emitting system of Cu-doped CdS/ZnSe core/shell QDs, with red color originating from Cu-doped CdS and green color from recombination at the Type-II CdS/ZnSe interface. These

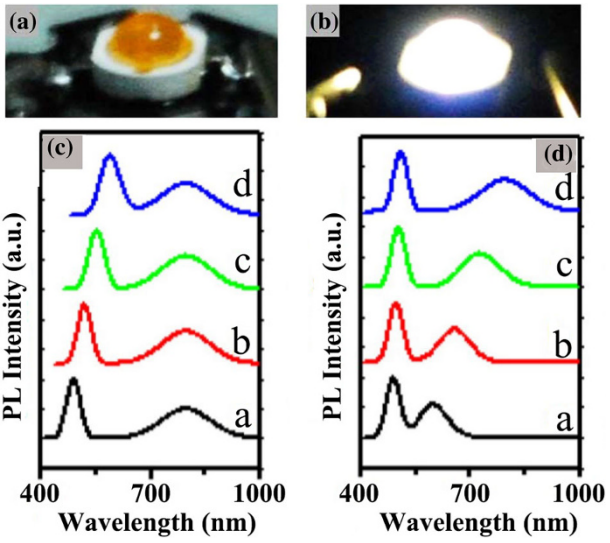

Fig. 9 Photographs of **a** WLED fabricated with dual emissive Cu-doped InP/ZnS/InP/ZnS QDs, and **b** WLED operated at 50 mA. **c** PL spectra of various Cu:InP/ZnS/InP/ZnS QDs, which have the same Cu:InP core size (2.6 nm with the emission at ~800 nm) and different InP quantum well thickness (*a* 0.35 nm, *b* 0.5 nm, *c* 0.8 nm, and *d* 1.2 nm). **d** PL spectra of various Cu:InP/ZnS/InP/ZnS QDs, which have different Cu:InP core diameter sizes (*a* 1.5 nm, *b* 1.8 nm, *c* 2.1 nm, and *d* 2.6 nm) and the same quantum well thickness of ~1 monolayer of InP (~0.35 nm). In all cases, the thicknesses of the quantum well barriers are three monolayer ZnS. Reproduced with permission from [76], © 2015 American Chemical Society

QDs were used as color converters to fabricate WLEDs on a blue LED chip, which emitted white light with CRI of 90, CIE coordinates of (0.325, 0.330) and CCT of 5850 K. Other kinds of Cd-free doped QDs with dual emission have been used as color convertors in WLEDs as well [76–78]. As shown in Fig. 9, high-quality white light (CRI 91) was realized by combining a blue LED with red and green dual-emitting Cu-doped InP/ZnS/InP/ZnS QDs [76]; their emission wavelength could be tuned from visible to near infrared by carefully controlling the size of the Cu-doped InP core and the thickness of the InP quantum (Fig. 9c, d). Dual color Mn-doped CIS/ZnS QDs with green and orange emission were integrated on blue LED chips, to realize WLEDs with CRI of 83 and LE of 61 lm/W [77]. In a recent study, an optimized non-injection method was developed to produce such Mn-doped QDs on

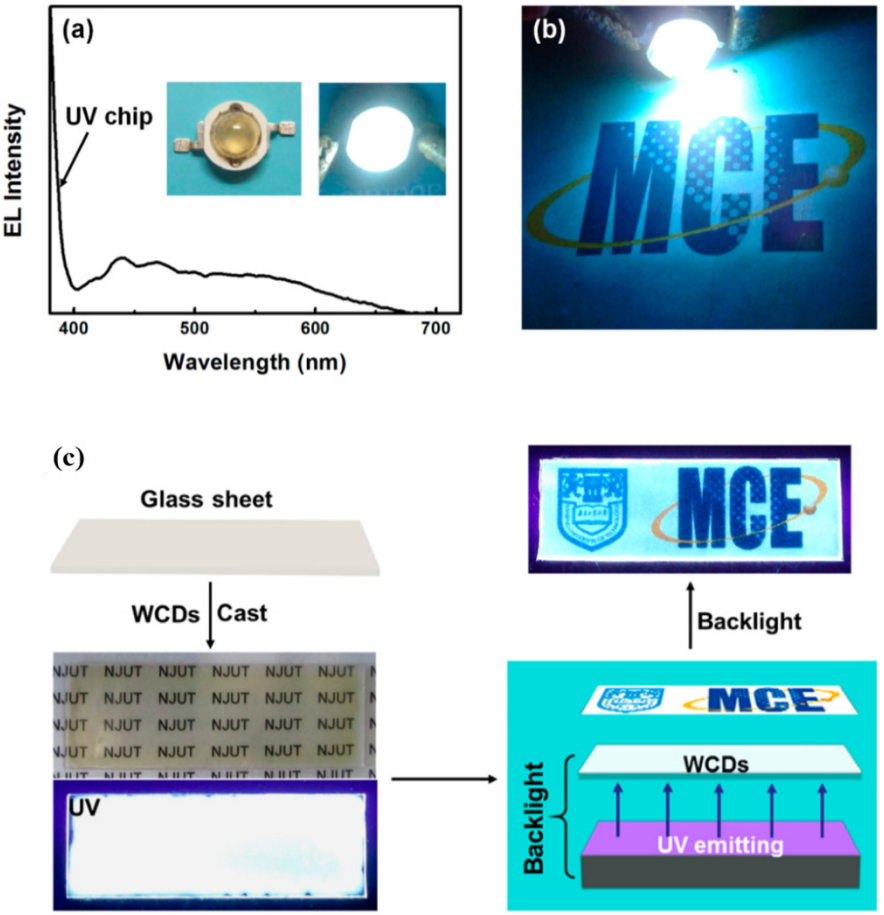

Fig. 10 **a** Emission spectrum of a WLED based on white light emitting CDs operated at 350 mA, *insets* photographs of WLEDs under daylight (*left*) and when operating (*right*). **b** The photograph of the *white* LED in the *dark*, with **c** illustration of the route of fabrication of the respective backlight. Reproduced with permission from [101], © 2014 American Chemical Society

a large scale [78], which were used to produce WLEDs with high CRI of 90 and CIE coordinates of (0.332, 0.321).

Several kinds of white-emitting nanocrystals have been reported so far, such as trap-rich CdS QDs [79–83], magic-sized CdSe QDs [84–88], alloyed Zn_xCd_{1-x}-Se(S) QDs [89, 90], onion-like CdSe/ZnS/CdSe/ZnS QDs [80], and ZnSe QDs [91, 92]. Their broad emission profiles typically combine the band-edge and the surface trap state emission. Transition-metal-ion-doped QDs are yet another type of system with white light emission, including Mn^{2+}-doped CdS [93] and ZnS QDs [94], Mn^{2+}-doped ZnSe QDs [95–98], which typically combine emission of the surface state of the QDs with emission of the Mn^{2+} dopant. However, the surface state emission from all these kinds of QDs is rather difficult to control on demand.

CDs are yet another material system able to emit white light [99]. Chen and co-workers [100] reported on blue-, orange- and white-emitting CDs made from poly(styrene-co-glycidylmethacrylate) via a simple one-step pyrolysis procedure, which could be well dispersed in various polar organic solvents and in water, with maximum PL QYs of 47 %. WLEDs employing such white-emitting CDs were fabricated and used as backlights (Fig. 10) [101]. Another example of white light emitting CDs synthesized via a one-step pyrolysis of poly(acrylic acid) in the presence of glycerol has been reported by Chen et al. [102], who combined them within silica-based CDs/CdS QDs hybrids easily compatible with silicone to fabricate WLEDs with CIE coordinates of (0.27, 0.32).

Recently, WLEDs based on boehmite hybrid nanophosphors with PL QY up to 38 % were reported by Bai et al. [103], showing CIE of (0.32, 0.33), CRI of 85.5 and CCT of 6111 K. The white emission originating from metal oxide defects has been sensitized by a light harvesting carboxylate chromophore, leading to an enhancement of the emission quantum yield (EQY) and to a lowering of the excitation energy.

4 Electroluminescent WLEDs

All previously considered optically excited QD-based WLEDs are intrinsically point sources, wherein the pumping LED sources require complicated and expensive technological processing when integration on diffuse sources is required. In contrast, QD-based electroluminescent WLEDs (EL-WLEDs) relying on the direct charge carrier injection into the light emitting QD layer allow us to make full use of the easy solution processability of colloidal QDs, in order to achieve large-area, flat-panel, and even flexible light sources.

In the early stages of EL-WLED developments, predominantly inorganic/organic composite materials were used, with QDs providing red or orange color constituents of white light, whereas the blue and/or green color came from organic emitters. Park et al. [104] realized white light emission from polymer/QD nanocomposites consisting of blue emitting poly (9,9-dihexylfluorene-2,7-divinylene-m-phenylene-vinylene-stat-p-phenylenevinylene) and two kinds of CdSe QDs with red and green emission. In those and similar devices [105, 106], polymer/QD nanocomposites served not only as emitters, but also as charge transport materials. Tan and co-

workers [107] improved the color stability of binary complementary WLEDs over a wide voltage range using separately layered poly-TPD and CdSe/ZnS QD films. The CIE coordinates shifted only slightly from (0.32, 0.36) to (0.33, 0.37) with the bias voltage, varying from 7 V to 11 V, accompanying the luminance growing from 400 cd/m^2 to 2600 cd/m^2. In order to improve the electron injection efficiency and balance the charge carriers within the emissive layer, electron transport layers (ETL) were introduced. Li et al. [108] demonstrated hybrid organic/inorganic WLEDs with the introduction of a thin layer of electron-injecting and transporting metal chelate complex Alq_3 to accurately control and balance FRET and charge transfer processes between different components, achieving CIE of (0.30, 0.33) and EL efficiency of 0.24 %. Kang et al. [109] used the same ETL and optimized the hole transport layer (HTL) to fabricate WLEDs employing green and red emitting CdSe/ZnS QDs and blue emissive poly(9,9-dioctylfluorenyl-2,7-diyl) (PFO), achieving CIE coordinate of (0.33, 0.36). Cheng et al. [110] used a 2,2′,2″-(1,3,5-phenylene)tris(1-phenyl-1H-benzimidazole) (TPBi) layer as the ETL to fabricate WLEDs, relying on red emission from CdSe/ZnS QDs, green emission from tris[2-4(4-toltyl)phenylpyridine]iridium [Ir(mppy)$_3$], and blue emission from 2,2′,7,7′-tetrakis(2,2-diphenylvinyl)spiro-9,9′-bifluorene (Spiro-DPVBi), exhibiting CRI of 89.8 and reasonable EQE of 2.1 %.

In such QD/polymer-based WLEDs, a relatively easy degradation of the organic polymer resulted in shorter lifetimes and instability of the emitted color. With improvements in the quantum efficiency and photochemical stability of different color emitting QDs, the trend changed to employ solely QDs as active materials to realize WLEDs. Li et al. blended three differently sized CdSe/ZnS QDs in a 4,4′,*N*,*N*′-diphenylcarbazole (CBP) matrix to fabricate WLEDs while paying attention to balance the FRET, and charge trapping processes between them [111]. Anikeeva et al. [112] fabricated WLEDs by independently processing the organic charge transport layer (CTL) and the QD luminescent layer, allowing for the precise tuning of emission spectrum simply by altering the ratio of differently colored QDs in the active layer, without changing the device structure. Bae et al. [113] reported direct exciton formation within CdSe-based QDs active layers sandwiched between organic HTL and inorganic ETL, and demonstrated tetrachromatic (blue, cyan, yellow, red) WLEDs with high CRI (>92) and brightness

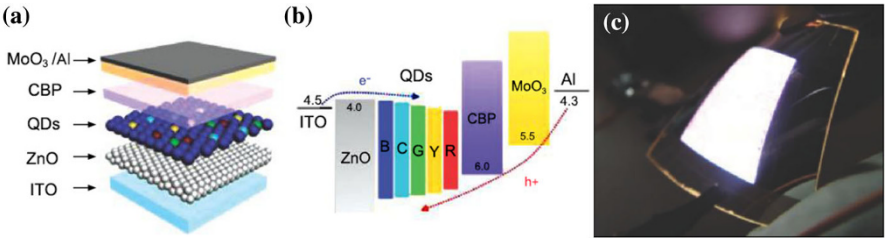

Fig. 11 Schematic illustrations of **a** device architecture; and **b** the energy band diagram of CdSe QD-based WLEDs, used to realise **c** a flexible plane lighting source on polyethersulphone substrate (pixel size 1.2 cm × 1.2 cm). Reproduced with permission from [113], © 2014 Wiley InterScience

satisfying the criteria for lighting (Fig. 11). The use of inorganic ETL prevented the underlying organic HTL from degradation by moisture and oxygen, and contributed to better performance of these devices. Most recently, all-solution processed WLEDs based on such organic/inorganic hybrid structures have been demonstrated, with record performance including maximum brightness of 23,352 cd/m^2, EQE of 10.9 % and current efficiency of 21.8 cd/A [114].

While initial efforts in EL-WLEDs were focused on the use of traditional CdSe-based core–shell QDs, upon improvement of PL QY and photostability of InP and CIS QDs, these low toxic nanoparticles attracted increasing attention as well. In 2011, Zhang et al. [115] demonstrated WLEDs with CRI of 92 using a bilayer of ZnCuInS/ZnS QDs and poly-TPD polymer as emissive components (Fig. 12a). One year later, similar device architecture was chosen for WLEDs using InP/ZnS QDs [116, 117]. The combined emission from red-emitting InP/ZnS QDs and blue-emitting poly-TPD was used to generate white light with CRI of 91 (Fig. 12d) [116]. In subsequent work, they deposited a loosely packed QD layer to form direct contact between HTL of poly-TPD and ETL of TPBi, and realized ternary white light with a blue emission from poly-TPD, green emission from InP/ZnS QDs and red exciplex emission from the interface between poly-TPD and TPBi, with a high CRI of 95 [117].

As discussed above, it may be advantageous to use single type QDs to generate white light. Schreuder et al. [118] reported on white electroluminescence from ultrasmall CdSe QDs (<2 nm) originated from trap states emission; their devices exhibited pure white CIE coordinates of (0.33, 0.33), high CRI up to 96.6, as well as cool white light ranging from 5461 to 6007 K. In another work, $CdSe_xS_{1-x}$ QDs with a green emission originating from the band edge recombination and a red

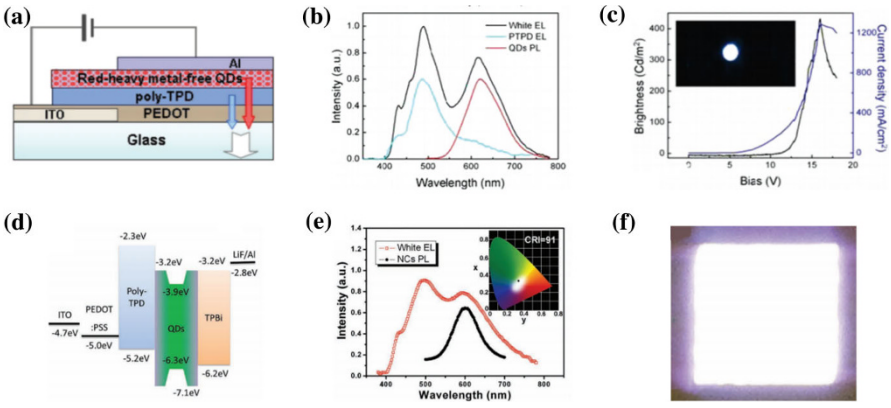

Fig. 12 **a** Structure of ZCIS/ZnS QDs/poly-TPD bilayer WLED, with **b** spectra of LED emission (*black*) at 15 V-bias, EL of net poly-TPD molecules (*blue*), and PL of QDs (*red*) in solution, and **c** brightness–voltage and current–voltage curves (*inset* image of LED with a brightness of 300 cd/m^2). **d** Energy band diagram of a WLED based on InP/ZnS QDs. **e** PL spectrum of red-emitting InP/ZnS QDs and EL spectrum of WLED (*inset* CIE coordinate of WLED). **f** Photograph of latter WLED with a pixel size of 3 mm × 3 mm. Reproduced with permission from [115], © 2011 American Chemical Society. Reproduced with permission from [116], © 2012 Wiley InterScience

emission from the surface states were employed in WLEDs to generate white light when combined with the blue emission from the hole transport material TPD [119]. One drawback of this kind of QDs is that the intensity of trap states emission depends strongly on the driven voltage, whereas the intensity of the band edge emission remains constant when the saturation emission is attained, causing overall instability of white light.

CD have also been employed recently as light-emissive layers of EL-WLEDs, reaching CRI of 82 [120]. Our own work on CD based EL-QLEDs [121] demonstrated the driving current controlled tunable emission color (blue, cyan, magenta, white, shown in Fig. 13b). By increasing the current density through the use of ZnO nanoparticles as ETL (Fig. 13c), WLEDs were realized (Fig. 13d).

5 FRET-Assisted WLEDs

Unlike previously considered down-conversion devices where excitons are formed as a result of a direct optical excitation by light, or EL-LEDs where they are formed by injection of charge carriers, Förster resonance energy transfer (FRET)-assisted devices may also result in white light, whereas excitons are non-radiatively

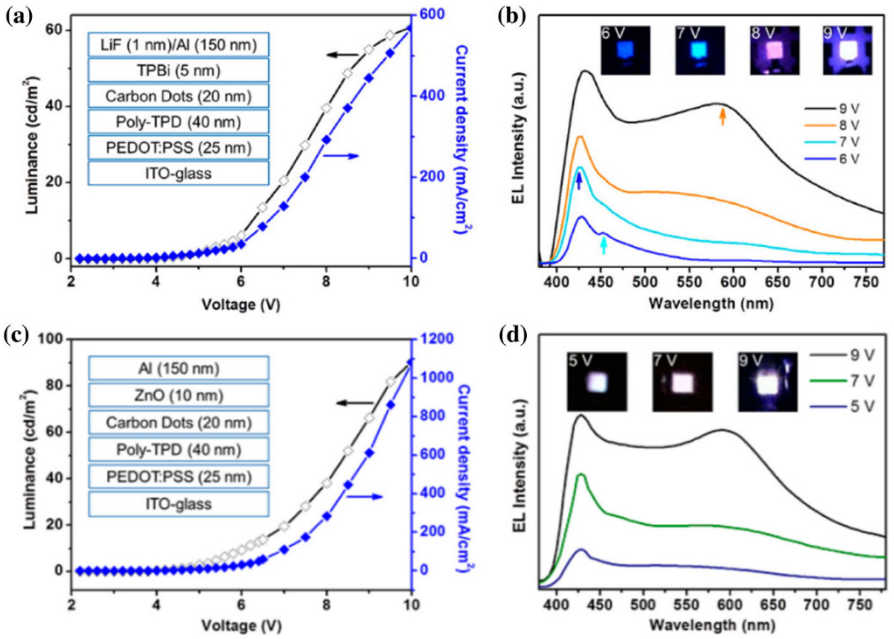

Fig. 13 **a** Current density and brightness of CD-based EL-QLEDs emitting *blue*, *cyan*, *magenta*, and *white light*, with an *inset* showing the device structure. **b** EL spectra and true-color photographs of *blue*, *cyan*, *magenta*, and *white* emissions. **c** current density and brightness of CD-WLEDs, with an *inset* showing the WLED architecture using ZnO nanoparticles as an ETL. **d** EL spectra of CD-WLEDs, with true-color photographs operated at different applied voltages. Reproduced with permission from [121], © 2013 American Chemical Society

transferred from the donor component (often a semiconductor quantum well, QWs) to the acceptor QDs. The occurrence of an efficient FRET requires a strong overlap between emission of the donor and absorption of the acceptor, and a short distance between both [122]. In 2004, Achermann et al. [123] reported the first demonstration of this concept, placing CdSe/ZnS QDs on a InGaN/GaN QW with a thin GaN capping layer (ca. 2 nm), and achieving FRET efficiency of 55 %. Thereafter, white light was generated by combining cyan emission from optically excited InGaN/GaN QW with a red emission from CdSe/ZnS QDs, with the emission intensity of the latter enhanced by 63 % as a result of FRET. CIE coordinates of (0.42, 0.39) and low CCT of 3135 K were obtained [124]. As pointed out by Achermann et al. [125], the reduction of coupling with an increasing QW–QDs separation (coupling being proportional to d^{-4}) dictated the use of exceedingly thin QW barrier layers, which would in turn increase nonradiative carrier losses in the QW and reduce injection efficiencies because of reduced carrier mobilities. In order to solve this issue, an inverted diode structure of *n-i-p* type instead of the regular *p-i-n* type was employed, where *n*-doped GaN layer had higher carrier mobility than in the *p*-doped region, allowing for higher current injection densities despite of a barrier layer of ca. 3 nm. The color conversion efficiency of the resulting devices reached nearly 10 %, compared with 3.5 % without FRET assistance.

As an alternative approach to increase the exciton transfer rate, and address the conflict between the need for close proximity of QWs and QDs and the use of a sufficiently thick capping layer on QW with a high current injection, top-down dry-etched nanohole [126, 127] or nanopillar [128–131] III-nitride structures have been demonstrated. Chanyawadee et al. [126] designed a QW–QD system where

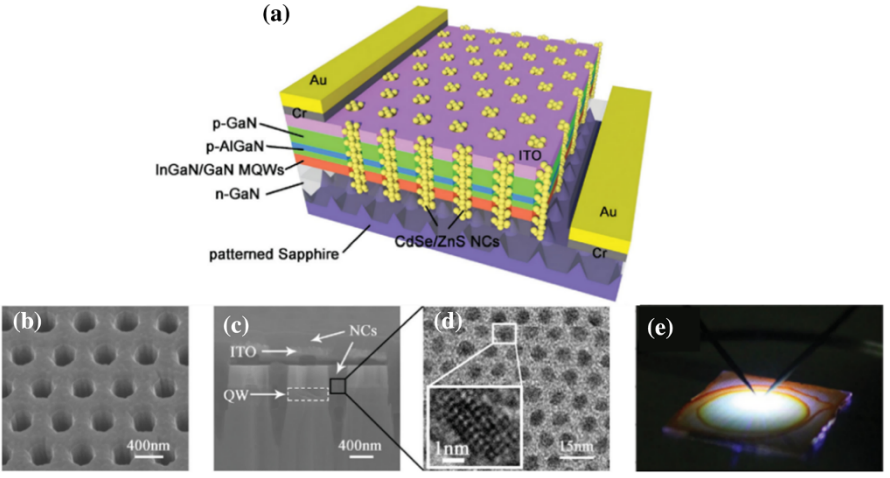

Fig. 14 **a** Schematic diagram of a hybrid nanohole-LED. **b** Scanning electron micrograph (SEM) image of ordered nanohole arrays with a transient outward potassium current (ITO) current spreading layer on the surface. **c** Cross-sectional view SEM image of nanoholes filled with QDs. **d** Transmission electron micrograph (TEM) image of CdSe/ZnS QDs; *inset* high-resolution image. **e** Photograph of the generated white light of hybrid nanohole-LED at the injection current of 20 mA. Reproduced with permission from [127], © 2015 Wiley InterScience

elliptical holes filled with QDs reached down to multi-QWs (called deep-etched LED), so that more excitons could be transferred to QDs. In this work, a reference LED—called shallow-etched LED in which QDs were far from multi-QWs—was fabricated. A color conversion efficiency of 20 %, as well as an energy transfer efficiency of 82 %, was achieved in deep-etched LED, which was 43 % higher than in the shallow-etched LED. Most recently, an excellent hybrid III-nitride (InGaN/GaN)/nanocrystal (CdSe/ZnS) nanohole light-emitting diode (h-LED) was demonstrated as shown in Fig. 14, which generated white light with CRI up to 82, and tunable CCT ranging from 2629 to 6636 K [127]. In such WLEDs, various color-emitting QDs were blended into nanohole arrays, and high color conversion efficiency (up to 69 %) and high QY (up to 93 %) were achieved, attributed to an efficient energy transfer efficiency of 80 %.

6 Summary and Outlook

In this review, we highlighted recent progress in QD-based WLEDs relying on optical excitation, direct charge injection, or FRET. Among these three kinds of devices, WLEDs based on the optical excitation of QDs nowadays achieve the best performance, reaching the criteria needed for commercial application. For instance, QD Vision Inc., in partnership with Nexxus Lighting, had already launched commercial products of QD-converted WLEDs. At the same time, the QDs in most widespread use are mostly Cd based II–VI materials, which raises concerns regarding the practical applicability of such devices due to restrictions on the toxic element cadmium. In response to this issue, cadmium-free InP, $CuInS_2$ and carbon-based nanoparticles have been considered as possible substitutes, while their PL QY still need further improvements to be able to compete with Cd based core–shell QD materials. Another issue for the large-scale production of QD-based down-conversion WLEDs is the compatibility of QDs with silicone or epoxy matrix. The exploration of other polymeric candidates with better compatibility with QDs is the focus of ongoing research. For EL-WLEDs, QD charging, QD luminescence quenching in closely packed nanoparticle films, and the large injection barrier from hole transport layer to QD emissive layer are still to be fully addressed. Despite these challenges, QDs are expected to occupy a solid placement in the lighting industry within the next decade.

Acknowledgments This work was supported financially by the National Natural Science Foundation of China (51272084, 61306078, 61225018, 61475062), the Jilin Province Key Fund (20140204079GX), Research Fund for the Doctoral Program of Higher Education (20130061110046), the Opened Fund of the State Key Laboratory on Integrated Optoelectronics (IOSKL2014KF14), and the Research Grant Council of Hong Kong S.A.R. (T23-713/11).

References

1. Tsao JY (2002) Light emitting diodes (LEDS) for general illumination. Optoelectronics Industry Development Association, Washington DC, pp 289–290

2. Bardsley N, Bland S, Pattison L, Pattison M, Stober K, Welsh F, Yamada M (2014) Solid-state-lighting research and development: multi-year program plan, No. DOE/EE-1089. US Department ofEnergy, Washington, DC
3. Shur MS, Žukauskas A (2005) Proc IEEE 93:1691–1703
4. Nizamoglu S, Zengin G, Demir HV (2008) Appl Phys Lett 92:031102–031104
5. Erdem T, Nizamoglu S, Sun XW, Demir HV (2010) Opt Express 18:340–347
6. Tsao JY (2004) Circuits and devices magazine. IEEE 20:28–37
7. Nakamura S, Fasol G (1997) The blue laser diode: GaN based light emitters and lasers. Springer, Berlin
8. Jang HS, Im WB, Dong CL, Jeon DY, Shi SK (2007) J Lumin 126:371–377
9. Wu H, Zhang X, Guo C, Xu J (2005) IEEE Photon Technol Lett 17:1160–1162
10. Xie RJ, Hirosaki N, Kimura N, Sakuma K, Mitomo M (2007) Appl Phys Lett 90:191101–191103
11. Xue B, Pucci A, Freitas VT, Ferreira RAS, Pinna N (2012) Adv Funct Mater 22:4275–4283
12. Wyszecki G, Stiles W (2000) Color science, 2nd edn. Wiley Interscience, New York
13. Krames MR, Shchekin OB, Mueller MR, Mueller GO, Zhou L, Harbers G, Craford MG (2007) J Disp Technol 3:160–175
14. Schubert EF (2006) Light-emitting diodes. University Press, Cambridge
15. Jang HS, Yang H, Kim SW, Han JY, Lee SG, Jeon DY (2008) Adv Mater 20:2696–2702
16. Jang HS, Kwon BH, Yang H, Jeon DY (2009) Appl Phys Lett 95:161901–161903
17. Shen CY, Li K, Hou QL, Feng HJ, Dong XY (2010) IEEE Photon Technol Lett 22:884–886
18. Chung W, Jung H, Lee CH, Kim SH (2013) J Ind Eng Chem 19:1743–1746
19. Kim K, Han CS, Jeong S (2012) J Mater Chem 22:21370–21372
20. Kim S, Kim T, Kang M, Kwak SK, Yoo TW, Park LS, Yang I, Hwang S, Lee JE, Kim SK (2012) J Am Chem Soc 134:3804–3809
21. Aboulaich A, Michalska M, Schneider RL, Potdevin A, Deschamps J, Deloncle R, Chadeyron GV, Mahiou R (2013) ACS Appl Mater Int 6:252–258
22. Chuang PH, Lin CC, Yang H, Liu RS (2013) J Chin Chem Soc 60:801–806
23. Chen B, Zhou Q, Li J, Zhang F, Liu R, Zhong H, Zou B (2013) Opt Express 21:10105–10110
24. Chuang PH, Lin CC, Liu RS (2014) ACS Appl Mater Int 6:15379–15387
25. Kim JU, Lee MH, Yang H (2008) Nanotechnology 19:465605–465609
26. Kim JU, Kim YS, Yang H (2009) Mater Lett 63:614–616
27. Wang X, Yan X, Li W, Sun K (2012) Adv Mater 24:2742–2747
28. Xuan TT, Liu JQ, Xie RJ, Li HL, Sun Z (2015) Chem Mater 27:1187–1193
29. Chen HS, Hsu CK, Hong HY (2006) IEEE Photon Technol Lett 18:193–195
30. Nizamoglu S, Demir H (2007) J Opt A Pure Appl Opt 9:S419–S424
31. Nizamoglu S, Ozel T, Sari E, Demir H (2007) Nanotechnology 18:065709–065713
32. Nizamoglu S, Erdem T, Sun XW, Demir HV (2010) Opt Lett 35:3372–3374
33. Adam M, Erdem T, Stachowski GM, Soranerdem Z, Lox J, Bauer C, Poppe J, Demir HV, Gaponik N, Eychmueller A (2015) ACS Appl Mater Int 7:23364–23371
34. Jing L, Kershaw SV, Kipp T, Kalytchuk S, Ding K, Zeng J, Jiao M, Sun X, Mews A, Rogach AL (2015) J Am Chem Soc 137:2073–2084
35. Lim J, Jun S, Jang E, Baik H, Kim H, Cho J (2007) Adv Mater 19:1927–1932
36. Talapin DV, Mekis I, Götzinger S, Kornowski A, Benson O, Weller H (2004) J Phys Chem B 108:18826–18831
37. Shea-Rohwer LE, Martin JE, Cai X, Kelley DF (2013) ECS J Solid State Sci Technol 2:R3112–R3118
38. Regulacio MD, Han MY (2010) Acc Chem Res 43:621–630
39. Deng Z, Yan H, Liu Y (2009) J Am Chem Soc 131:17744–17745
40. Xie R, Kolb U, Li J, Basché T, Mews A (2005) J Am Chem Soc 127:7480–7488
41. Bae WK, Char K, Hur H, Lee S (2008) Chem Mater 20:531–539
42. Bae WK, Nam MK, Char K, Lee S (2008) Chem Mater 20:5307–5313
43. Jang E, Jun S, Jang H, Lim J, Kim B, Kim Y (2010) Adv Mater 22:3076–3080
44. Kim K, Jeong S, Woo JY, Han CS (2012) Nanotechnology 23:065602–065608
45. Lee SH, Lee KH, Jo JH, Park B, Kwon Y, Jang HS, Yang H (2014) Opt Mater Express 4:1297–1302
46. Song WS, Yang H (2012) Chem Mater 24:1961–1967
47. Song WS, Kim JH, Lee JH, Lee HS, Do YR, Yang H (2012) J Mater Chem 22:21901–21908
48. Park SH, Hong A, Kim JH, Yang H, Lee K, Jang HS (2015) ACS Appl Mater Int 7:6764–6771
49. Chung W, Jung H, Lee CH, Kim SH (2012) Opt Express 20:25071–25076

50. Chen B, Zhong H, Wang M, Liu R, Zou B (2013) Nanoscale 5:3514–3519
51. Yuan X, Hua J, Zeng R, Zhu D, Ji W, Jing P, Meng X, Zhao J, Li H (2014) Nanotechnology 25:435202–435209
52. Kanelidis I, Vaneski A, Lenkeit D, Pelz S, Elsner V, Stewart RM, Rodríguez FJ, Lutich AA, Susha AS, Theissmann R (2011) J Mater Chem 21:2656–2662
53. Ziegler J, Xu S, Kucur E, Meister F, Batentschuk M, Gindele F, Nann T (2008) Adv Mater 20:4068–4073
54. Yang P, Ando M, Murase N (2011) Langmuir 27:9535–9540
55. Zhou C, Shen H, Wang H, Xu W, Mao M, Wang S, Li LS (2012) Nanotechnology 23:425601–435607
56. Kim H, Jang HS, Kwon BH, Suh M, Youngsun K, Cheong SH, Jeon DY (2011) Electrochem Solid State Lett 15:K16–K18
57. Kim YK, Choi KC, Ahn SH, Cho YS (2012) RSC Adv 2:6411–6413
58. Jang EP, Song WS, Lee KH, Yang H (2013) Nanotechnology 24:045607–045615
59. Song WS, Kim JH, Yang H (2013) Mater Lett 111:104–107
60. Jun S, Lee J, Jang E (2013) ACS Nano 7:1472–1477
61. Sohn IS, Unithrattil S, Im WB (2014) ACS Appl Mater Int 6:5744–5748
62. Kim YK, Choi KC, Baek YK, Shin PW (2014) Mater Lett 124:129–132
63. Zhou Z, Zhu Y, Chen W, Chen Y, Hao J, Wang K (2015) Electronic packaging technology (ICEPT). In: 2015 16th International Conference on. IEEE, pp 1287–1290
64. Xu X, Ray R, Gu Y, Ploehn HJ, Gearheart L, Raker K, Scrivens WA (2004) J Am Chem Soc 126:12736–12737
65. Wang Y, Hu A (2014) J Mater Chem C 2:6921–6939
66. Li CX, Yu C, Wang CF, Chen S (2013) J Mater Sci 48:6307–6311
67. Chen QL, Wang CF, Chen S (2013) J Mater Sci 48:2352–2357
68. Sun C, Zhang Y, Wang Y, Liu W, Kalytchuk S, Kershaw SV, Zhang T, Zhang X, Zhao J, William WY (2014) Appl Phys Lett 104:261106–261109
69. Sun C, Zhang Y, Sun K, Reckmeier C, Zhang T, Zhang X, Zhao J, Wu C, Yu WW, Rogach AL (2015) Nanoscale 7:12045–12050
70. Wang Y, Kalytchuk S, Zhang Y, Shi H, Kershaw SV, Rogach AL (2014) J Phys Chem Lett 5:1412–1420
71. Sun C, Zhang Y, Kalytchuk S, Wang Y, Zhang X, Gao W, Zhao J, Cepe K, Zboril R, Yu WW (2015) J Mater Chem C 3:6613–6615
72. Luk C, Tang L, Zhang W, Yu S, Teng K, Lau S (2012) J Mater Chem 22:22378–22381
73. Nizamoglu S, Mutlugun E, Ozel T, Demir HV, Sapra S, Gaponik N, Eychmuller A (2008) Appl Phys Lett 92:113110–113113
74. Soni U, Pal A, Singh S, Mittal M, Yadav S, Elangovan R, Sapra S (2013) ACS Nano 8:113–123
75. Zhang Z, Luan S, Huang K, Zhang Y, Shi Z, Xie R, Yang W (2015) J Mater Chem C 3:3614–3622
76. Zhang Z, Liu D, Li D, Huang K, Zhang Y, Shi Z, Xie R, Han MY, Wang Y, Yang W (2015) Chem Mater 27:1405–1411
77. Huang B, Dai Q, Zhuo N, Jiang Q, Shi F, Wang H, Zhang H, Liao C, Cui Y, Zhang J (2014) J Appl Phys 116:094303–094307
78. Peng L, Li D, Zhang Z, Huang K, Zhang Y, Shi Z, Xie R, Yang W (2015) Nano Res 8:3316–3331
79. Shea-Rohwer LE, Martin JE (2007) J Lumin 127:499–507
80. Sapra S, Mayilo S, Klar TA, Rogach AL, Feldmann J (2007) Adv Mater 19:569–572
81. Ozel T, Soganci IM, Nizamoglu S, Huyal IO, Mutlugun E, Sapra S, Gaponik N, Eychmüller A, Demir HV (2008) New J Phys 10:083035–083042
82. Nizamoglu S, Mutlugun E, Akyuz O, Perkgoz NK, Demir HV, Liebscher L, Sapra S, Gaponik N, Eychmüller A (2008) New J Phys 10:023026–023034
83. Padmaja S, Jayakumar S, Balaji R (2014) Mater Technol Adv Perform Mater 30:276–281
84. Bowers MJ, McBride JR, Rosenthal SJ (2005) J Am Chem Soc 127:15378–15379
85. Schreuder MA, Gosnell JD, Smith NJ, Warnement MR, Weiss SM, Rosenthal SJ (2008) J Mater Chem 18:970–975
86. Gosnell JD, Rosenthal SJ, Weiss SM (2010) IEEE Photon Technol Lett 2:541–543
87. Rosson TE, Claiborne SM, McBride JR, Stratton BS, Rosenthal SJ (2012) J Am Chem Soc 134:8006–8009
88. Harrell SM, McBride JR, Rosenthal SJ (2013) Chem Mater 25:1199–1210
89. Shen CC, Tseng WL (2009) Inorg Chem 48:8689–8694

90. Chen HS, Wang KW, Chen SS, Chung SR (2013) Opt Lett 38:2080–2082
91. Chen HS, Wang SJJ, Lo CJ, Chi JY (2005) Appl Phys Lett 86:131905–131907
92. Kwon BH, Jang HS, Yoo HS, Kim SW, Kang DS, Maeng S, Jang DS, Kim H, Jeon DY (2011) J Mater Chem 21:12812–12818
93. Nag A, Sarma D (2007) J Phys Chem C 111:13641–13644
94. Lü X, Yang J, Fu Y, Liu Q, Qi B, Lü C, Su Z (2010) Nanotechnology 21:115702–115711
95. Shao P, Wang H, Zhang Q, Li Y (2011) J Mater Chem 21:17972–17977
96. Panda SK, Hickey SG, Demir HV, Eychmüller A (2011) Angew Chem Int Ed 123:4524–4528
97. Lee SM, Hwang CS (2013) Bull Korean Chem Soc 34:321–324
98. Sharma VK, Guzelturk B, Erdem T, Kelestemur Y, Demir HV (2014) ACS App Mater Int 6:3654–3660
99. Wang F, Kreiter M, He B, Pang S, Liu CY (2010) Chem Commun 46:3309–3311
100. Guo X, Wang CF, Yu ZY, Chen L, Chen S (2012) Chem Commun 48:2692–2694
101. Mao LH, Tang WQ, Deng ZY, Liu SS, Wang CF, Chen S (2014) Ind Eng Chem Res 53:6417–6425
102. Chen J, Liu W, Mao LH, Yin YJ, Wang CF, Chen S (2014) J Mater Sci 49:7391–7398
103. Bai X, Caputo G, Hao Z, Freitas VT, Zhang J, Longo RL, Malta OL, Ferreira RA, Pinna N (2014) Nat Commun 5:5702–5709
104. Park JH, Kim JY, Chin BD, Kim YC, Kim JK, Park OO (2004) Nanotechnology 15:1217–1220
105. Xuan Y, Pan D, Zhao N, Ji X, Ma D (2006) Nanotechnology 17:4966–4969
106. Ahn JH, Bertoni C, Dunn S, Wang C, Talapin DV, Gaponik N, Eychmüller A, Hua Y, Bryce MR, Petty MC (2007) Nanotechnology 18:335202–335208
107. Tan Z, Hedrick B, Zhang F, Zhu T, Xu J, Henderson RH, Ruzyllo J, Wang AY (2008) IEEE Photon Technol Lett 20:1998–2000
108. Li Y, Rizzo A, Mazzeo M, Carbone L, Manna L, Cingolani R, Gigli G (2005) J Appl Phys 97:113501–113504
109. Kang BH, You TY, Yeom SH, Kim KJ, Kim SH, Lee SW, Yuan H, Kwon DH, Kang SW (2012) IEEE Photon Technol Lett 24:1594–1596
110. Cheng G, Mazzeo M, Rizzo A, Li Y, Duan Y, Gigli G (2009) Appl Phys Lett 94:243506–243508
111. Li Y, Rizzo A, Cingolani R, Gigli G (2006) Adv Mater 18:2545–2548
112. Anikeeva PO, Halpert JE, Bawendi MG, Bulovic V (2007) Nano Lett 7:2196–2200
113. Bae WK, Lim J, Lee D, Park M, Lee H, Kwak J, Char K, Lee C, Lee S (2014) Adv Mater 26:6387–6393
114. Lee KH, Han CY, Kang HD, Ko H, Lee C, Lee J, Myoung N, Yim SY, Yang H (2015) ACS Nano 9:10941–10949
115. Zhang Y, Xie C, Su H, Liu J, Pickering S, Wang Y, Yu WW, Wang J, Wang Y, Hahm JI (2010) Nano Lett 11:329–332
116. Yang X, Zhao D, Leck KS, Tan ST, Tang YX, Zhao J, Demir HV, Sun XW (2012) Adv Mater 24:4180–4185
117. Yang X, Divayana Y, Zhao D, Leck KS, Lu F, Tan ST, Abiyasa AP, Zhao Y, Demir HV, Sun XW (2012) Appl Phys Lett 101:233110–233113
118. Schreuder MA, Xiao K, Ivanov IN, Weiss SM, Rosenthal SJ (2010) Nano Lett 10:573–576
119. Liu B, Li R, Hu L, Wu H (2014) Appl Phys A 116:941–945
120. Wang F, Chen YH, Liu CY, Ma DG (2011) Chem Commun 47:3502–3504
121. Zhang X, Zhang Y, Wang Y, Kalytchuk S, Kershaw SV, Wang Y, Wang P, Zhang T, Zhao Y, Zhang H (2013) ACS Nano 7:11234–11241
122. Basko D, La Rocca G, Bassani F, Agranovich V (1999) Eur Phys J B 8:353–362
123. Achermann M, Petruska MA, Kos S, Smith DL, Koleske DD, Klimov VI (2004) Nature 429:642–646
124. Nizamoglu S, Sari E, Baek JH, Lee IH, Demir HV (2008) New J Phys 10:123001–123010
125. Achermann M, Petruska MA, Koleske DD, Crawford MH, Klimov VI (2006) Nano Lett 6:1396–1400
126. Chanyawadee S, Lagoudakis PG, Harley RT, Charlton MD, Talapin DV, Huang HW, Lin CH (2010) Adv Mater 22:602–606
127. Zhuang Z, Guo X, Liu B, Hu F, Li Y, Tao T, Dai J, Zhi T, Xie Z, Chen P (2015) Adv Funct Mater 26:36–43
128. Smith R, Liu B, Bai J, Wang T (2013) Nano Lett 13:3042–3047
129. Zhang F, Liu J, You G, Zhang C, Mohney SE, Park MJ, Kwak JS, Wang Y, Koleske DD, Xu J (2012) Opt Express 20:A333–A339

130. Nizamoglu S, Guzelturk B, Jeon DW, Lee IH, Demir HV (2011) Appl Phys Lett 98:163108–163110
131. Jiang B, Zhang C, Wang X, Park MJ, Kwak JS, Xu J, Zhang H, Zhang J, Xue F, Xiao M (2012) Adv Funct Mater 22:3146–3152

Top Curr Chem (Z) (2016) 374:54
DOI 10.1007/s41061-016-0052-0

REVIEW

Hybrid Semiconductor–Metal Nanorods as Photocatalysts

Yuval Ben-Shahar[1] · **Uri Banin**[1]

Received: 29 April 2016 / Accepted: 7 July 2016 / Published online: 1 August 2016

Abstract Semiconductor–metal hybrid nanoparticles manifest combined and often synergistic properties exceeding the functionality of the individual components, thereby opening up interesting opportunities for controlling their properties through the direct manipulation of their unique semiconductor–metal interface. Upon light absorption, these structures exhibit spatial charge separation across the semiconductor–metal junction. A significant and challenging application involves the use of these nanoparticles as photocatalysts. Through this process, the charge carriers transferred to the metal co-catalyst are available as reduction or oxidation reagents to drive the surface chemical reactions. In this review, we discuss synthesis approaches that offer a high degree of control over the hybrid nanoparticle structure and composition, the number of catalytic sites and the interfacial characteristics, including examples of a variety of photocatalyst architectures. We describe the structural and surface effects with regard to the functionality of hybrid nanosystems in photocatalysis, along with the effects of solution and chemical conditions on photocatalytic activity and efficiency. We conclude with a perspective on the rational design of advanced semiconductor–metal hybrid nanoparticles towards their functionality as highly efficient photocatalysts.

Keywords Hybrid nanoparticles · Photocatalysis · Charge separation and transfer dynamics · Hydrogen generation

This article is part of the Topical Collection “Photoactive Semiconductor Nanocrystal Quantum Dots” edited by Alberto Credi.

✉ Uri Banin
Uri.Banin@mail.huji.ac.il

[1] The Institute of Chemistry and Center for Nanoscience and Nanotechnology, The Hebrew University of Jerusalem, 91904 Jerusalem, Israel

1 Introduction

Over the last decade, hybrid semiconductor–metal nanoparticles (abbreviated as hybrid nanoparticles, HNPs) have garnered great interest in a variety of research fields and applications, including optics, electronics and catalytic reactions. Since the pioneering demonstration of site-selective Au metal growth on the apexes of CdSe nanorod structures [1, 2], the diversity of semiconductor–metal HNPs has been developed extensively. Through the use of advanced synthesis strategies, control over the size, position, composition and shape of the different HNP components has been achieved, allowing for further investigation of their unique synergistic properties and utilization in various applications [3–6]. One of the most appealing properties that arises at the semiconductor–metal nanojunction is charge separation following light absorption by the semiconductor component. Spatial separation is obtained due to the distinctive semiconductor–metal interface, where the Fermi level of the metal component is located within the band gap of the semiconductor valence and conduction band levels. Upon light excitation, an electron–hole pair is formed (exciton) at the semiconductor component, which is

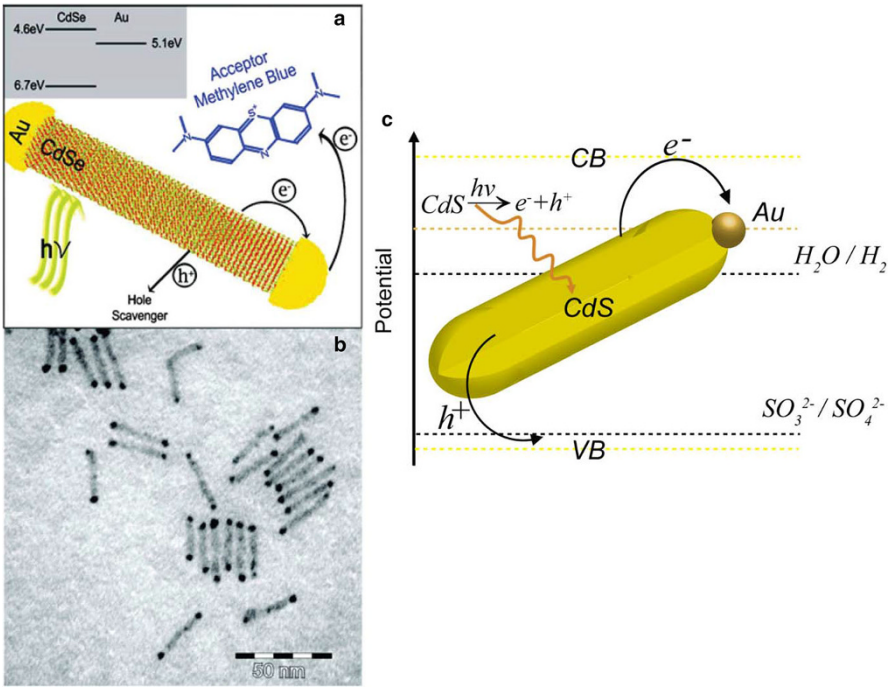

Fig. 1 **a** Scheme of a light-induced reduction of methylene blue molecules by CdSe–Au hybrid nanoparticles. The *inset* shows the energy band alignment between the CdSe rod and the Au domain. **b** TEM image of CdSe–Au hybrid nanodumbbells synthesized in aqueous solution. **c** Scheme of the photocatalytic water reduction reaction to evolve hydrogen by single-tipped CdS–Au semiconductor–metal hybrid nanorods in the presence of hole scavengers (e.g. sulfite) Adapted with permission from [7] and [20]. Copyright 2008 American Chemical Society and 2016 Nature Publishing Group

bound through the Coulomb interaction. The exciton can decay through recombination via radiative or non-radiative paths. In a typical situation, the presence of the co-joined metal provides an electron sink to promote the transfer of the excited electrons from the semiconductor conduction band into the metal energy levels, while the hole remains confined to the semiconductor component.

This characteristic light-induced charge transfer resulting in free charge carriers at the metallic domain has been found to be highly attractive for harvesting of light energy for photocatalytic reactions such as light-induced reduction of dyes, as was reported for CdSe–Au nanodumbbells [7] and shown in Fig. 1a, b. An additional challenging photocatalytic route that has been widely explored in recent years is water splitting for hydrogen generation [8–10], which opens the way for direct conversion of sustainable solar energy to chemical energy stored in chemical bonds of an alternative fuel. The proper combination of the two components, semiconductor and metal, allows tailoring of the band alignment of the system and therefore its potential to match the reduction potential of the desired redox reaction. In order to perform complete water splitting, the equilibrated Fermi level of the electrons must be more negative than the redox potential of H^+/H_2 (0 V versus NHE), while the edge of the valence band that accumulates the holes should be more positive than the redox potential of O_2/H_2O (1.23 V) [11]. A band alignment diagram of the CdS–Au HNPs is presented in Fig. 1c, alongside an illustration of photocatalytic hydrogen generation by HNPs in the presence of sacrificial hole scavengers (e.g. sulfite-Na_2SO_3).

An additional potential avenue in photocatalysis relates to the photoreduction of carbon dioxide using solar energy. This possibility is clearly thought-provoking, as it addresses the difficult problems of global warming through the reduction of greenhouse gas content while simultaneously offering a sustainable alternative pathway for the production of methane and other hydrocarbon fuels [12–14].

These charge separation and transfer processes, which promote the photocatalytic activity, require precise analysis and understanding, particularly with regard to the initial photophysical dynamics, which are essential for tailoring an optimal photocatalytic system with high efficiency. Recent research efforts in this promising direction have focused primarily on Cd chalcogenide-based nanoparticles [8, 15–20], which were the natural first choice due to their highly advanced synthesis, along with the highly developed understanding of their optical and electronic properties. In particular, quasi-one-dimensional rod structures were addressed, and were found to provide efficient spatial charge separation by limiting the loss of carriers through the competing route of direct recombination [21, 22].

Within this review, Sect. 2 presents the synthesis and structural characterization of different hybrid semiconductor–metal nanorods serving as photocatalyst model systems. Section 3 describes the effects of the structure of the HNPs, including their material composition, size and architecture, on charge separation dynamics and hydrogen generation efficiency. Followed by a discussion of the dependence of photocatalytic activity on the surface of HNPs, and the contribution of chemical solution conditions to the overall efficiency of photocatalytic reactions via HNPs. Section 4 provides a perspective on near-term future directions of research in such HNPs as photocatalysts.

2 Structural Properties of Hybrid Semiconductor–Metal Nanorods

Several synthesis mechanisms have been reported for growth of HNPs, and were reviewed previously [3, 5, 23]. Among these, metal growth at room temperature or at higher temperatures (thermal growth) and light-induced photodeposition are the most commonly applied. These growth strategies are based on the presence of a lower energy barrier for heterogeneous nucleation than with the homogeneous nucleation process of the secondary metal component on the semiconductor rod. This allows for the preferential growth of the metal on the rod rather than the formation of undesirable freestanding metal nanoparticles, and hence leads to the formation of crystalline phases of both components on the same HNP. Applying one or a sequential combination of these strategies allows for good control over the structural characteristics of the HNPs in terms of their morphology and composition, which ultimately lead to different chemical and physical properties. This section focuses on the synthesis and structural characterization of semiconductor–metal quasi-one-dimensional hybrid nanorod structures, with particular emphasis on their investigation and utilization as photocatalysts.

2.1 Selective Metal Deposition

Selective deposition of the metal phase may be dictated by the morphology and crystal structure of the semiconductor phase. The crystal morphology and surface capping provide different chemical reactivity for different facets of the semiconductor nanocrystal, which can lead to specific growth of the second-phase material on the more reactive facets of the nanocrystals of the first-phase material. The architecture of site deposition can be determined through various synthetic approaches. Both thermal and photochemical-induced metal growth methods can be used, resulting in different deposition patterns dependent on surface coating, reaction temperature, metal type, precursors and concentrations. Single-tipped CdS–Au and CdSe–Au nanorods were reportedly achieved via an electrochemical Ostwald ripening mechanism following multiple-site deposition on defect sites on the surface of the semiconductor component [2, 24]. However, the growth of metal islands on defects was found to be substantially suppressed by effective surface ligand capping and suitable temperature control, leading directly to selective growth of a single metal domain at the rod apex [25]. Moreover, in addition to thermodynamic factors that affect the metal decoration of the semiconductor surface, chemical conditions can promote single sites versus two sites on each apex, yielding dumbbell-like structures or multiple ‘body decorated’ HNPs, as was demonstrated for CdS–Au nanorods. While an inert atmosphere led to the growth of single metal domains on the apexes of the rod structure, in the presence of air and humidity, multiple-defect-site Au growth was obtained (Fig. 2) [26].

The effects of the semiconductor nanocrystal structure on site-specific metal deposition have also been also reported, in particular the influence of the CdSe seed domain in heterostructured seeded CdSe/CdS–Au HNPs. Metal growth preferentially occurred at the CdSe seed location following light-induced deposition

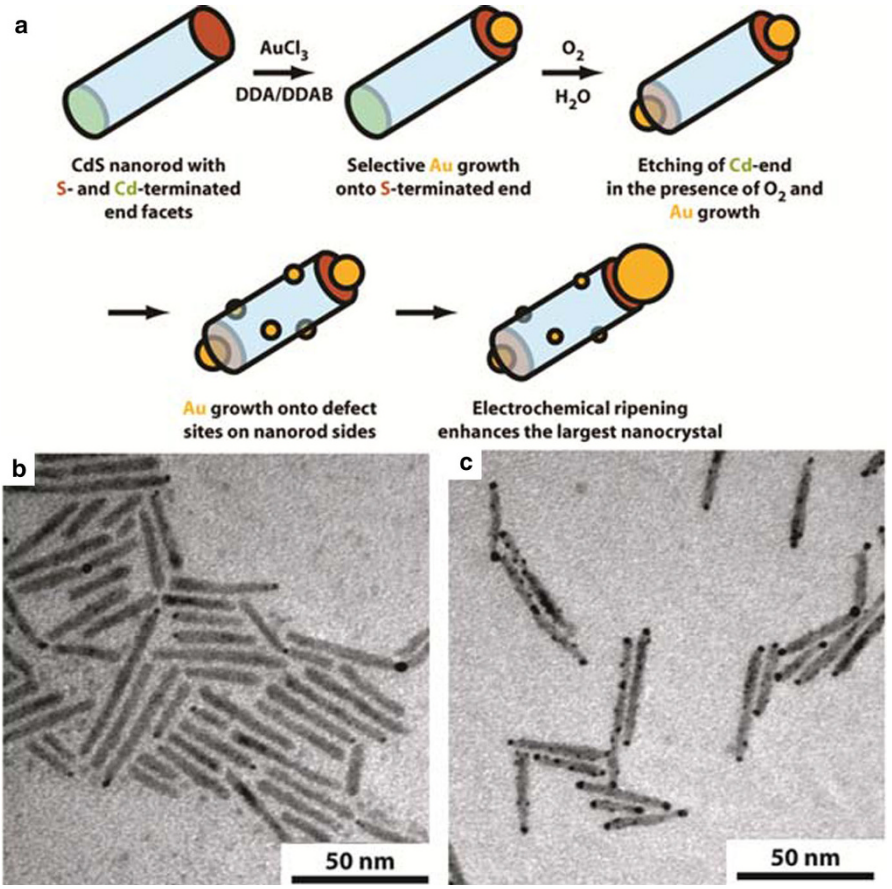

Fig. 2 **a** Schematic of the growth process of Au nanocrystals onto CdS nanorods. Without oxygen, gold grows only at one tip. In the presence of oxygen, the Cd-terminated end is etched, providing a second high-energy site for gold growth, followed by side growth. Comparison of gold growth under argon (**b**) and under air (**c**) after 3 h. Without oxygen, gold growth is slowed and occurs only at one end, producing small (typically $\leq$2 nm) nanocrystals. With oxygen, growth occurs at both tips, followed by growth onto defect sites Reproduced with permission from [26]. Copyright 2006 American Chemical Society

synthesis [27]. Another example of morphology dependence was demonstrated for cone-like CdSe/CdS tetrapods, which exhibited increased selectivity towards single-Au-tipped deposition as a result of the tapered arm structure, in comparison to regular tetrapods with cylinder-like arms [28]. The epitaxial relationship between the two components across the semiconductor–metal interface is important with respect to the charge transfer and hence the photocatalytic properties of the HNPs.

A different mechanism was suggested by Pyun and co-workers, whereby favorable heterogeneous growth on a pre-existing metal tip serving as a substrate allowed the growth of a second metal phase. Successive selective deposition of Co and Co_xO_y on Pt-tipped CdSe/CdS core/shell nanorods was obtained via kinetically

controlled synthesis [29]. The hollow cobalt oxide shell was achieved via the Kirkendall effect in the presence of O_2 under high temperature. Moreover, the formation of single or double Co/Pt core/shell tips was found to be determined by the Pt activation conditions. Very short activation times (<1 min), which resulted in the formation of Pt clusters on one apex of the CdSe/CdS nanorod structure, tended to afford matchstick Co-tipped nanorods. Longer activation times, which formed metallic Pt nanoparticles on the CdSe/CdS nanorod structure, yielded mostly dumbbell Co-tipped nanorods [30].

2.2 Morphology: Size and Shape Control

Although this section is focused on the quasi-one-dimensional nanorod structure, which relates mainly to the semiconductor component , the morphology of the metal co-catalyst has also been reported to play a key role in controlling and modifying photocatalytic performance. Morphological changes in shape and size are strongly associated with catalytic activity. This is well known and demonstrated for metal nanoparticles, which have revealed specific surface geometry and facet-dependent catalytic activity [31, 32]. HNPs with different sizes of metal co-catalyst domains can be obtained across extended regimes via diverse synthetic approaches. Deposition of small-cluster-size domain metal particles (up to ~200 atoms) was achieved using laser ablation methods [33],

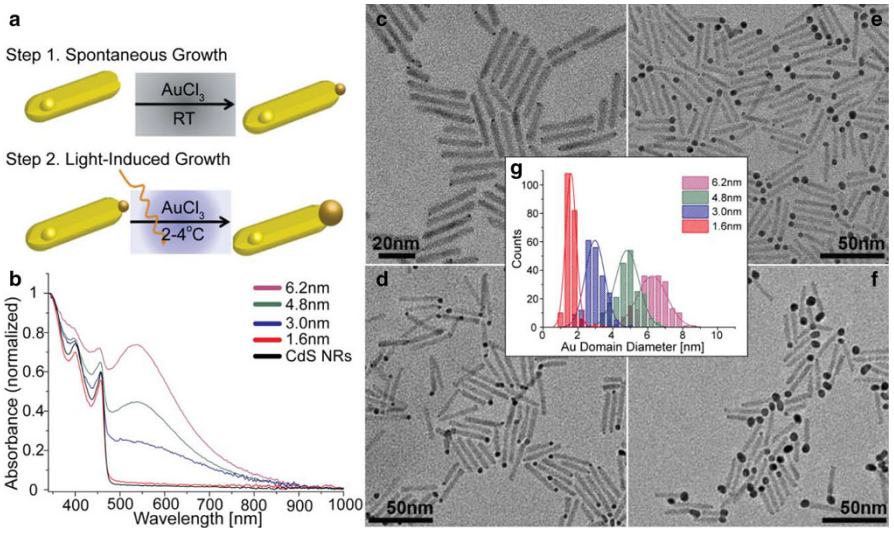

Fig. 3 **a** A scheme of the two-step metal growth deposition. **b** UV–vis absorbance spectra of CdS–Au hybrid nanorods showing the development of the plasmonic feature around 540 nm as the Au tip size increases. TEM images of CdS–Au hybrid nanoparticles with 1.5 ± 0.2-nm Au tip size after 1 h dark synthesis (**c**) and light-induced synthesis for 30 min with various CdS:Au molar ratios, leading to Au tip sizes of 3.0 ± 0.5 nm (**d**), 4.8 ± 0.7 nm (**e**) and 6.2 ± 0.8 nm (**f**). **g** Size distribution histogram of the Au metal tip diameters Adapted with permission from [20]. Copyright 2016 Nature Publishing Group

while larger sizes, from several to a few tens of nanometers, were achieved via controlling the reaction temperature [34] and/or precursor concentration [35]. An example of successful metal domain size control was reported for CdS–Au HNPs, where consecutive thermal and light-induced deposition strategies were used, as presented schematically in Fig. 3a [20]. First, a dark reaction was used to obtain site-selective growth of small metal islands on the apexes of the CdS nanorods (Fig. 3c). These small Au domains served as seeds for the second step, utilizing light-induced Au growth under an inert atmosphere and at low temperatures, 2–4 °C. This approach allows for size control by changing the irradiation time and the Au^{3+}/nanorod ratio. Figure 3d–f shows TEM images of CdS–Au hybrid nanoparticles with different Au tip sizes and with narrow size distribution (Fig. 3g). Absorption spectra of the bare CdS nanorods and CdS–Au hybrid nanoparticles with different Au tip sizes are presented in Fig. 3b. All spectra exhibit a similar sharp rise at 460 nm related to the onset of the CdS nanorod absorption, and a plasmon peak develops at 540 nm, correlated with the increase in the metal tip size.

In addition, control of the metal domain shape was achieved by selective deposition of faceted Pt metal tips on CdS nanorods [36]. This high level of morphology control may chart a path towards higher selectivity in photocatalysis, since the obtained cube-shaped Pt tips possess well-defined (100)-facets associated with higher catalytic selectivity [32].

2.3 Material Composition

In addition to the different metal domain architectures, the composition of different types of metals that serve as co-catalysts in HNPs has a significant effect on the efficiency of the charge dynamics and photocatalytic activity. Similar to Au growth strategies for different semiconductor nanoparticles presented above, the deposition of Pt metal domains on other semiconductor systems is widely reported [37–40]. Synthetic methods for both photodeposition [38] and thermal growth [37] can be used for the deposition of Pt, forming either single or multiple sites, similar to Au deposition. Pt metal growth has also been obtained in organic as well as in aqueous solutions [39]. Other metals have been grown as co-catalysts and have shown significant photocatalytic activity, including Ni [19, 41] and Pd [42, 43]. The choice of the metal co-catalyst is not only important for its catalytic properties, but it can also dictate the electronic properties and charge accumulation behavior. Whereas Pt deposition leads to ohmic-like contacts, Au spherical nanoparticles have exhibited charging and capacitance properties, as demonstrated for ZnO-Pt and ZnO–Au HNPs, respectively [44]. Moreover, combining two different metals on the same semiconductor–metal hybrid system through core/shell structures or by interfacial alloys can lead to new and improved chemical and physical characteristics. This concept mirrors the change in catalytic properties observed previously in bimetallic nanoparticle systems (Fig. 4) [45]. Studies have reported the deposition of alloys and core/shell co-catalyst structures such as PtNi [37], AuPt [46] and AuPd [43, 47, 48] on semiconductor nanorods, and have demonstrated their positive or negative effects on photocatalytic activity

and their effectiveness and stability in comparison to mono-metal domains. Recently synthesized ZnO-AuNi HNPs likewise showed enhanced photocatalytic reduction of rhodamine B dye molecules along with superparamagnetic properties [49].

Alongside the variety of metal co-catalyst materials, heterostructures of the semiconductor component have also been explored and tested for their effect on

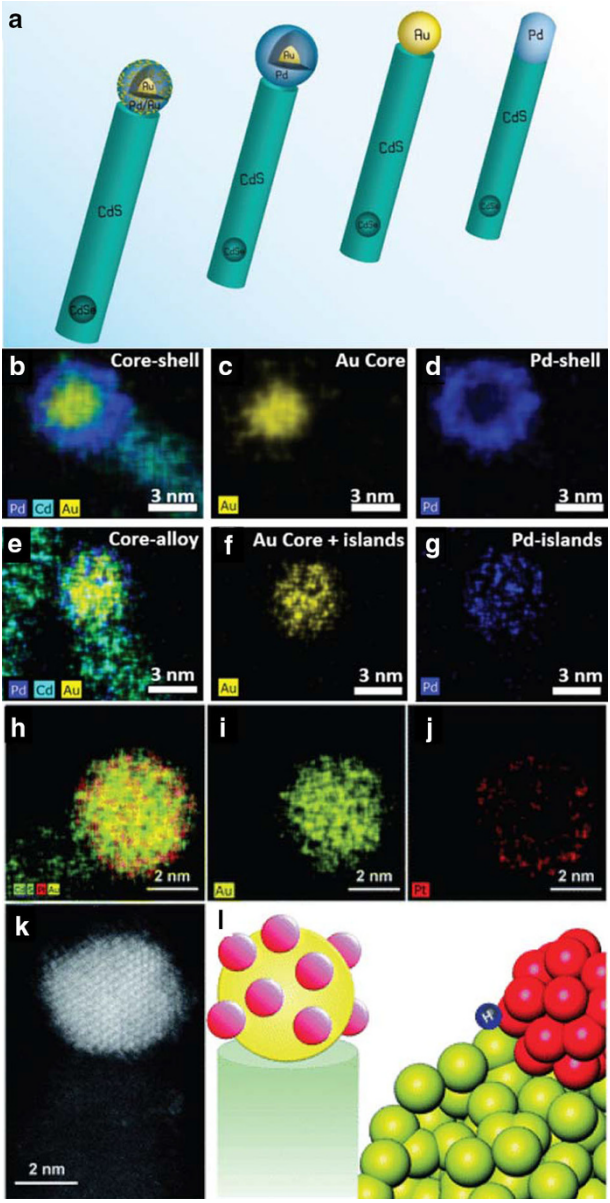

charge carrier separation and transfer and their photocatalytic efficiency. Initially, interior band alignment effects were found to be important. In particular, type II band alignment, where the two semiconductors display a staggered band structure, supports and promotes interior charge separation effects. Accordingly, quasi-type II and type II systems such as CdSe/CdS nanorods with small-diameter CdSe seed [8, 22] or ZnSe/CdS [18], respectively, were reported to be more efficient than CdS nanorods in photocatalysis. This is due to their enhanced charge separation behavior attributed to the confinement of the hole to the seed site, whereas the electron de-localizes and its wave function spreads along the CdS rod region [50]. Other strategies include the alloying of different elements in the semiconductor component, as was reported for $Cu_{1.94}S$–$Zn_xCd_{1-x}S$–Pt HNPs, in order to control and tailor its energy band gap, and therefore the hybrid band alignment, to achieve a material combination that manifests two light-absorbing regions towards more efficient charge transfer [51, 52]. Similar approaches have been taken in coupling between different semiconductor materials in a single rod structure such as CdS with Cu_2S via cation exchange or epitaxial growth [53, 54].

More recent synthesis efforts have addressed dual dissimilar-metal-site deposition, which will allow the promotion of different complementary catalytic reactions on the same nanosystem. In these multi-component hybrid architectures, both charge carriers, electron and hole, are expected to be exploited, resulting in a full catalytic cycle. For example, this strategy is especially important for performing a full water splitting reaction, where in a single excitonic cycle, both reduction and oxidation of water may take place. A demonstration of such a hybrid system was shown via synthetic combination of Ru–CdSe/CdS–Pt HNPs, in which the Ru and Pt metal sites served as co-catalysts for the water oxidation and reduction reactions, respectively [55].

3 Photo-Induced Charge Carrier Dynamics and Photocatalytic Efficiency

Understanding the dynamics of the excited charge carriers within the semiconductor component and across the semiconductor–metal junction enables the development of efficient light-harvesting materials. The fundamental exciton dynamics in the quasi-one-dimensional semiconductor nanorod structure have been extensively studied over the past decade [56–58]. Diverse electronic profiles such as single-phase CdS nanorods [17] and type I and quasi-type II CdSe/CdS nanorods [59] were

◀ **Fig. 4** **a** Schematic representation of the photocatalysts. CdS rod was grown on a CdSe core and then photo-deposited with metal tips. *From the left* Au-alloy, Au/Pd, Au and Pd tips. Energy-dispersive spectroscopy [EDS] elemental mapping of the bimetallic photocatalyst systems. The Au is in *yellow* and the Pd is in *blue*. The images to the *left* are overlays of the individual Au, Pd and Cd maps. Au/Pd core/shell tip (**b**), Au-alloy tip (**e**). Energy-dispersive X-ray spectroscopy micrographs with elemental mapping (**h**–**j**) and an atomic-resolution high-angle annular dark-field [HAADF] image (**k**) of the bimetallic tip, demonstrating the formation of an Au core that is decorated with islands of Pt (**l**). The Au–Pt boundary is suggested to be the catalytic active site Reproduced with permission from [43] and [46]. Copyright 2015 American Chemical Society and 2015 Royal Society of Chemistry

explored, and revealed different competitive relaxation routes with various decay lifetimes, including band gap radiative/non-radiative recombination routes and in-gap surface-state trapping. Controlling the material composition (e.g. heterostructured nanorods) [60], shape [61] and size [62] permits regulation of the spatial charge separation and affects photoluminescence properties. This inherent behavior is one of the foundations for the use of hybrid nanosystems in photocatalytic applications.

The primary synergistic property of HNPs that allows their use as efficient photocatalysts is the spatial charge separation upon light irradiation. As described above, following light absorption by the semiconductor component, an exciton (electron–hole pair) is formed. Due to band alignment between the semiconductor and the metal components, charge carriers separation is obtained where one carrier transfers to the metal domain states while the opposite carrier remains confined within the semiconductor region. For example, in CdS–Au, the electrons are transferred to the co-catalyst metal domain and are then able to perform surface redox reactions.

Reported light-induced charge separation times in HNPs are on the order of tens of picoseconds. Considering that the typical electron–hole radiative recombination times in semiconductor rods are tens of nanoseconds [1, 50], this route does not compete effectively with the charge transfer and separation processes [17, 18]. Other competing decay routes should also be considered and taken into account in efforts to develop highly effective HNP photocatalysts. The typical schematic energy level diagram for CdS–Au hybrid nanorods presented in Fig. 7b summarizes the charge transfer decay route along with the competing routes, including surface trapping and non-radiative back-recombination. In this specific case, the electrons are transferred to the Au metal domain (k_{ET}) by the favorable energy band offset, while the holes remain in the semiconducting CdS region. Following the charge separation, the holes can be extracted by suitable hole acceptor sacrificial agents (k_{HT}), which enables the accumulation of electrons in the metal tip to carry out the catalytic redox reaction (k_{WR}). These described routes compete with backward recombination processes, including electron–hole recombination (k_{e-h}) and the loss of electrons in the metal, by recombination with the holes in the CdS (k_{rec}) [20]. Furthermore, trapping of holes in surface defect states often takes place at a rate comparable to that of the electron transfer into the metal tip [22]. Once the hole is trapped, it blocks the electron transfer channel by the electron–hole Coulomb interaction, which also leads to a localization of the electron [9, 21]. This results in the loss of free electrons on the metal domain and thus the loss of catalytic reaction cycles.

Examination and evaluation of photocatalytic efficiency and charge carrier dynamics are commonly accomplished using gas chromatography and ultrafast spectroscopy techniques, respectively. Transient absorption (TA) and time-resolved fluorescence enable an unraveling of the primary physical processes taking place in the semiconductor–metal nanojunction following photoexcitation. Diverse temporal resolution is a prerequisite for understanding the processes occurring on a variety of time scales, in the range of 10^{-7} and 10^{-14} s, as described above.

As discussed in the previous section, several different model systems of HNPs have been investigated, with an emphasis on the charge carrier dynamics along with their associated photocatalytic activity. In each of these studies, structural

modulations, surface characteristics or environment condition parameters were altered and explored for their specific effects on the efficiency of both charge separation and photocatalysis. In this section, such case studies demonstrating the physical and chemical effects are presented. First, we discuss the structural effects, including the influence of size, type and composition of the metal co-catalysts, the selective versus multiple site metal deposition, and the characteristics of the heterostructured semiconductor component (Sect. 3.1). Next, we discuss the surface effects (Sect. 3.2), and lastly, we review the dependence on chemical/environmental conditions such as pH and hole scavenger identity (Sect. 3.3).

3.1 Structural Effects

The role of the exciton dynamics in relation to the semiconductor structure has been investigated primarily in prototypical TiO_2-based systems, and more recently in colloidal semiconductor–metal hybrid nanorods. These studies point to the potential for tailoring of the semiconductor component in the hybrid nanoparticles, permitting fine-tuning of the light absorption and electron–hole separation as preliminary steps towards charge separation and catalysis. HNPs with a type II or quasi-type II heterostructured semiconductor component, such as CdSe/CdS–Pt and ZnSe/CdS–Pt, have been reported to exhibit enhanced photocatalytic hydrogen generation in comparison to HNPs with single-phase semiconductor components [8, 18, 22]. Measurements of the charge carrier dynamics of the excited electron transfer to the metal domain were found to be slower ($\sim$14 ps) than with the single-phased CdS–Pt ($\sim$4 ps), due to reduced overlap between the semiconductor excited states and the metal unoccupied states. However, the hole localization at the seed region, which reduces both the electron–hole back-recombination and the hole trapping at the surface of the semiconductor shell, leads to overall improvement in the efficiency of photocatalytic hydrogen generation [18]. This trend was similarly shown for the reduction of organic dyes (MV^{2+}), in which 1.5-fold greater efficiency of activity was observed for a quasi-type II CdSe/CdS rod structure than with CdS rods [63].

Photocatalysis is also affected by the band alignment of the semiconductor and the stabilizing ligands on the HNP surface, as the ligands must still allow the extraction of holes and prevent electron–hole recombination. This was studied for ZnSe/CdS–Pt and ZnTe/CdS–Pt nanorods. Even though both of the HNPs possess a type II band structure, the latter showed no significant photocatalytic activity due to a mismatch of the ZnTe conduction band compared with the highest occupied molecular orbital (HOMO) of the surface ligand (mercaptoundecanoic acid, MUA) [64]. Another structural design was suggested for enhanced hole scavenging with regard to the semiconductor component. Etching of the rod shell in CdSe/CdS–Pt and exposing the holes at both the CdSe core and the electron-rich shell region to the external environment revealed improved catalytic performance of etched HNPs, with a three- to fourfold increase in the rate of hydrogen production (Fig. 5). Complementary time-resolved fluorescence measurements indicated that the etching treatment lowered the CdSe-to-ligand hole transfer time from 3.7 to 1.3 ns [65].

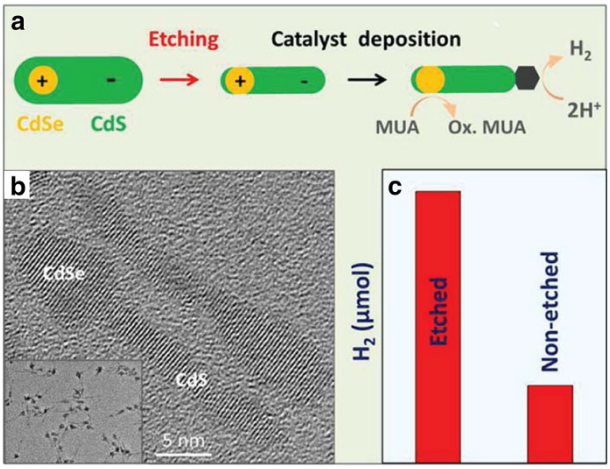

Fig. 5 **a** Removal of the outer CdS layer in a CdSe/CdS dot-in-a-rod structure results in a morphology where both donor and acceptor components are in direct contact with the external environment. Such modification increases the rate of hole regeneration, thereby improving the rate of sacrificial H_2 production. **b** A characteristic TEM image of an etched CdSe/CdS heterostructure is shown in the *inset*. **c** The associated rates of H_2 generation by etched and non-etched CdSe/CdS/Pt nanorods are shown in a *bar graph* Adapted with permission from [10]. Copyright 2015 American Chemical Society

The heterostructured semiconductor component effect can also govern the reactivity of the photocatalytic system. For example, a recent study showed that altering the structural composition enabled tuning of the photocatalytic function. CdS–Pt nanorods that were photoactive in water reduction were transformed via cation exchange to give CdS/Cu_2S-Pt, which revealed photocatalytic activity towards CO_2 reduction [54].

Another factor influencing the probability of recombination is the size of the semiconductor component [62]. However, several effects should be considered in this respect. For smaller nanoparticles, the distance that the charge carriers have to migrate to the active site decreases, and therefore the probability of recombining decreases accordingly [66]. On the other hand, size dependence can cause an opposite effect when dealing with heterostructured type II HNPs, as was demonstrated for CdSe/CdS–Pt nanorods, in which longer rods provided higher hydrogen production quantum yields due to better spatial charge separation along the rod length and reduced back-recombination [8].

In addition to semiconductor component dimension and composition, the characteristics of the metal co-catalyst may affect the total photocatalytic activity and charge carrier dynamics. As described above, synthetic development allowed either selective deposition of the metal domain on a single tip of the semiconductor rod or other types of decorations including double-tipped nanorods (dumbbells) and multiple metal islands across the entire semiconductor rod surface (defect growth). The photocatalytic efficiency of the site-selective single-tipped HNP exceeds that of the other architectures. The CdSe–Pt single tip revealed $\sim$50 % higher hydrogen

evolution rates in comparison to dumbbell CdSe–Pt nanorods [67]. CdSe/CdS–Pt HNPs have shown a similar trend, reflecting the advantage of the single site for the requirement of a photocatalytic reaction cycle in which two electrons on the same catalytic site are needed for hydrogen generation (Fig. 6). The probability of harvesting two electrons following two sequential photon absorption incidents is more likely to occur in the presence of a single metal site, whereas multiple sites randomly share the excited electrons, and larger overall successful charge transfer events are necessary for hydrogen evolution [68].

The type of metal co-catalyst also has a significant effect on both charge separation and photocatalytic performance. The two noble metals most commonly studied as co-catalysts in HNP systems are Au and Pt. Their charge separation and transfer processes are quite different, leading to differences in their photocatalytic activity. The Fermi-level equilibration and charge accumulation properties of Au-tipped HNPs [69] can promote rapid hot electron transfer from the semiconductor to the metal. In contrast, the ohmic behavior of Pt-tipped HNPs enables the full extraction of electrons from the lowest-excited states in the semiconductor rod. These effects were studied by ultrafast transient absorption measurements of CdSe–Au and CdSe–Pt HNPs, in which faster recovery of the bleach signal, which is attributable to the electron charge transfer, was seen for the CdSe–Au versus CdSe–Pt nanorods. However, the bleach recovery of the CdSe–Au was reported to reach only 80 % of the initial bleach signal, indicating remaining excited electrons at the CdSe rod due to suppressed charge transfer, in comparison to 100 % bleach recovery in the CdSe–Pt system [70]. Photocatalytic activity measurements comparing these two systems showed higher efficiency in the hydrogen generation reaction of the Pt-decorated HNPs due to the efficient depletion of excited electrons and well-known superior catalytic activity of Pt [46, 67]. In addition, photocatalytic systems of CdS and ZnS–$CuInS_2$ nanorods with various Pd_4S and PdO co-catalyst structures showed differences in photocatalytic hydrogen production efficiency. These differences were explained by the electronic effects of Fermi-level shifting or by structural effects leading to enhanced electron–hole recombination at different depositions [42, 71].

In addition to the type of metal domain, its composition can play a decisive role in photocatalysis. Alloys and core/shell bimetal sites such as CdSe/CdS–Au/Pd

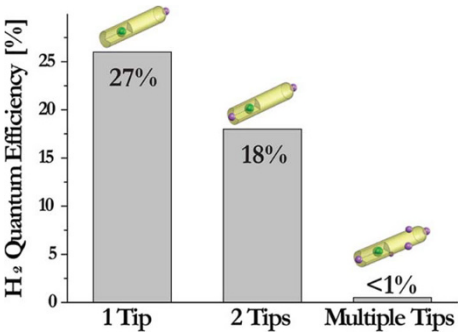

Fig. 6 Photocatalytic quantum efficiency for hydrogen generation by water reduction reaction obtained with CdSe/CdS nanorod photocatalysts decorated with single, double or multiple Pt reduction sites. Adapted with permission from [68] Copyright 2015 American Chemical Society

HNPs have demonstrated superior photocatalytic rates and efficiency compared to the single-phased metal deposition, showing an approximately fivefold increase, which was attributed to the synergistic electronic effects of bimetal catalysts [43]. Interestingly, the photocatalytic activity exhibited by islands with an alloy composition exceeded that of core/shell structures, along with improved longer-term stability. This enhanced stability was attributed to the suppression of cation exchange of Cd atoms in the rod structure with the presence of Au versus Pd tips upon light excitation, which leads to cation exchange [48]. A similar photocatalytic trend was demonstrated for CdSe/CdS–Au/Pt HNPs, where known catalytic properties of bimetallic nanoparticles were applied for hybrid semiconductor–metal

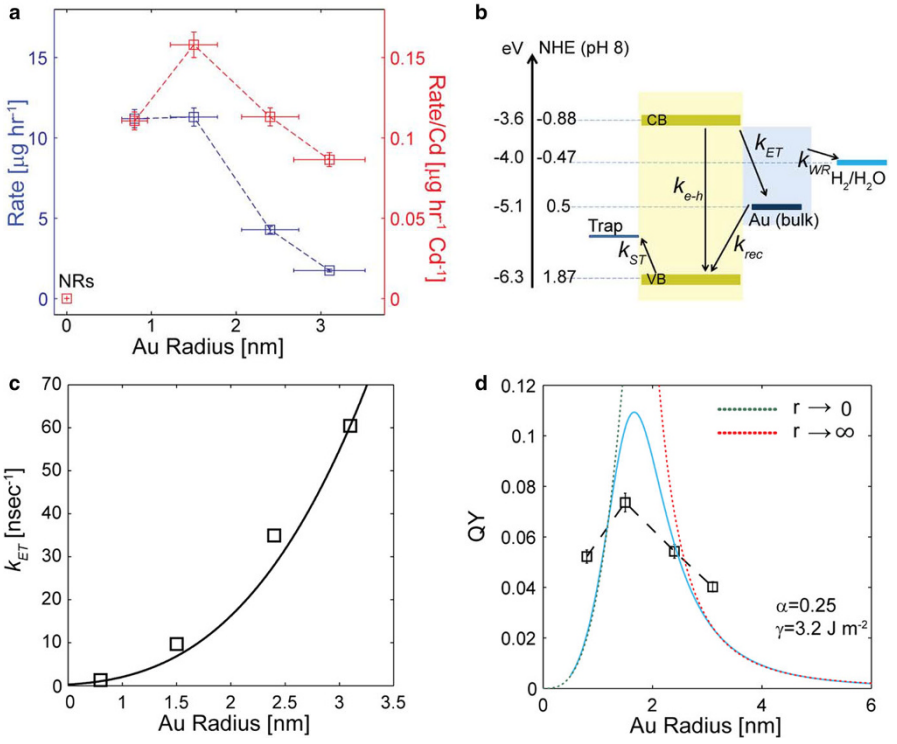

Fig. 7 **a** Hydrogen production rate (*blue*) and Cd normalized rate (*red*) curves as a function of Au size domain in the hybrid nanoparticles. Negligible rates are measured for the CdS nanorods. **b** Energy band alignment diagram with relevant photocatalytic processes kinetic routes. k_{ET} is the electron transfer rate from the CdS excited state to the Au metal domain. k_{rec} is the electron transfer rate from the Au metal domain to the ground state of CdS nanorods (this equals the rate of hole transfer to the metal). k_{WR} is the electron reduction rate of water molecules at the surface of the Au domain. k_{ST} is the electron or hole trapping rate. $k_{e\text{-}h}$ is the recombination rate to the ground state of the CdS valance band. **c** Measured semiconductor–metal electron transfer (k_{ET}) rates (*squares*) and fitting modified Fermi golden rule model for this process (*solid line*). **d** Measured QY (*black squares connected by dashed line*) along with the non-monotonic kinetic model behavior (*blue solid line*). *Green* and *red dotted lines* represent limiting behaviors of the model for zero and infinite metal domain sizes, respectively Adapted with permission from [20]. Copyright 2016 Nature Publishing Group

photocatalyst use. Co-catalyst Au tips decorated by Pt islands exhibited higher photocatalytic water reduction rates than Au and Pt mono-metal deposition. It was hypothesized that surface-bonding interactions favored for the Au–Pt interface contributed to the enhanced rate and efficiency [46].

Control over the size of the metal domain and its optimization is also suggested as an essential parameter for rational photocatalytic system design. Early studies discussed the effect of size on Fermi-level equilibration related to charging of the metal domain following irradiation of the system [44, 69]. The effect of the metal co-catalyst size, particularly with regard to hydrogen generation, was addressed in the context of TiO_2–Au HNPs and CdS–Pt nanorods with multiple metal domains [33, 72]. While no size effect was observed in the former for Au domains between 3 and 12 nm, optimal hydrogen generation in extremely small Pt clusters ($\sim$50 atoms) was reported in the latter. This size dependence has recently been explored in various semiconductor–metal nanostructures, with favorable photocatalytic activity reported for smaller co-catalyst domains [73–76]. However, the majority of these reports tested HNPs with multiple site deposition; hence, the ability to isolate the size effect from other contributing effects and to control the actual size of the co-catalysts rather than the weight percentage loading of the metal is quite limited. This was addressed in a systematic investigation of CdS–Au with a single catalytic domain in various metal sizes with narrow size distributions. Figure 7a (blue curve) shows the hydrogen generation rate versus Au tip size. A weak dependence observed for the two smallest sizes is followed by a marked rate decrease in the larger tips, overall by a factor of nearly 10, comparing the maximum and minimum rates. These results represent the actual hydrogen evolution rates, but they do not account for photons that are absorbed directly by the intraband transitions of the metal tip, and do not contribute to the generation of hydrogen due to their rapid relaxation. The total absorption of such CdS–Au hybrid nanoparticles can be considered in first approximation as the superposition of the contributions of the exciton and the plasmon [77]. The red curve in Fig. 7a corrects for this, by normalizing the rates to the semiconductor component absorption. Therefore, the red curve is normalized to the overall Cd content, which is proportional to the contribution of the semiconductor to the nanohybrid absorption. This normalization therefore expresses more cleanly the essential metal domain size effect in hydrogen reduction, revealing a non-monotonic dependence in which an intermediate Au tip size provides the optimal hydrogen evolution rate. In contrast, ultrafast TA measurements showed a monotonic increase in the electron transfer rate with Au tip size.

The essential behavior was captured by a minimal kinetic model. This model included all optional decay routes of the excited charge carriers (Fig. 7b), while charge separation was accounted for by applying a Fermi golden rule formula along with the water reduction reaction at the metal domain surface considered to behave as a Butler–Volmer equation. Figure 7c shows a calculation of the electron transfer rates by the kinetic model compared with the measured electron transfer rates obtained from the TA. The overall size dependence of this route is in good agreement with the theoretical prediction. The kinetic model simulation for hydrogen generation efficiency is presented in Fig. 7d (solid blue curve), and

manifests the non-monotonic dependence of the overall efficiency of photocatalytic hydrogen production on the Au tip size, consistent with the experimental measurements (squares connected by dashed line) [20].

3.2 Surface Effects

Colloidal nanosystems can be differentiated from other types of photocatalysts by the surrounding organic layer of ligands on their surface. The surface coating is required in order to provide colloidal stability in the relevant solvent, while at the same time maintaining good accessibility to the active surface sites from which charge carriers must be transferred for the reaction cycle to occur. As is known for optical and electronic applications, the surface coating can also affect trapping of light-generated charge carriers at surface defects, and therefore leads to changes in the radiative photoluminescence and inter-particle charge transport. This surface effect on photoluminescence (PL) quenching of CdSe/CdS nanorods was recently demonstrated by a comparison of CdSe/CdS–Au HNPs and CdSe/CdS nanorods in the presence of an Au precursor. Surprisingly, similar kinetic behavior of PL lifetime was observed, specifically during the first 3 ns, which are attributed to excited hole trapping, regardless of the formation or absence of Au metal domains. It was hypothesized that Au ion precursors could act as surface ligands [Au(I)-S bond], and by binding to the surface of the nanocrystal, promote efficient hole trapping, occurring in less than 3 ps, leading to PL quenching. Electron transfer in this case was observed only for the hybrid sample. However, the dynamics of the later process were significantly slower ($\sim$tens of ps) [78]. In photocatalysis applications, especially in the case of HNPs, trapping of excited charge carriers, usually holes, may reduce photocatalytic efficiency.

A comparison of the photocatalytic activity and efficiency of CdS–Au nanorods with different types of surface coatings, including common ligand exchange by thiolated alkyl molecules and polymer encapsulation by amphiphilic or branched polymers, has revealed a significant surface effect. As shown in Fig. 8, polyethylenimine (PEI) as polymer surface coating was found to exhibit a sixfold increase in the hydrogen generation quantum yield compared with several types of mercapto-alkyl ligands with different chain lengths or polar functional groups. The amphiphilic polymer coating in the form of poly(styrene-co-maleic anhydride) exhibited an intermediate quantum yield [9]. This trend in photocatalytic quantum yield was consistent with the electron transfer dynamics studied by transient absorption. The surface effect was attributed to the higher degree of surface passivation by the PEI polymer, resulting in reduced hole trapping and thus limited electron transfer to the metal domain due to electron–hole Coulomb interactions [21]. Time-resolved fluorescence measurements of related seeded nanorod systems were consistent with this explanation.

Notably, for quantum dot-based HNPs as photocatalysts, an inverse trend was reported, where better surface passivation caused poorer photocatalytic performance, since the catalytic mechanism is governed in those systems via defect

surface states [79]. This latter observation further underscores the role of the metal domain as an electron sink and co-catalyst site, and—more importantly—the complexity of the surface chemistry and its relevance for achieving efficient HNP photocatalysis.

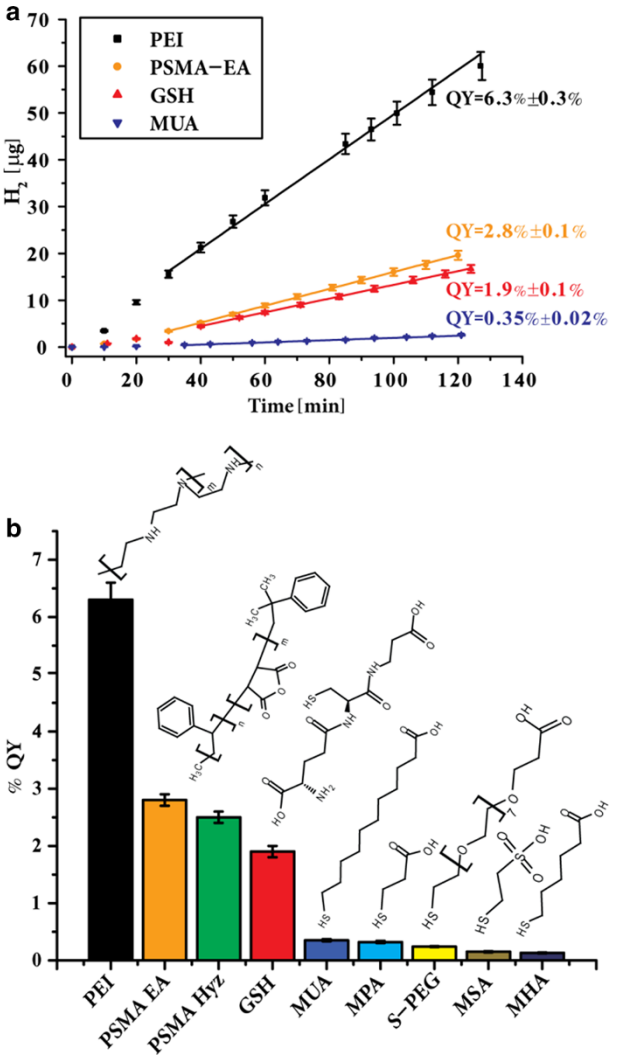

Fig. 8 **a** Kinetic hydrogen evolution measurements by CdS–Au HNPs for different surface coatings. *Straight lines* represent the linear fits from which the quantum yield was extracted. **b** Apparent photocatalysis quantum yield values for a wide range of surface coatings including thiolated alkyl ligands, glutathione (GSH), and polymer coating. PEI exhibits the highest quantum yield Adapted with permission from [9]. Copyright 2015 Wiley

3.3 Solution and Chemical Effects

The use of colloidal HNPs in photocatalysis is also affected by additional parameters of the solution and chemical conditions. As was described earlier, the ability to induce efficient spatial charge separation through the hybrid nanosystem is largely dependent on significant suppression of recombination and trapping routes of the excited charge carriers. In previous sections, we presented several strategies for enhancing electron transfer to the metal domain in order to avoid electron–hole recombination. Within this section, we focus on the extraction of holes as a factor in HNP photocatalysis. The effects of sacrificial hole acceptor agents and catalytic conditions on hole dynamics and photocatalysis are presented next.

The use of sacrificial agents such as sulfide/sulfite pair, alcohols, amines and other electron-donating molecules (ascorbic acid, cysteine, disodium ethylenediaminetetraacetic acid) or electron acceptors such as organic dyes (MV^{2+}, methylene blue), C60 or metal ions (Ag^{+}, Fe^{3+}) is commonly imposed where the counter charge carrier cannot be exploited to a complementary redox reaction. For photocatalytic hydrogen generation, to date there has been no report on full water-splitting HNP single-system photocatalysts that can effectively promote both reduction and oxidation of water. Therefore, in semiconductor–metal HNPs, the addition of a hole scavenger is used for extracting excited holes from the semiconductor component. The presence of a hole scavenger agent in the charge separation process was found to delay the electron transfer to the metal domain in CdS–Pt multiple-site deposition (Fig. 9a). Simulations of the presence and absence of sodium sulfite indicate that without the hole scavenger, electron–hole Coulomb interactions led to fast recombination near the metal domain that was formed at the surface trap site. However, upon the addition of a hole scavenger, the electron wave function is no longer localized, and therefore the transfer is delayed (Fig. 9b–d). A delayed charge transfer (8 ns) to the Pt islands was observed in comparison with the same HNP system without hole scavengers (0.4 ns) [21].

The type of hole scavenger is another factor in the photocatalytic activity of HNPs, as observed by introducing different hole scavengers to CdS–Pt nanorods, including SO_3^{2-}, triethanolamine, $EDTA^{4-}$, and methanol [80]. The effect of the hole scavenger identity was attributed to the redox potential of each of the tested agents, in that higher oxidation potential leads to more efficient hole removal, since more energy is gained by the recombination of the electron and excited hole. The low hole reduction rate correlated with loss of stability, attributed to photooxidation of the semiconductor rod itself.

However, the rational choice of hole acceptor should also take into account the composition and type of HNP photocatalyst. A comparison of the effect of two hole scavengers, methanol and sulfite, on the same HNPs, either CdS–Pt or CdSe/CdS–Pt, both coated by 11-mercaptoundecanoic acid (MUA), revealed different photocatalytic behavior. Although sulfite was found to enhance the rates of catalysis compared with methanol for both HNPs, relatively higher quantum efficiency was observed for CdSe/CdS–Pt using methanol, while higher quantum efficiency with sulfite was achieved in CdS–Pt (Fig. 10). In both HNPs, similar

electron transfer rates were measured, demonstrating that the hole transfer is a promising strategy for improving the photocatalytic reaction [22].

An additional approach for enhancing hole extraction was recently presented, which demonstrated that, in addition to the nature of the hole acceptor reagent, the reaction conditions had a significant effect on efficiency and rates of catalysis, particularly for hydrogen evolution in the water reduction reaction. Significant dependence on pH was observed for the photocatalytic activity of CdS–Ni HNPs. Under highly alkaline conditions, above pH 14, a steep increase in the reaction rate

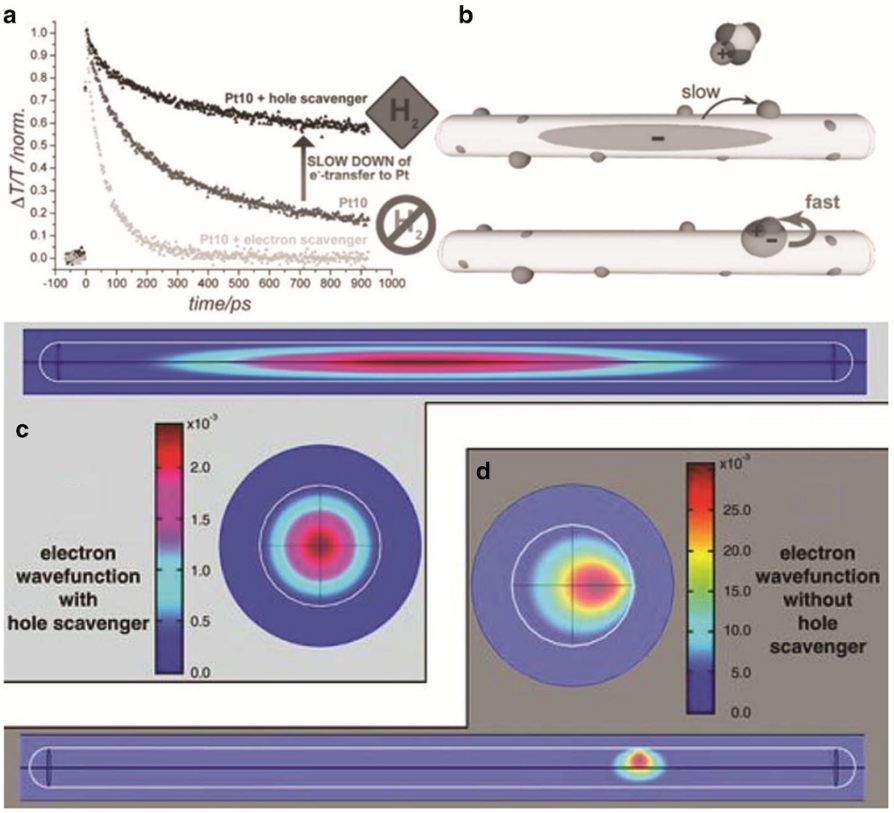

Fig. 9 **a** Experimental transient absorption traces of CdS–Pt HNPs without additives and in the presence of either hole or electron scavenger. **b** Schematic representation of the hypothesized explanation: under hydrogen generation conditions (i.e., in the absence of the holes on the nanorod), the electron wave function is de-localized, which leads to smaller spatial overlap with Pt clusters, and consequently lower transfer rate and subsequent hydrogen generation. In the presence of holes, the electron wave function is localized at the surface hole trap/Pt cluster site, which allows for fast electron transfer to the Pt but also oxidation of CdS, preventing significant hydrogen generation. Color plots of the calculated electron wave functions in the nanorods in the absence of a hole (**c**) and the presence of a hole in a surface trap (**d**). In the absence of the hole, the electron de-localizes symmetrically, while in its presence the electron is localized closer to the surface, with a larger local "spill-out" of the wave function into the classically forbidden region in the vicinity of the surface hole trap site Reproduced with permission from [21]. Copyright 2011 Wiley

appeared (Fig. 11b) and an improvement in the photocatalytic function reached 53 % external and 71 % internal quantum yield [19]. This substantial enhancement was ascribed to a redox shuttle mechanism, as suggested in the energy diagram in Fig. 11c. At high pH values, the redox potential of hydroxyl ($^{\cdot}OH/OH^{-}$), which follows Nernstian dependence (59 mV per pH unit), crosses and exceeds the energy level of the semiconductor valance band, which has a weaker pH dependence (33 mV per pH unit). This crossing allows the efficient reduction of excited holes at the valance band by the small molecular shuttle with higher mobility than the common hole scavengers. The intermediate product formation of the hydroxyl radical further promotes the hole acceptor molecule oxidation , such as ethanol to acetaldehyde and acetate, as illustrated in Fig. 11a. In contrast, at neutral pH, the hole scavenger oxidation is a direct process that slows the photocatalytic reaction due to loss of potential electrons via recombination routes when the holes are not reduced rapidly and efficiently. This trend was also observed for CdS–Pt nanorods, achieving a sixfold increase in hydrogen generation efficiency from pH 12 to pH 13 [81]. Similarly, in the case of CdSe/CdS–Pt nanorods, increasing the pH conditions even higher, up to pH 16, resulted in unity conversion of photons absorbed to hydrogen [82].

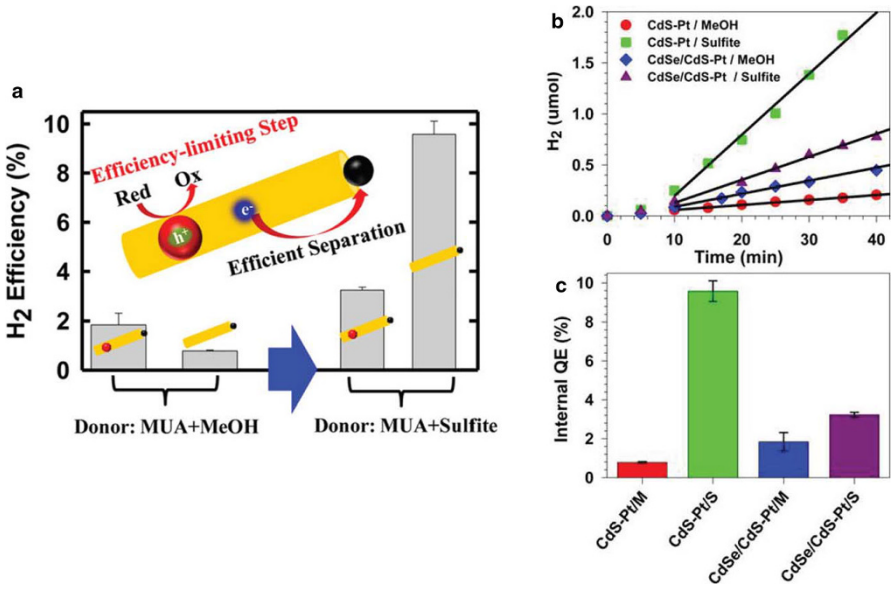

Fig. 10 **a** Steady-state H_2 photogeneration efficiency using MUA-capped CdSe/CdS–Pt and CdS–Pt nanorods. **b** Hydrogen evolution kinetics traces for CdS–Pt with methanol (*red circles*) and sulfite (*green squares*), and CdSe/CdS–Pt with methanol (*blue diamonds*) and sulfite (*purple triangles*) as electron donors. The *solid black lines* are linear fits to the traces from 10 to 40 min, from which the H_2 generation rates were determined. **c** Calculated H_2 generation internal quantum yields for CdS–Pt and CdSe/CdS–Pt with methanol or sulfite electron donors Adapted with permission from [22]. Copyright 2014 American Chemical Society

4 Outlook and Perspective

Semiconductor–metal hybrid nanoparticles have been proven to serve as efficient photocatalysts, with unique synergistic properties distinguished by their ability to fine-tune their optical, chemical and physical characteristics to address the extensive and diverse requirements of photocatalytic reactions. Recent research has led to an understanding of the primary physical mechanisms of charge carrier dynamics and design principles for achieving efficient photocatalytic activity. Thus far, however, these have been addressed on specific model systems. Yet to be developed are nanosystems that are more advanced in several aspects. First, as discussed above, the desired function of exploiting both charge carriers, electrons and holes, for the catalytic cycle following charge separation—in particular, full water splitting—is still challenging, and demands the implementation and integration of the obtained principles alongside further synthetic developments. Next, as products of these

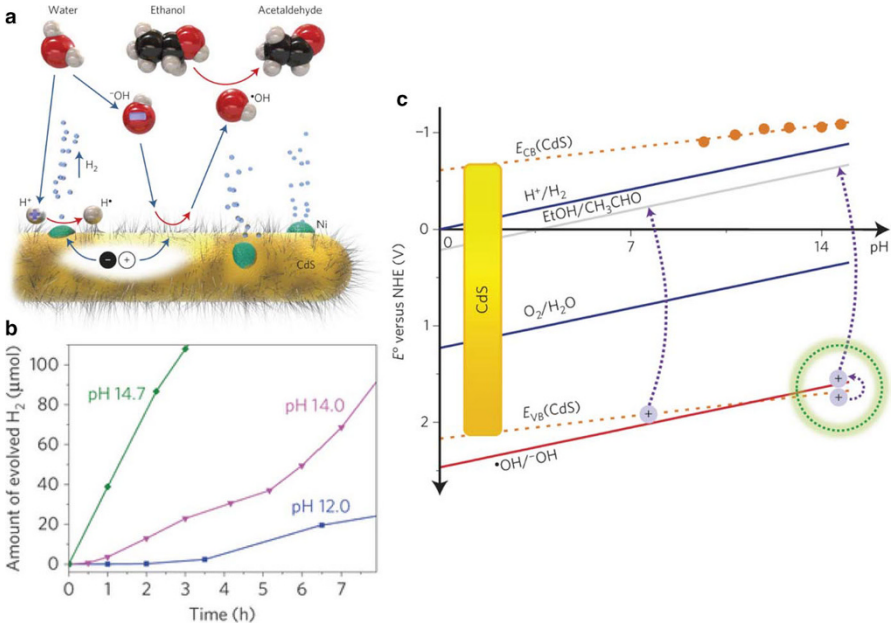

Fig. 11 **a** Scheme of the photocatalytic water reduction by CdS-Ni nanorods (cysteine-stabilized) at alkaline conditions. The photo-excited holes oxidize hydroxyl anions that, as a radical, carry away the positive charges and in turn oxidize ethanol to acetaldehyde. The *blue arrows* denote movement of the species; the *red arrows* denote a redox reaction. **b** Evolution of H_2 versus time under illumination by 20 mW cm^{-2} 447 nm laser light for pH 12.0, 14.0 and 14.7. **c** The electrochemical potentials of water reduction and oxidation, hydroxyl anion and ethanol oxidation follow Nernstian behavior (slope −59 mV/pH), but the dependence of CdS conduction and valence bands on pH is only −33 mV/pH. *Orange dots* correspond to measured conduction band minima. The *green circle* marks the region where energy of the valance band (CdS) is more positive than E°(·OH/−OH); the *violet arrows* denote the possibility of a two-step oxidation pathway at high pH versus a single-step process at lower pH Reproduced with permission from [19]. Copyright 2014 Nature Publishing Group

synthetic efforts towards more efficient HNP photocatalysts, a significant benefit can be achieved by expanding the diversity of HNPs, leading to the discovery of other photocatalytic pathways and reactions, as was recently demonstrated by promoting CO_2 reduction following cation exchange processes to form new heterostructured HNPs [54]. Moreover, HNP photocatalysts and co-catalysts of more earth-abundant elements are highly desired.

An additional aspect for enhancement of photocatalytic activity by HNPs lies in the nature of the semiconductor–metal nanojunction. Harvesting the absorbed photons in the metal domain and facilitating the hot plasmonic electron transfer to the semiconductor component may increase the overall photocatalytic quantum efficiency due to the preferable metallic light-absorption characteristics. However, efficient plasmon hot electron transfer requires interfacial charge separation at faster time scales, which is difficult to realize in many semiconductor–metal hybrid materials. Nevertheless, a new type of pathway, which allows direct generation of an electron in the semiconductor and a hole in the metal, was recently reported. The quantum efficiency of this process was found to exceed 24 %, which was attributed to the strong inter-domain coupling and mixing of the metal and semiconductor levels [83].

In summary, the high potential for semiconductor–metal hybrid nanoparticles as photocatalysts is far from being exhausted. The ongoing promising research in this field aims to develop more efficient and stable photocatalysts by further combination of systematic physical investigation and synthetic development based on the fundamental principles already established by the current HNP model systems.

Acknowledgments U.B. thanks the Alfred & Erica Larisch Memorial Chair. Y.B.S. acknowledges support from the Ministry of Science, Technology and Space, Israel, and the Camber Scholarship.

Funding This work was supported by The Israel Science Foundation (grant No. 1560/13).

References

1. Mokari T (2004) Selective growth of metal tips onto semiconductor quantum rods and tetrapods. Science (80-) 304:1787–1790. doi:10.1126/science.1097830
2. Mokari T, Sztrum CG, Salant A et al (2005) Formation of asymmetric one-sided metal-tipped semiconductor nanocrystal dots and rods. Nat Mater 4:855–863. doi:10.1038/nmat1505
3. Banin U, Ben-Shahar Y, Vinokurov K (2014) Hybrid semiconductor-metal nanoparticles: from architecture to function. Chem Mater 26:97–110. doi:10.1021/cm402131n
4. Vaneski A, Susha AS, Rodríguez-Fernández J et al (2011) Hybrid colloidal heterostructures of anisotropic semiconductor nanocrystals decorated with noble metals: synthesis and function. Adv Funct Mater 21:1547–1556. doi:10.1002/adfm.201002444
5. Costi R, Saunders AE, Banin U (2010) Colloidal hybrid nanostructures: a new type of functional materials. Angew Chem Int Ed 49:4878–4897. doi:10.1002/anie.200906010
6. Wu K, Lian T (2016) Quantum confined colloidal nanorod heterostructures for solar-to-fuel conversion. Chem Soc Rev 45:3781–3810. doi:10.1039/C5CS00472A
7. Costi R, Saunders AE, Elmalem E et al (2008) Visible light-induced charge retention and photocatalysis with hybrid cdse—au nanodumbbells. Nano Lett 8:637–641. doi:10.1021/nl0730514

8. Amirav L, Alivisatos AP (2010) Photocatalytic hydrogen production with tunable nanorod heterostructures. J Phys Chem Lett 1:1051–1054. doi:10.1021/jz100075c
9. Ben-Shahar Y, Scotognella F, Waiskopf N et al (2015) Effect of surface coating on the photocatalytic function of hybrid Cds-Au nanorods. Small 11:462–471. doi:10.1002/smll.201402262
10. Razgoniaeva N, Moroz P, Lambright S, Zamkov M (2015) photocatalytic applications of colloidal heterostructured nanocrystals: what's next? J Phys Chem Lett 6:4352–4359. doi:10.1021/acs.jpclett.5b01883
11. Maeda K, Domen K (2010) Photocatalytic water splitting: recent progress and future challenges. J Phys Chem Lett 1:2655–2661. doi:10.1021/jz1007966
12. Varghese OK, Paulose M, LaTempa TJ, Grimes CA (2009) High-rate solar photocatalytic conversion of co 2 and water vapor to hydrocarbon fuels. Nano Lett 9:731–737. doi:10.1021/nl803258p
13. Roy SC, Varghese OK, Paulose M, Grimes CA (2010) Toward solar fuels: photocatalytic conversion of carbon dioxide to hydrocarbons. ACS Nano 4:1259–1278. doi:10.1021/nn9015423
14. Habisreutinger SN, Schmidt-Mende L, Stolarczyk JK (2013) Photocatalytic reduction of CO_2 on TiO_2 and other semiconductors. Angew Chem Int Ed 52:7372–7408. doi:10.1002/anie.201207199
15. Bao N, Shen L, Takata T, Domen K (2008) Self-templated synthesis of nanoporous cds nanostructures for highly efficient photocatalytic hydrogen production under visible light. Chem Mater 20:110–117. doi:10.1021/cm7029344
16. Costi R, Cohen G, Salant A et al (2009) Electrostatic Force Microscopy Study of Single Au–CdSe hybrid nanodumbbells: evidence for light-induced charge separation. Nano Lett 9:2031–2039. doi:10.1021/nl900301v
17. Wu K, Zhu H, Liu Z et al (2012) Ultrafast charge separation and long-lived charge separated state in photocatalytic CdS-Pt nanorod heterostructures. J Am Chem Soc 134:10337–10340. doi:10.1021/ja303306u
18. O'Connor T, Panov MS, Mereshchenko A et al (2012) The effect of the charge-separating interface on exciton dynamics in photocatalytic colloidal heteronanocrystals. ACS Nano 6:8156–8165. doi:10.1021/nn302810y
19. Simon T, Bouchonville N, Berr MJ et al (2014) Redox shuttle mechanism enhances photocatalytic H_2 generation on Ni-decorated CdS nanorods. Nat Mater 13:1013–1018. doi:10.1038/nmat4049
20. Ben-Shahar Y, Scotognella F, Kriegel I et al (2016) Optimal metal domain size for photocatalysis with hybrid semiconductor-metal nanorods. Nat Commun 7:10413. doi:10.1038/ncomms10413
21. Berr MJ, Vaneski A, Mauser C et al (2012) Delayed photoelectron transfer in Pt-decorated CdS nanorods under hydrogen generation conditions. Small 8:291–297. doi:10.1002/smll.201101317
22. Wu K, Chen Z, Lv H et al (2014) Hole removal rate limits photodriven H_2 generation efficiency in CdS-Pt and CdSe/CdS-Pt semiconductor nanorod-metal tip heterostructures. J Am Chem Soc 136:7708–7716. doi:10.1021/ja5023893
23. Carbone L, Cozzoli PD (2010) Colloidal heterostructured nanocrystals: synthesis and growth mechanisms. Nano Today 5:449–493. doi:10.1016/j.nantod.2010.08.006
24. Figuerola A, Van Huis M, Zanella M et al (2010) Epitaxial CdSe-Au nanocrystal heterostructures by thermal annealing. Nano Lett 10:3028–3036. doi:10.1021/nl101482q
25. Menagen G, Macdonald JE, Shemesh Y et al (2009) Au growth on semiconductor nanorods: photoinduced versus thermal growth mechanisms. J Am Chem Soc 131:17406–17411. doi:10.1021/ja9077733
26. Saunders AE, Popov I, Banin U (2006) Synthesis of hybrid CdS–Au colloidal nanostructures. J Phys Chem B 110:25421–25429. doi:10.1021/jp065594s
27. Sitt A, Della Sala F, Menagen G, Banin U (2009) Multiexciton engineering in seeded core/shell nanorods: transfer from type-I to quasi-type-II regimes. Nano Lett 9:3470–3476. doi:10.1021/nl901679q
28. Mishra N, Lian J, Chakrabortty S et al (2012) Unusual selectivity of metal deposition on tapered semiconductor nanostructures. Chem Mater 24:2040–2046. doi:10.1021/cm300161m
29. Hill LJ, Bull MM, Sung Y et al (2012) Directing the deposition of ferromagnetic cobalt onto Pt-tipped CdSe@CdS nanorods: synthetic and mechanistic insights. ACS Nano 6:8632–8645. doi:10.1021/nn3019859
30. Hill LJ, Richey NE, Sung Y et al (2014) Synthesis of ferromagnetic cobalt nanoparticle tipped CdSe@CdS nanorods: critical role of Pt-activation. Cryst Eng Comm 16:9461–9468. doi:10.1039/C4CE00680A

31. Wang C, Daimon H, Onodera T et al (2008) A general approach to the size- and shape-controlled synthesis of platinum nanoparticles and their catalytic reduction of oxygen. Angew Chem Int Ed 47:3588–3591. doi:10.1002/anie.200800073
32. Bratlie KM, Lee H, Komvopoulos K et al (2007) Platinum nanoparticle shape effects on benzene hydrogenation selectivity. Nano Lett 7:3097–3101. doi:10.1021/nl0716000
33. Schweinberger FF, Berr MJ, Döblinger M et al (2013) Cluster size effects in the photocatalytic hydrogen evolution reaction. J Am Chem Soc 135:13262–13265. doi:10.1021/ja406070q
34. Khon E, Hewa-Kasakarage NN, Nemitz I et al (2010) Tuning the morphology of Au/CdS nanocomposites through temperature-controlled reduction of gold-oleate complexes. Chem Mater 22:5929–5936. doi:10.1021/cm101922m
35. O'Sullivan C, Gunning RD, Barrett CA et al (2010) Size controlled gold tip growth onto II–VI nanorods. J Mater Chem 20:7875. doi:10.1039/c0jm01689f
36. Schlicke H, Ghosh D, Fong L-K et al (2013) Selective placement of faceted metal tips on semiconductor nanorods. Angew Chem 125:1014–1016. doi:10.1002/ange.201205958
37. Habas SE, Yang P, Mokari T (2008) Selective growth of metal and binary metal tips on CdS nanorods. J Am Chem Soc 130:3294–3295. doi:10.1021/ja800104w
38. Dukovic G, Merkle MGMG, Nelson JHJH et al (2008) Photodeposition of Pt on colloidal CdS and CdSe/CdS semiconductor nanostructures. Adv Mater 20:4306–4311. doi:10.1002/adma.200800384
39. Elmalem E, Saunders AE, Costi R et al (2008) Growth of photocatalytic CdSe-Pt nanorods and nanonets. Adv Mater 20:4312–4317. doi:10.1002/adma.200800044
40. Berr M, Vaneski A, Susha AS et al (2010) Colloidal CdS nanorods decorated with subnanometer sized Pt clusters for photocatalytic hydrogen generation. Appl Phys Lett 97:093108. doi:10.1063/1.3480613
41. Han Z, Qiu F, Eisenberg R et al (2012) Robust photogeneration of H_2 in water using semiconductor nanocrystals and a nickel catalyst. Science (80-) 338:1321–1324. doi:10.1126/science.1227775
42. Shemesh Y, Macdonald JE, Menagen G, Banin U (2011) Synthesis and photocatalytic properties of a family of CdS-PdX hybrid nanoparticles. Angew Chem Int Ed 50:1185–1189. doi:10.1002/anie.201006407
43. Aronovitch E, Kalisman P, Mangel S et al (2015) Designing bimetallic co-catalysts: a party of two. J Phys Chem Lett 6:3760–3764. doi:10.1021/acs.jpclett.5b01687
44. Wood A, Giersig M, Mulvaney P (2001) Fermi level equilibration in quantum dot—metal nanojunctions. J Phys Chem B 105:8810–8815. doi:10.1021/jp011576t
45. Xia Y, Xiong Y, Lim B, Skrabalak SE (2009) Shape-controlled synthesis of metal nanocrystals: simple chemistry meets complex physics? Angew Chem Int Ed 48:60–103. doi:10.1002/anie.200802248
46. Kalisman P, Houben L, Aronovitch E et al (2015) The golden gate to photocatalytic hydrogen production. J Mater Chem A 3:19679–19682. doi:10.1039/C5TA05784A
47. Li X, Lian J, Lin M, Chan Y (2011) Light-induced selective deposition of metals on gold-tipped CdSe-seeded CdS nanorods. J Am Chem Soc 133:672–675. doi:10.1021/ja1076603
48. Aronovitch E, Kalisman P, Houben L et al (2016) Stability of seeded rod photocatalysts: atomic scale view. Chem Mater 28:1546–1552. doi:10.1021/acs.chemmater.6b00040
49. Zeng D, Chen Y, Wang Z et al (2015) Synthesis of Ni–Au–ZnO ternary magnetic hybrid nanocrystals with enhanced photocatalytic activity. Nanoscale 7:11371–11378. doi:10.1039/C5NR01124H
50. Sitt A, Hadar I, Banin U (2013) Band-gap engineering, optoelectronic properties and applications of colloidal heterostructured semiconductor nanorods. Nano Today 8:494–513. doi:10.1016/j.nantod.2013.08.002
51. Li Q, Meng H, Zhou P et al (2013) Zn 1 − x Cd × S solid solutions with controlled bandgap and enhanced visible-light photocatalytic H_2—production activity. ACS Catal 3:882–889. doi:10.1021/cs4000975
52. Chen Y, Zhao S, Wang X et al (2016) Synergetic integration of Cu 1.94 S-Zn × Cd 1 – x S heteronanorods for enhanced visible-light-driven photocatalytic hydrogen production. J Am Chem Soc 138:4286–4289. doi:10.1021/jacs.5b12666
53. Plante IJ, Teitelboim A, Pinkas I et al (2014) Exciton quenching due to copper diffusion limits the photocatalytic activity of CdS/Cu 2 S nanorod heterostructures. J Phys Chem Lett 5:590–596. doi:10.1021/jz500041g
54. Manzi A, Simon T, Sonnleitner C et al (2015) Light-induced cation exchange for copper sulfide based CO_2 reduction. J Am Chem Soc 137:14007–14010. doi:10.1021/jacs.5b06778

55. Amirav L, Oba F, Aloni S, Alivisatos AP (2015) Modular synthesis of a dual metal-dual semiconductor nano-heterostructure. Angew Chem Int Ed 54:7007–7011. doi:10.1002/anie.201411461
56. Müller J, Lupton JM, Lagoudakis PG et al (2005) Wave function engineering in elongated semiconductor nanocrystals with heterogeneous carrier confinement. Nano Lett 5:2044–2049. doi:10.1021/nl051596x
57. Kraus RM, Lagoudakis PG, Rogach AL et al (2007) Room-temperature exciton storage in elongated semiconductor nanocrystals. Phys Rev Lett 98:017401. doi:10.1103/PhysRevLett.98.017401
58. Rainò G, Stöferle T, Moreels I et al (2011) Probing the wave function delocalization in CdSe/CdS dot-in-rod nanocrystals by time- and temperature-resolved spectroscopy. ACS Nano 5:4031–4036. doi:10.1021/nn2005969
59. Wu K, Rodríguez-Córdoba WE, Liu Z et al (2013) Beyond band alignment: hole localization driven formation of three spatially separated long-lived exciton states in CdSe/CdS nanorods. ACS Nano 7:7173–7185. doi:10.1021/nn402597p
60. She C, Bryant GW, Demortière A et al (2013) Controlling the spatial location of photoexcited electrons in semiconductor CdSe/CdS core/shell nanorods. Phys Rev B 87:155427. doi:10.1103/PhysRevB.87.155427
61. She C, Demortière A, Shevchenko EV, Pelton M (2011) Using Shape to control photoluminescence from CdSe/CdS core/shell nanorods. J Phys Chem Lett 2:1469–1475. doi:10.1021/jz200510f
62. Wu K, Hill LJ, Chen J et al (2015) Universal length dependence of rod-to-seed exciton localization efficiency in type I and quasi-type II CdSe@CdS nanorods. ACS Nano 9:4591–4599. doi:10.1021/acsnano.5b01245
63. Zhu H, Song N, Lv H et al (2012) Near unity quantum yield of light-driven redox mediator reduction and efficient H_2 generation using colloidal nanorod heterostructures. J Am Chem Soc 134:11701–11708. doi:10.1021/ja303698e
64. Acharya KP, Khnayzer RS, O'Connor T et al (2011) The role of hole localization in sacrificial hydrogen production by semiconductor-metal heterostructured nanocrystals. Nano Lett 11:2919–2926. doi:10.1021/nl201388c
65. Khon E, Lambright K, Khnayzer RS et al (2013) Improving the catalytic activity of semiconductor nanocrystals through selective domain etching. Nano Lett 13:2016–2023. doi:10.1021/nl400715n
66. Tong H, Ouyang S, Bi Y et al (2012) Nano-photocatalytic materials: possibilities and challenges. Adv Mater 24:229–251. doi:10.1002/adma.201102752
67. Bang JU, Lee SJ, Jang JS et al (2012) Geometric effect of single or double metal-tipped cdse nanorods on photocatalytic H_2 generation. J Phys Chem Lett 3:3781–3785. doi:10.1021/jz301732n
68. Nakibli Y, Kalisman P, Amirav L (2015) Less is more: the case of metal cocatalysts. J Phys Chem Lett 6:2265–2268. doi:10.1021/acs.jpclett.5b00872
69. Subramanian V, Wolf EE, Kamat PV (2004) Catalysis with TiO $_2$/gold nanocomposites. effect of metal particle size on the fermi level equilibration. J Am Chem Soc 126:4943–4950. doi:10.1021/ja0315199
70. Yu P, Wen X, Lee Y-C et al (2013) Photoinduced ultrafast charge separation in plexcitonic CdSe/Au and CdSe/Pt nanorods. J Phys Chem Lett 4:3596–3601. doi:10.1021/jz401985k
71. Ye C, Regulacio MD, Lim SH et al (2015) Alloyed ZnS-$CuInS_2$ semiconductor nanorods and their nanoscale heterostructures for visible-light-driven photocatalytic hydrogen generation. Chem Eur J 21:9514–9519. doi:10.1002/chem.201500781
72. Murdoch M, Waterhouse GIN, Nadeem MA et al (2011) The effect of gold loading and particle size on photocatalytic hydrogen production from ethanol over Au/TiO_2 nanoparticles. Nat Chem 3:489–492. doi:10.1038/Nchem.1048
73. Sung Y, Lim J, Koh JH et al (2015) Uniform decoration of Pt nanoparticles on well-defined CdSe tetrapods and the effect of their Pt cluster size on photocatalytic H_2 generation. Cryst Eng Comm 17:8423–8427. doi:10.1039/C5CE01502B
74. Ehrat F, Simon T, Stolarczyk JK, Feldmann J (2015) Size effects on photocatalytic H_2 generation with CdSe/CdS core–shell nanocrystals. Z Phys Chem 229:205–219. doi:10.1515/zpch-2014-0635
75. Al-Otaify A, Leontiadou MA, dos Reis FVE et al (2014) Size dependence of ultrafast charge dynamics in monodisperse Au nanoparticles supported on TiO_2 colloidal spheres. Phys Chem Chem Phys 16:14189. doi:10.1039/c4cp01475h
76. Sagarzazu G, Inoue K, Saruyama M et al (2013) Ultrafast dynamics and single particle spectroscopy of Au–CdSe nanorods. Phys Chem Chem Phys 15:2141. doi:10.1039/c2cp43458j
77. Shaviv E, Schubert O, Alves-Santos M et al (2011) Absorption properties of metal-semiconductor hybrid nanoparticles. ACS Nano 5:4712–4719. doi:10.1021/nn200645h

78. Demortière A, Schaller RD, Li T et al (2014) In situ optical and structural studies on photoluminescence quenching in CdSe/CdS/Au heterostructures. J Am Chem Soc 136:2342–2350. doi:10.1021/ja4092616
79. Wang P, Zhang J, He H et al (2015) The important role of surface ligand on CdSe/CdS core/shell nanocrystals in affecting the efficiency of H_2 photogeneration from water. Nanoscale 7:5767–5775. doi:10.1039/C4NR07343F
80. Berr MJ, Wagner P, Fischbach S et al (2012) Hole scavenger redox potentials determine quantum efficiency and stability of Pt-decorated CdS nanorods for photocatalytic hydrogen generation. Appl Phys Lett 100:223903. doi:10.1063/1.4723575
81. Schneider J, Vaneski A, Pesch GR et al (2014) Enhanced hydrogen evolution rates at high pH with a colloidal cadmium sulphide–platinum hybrid system. APL Mater 2:126102. doi:10.1063/1.4904070
82. Kalisman P, Nakibli Y, Amirav L (2016) Perfect photon-to-hydrogen conversion efficiency. Nano Lett 16:1776–1781. doi:10.1021/acs.nanolett.5b04813
83. Wu K, Chen J, McBride JR, Lian T (2015) Efficient hot-electron transfer by a plasmon-induced interfacial charge-transfer transition. Science (80-) 349:632–635. doi:10.1126/science.aac5443